Dissertation

submitted to the
Combined Faculties for the Natural Sciences and for Mathematics
of the Ruperto-Carola University of Heidelberg, Germany
for the degree of
Doctor of Natural Sciences

presented by
Dipl.-Phys. Jochen Steinmann
born in Stuttgart

Oral examination: 18.07.2007

Multiphoton Ionization of Laser Cooled Lithium

Gutachter: **Priv.-Doz. Dr. Alexander Dorn**
Junior-Prof. Dr. Selim Jochim

Zusammenfassung:

Reaktionsmikroskope ermöglichen die kinematisch vollständige Erfassung von atomaren und molekularen Fragmentationsprozessen. Wurden bisher überwiegend Überschall-Gasstrahlen zur Erzeugung ultrakalter Target-Atome verwendet, kombiniert die im Rahmen dieser Arbeit entwickelte Apparatur erstmalig das Prinzip des Reaktionsmikroskops mit einer magneto-optischen Falle. Diese ermöglicht die Präparation von Lithium-Atomen mit Temperaturen im sub-mK-Bereich. Lithium ist auf Grund seiner einfachen atomaren Struktur mit nur drei Elektronen als Modellsystem für verschiedenste Arten von Ionisationsprozessen von besonderem Interesse. Um die Impulsbestimmung der geladenen Fragmente nicht durch das magnetische Feld der Atomfalle zu beeinträchtigen, wird die Falle selbst in einem gepulsten Modus bei einer Schaltrate bis zu 300 Hz betrieben. Hieraus resultieren feldfreie Bedingungen während der Detektionsphasen, gleichzeitig gewährleistet dies eine effiziente Nutzung der gespeicherten Atome. Mit der neuartigen Apparatur steht nun ein universelles Target zur Untersuchung der Ionisation von Lithium durch Elektronen- und Ionenstoss sowie der Photoionisation zur Verfügung. Erstmalig wurde die Multiphotonionisation von Lithium in intensiven Laserfeldern mit Pulsdauern von 25 fs und Spitzenintensitäten zwischen 10^{11} W/cm^2 und 10^{16} W/cm^2 impulsaufgelöst vermessen. Dabei zeigten sich unerwartete Strukturen in den Photoelektronenspektren, wie z.B. eine bevorzugte Emission senkrecht zur Polarisationsachse des Lichtfeldes, welche derzeit noch nicht vollständig verstanden sind. Entsprechende Rechnungen sind bei mehreren Theoriegruppen in Arbeit.

Abstract:

Reaction microscopes enable kinematically complete measurements of atomic and molecular fragmentation. An ultracold atomic target is usually provided by a supersonic gas jet. The apparatus developed in the course of this thesis for the first time combines the principle of the reaction microscope with a magneto-optical trap. This allows for the preparation of lithium atoms in the sub-mK range. Being a three-electron system, its simple atomic structure makes lithium a model system of great topical interest for all kinds of ionization reactions. In order not to deteriorate the determination of the momenta of the charged fragments by the magnetic field of the trap, a pulsed mode of operation is adopted, creating field-free conditions during data acquisition and making efficient use of the stored target. The novel apparatus provides a versatile target for investigations on fragmentation of lithium by electron, ion and photon impact. For the first time, momentum-resolved measurements on multiphoton ionization in intense laser fields with pulse durations of 25 fs and peak intensities in the range between 10^{11} W/cm^2 and 10^{16} W/cm^2 were performed. The acquired photoelectron spectra exhibit unexpected structures such as a preferred emission in the direction perpendicular to the laser polarization axis, which are not fully understood yet. Presently, corresponding calculations are being done in several theory groups.

Contents

Introduction and motivation

Atoms, molecules and ions are the basic building blocks of all complex structures in the universe and the understanding of their structure and the dynamics of their interaction is of fundamental relevance not only in physics, but also in chemistry, biology, astronomy, medicine and material science and a scientific treatment of many systems on a quantum physical level is becoming of increasing importance. There has been a tremendous progress in both the theoretical description and experimental determination and verification of the properties of stationary quantum systems, i.e. atoms, ions and molecules in terms of their energy levels and wave functions. On the experimental side, there is a continued development in spectroscopic tools and techniques. This concerns radiation sources, as well as methods of preparation of atoms, ions and molecules for precision spectroscopy and means of detection.

State-of-the-art atomic structure calculations, incorporating quantum-electrodynamic effects, can in many cases match the degree of precision of the most refined measurements, as impressively demonstrated by experimental determination [Fis04] and theoretical prediction of the 1s–2s transition energy of the hydrogen atom [Jen05].

For the dynamics of interacting quantum systems at the most basic level, the picture looks quite different. As yet, there is no unified theoretical approach to describe real few-body time-dependent quantum systems, such as single or double ionization of a multi-electron atom by charged particle impact. Even today, in times of almost ubiquitous availability of computing power, a brute force approach to a numerical solution of the full multidimensional Schrödinger equation (for the simplest non-relativistic case) is still beyond present day's computing capacities. Most of the calculational techniques rely on an approximative treatment of the system under consideration, making them applicable only under certain conditions, such as a particular range of impact energies or collision geometries. It was not until 1999, when it was claimed, that an exact description of the most fundamental three-body Coulomb problem, the ionization of a hydrogen atom by an electron 'has been reduced to practical computation' [Res99]. It shall be noted here, that despite all the difficulties to find an adequate theoretical description within the framework of quantum mechanics, many of the processes and fragmentation channels can be cast into appealingly intuitive and simple mechanistic pictures, which greatly facilitate their identification and the interpretation of experimental data.

For a thorough understanding of atomic reactions and the development and benchmarking

of theories with high predictive power, high quality experimental data are indispensable. A complete mapping of an atomic or molecular fragmentation process requires knowledge of the initial state and the registration of the complete final state. Most experiments devoted to atomic fragmentation were only capable of covering a small selected fraction of the final state phase space and/or integrated over large parts of it, be it by detecting only one particle out of three or detecting only the energy or direction of emission. One exception were the so called (e,2e) experiments which were performed starting from 1969 [Ehr69], in which single ionization of atoms and molecules was studied in a kinematically complete way for the first time. This was achieved by detection of both final state electrons in coincidence by electrostatic spectrometers. Nevertheless, the phase space acceptance was rather limited and the technique was applicable to processes with large cross sections only. A big leap forward was made with the invention of the 'reaction microscope' in 1994 by Ullrich and Moshammer [Mos94], [Mos96], [Ull03a]: Combining a recoil-ion momentum spectrometer with momentum resolved electron detection and using appropriate guiding fields, a solid angle acceptance of 4π for all low energetic target fragments can be achieved. A well defined initial state is prepared by cooling the target atoms or molecules down to the sub-K range in a supersonic gas jet (therefore the method is also called COLTRIMS for COLd Target Recoil Ion Momentum Spectroscopy). Thus real 'momentum spectroscopy', i.e. the experimental determination of all observables of the quantum-mechanical process and a mapping of the whole final state phase space, became feasible.

The possibility of measuring fully differential cross sections, preserving the information on all correlations between the involved particles, has since been successfully applied to many collision systems. Some of the most notable achievements shall be briefly mentioned: In ionizing collisions of fast ions (MeV/amu) with helium atoms, otherwise unmeasurably small relative projectile energy losses of $\Delta E/E \approx 10^{-7}$ and scattering angles in the μrad range could be reconstructed by the momentum balance of the collision system [Mos94], [Ull03b]. Further fully differential studies in fast ion-helium collisions revealed discrepancies with all existing theoretical treatments, uncovering subtle higher order effects due to additional interaction of the projectile with the target core, not included in state-of-the-art ion collision theories [Sch03].

It were reaction microscopes, that enabled the doubtless identification of the recollision mechanism, where an electron ionized in an intense femtosecond laser pulse is driven back to the parent ion by the electric field and knocks out a second electron, as the dominant channel in double ionization in strong laser fields [Mos00], [Web00], [Feu01], [Rud04a]. The application of reaction microscopes to atomic and molecular systems subjected to intense laser fields culminated in a series of pump-probe experiments on H_2 and D_2, where temporal evolution of the rovibrational wave-packet of the vibrationally excited D_2^+ molecule could be mapped in real-time over hundreds of vibrational periods via Coulomb explosion imaging [Erg05], [Aln05], [Erg06], [Che99].

The field of electron-atom collisions has likewise profited from application of advanced multiparticle imaging techniques: In particular for the model system helium fully differential data sets of single ionization (e,2e) and double ionization (e,3e) have been acquired

in the high energy impact regime at 1-2 keV [Dor02a], [Dor01], [Dür06c] as well as close to ionization threshold [Dür06b], [Dür07], giving a complete picture of the correlated dynamics of the target- and projectile electrons as well as the ion in the three- and four-body Coulomb continuum. These datasets represent an ultimate benchmark for recently developed theoretical descriptions and calculational methods of the most fundamental three- and four-body quantum systems.
Other fields of atomic and molecular physics, where reaction microscopes have enabled new insights into dynamics of basic quantum systems include the interaction of atoms and small molecules with soft X-ray radiation from synchrotrons, as demonstrated with helium [Spi95] or deuterium [Web06]. Recently a new line of experiments has been launched [Mos07], employing newest generation light sources such as the free electron laser (FEL) FLASH in Hamburg, capable of delivering ultrashort (30 fs) and ultraintense ($>10^{13}$ W/cm^2) coherent pulses of soft X-ray photons, opening the door to a completely new terrain of light-matter interaction studies.

There is another domain of atomic physics, that has revolutionized and rejuvenated atomic physics during the last two decades which is the field of laser cooling of neutral atoms and ultracold atomic gases. The idea of actively cooling an atomic gas by scattering of near resonant laser light was proposed in 1975 by Hänsch and Schawlow [Hän75]. First demonstrations of this application of laser light were performed in form of experiments where sodium atomic beams could be slowed down and cooled to almost zero velocities [Bal79], [Ert85], [Ste86] by a counterpropagating laser beam. In 1985 Chu *et al.* succeeded in employing the light forces for three-dimensional confinement of slow atoms, first in an three-dimensional optical molasses (acting only in velocity space), later position dependent restoring forces were added to bring about real spatial confinement with long storage times. This was accomplished by trapping the molasses-cooled atoms in the focus of a far red detuned laser beam [Chu86] by means of the optically induced dipole force [Gri00]. Raab *et al.* relized a spatial confinement by adding a magnetic field gradient to invoke a position-dependent light scattering force via the Zeeman effect [Raa87]. This type of trap became known as the magneto-optical trap, or shortly MOT, which can accumulate between 10^6 and 10^{10} atoms at temperatures of typically 100 μK.
Quickly the magneto-optical trap evolved into a standard tool of atomic physics and quantum optics, e.g. for precision spectroscopy, atomic clocks [Kas89] and the study of cold collisions [Wal94b]. Its implementation and the theoretical description of the subtle cooling effects taking place in an optical molasses [Dal89] was rewarded with a nobel-prize for S. Chu, W. Phillips and C. Cohen-Tannoudji in 1997.
The perhaps greatest relevance of magneto-optical trapping for modern physics lies in the fact, that magneto-optical traps are an essential step and indispensable pre-stage in the preparation of degenrate quantum gases, which has become a rapidly growing field since the mid-nineties of the last century, when two research groups achieved Bose-Einstein condensation (BEC) of magnetically trapped sodium atoms independently at almost the same time in 1995 [And95], [Dav95], resulting in a nobel prize awarded to C. Wieman

and E. Cornell and to W. Ketterle in 2001. We only want to briefly list some highlights out of the broad range of cold atom based research. These include nonlinear atom optics with coherent matter waves like the atom laser [Ino99], [Blo99] and four wave mixing [Den99], or the observation of condensed-matter phenomena in quantum state prepared Bose- and Fermi-gases in optical lattices, such as Bloch-oscillations [Dah96] and quantum phase transitions [Gre02]. Newest developments are the production of molecular Bose-Einstein condensates [Don02], [Her03] and the recent successes to exploit the tunability of the two-body interaction strength between ultracold atoms to probe the BEC-BCS crossover regime [Bar04] or to create peculiar bound states between atoms like Efimov trimers [Kra06].

The magneto-optical trap also found applications in scattering experiments, since it provides a well characterizable ensemble of target atoms, in terms of its atom number, density, its quantum state and its internal temperature. One method to measure absolute ionization cross sections is irradiating the MOT-target with a projectile beam and to measure the ionization induced loss of atoms by monitoring the fluorescence emitted by the laser trapped atoms. Such measurements have been performed for electron impact ionization, e.g. on rubidium [Sch96], [Kee00], cesium [Mac02] and lithium and metastable neon [Uhl05], and for photoionization (Rb: [Din92], Cs: [Mar98]).
Exploiting its main benefit, the intrinsically low temperature, a MOT lends itself as a target for high resolution momentum spectroscopy. This was demonstrated in the pioneering experiment by Wolf and Helm, who performed time-of-flight spectroscopy with recoil-ions from multiphoton ionization of atoms in a rubidium MOT of 300 μK temperature with an energy resolution of 1 μeV [Wol97], [Wol00]. Since then, alkaline metal MOTs have become particularly popular for kinematically complete experiments on charge transfer and electron capture reactions between the neutral laser-cooled atoms and slow ions. Since in charge transfer reactions there are only two particles in the final state – the scattered projectile and the residual target ion, whose initial state has been well prepared – it is sufficient to detect the recoiling target ion in order to obtain the complete kinematics of the reaction. Studies have been performed e.g. with sodium [Tur01], [Poe01] and rubidium [Bre03], where Flechard *et al.* claim a momentum resolution of 0.03 a.u., meaning the velocity of the recoiling Rb^+ has been measured with an accuracy better than 1m/s [Fle01]. Being a variation on the COLTRIMS theme, this method was named MOTRIMS.

Taking the next step in development, the work presented in this thesis aims to study ionization reactions involving ultracold atoms, where ions and ejected electrons have to be detected in coincidence. Therefore the technically challenging task to combine for the first time modern optical target cooling and trapping methods in form of a magneto-optical trap with most-advanced multi-particle imaging technologies (reaction microscope), allowing for the coincident detection of the recoil-ion as well as the electron from ionization of an ultracold lithium target. The goal was, to develop a versatile apparatus, that would be equally suitable for fully differential measurements involving all kinds of projectiles,

namely electrons, photons and ions, with unprecedented momentum resolution. Besides, a MOT-target offers the intriguing possibility of further manipulation of the atoms and the preparation of specific target states, such as highly excited states or the population of specific angular momentum states by optical pumping.
The element of choice is lithium. Being a three-electron system, it forms the next step in complexity after helium. Its loosely bound outer electron and deeply bound closed inner shell makes it a qualitatively completely different target as compared to the noble gases, which have so far been used in fully differential investigations of ionization reactions with reaction microscopes. Though its preparation in a MOT is afflicted with more experimental hardships than for example rubidium or cesium, lithium has more advantages at hand: It enables a better momentum resolution than the heavier alkaline metals due to its low mass (7 amu), meaning, when cooled to the same temperature, it will have a momentum 3.5 times lower than a rubidium atom. Furthermore, if stripped of one or two of its electrons, its ionic core will find itself in a helium-like or hydrogen-like configuration, two well known model systems of atomic physics, which greatly simplifies theoretical treatment. In triple ionization finally, a structureless nucleus is left behind, so there are no excitations or correlations of electrons in deeper shells which could complicate the analysis of the process. Therefore, it is not surprising, that, with advances in theoretical modeling, lithium has attracted considerable attention from theorists. There are numerous approaches to tackle the problem of triple electron ejection from lithium, including large scale numerical calculations [Col04], [Col06], so-called half collision models [Pat01] and quasiclassical Monte Carlo trajectory simulations [Emm06b], [Emm06a]. It is therefore destined, to become a benchmark atomic system of the future, as helium is now [Col01].

In the course of this thesis, a novel apparatus has been designed, built and taken into operation virtually from scratch, combining the basically incompatible techniques of the reaction microscope and the magneto-optical trap. The principle of the magneto-optical trap relies on the application of a strong magnetic gradient field to the atomic sample in the presence of the laser field. Since this is in conflict with the requirements of electron momentum spectroscopy, which demands an extraction field of excellent homogeneity and stability, the atoms cannot be held trapped, when charged particles are to be detected: The gradient field of the MOT would severely distort their trajectories and render reconstruction of the momentum vectors impossible. To overcome this problem, the trap is operated in a pulsed fashion, where the cold atoms are subsequently released from the trap, leaving a short field free period in the range of milliseconds for charged particle detection and then recaptured to cool and recompress the atomic cloud for the next projectile shots. From the technical side this required, that the design of both the apparatus of the MOT and the reaction microscope had to be adapted to each other without compromising performance or operability.
The realization of the experimental setup comprised the design and implementation of all the essential components of a reaction microscope, such as a combined electron and ion spectrometer and position-sensitive detectors. The magneto-optical trap made the devel-

opment of a diode laser-based laser system suitable for laser cooling of lithium necessary, since at the time the project was started, no high power semiconductor laser sources were available at the wavelength of the lithium cooling transition. Other key building blocks included a slow atomic beam source for loading the trap, a viable switching circuitry for pulsed MOT-operation and a computer based control and data acquisition system.
After succesfull comissioning, a first measurement on multiphoton ionization of lithium in intense laser pulses of femtoseconds duration and intensities up to the Petawatt range was conducted, in order to shed light on the different characteristics with respect to ionizaton between our alkali target and the extensively studied rare gases. Indeed a qualitatively completely different signature is observed in the spectra. To our knowledge only two measurements on alkali atoms (namely cesium) at comparable peak intensities and pulse durations have been conducted so far [Nic92], [Dru95], actually more than ten years ago. Thus our efforts should help to shift the attention to this class of targets again, given the fact that now advanced means for the acquisition of fully differential cross sections with unsurpassed momentum and energy resolution are at hand. The obtained results have also brought this topic to the attention of theorists and have triggered a series of calculations. Further measurements to confirm our results and eludicate the mechanisms and dynamics of the ionizaton process, also at other wavelengths than the previously used 800 nm radiation from a titanium-sapphire laser, are presently under way.
This thesis is organized as follows: Chapter one introduces the reader to the phenomena and theoretical basics of multiphoton ionization, while the second chapter reviews the principles of laser cooling and trapping of neutral atoms, and the properties of lithium specific to laser cooling. The third chapter is dedicated to the experimental setup, starting with the concept of the reaction microscope and the implications of combining it with a magneto-optical trap. Detailed information about the numerous different components of the setup is given in the following. Chapter four reviews measurements on the lithium MOT in view of its properties as a target for ionization experiments. Particularly the response of the trapped atoms to the rapidly switched magnetic field of the trap is studied in detail. Chapter five finally presents results of the first experiment on multiphoton ionization of lithium in intense laser fields. Starting with a description of the experimental procedure and conditions, the properties of lithium in the context of multiphoton ionization and the implications of using a MOT-target are discussed. The results of the measurements are critically analyzed and compared to first theoretical calculations. This work finishes with a conclusion and gives an outlook on future perspectives for experiments with this unique research tool.

Chapter 1

Basics of Multiphoton Ionization

This chapter aims at introducing the reader to the variety of phenomena encountered in ionization of atoms by intense light fields. Progress in laser technology has steadily made new regimes of intensity, frequency and pulse length accessible to science and application. In the field of atomic physics, this has led to ever new insights into the ionization dynamics of an atom subjected to strong laser pulses which goes far beyond the simple ejection of an electron.

1.1 Mechanisms of Multiphoton Ionization

It is a commonly known textbook fact, that the ejection of an electron from its bound state, say, in an atom or a solid, by a photon into the continuum can only occur, if the energy of the incident photon is larger than the binding energy of the electron. At sufficiently high photon flux densities, however, there is an increasing probability for a simultaneous absorption of two or even more photons by the atom. If the total energy of these n absorbed photons is higher than the ionization potential IP, the atom A is ionized by the light field, whose single photon energy $\hbar\omega$ is much less than the ionization potential:

$$A + n \cdot \hbar\omega \longrightarrow A^+ + e. \tag{1.1}$$

In the case of a free atom, as encountered in the usual experimental situation, it follows from momentum conservation between the residual ion and the photoelectron, that the latter carries away all but a tiny fraction of less than 1/2000 of the excess energy

$$E_{\mathrm{ex}} = n \cdot \hbar\omega - \mathrm{IP}. \tag{1.2}$$

Basically two regimes of multiphoton ionization are commonly distinguished: At low intensities, the light field represents only a small perturbation of the atomic system and the transition of an electron from the ground state to the continuum can be reasonably described by the common perturbative approach in terms of time-dependent perturbation theory. Going to higher intensities, the atomic structure becomes more strongly affected and a pertubative treatment will run into difficulties [Pro96]. However, as long as the

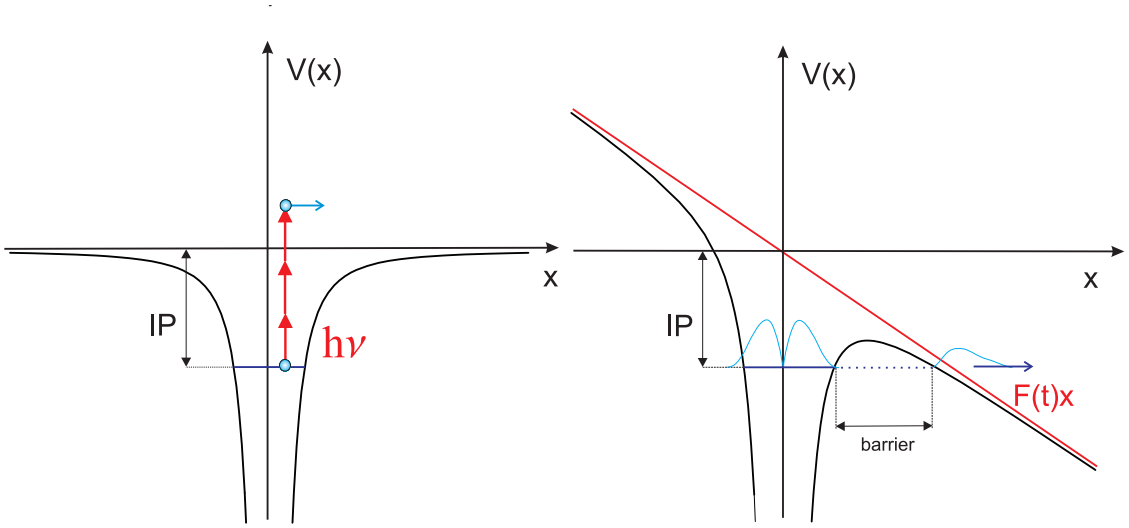

Figure 1.1: Multiphoton and tunneling ionization: At low field intensities or high photon energies / field frequencies, the ionization process proceeds through absorption of several photons. In intense laser fields with field strength close to the effective field of the nucleus, the coulomb potential is tilted by the light field. A finite potential barrier is created, through which the electron wave packet leaks out, analogous to DC-field ionization. IP refers to the binding energy of the electron in the unperturbed atomic system.

ionization processes can be at least phenomenologically described by the absorption of n photons by discrete bound states, they are subsumed under the label *multiphoton ionization* (MPI). At the extremely high photon flux densities (or intensities) achievable by modern pulsed laser sources, the electric field strength of the light field becomes comparable in magnitude to the field the outer electrons experience in the atomic potential. If one adopts a classical field perspective on the laser field, the atomic potential well is strongly deformed by the laser's electric field, and at sufficiently high field strength, a finite potential barrier is created, through which the electron can tunnel out. If the field frequency is low compared to the classical frequency of the bound electron's motion, the ionization probability is greatly enhanced by this process, which is called *tunneling* or *tunneling ionization* (TI).
Both regimes are distinguished by the so-called adiabaticity- or Keldysh parameter γ, which relates the time-scales of atomic motion and the laser field [Kel64]:

$$\gamma = \frac{\omega_{\text{laser}}}{\omega_{\text{tunnel}}}. \tag{1.3}$$

The Keldysh parameter can be expressed in terms of the ionization potential IP and the ponderomotive potential U_p,

$$\gamma = \sqrt{\frac{\text{IP}}{2U_p}}. \tag{1.4}$$

The ponderomotive potential U_p is the time averaged kinetic energy (quiver energy) of a free electron oscillating back and forth in the driving laser field and contains the characteristic parameters of the laser field, namely the peak field strength F/intensity I and

frequency ω.

$$U_p = \frac{F^2}{4\omega^2} = \frac{I}{4\omega^2}. \tag{1.5}$$

Here, atomic units have been employed (m_e=1, q_e=e=1, c=1, $\hbar$=1). If the intensity is specified in W/cm^2 and the frequency of the laser field in terms of the wavelength λ in μm, one gets for the ponderomotive energy in eV:

$$U_p = 9.33 \times 10^{-14} I[\mathrm{W/cm^2}]\lambda^2[\mu\mathrm{m}]. \tag{1.6}$$

1.1.1 Free Electrons in a Laser Field

In the interpretation of the physics taking place in multiphoton ionization at high intensities, not only the reaction of the bound system to the field has to be taken into account, the response of the ionized charged particles to the external field is of equally decisive importance. To clarify this, it is instructive, to inspect the classical equation of motion of an electron in a laser field. A charged particle of mass m in a time-varying electric field $E(t)$ of linear polarization oriented along direction x experiences the acceleration

$$\ddot{x} = \frac{q}{m} E(t). \tag{1.7}$$

The electric field $E(t)$ of a laser pulse with a carrier frequency ω and peak field strength F_0 can be described by the expression

$$E(t) = F(t) \cdot \sin(\omega t) = F_0 \cdot f(t) \cdot \sin(\omega t), \tag{1.8}$$

where $f(t)$ is the envelope of the pulse, which is assumed to vary slowly compared to the time scale of an optical cycle. With this prerequisite the velocity $\dot{x}$ and position x of an electron ionized at instant t_0 (or in a field of constant amplitude F_0) are given by

$$\dot{x}(t) = v_0 - \tfrac{q}{m\omega} F_0(\cos(\omega t) - \cos(\omega t_0)) \tag{1.9}$$

$$x(t) = x_0 + (v_0 + \tfrac{q}{m\omega} F_0 \cos(\omega t_0))(t - t_0) - \tfrac{q}{m\omega^2} F_0(\sin(\omega t) - \sin(\omega t_0)), \tag{1.10}$$

where x_0, v_0 are the initial position and velocity of the electron, respectively.
From (1.10) it can be seen, that $\dot{x}(t)$ is the sum of three contributions, the initial velocity v_0, an additional drift velocity dependent on the phase of the field at time t_0 and an oscillatory motion with frequency ω, the quiver motion of the particle. The kinetic energy T of the particle is

$$T(t) = \frac{1}{2} m \dot{x}(t)^2. \tag{1.11}$$

Averaging over one or several optical cycles yields

$$\int_{t=t_0}^{t_0+2\pi/\omega} \mathrm{d}t \frac{T(t)}{(2\pi/\omega)} = \frac{1}{2} m v_0^2 + \frac{1}{4} \frac{q^2 F_0(t_0)^2}{m\omega^2} + \frac{1}{2} \frac{q^2 F_0(t_0)^2}{m\omega^2} \cos^2(\omega t_0) - \frac{1}{2} \frac{q F_0(t_0)}{\omega} \cos(\omega t_0) v_0. \tag{1.12}$$

The first term is the initial kinetic energy of the particle, while the phase-independent second term in (1.5) stems from the quiver motion and represents the ponderomotive

potential U_p introduced in (1.5). The phase-dependent third term maps the drift energy of the particle gained in the laser field, the fourth term is called the cross term.
The defining equation for U_p consequently is

$$U_p = \frac{1}{4}\frac{q^2 F_0(t_0)^2}{m\omega^2}. \tag{1.13}$$

Expressing the above equations in atomic units and regarding only electrons, reproduces equation (1.5), U_p=$F_0(t_0)^2/(4\omega^2)$. We rewrite (1.12) in terms of U_p:

$$T = T_0 + U_p + 2U_p \cos^2(\omega t_0) - 2\sqrt{2U_p T_0} cos(\omega t_0), \tag{1.14}$$

where T_0 is the initial energy of the electron, e.g. the excess energy gained from the ionization process.
Equation (1.14) tells us a lot about what information can be extracted from the registration of the energies of ionized electrons: At low intensities, the ponderomotive potential will be small compared to the excess energy of the photoionization which is on the order of the photon energy, and the electron energy will carry information about the atomic energy levels and the number of photons involved in the process.
In strong laser fields with peak intensities beyond 10^{14} W/cm^2, U_p reaches values of several 10 eV and more, easily exceeding T_0, so that it becomes negligible and the energy of the detected electron will depend on the phase and intensity of the laser field at the time it was liberated.

Short Pulses vs. Long Pulses

Since the ponderomotive potential is linear in the instantaneous intensity $I(t)$, it varies with the envelope of the pulse. The laser field is not only inhomogeneous in time, but also in space, to achieve reasonably high intensities, strongly focused laser beams with typical waist radii on the order of 10 μm have to be used. Thus a spatially varying effective potential $U_p(\mathbf{r}, \mathbf{t})$ is created. A 'long' pulse of 100 ps duration will not considerably change in intensity on the timescale of the electron's motion out of the focus due to the gradient force F_p=∇U_p, and the electron will have time to surf down the edge of the focus and convert its initial ponderomotive energy to kinetic energy. Thus, the maximum electron energy in the long pulse limit is $3U_p$. In femtosecond laser pulses of 100 fs and less duration, the intensity will level off, before the electron has changed its position, so U_p is not a conservative potential any more and the ponderomotive term of (1.14) approaches zero, leading to a maximum electron energy in the short pulse limit of $2U_p$.
In the high intensity regime, the repulsion of the photoelectrons from the laser focus leads to a severe distortion of the electron's angular emission pattern [Fre86], because the detected final state of the electrons now depends not only on their initial energy and the time they were created, but also on their source point within the focus and the spatial intensity distribution, so it is desirable to perform angle or momentum resolved experiments in the short pulse domain.

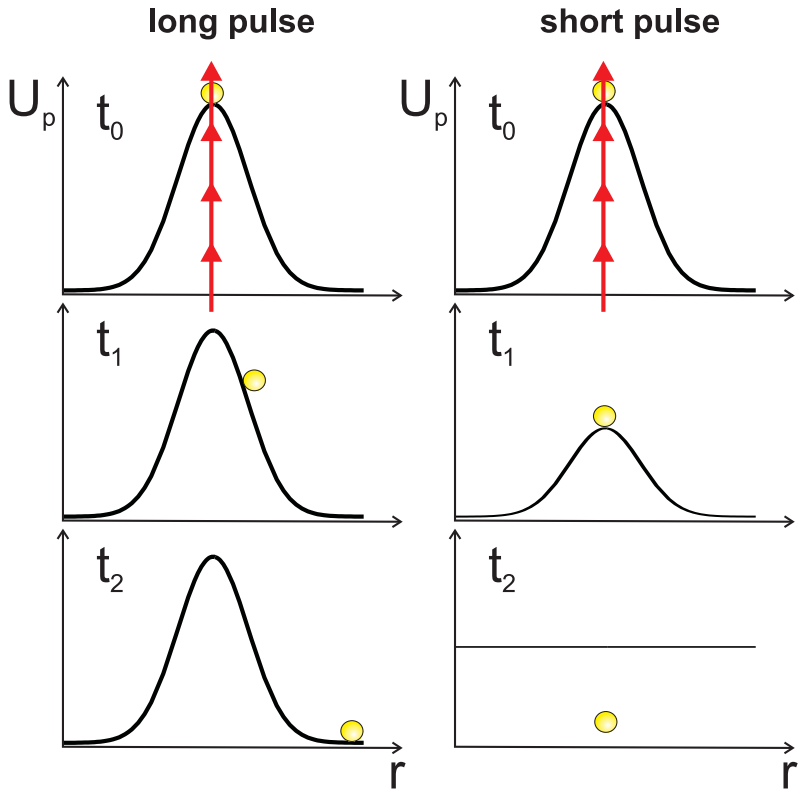

Figure 1.2: In the long pulse regime (*left*), the pulse is quasi-static with respect to the electron's motion in the ponderomotive potential of the laser focus. In the short pulse regime (*right*), the intensity reduces to almost zero before the electron has significantly moved out of the focus.

In the short pulse regime, ponderomotive scattering plays no role and the observed electron energies faithfully map the kinetic energy of the photoelectrons at the time they were separated from their parent ion. If instead of the electrons the recoil-ions are detected (as in our experiment), ponderomotive effects on the ions' momenta can be neglected, as their U_p is some 10^4 times weaker due to their large mass. The same information is retrieved by both methods, since the electron can only gain its drift momentum in the presence of the residual ion as a collision partner for momentum conservation.

1.1.2 Multiphoton Ionization

In the regime of multiphoton ionization, the ionization rate $R(\omega)$ obeys a characteristic scaling law,

$$R(\omega) = \sigma_k(\omega)\Phi^k = \kappa_k(\omega)I^k, \tag{1.15}$$

with k being the number of absorbed photons needed in the ionization process under consideration and Φ the photon flux. σ_k and κ_k are generalized cross section of dimension $[\sigma_k]$=cm^{2k}s^{k-1} and $[\kappa_k]$=W^{-k}cm^{2k}s^{-1}. k is called the order of nonlinearity.
The generalized cross section can be derived from time-dependent perturbation theory (e.g. by the evolution operator expansion method) and formulated in terms of a n-th

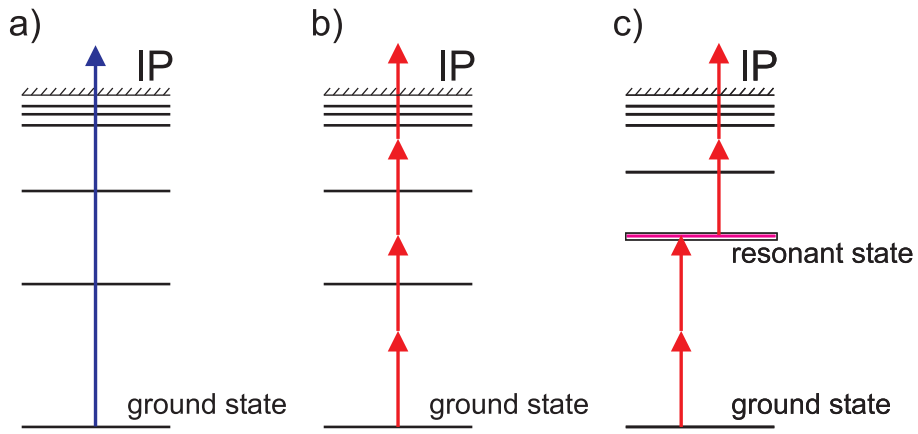

Figure 1.3: Photoionization of an atom:**a)** Single photon ionization (photo effect); **b)** Non-resonant multiphoton ionization (NRMPI or simply MPI); **c)** Resonance enhanced multiphoton ionization (REMPI).

order matrix element between the initial state $|i\rangle$ and the continuum states $|f\rangle$ [Beb66]:

$$\sigma_n \propto \sum_f \sum_{k_{n-1}} \sum_{k_{n-2}} \cdots \sum_{k_2} \sum_{k_1} \times \left| \frac{\langle f|\hat{\mu}|k_{n-1}\rangle\langle k_{n-1}|\hat{\mu}|k_{n-2}\rangle \ldots \langle k_2|\hat{\mu}|k_1\rangle\langle k_1|\hat{\mu}|i\rangle}{(\Delta E_{k_{n-1},f} - (n-1)\hbar\omega + \imath\hbar\Gamma/2)\ldots(\Delta E_{k_2,k_1} - 2\hbar\omega + \imath\hbar\Gamma/2)(\Delta E_{k_1,i} - \hbar\omega + \imath\hbar\Gamma/2)} \right|^2. \tag{1.16}$$

This matrix element consists of the sum of products of dipole matrix elements, weighted with the detunings $(\Delta E_{j,k} - m \cdot \hbar\omega)$ of m-photon resonances, with $E_{j,k}$ as the energy differences between states $|j\rangle$ and $|k\rangle$. These are the energy denominators known from perturbation theory. $\hat{\mu}$ is the electric dipole operator. The summations are carried out over the complete set of basis states, i.e. extended over all bound and continuum states. In order to prevent an energy denominator from diverging in the case of an intermediate m-photon resonance, a damping term $\imath\hbar\Gamma/2$ is added, often on phenomenological grounds [Beb66]. The rate Γ can account for the lifetime of the intermediate state and the linewidth of the transition, respectively or other effects leading to line broadening, such as a possible AC-Stark shift, and a finite bandwidth of the driving field [Del99]. For an accurate treatment of the near resonant case, higher order terms of the evolution operator expansion have to be taken into account [Mor76]. This indicates, that the occurrence of such intermediate resonances strongly modifies the multiphoton ionization cross section: Basically two mechanisms of multiphoton ionization are distinguished, non-resonant multiphoton ionization (NRMPI) and resonance-enhanced multiphoton ionization (REMPI): In a REMPI-process (Figure 1.3 c)), an intermediate atomic level is (near-) resonantly excited by a m-photon transition from the ground-state and strongly populated. This excited state is then ionized by subsequent absorption of n further photons, wheras in the case of NRMPI no such resonance occurs (Figure 1.3 b)):

$$\begin{aligned} A + m \cdot \hbar\omega &\rightarrow A^* \\ A^* + m \cdot \hbar\omega &\rightarrow A^+ + e. \end{aligned} \tag{1.17}$$

Since the net-number of photons needed to ionize from the excited state A^* is less than that for a direct transition from the ground state to the continuum, the ionization rate is greatly enhanced by the occurrence of such intermediate m-photon resonances. In the example of Figure 1.3, the four-photon transition of the non-resonant case is replaced by a resonant two-photon excitation, followed by two-photon ionization. In many cases, the resonant state is a high lying state (Rydberg state) so that the number of photons m absorbed to reach this state is higher than the number of photons n needed to ionize from there [Sch98b]. In this case, the process can be regarded as a n-th order process followed by a m-th order process (where m is often one) and its probability is much larger than the probability for the direct process in the non-resonant case [Mor76].
Consequently the multiphoton cross section exhibit a strong dependence on the photon energy and, for high intensities ($> 10^9$ W/cm^2), on the intensity itself, because AC-Stark shifted intermediate atomic levels can become resonant with the driving field for a certain intensity [Cam89].

1.1.3 Above-Threshold Ionization

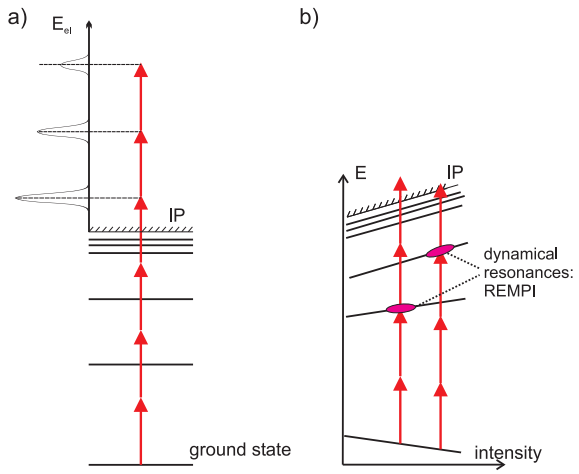

Figure 1.4: **a)** Above threshold ionization (ATI); **b)** Resonance enhancement of ionization at high laser intensities: An initially non-resonant intermediate state is shifted into resonance in the course of the laser pulse due to the intensity dependent AC-Stark shift (Section 1.1.4).

At sufficiently high intensities, a bound electron can absorb more photons, than the n ones necessary to reach the continuum. This effect was first observed in 1979 by Agostini *et al.* [Ago79] in 6-photon ionization of xenon at an intensity of $8{\cdot}10^{12}$ W/cm^2 with laser pulses of 10 ns duration (deeply in the long pulse regime). These experimental results were rather surprising, since a free electron cannot gain asymptotic energy by absorption of photons from an oscillating light field alone (as discussed in section 1.1.1). It is the presence of the Coulomb field of the still nearby ion, that enables the absorption of additional photons by the continuum electrons. Experimentally, a second peak in the electron energy spectrum besides the expected one produced by 6-photon absorption, shifted by one photon-energy

was found, which was attributed to the absorption of a 7th photon. For higher intensities, whole series of equidistant electron peaks have been observed. This phenomenon is called Above-Threshold Ionization (ATI). Consequently, the electron energy of an ATI-peak of order s is

$$E^s_{\mathrm{ATI}} = n \cdot \hbar\omega + s \cdot \hbar\omega - \mathrm{IP} - U_p, \tag{1.18}$$

where n is the threshold number of photons to ionize the atom. The ponderomotive potential has been included into the above equation, because at the intensities where higher-order ATI becomes observable, the ponderomotive potential attains the same order of magnitude as the electron- and photon energy (see below). In experiments with long pulses, the U_p-term of (1.18) reduces to zero, because the photoelectrons regain this energy on their way out of the laser focus, so the ponderomotive shift of the ionization potential was not directly visible in these experiments. Instead, a long pulse ATI spectrum consists of a series of peaks, spaced by the photon energy. The number of photons absorbed is directly inferred from the energy of the peaks (see Figure 1.5). A perturbative treatment of ATI predicted a power law analog to equation (1.15) [Gon80] to describe the relative peak heights of the individual ATI-peaks,

$$\Gamma_{n+s} \propto I^{n+s}, \tag{1.19}$$

which was confirmed experimentally by Fabre *et al.* [Fab82]. With increasing availability of high intensity laser pulses approaching peak intensities of 10^{14} W/cm^2, soon deviations from the expected form of the spectra were observed, such as a strong suppression of the n-photon peak compared to the $(n+1)$-photon peak [Kru83]. It was soon clarified, that the intensity dependent effects of the ponderomotive potential have to be taken into account in the interpretation of the experimental data [Mul83].

1.1.4 Ponderomotive Shift and Dynamical Resonances

At higher intensities the atomic level structure and the ionization process becomes increasingly influenced by the laser field: As discussed above, the ponderomotive energy U_p represents the energy of a free electron in the presence of a laser field. If an electron is to be promoted to the continuum, this additional energy has to be provided by the absorption of photons, leading to an modified, effective ionization potential IP*:

$$\mathrm{IP}^* = IP + U_p. \tag{1.20}$$

Consequently the energy of a photoelectron $E_{\mathrm{ex}} = n \cdot \hbar\omega - \mathrm{IP}^*$ now does not only depend on the initial state and the number of photons absorbed, but also on the intensity at the instant it was produced. As stated in Section 1.1.3, the ponderomotive shift of the ionization threshold is not directly visible in electron energy spectra recorded with long laser pulses, but modifies the relative intensity of the individual ATI-peaks by the effects of *channel opening* and *channel closing*. The left hand side of Figure 1.5 shows a schematic of above-threshold ionization of xenon by 1064 nm laser light (1.165 eV photons), together with

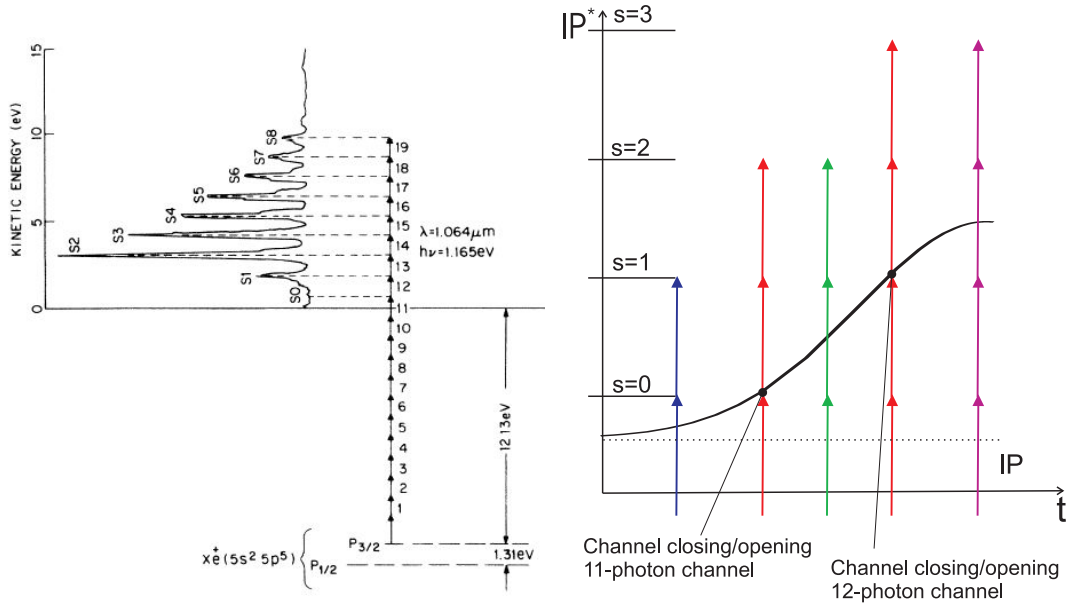

Figure 1.5: Illustration of the effect of channel closing and channel opening on ATI-spectra: The 11- and 12-photon peak are strongly suppressed in the ATI-spectrum on the left hand side (from [Fre86]) since 11- and 12-photon ionization can only take place at the leading and trailing edge of the pulse due to the ponderomotive shift of the continuum.

an electron energy spectrum taken at a peak intensity of $2 \cdot 10^{13}$ W/cm^2 (from [Fre86]). The 11-photon MPI-peak (label S0) and the first ATI peak (S1) are strongly suppressed, while the 13-photon peak (S2) and higher order peaks dominate the spectrum. The left hand side of Figure 1.5 maps the temporal variation of the effective ionization potential IP* which is proportional to the instantaneous intensity of the laser pulse $I(t)$. Due to the increase of the ionization threshold, ionization by 11-photon absorption is only possible at the leading and trailing edge of the pulse. When IP* reaches the 11-photon energy, the 11-photon channel closes, and ionization can only occur by absorption of 12 or more photons. At the peak intensity, the 12-photon channel is energetically forbidden as well, and for the time the intensity remains close to the peak value, only ionization by 13 or more photons takes place. Since the ionization rate increases strongly with intensity, it is not surprising, that the pulse-integrated ion yield from the 13-photon process supercedes that of the 11-photon process: Albeit the 11-photon ionization rate is higher at the same intensity, it contributes only during periods, where the laser intensity is just a small fraction of the maximum intensity. A more thorough treatment of the distribution of photoelectrons over the different ionization channels, needs to take into account the spatial structure of the laser focus: For example, in an outer volume shell of the focal volume, the intensity never reaches the value to close, say, the 11-photon channel.

It is not only the continuum states, that are altered by high intensity laser fields, but due to the interaction of the field-induced dipole moment with the field itself, the atomic levels experience an intensity dependent shift as well. Compared to the low intensity case,

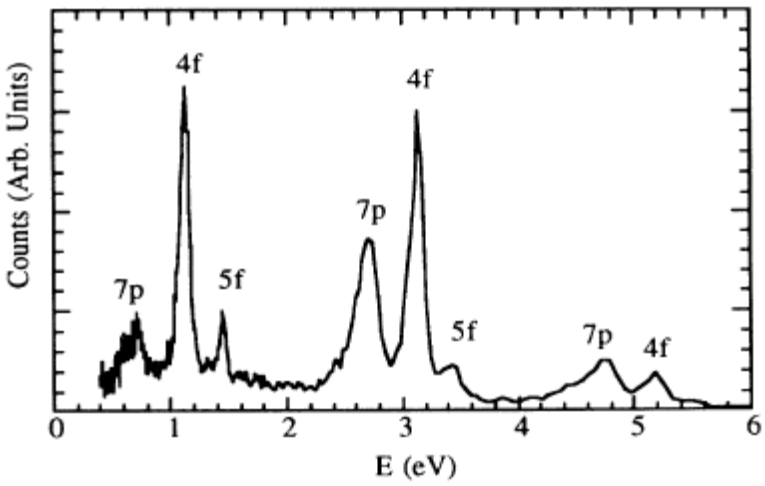

Figure 1.6: Short pulse ATI-series from xenon at 6.2·W/cm^2. The resonances repeat with the photon energy of 2 eV and are labeled according to the resonant intermediate states (from [Mev93]).

resonance enhancement of certain ionization channels, is not only observed as a function of photon energy, but as function of intensity as well.

Freeman Resonances

With progress in the generation of short laser pulses, it became possible to perform ATI-experiments in the short-pulse regime. In this regime, the measured electron energies correspond to those of the electron at the instant of ionization. By successively reducing the pulse duration from 13 ps down to 400 fs and thus eliminating the influence of the ponderomotive potential on the electron spectra, Freeman *et al.* found the individual ATI-peaks to split up into series of narrow lines [Fre87]. These fine-strucured peaks appeared repeatedly at positions separated by exactly one photon energy, which did not vary with laser intensity or focus size (Fig. 1.6).
The structure of the observed spectra is well explained in a simple model, where at a particular intensity, an AC-Stark shifted high-lying atomic level becomes m-photon resonant with the laser, leading to a strong enhancement of the ionization rate by 1-photon ionization from this state. This has the consequence, that all high-intensity ionization processes will exhibit some resonant contributions, though nominally non-resonant, when described by the unperturbed levels of the atom. These resonances known as *Freeman resonances*.
Figure 1.7 schematically depicts the mechanism leading to the fine structure in short pulse ATI. In this tentative explanation, one assumes, that the weakly bound Rydberg states close to the continuum respond to the laser field almost as a free electron and their AC-Stark shift will closely follow the threshold shift. The deeply bound ground states from which the atom ionizes (and that of the residual ionic core), are much less affected by the oscillating field, and the corresponding energy shift is usually neglected [Fre91], [Boe92].

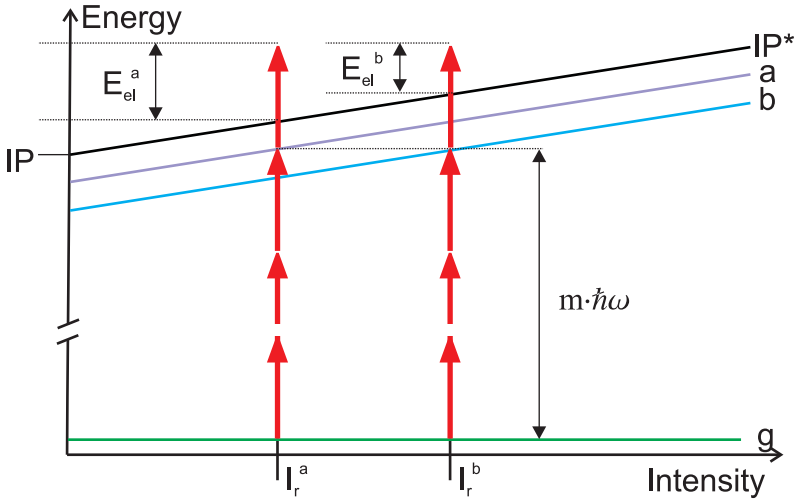

Figure 1.7: The origin of Freeman resonances. High lying excited states are resonantly populated at certain intensities $I_r^{a,b}$ and subsequently ionize from there. Since they experience the same ponderomotive shift as the continuum, the detected electron energies depend only on the binding energy of these states.

The model of Figure 1.7 shows the energy dependence of two Rydberg states (designated by a and b) on the field intensity. For certain intensities I_r^a and I_r^b, a m-photon resonance between the ground state $|g\rangle$ and the states $|a\rangle$, $|b\rangle$ occurs, which in the following ionizes by 1-photon absorption. The acquired electron drift energies E_el^a and E_el^b in the short pulse limit are then given by

$$\begin{aligned} E_\mathrm{el}^a &= (m+1)\hbar\omega - \mathrm{IP}^*(I_\mathrm{r}^a) = (m+1+s)\hbar\omega - \mathrm{IP} - U_p(I_\mathrm{r}^a) \\ E_\mathrm{el}^b &= (m+1)\hbar\omega - \mathrm{IP}^*(I_\mathrm{r}^b) = (m+1+s)\hbar\omega - \mathrm{IP} - U_p(I_\mathrm{r}^b). \end{aligned} \tag{1.21}$$

The energy difference of the fine structure peaks within the same ATI-order s is just the difference of the ponderomotive potentials $\Delta E = U_p(I_\mathrm{r}^b) - U_p(I_\mathrm{r}^a)$ at the respective resonance intensities. In contrast, for a long pulse, the U_p terms on the right hand side have to be added to the initial drift energies to reproduce the observable electron energies, obviously only the energy difference between different ATI-orders remains detectable.

AC-Stark Shift

The assumptions on the AC-Stark shift made above are supported by modeling the bound states as an electron bound to the nucleus by a harmonic oscillator potential and eigenfrequency ω_0, where $\hbar\omega_0$ is the binding energy of the respective state. This model yields the following estimate for the AC-Stark shift of a bound state U_p' [Ebe88]:

$$U_p' = U_p \frac{\omega^2}{(\omega - \omega_0)^2}. \tag{1.22}$$

Experimentally, the above assumptions have been confirmed for laser intensities up to $3 \cdot 10^{13}$ W/cm^2 ($U_p \approx$1.5 eV) by measurements of the resonance energies in ATI of xenon,

carried out at different intensities and wavelengths. They revealed linear shifts of the resonant states with Stark coefficients α_r ($U_p'=\alpha_r I$) close to the ponderomotive value, even for the low angular momentum $7p$ state. In contrast, the coefficients of the atomic and ionic ground state (which partly cancel out) amount to just a tenth of the ponderomotive one. A second-order perturbation theoretical calculation predicted the same linear behaviour and was found to be in reasonable agreement with the experimental findings [Ago89].
A rigorous theoretical treatment, deriving the AC-Stark shift and the ponderomotive potential from the Hamiltonian of a model atom in a classical radiation field is given in [Pan86], [Mul93], where Pan *et al.* [Pan86] also provide a general motivation for the observed behaviour in terms of two limiting cases of their second-order perturbation theory expansion.

1.1.5 Tunneling Ionization

For the Keldysh parameter γ approaching unity, as is the case for high laser intensities (or long wavelengths), the external field dominates the dynamics of the ionization process through its modification of the atomic potential.
For a low adiabaticity parameter, the rate at which an electron bound by an ionization potential IP tunnels through the potential barrier lowered by an electric field $F(t)$ can be calculated in the quasistatic limit, using an expression from DC-tunneling theory (expressed in atomic units a.u.) [Cor89], [Amm86]:

$$w_{\mathrm{ADK}}(t) = 4\frac{2\mathrm{IP}^{5/2}}{F(t)}\exp\left(-\frac{2(2\mathrm{IP})^{3/2}}{3F(t)}\right). \tag{1.23}$$

This formula became widely known as the ADK-formula, named after the russian physicists Ammosov, Krainov and Delone, who provided the first systematic theoretical treatment of tunneling ionization in atomic systems. Substituting $F(t)$ by $F_0\sin(\omega t)$ and averaging over the field period gives the tunneling rate at a particular intensity for a linearly polarized laser field.
The longitudinal (i.e. along the direction of polarization) momentum-/energy distribution is obtained by assuming that the electron emerges in the continuum with vanishing kinetic energy and its dynamic is governed by the laser field. According to (1.14) the longitudinal (drift) energy gained in the laser field depends on the phase $\phi_0=\omega t_0$ at which the electron was born. Weighting the drift energy of phase ϕ_0 with the instantaneous tunneling rate given in (1.23) and integrating over all phases yields the momentum distribution. A quantum mechanical calculation based on a theory for strong adiabatic perturbations gives the same result [Del98]. Since the laser field per definition acts only on the longitudinal degree of freedom, the (much narrower) distribution for the transversal momenta $p_\perp$ is determined by the tunneling process itself and is derived from the quantum mechanical calculation [Del91]:

$$w(p_\parallel, p_\perp) = w(0)\exp\left(-\frac{p_\parallel^2\omega^2(2\mathrm{IP})^{3/2}}{3F^2}\right)\exp\left(-\frac{p_\perp^2(2\mathrm{IP})^{1/2}}{F}\right). \tag{1.24}$$

Equation (1.24) is only an approximate expression, since the field strength $F(t)$ has been expanded to second order in time around its maximum value and the acceleration has been linearized around the field maximum:

$$F_0 \cos(\omega t) \approx F_0(1 - \frac{1}{2}\omega^2 t^2);\ t \approx p_{\|}/F_0. \tag{1.25}$$

Therefore, the momentum distribution should match best for low energetic electrons produced near the field maximum, where the tunneling rate is highest. Features in the high energy tail as the cut-off in electron energy at $2U_p$ are not reproduced. According to this expression, the spectrum in the tunneling regime obeys a smooth exponential distribution, and no modulation or resonant features are to be expected. Surprisingly, high momentum resolution measurements performed in our group, showed resonance-like structures at intensities deep in the tunneling regime, whose origin is not clear yet [Rud04b].

Rescattering

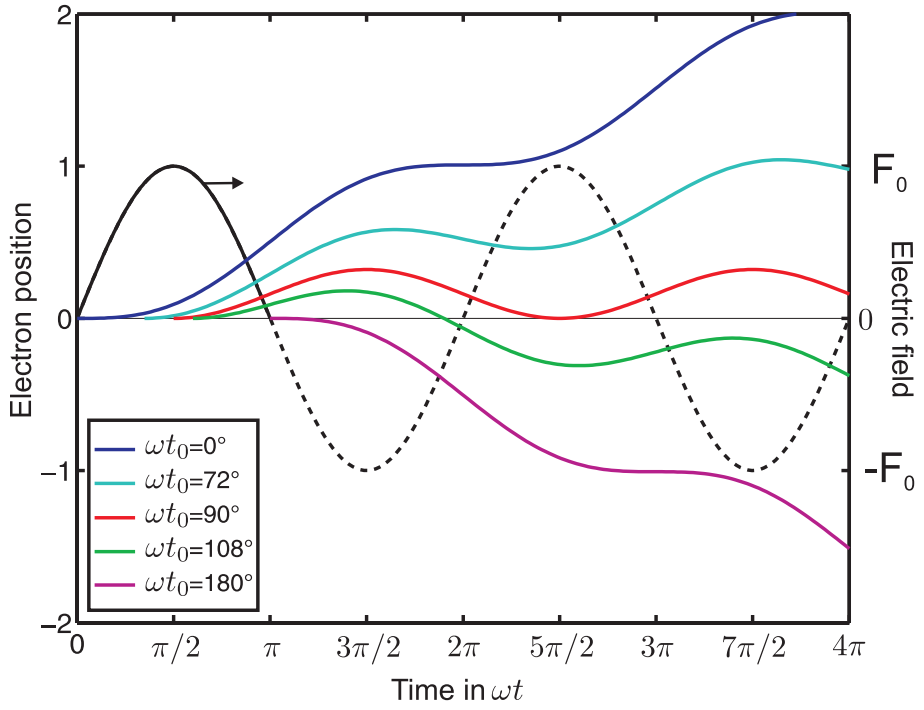

Figure 1.8: Electron trajectories along the direction of laser polarization, depending on the phase of the field ωt_0 at the instant of ionization.

In spectra with a high dynamic range in count rate, a small fraction of photoelectrons with energies beyond $2U_p$ is observed, forming a 'plateau' in the electron spectrum which reaches up to energies of $10U_p$ [Pau94b]. This observation is explained by the assumption, that the ionized electron propagating in the laser field is driven back to the remnant ionic core and is scattered elastically in the Coulomb potential of the ion, whereby it can acquire additional drift momentum. This process is known as *rescattering*. The main features of

this process could be understood by means of a simple mechanistic models based on the classical motion of the electron in the laser field (the *simple man's model*) [Pau94a], [Cor93]. Recalling equation (1.10), the position of an electron born at time t_0 at x_0=0 with a velocity close to zero $v_x \approx 0$ is (expressed in atomic units)

$$x(t) = \frac{F_0}{\omega}\left(\frac{1}{\omega}\sin(\omega t) - \frac{1}{\omega}\sin(\omega t_0) + (t_0 - t)\cos(\omega t_0)\right). \tag{1.26}$$

The first term describes the fast oscillation of the electron at the field frequency, the latter ones the linear drift motion, which depends on the tunneling time t_0.
Figure 1.8 shows electron trajectories for different instants of ionization t_0 within the first half cycle of the electric field. The corresponding trajectories for the second half cycle are just mirrored at the x-axis. If the electron ionizes close to a zero crossing of the field ($\omega t_0 = 0, \pi/2$, blue and violet curves), it acquires maximum drift energy. However, in this case the ionization probability is close to zero, explaining the decrease of count rate towards large longitudinal energies of $2U_p$.
An analysis of the solutions of the transcendental equation $x(\omega t, \omega t_0) = 0$ defining the times t_1 at which the electron returns to the parent ion, shows that there are two classes of trajectories: Some that have at least one return to the origin and such that never return. All trajectories between the red ($\omega t_0 = \pi/2$) and the violet trajectory ($\omega t_0 = \pi$ return to the origin at least once. As seen from the diagram the velocity of the electron at the return time ωt_1 corresponds to the slope of the trajectory curves at the zero crossing.
Calculating the maximum kinetic energy $T(t_1)$ an electron can have on recollision with the ion, yields a value of $3.17U_p$. This situation occurs for ionization times ωt_0=108°close to the maximum of the field. The corresponding return time ωt_1 is close to 2π, i.e. to a minimum of the field. On elastic backscattering under an angle of 180°, the electron now has an initial velocity when leaving the ion corresponding to $3.17U_p$ in line with the rising field and can gain additional drift momentum. According to (1.14), the maximum detectable drift enegy in the short pulse regime after elastic rescattering is $T_{\max}$=$10U_p$. This is not the only implication of the possibility, that the laser-driven photoelectron may return and interact with its parent ion after ionization. One is an enhancement of multiple ionization due to excitation or impact ionization of the ion by the returning electron, as discussed in section 1.1.7. The other is *High Harmonic Generation* (HHG) [Lew94], which has developed into one of the most rapidly advancing field of contemprary physics, culminating in the perspective to perform pump-probe studies on atomic systems with coherent soft X-ray pulses of attosecond duration [Dre01], [Bal03]. When an intene laser pulse is focused on a jet of noble gas atoms, higher order harmonics of the fundamental frequency are created. The spectrum shows a plateau of lines with constant intensity, which has a sharp cutoff [Fer88], [Li89], which was found to be

$$E_{\text{cutoff}} \approx I_p + 3.17U_p. \tag{1.27}$$

This hints at a close connection between rescattering and HHG. In a most simple picture, HHG can be viewed as the recombination of the returning electron with the ion by emission of a single photon carrying the excess energy gained in the laser field.

1.1.6 Over-the-Barrier Ionization

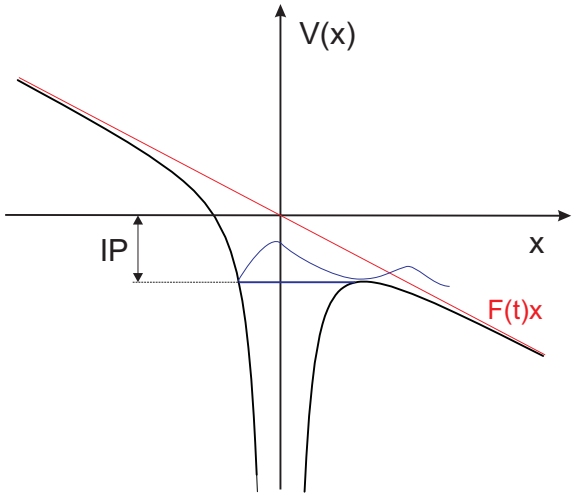

Figure 1.9: One-dimensional model of over-the-barrier ionization. The Coulomb-barrier is completely suppressed for a field strength $F > F_{\mathrm{OBI}}$.

With increasing field strength and intensity the width and height of the Coulomb barrier is reduced until it is completely suppressed by the external field $F(t)$ and even the ground state will become unbound (Figure 1.9) [Pro96]. This process is called *Barrier Suppression Ionization* (BSI) or *Over-the-Barrier Ionization* (OBI). Approximate values for field strength and intensity are derived from a simple 1-dimensional model. The combined potential of the atomic core with effective nuclear charge Z and the light field is given by

$$V(x) = -\frac{Z}{x} - Fx. \tag{1.28}$$

The threshold value for OBI is defined by the condition, that the potential of the saddle point $V(x_s)$, x_s defined by $\partial V(x)/\partial x = 0$, equals the binding energy -IP of the bound state [Aug89], [Fre91]. The critical field strength is

$$F_{\mathrm{OBI}} = \frac{\mathrm{IP}^2}{4Z} \tag{1.29}$$

and the corresponding laser intensity

$$I_{\mathrm{OBI}} = \frac{\mathrm{IP}^4}{16Z^2}, \tag{1.30}$$

or in SI-units

$$I_{\mathrm{OBI}} = \frac{c\pi^2\epsilon_0^3\mathrm{IP}^4}{2Z^2e^6} = 4 \cdot 10^9 \frac{\mathrm{IP[eV]}^4}{Z^2}\ \mathrm{W/cm^2}. \tag{1.31}$$

Numerical calculations of ionization rates in the intensity regime of the transition between tunneling ionization and over-the-barrier ionization and above show a marked difference between the ionization rates, that are obtained from (a possibly inadequate) application

of the ADK-formula and the numerical results [Bau99], [Ton05]. Quite counterintuitively, the ADK-prediction tends to overestimate the ionization rate. An attempt by Krainov to extend the analytical ADK-model in order to make it applicable to over-the-barrier ionization as well [Kra97], improved the agreement with exact calculations, but the discrepancies remain too large to make it safe for indiscriminate use [Ton05].
The benchmarking calculations are based on solving the time-dependent Schrödinger equation within the single active electron (SAE) model. Tong and Lin propose an empirical extension to the standard ADK-formula based on a range of model calculations for different species, which is (labeled w_{TBI}):

$$w_{\mathrm{TBI}}(F) = w_{\mathrm{ADK}}(F)\ \exp\left(-\alpha\left(\frac{Z^2}{\mathrm{IP}}\right)\left(\frac{F}{(2\mathrm{IP})^{3/2}}\right)\right). \tag{1.32}$$

The exponential correction factor essentially contains a scaled ionization potential and field strength along with a species dependent fit parameter α of unity order.
From the experimental side, there is little literature on over-the-barrier phenomena, which is not surprising since there is no unique signature of over-the-barrier ionization to separate it from tunneling ionization from electron or ion spectra. In an experiment with 1 ps pulses of 1053 nm wavelength the number of produced ions per shot was monitored over an intensity range of 10^{13} W/cm^2 and $3\cdot10^{16}$ W/cm^2 for all the noble gases from helium to xenon. The appearance intensity of a higher charge state A^{n+} was found to be in excellent agreement with the over-the-barrier intensity of the parent charge state $A^{(n-1)+}$, and reproduced the data better than a description based on the ADK-tunneling theory [Aug89]. The authors point out, that this approach is only justified for pulses short enough to preempt saturation of the ion yield (alike in optical spectroscopy saturation is defined as the nonlinear variation of the ionization signal rate with increasing intensity due to depletion of the ground state).

1.1.7 Multiple Ionization

The simplest approach to describe double- or multiple ionization of atoms is the assumption, that both processes proceed independently and in a stepwise manner: The subsequent removals of electrons are pictured as independent ionization events, where there is no correlation between them apart from the increase in ionization potential with each ionization step. This mode of ionization is called *sequential ionization*.
However, detailed studies on the intensity dependence of single- and double-ionization rates in the intensity range from 10^{13} to 10^{16} W/cm^2 ([Fit92], [Kon93], [Wal93], [Wal94a]) showed a significant enhancement in the yield of doubly charged ions at low intensities as compared to the prediction of the independent event model based on the ADK-tunneling rates. Figure 1.10 shows a measurement of the ion yield dependence on the laser intensity. The yield curve for doubly charged ions bends in a certain intensity regime, forming a prominent 'knee' structure which indicates the unexpected enhancement of the double-ionization rate. This enhancement of the ionization process was named '*Non-Sequential*

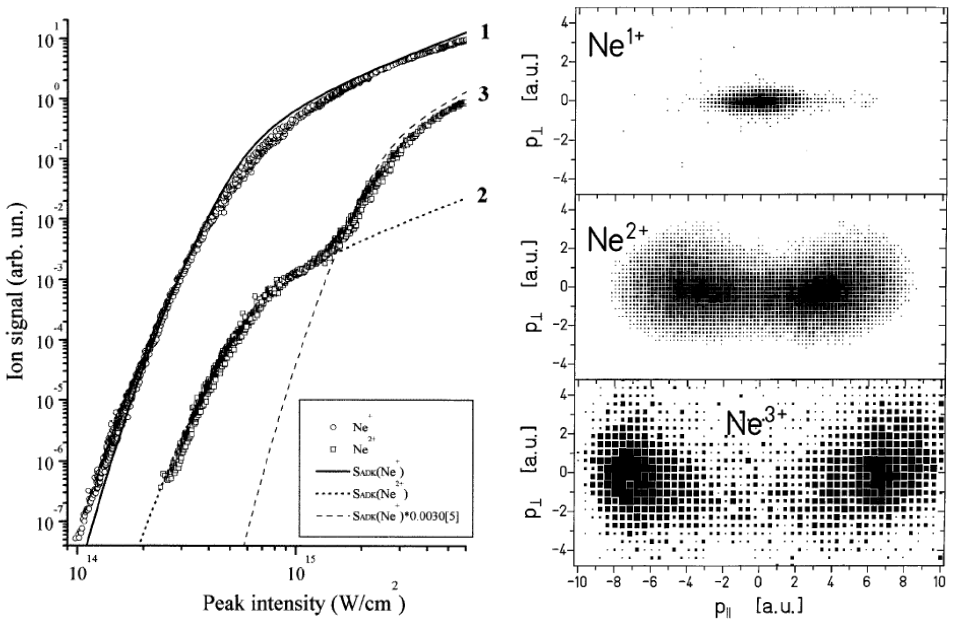

Figure 1.10: Double ionization of neon with 25 fs laser pulses at 800 nm wavelength. *Left*: Measurement of the intensity dependence of the ionization rate. The lines show the calculated rates of an independent event model based on ADK-theory (from [Lar98]). The theoretical curve 2 is obtained by muliplying curve 1 with a scaling factor. *Right*: Two dimensional recoil ion momentum distribution at intensities of 1.3 PW/cm^2 (Ne^+, Ne^{2+}) and 1.5 PW/cm^2 (Ne^{3+}) (from [Mos00]). $p_\parallel$, $p_\perp$ are the momenta parallel and perpendicular to the laser polarization axis, the distribution is integrated along the third cartesian coordinate.

Double Ionization' (NSDI), to distiguish it from the regime, that is well described by the 'statistical' independent event model. The origin of this phenomenon has been under long-standing discussion. There was little doubt, that this effect should be due to a correlation between the ionized electrons, though the nature of this mechanism was still unclear.
Several models (see for example the review by Dörner *et al.* [Dör02b]) have been proposed in the past to explain this behaviour, of which the most discussed and cited are briefly presented.

Collective Tunneling

The model of collective tunneling [Eic00] assumes the simultaneous tunneling of several bound electrons through the potential barrier. This theory combines several bound electrons to a quasi-particle bound with the total ionization potential of the N electrons, where the ionization probability is described in terms of a modified ADK-rate. This rate qualitatively agrees with the observed form of the yield curves for different species, but systematically underestimates the yield in doubly-charged ions at lower intensity. It was ruled out by the authors themselves to consider collective tunneling ionization as a dominant mechanism in the experimentally covered situations. But they point out, that for

very short pulse durations or large differences in the 1st and 2nd ionization potential, this process could play a role (one two-particle tunneling process at an effective IP of the sum of the 1st and 2nd IP should have a higher probability than the independent sequential tunneling of the outermost and 2nd electron through their individual tunneling barriers).

Shake Off

Another possible mechanism that had been extensively discussed, is a 'shake off' of a second electron. After instant removal, i.e. on a timescale short compared to the characteristic timescale of electronic motion within the atom ('sudden approximation'), the electron shell is not in an eigenstate of the ionic Hamiltonian and the wavefunction of the remaining electrons has an overlap with continuum states, so that there is a certain probability that another electron is projected to the continuum as the wave function relaxes to its new eigenstate. This mechanism is known to be the dominant contribution to double ionization by absorption of high-energetic photons (beyond the keV-range) [Spi95], where it could be identified by its kinematic signature in a COLTRIMS-experiment. It is also the dominant process in collisions of atoms with fast charged projectiles [McG97].
A related mechanism, occurring at lower energies, is the so-called Two-Step-One (TS1) process. In a simple picture, the photoionized electron strongly interacts with a second electron on its way out of the atom and knocks it out in a binary electron-electron collision [Sam90]. In both the above cases, the electron-electron correlation is confined to the size of the atom and on a timescale of attoseconds.

Recollision

The idea of an ionized electron driven by the laser field returning back to its parent ion and interacting with it was introduced in section 1.1.5 as an explanation for the high energy tail of the electron energy distribution in single ionization. It is clear, that besides elastic scattering and recombination (HHG) impact ionization is possible as well. Since the peak ponderomotive potentials of fs-pulses can easily reach several 100 eV and more for intensities of 10^{15} W/cm^2, enough impact energy for direct electron impact ionization is provided by the returning electron. In the picture of electronic correlation, one could say that rescattering is an electron correlation effect mediated by the laser field. Rescattering is nowadays commonly recognized as the dominant mechanism in non-sequential double ionization. First evidence was provided by the fact, that in fields of circular or elliptical polarization, double-ionization and HHG is supressed, which is explained by the fact, that in the rotating field the electron trajectories do not return to the parent ion [Die94], [Fit94].
A direct identification of rescattering as the mechanism responsible for NSDI was achieved in experiments, that were capable of recording fully differential cross sections of multiple ionization in intense laser fields, namely reaction microscopes in conjunction with Ti:Sa amplifiers delivering high intensity pulses at repetition rates in the kHz range [Mos00], [Web00]. Figure 1.10 b) displays a projection of the momentum distribution of singly, doubly and triply charged neon ions for peak intensities, at which the characteristic 'knee'-

structure manifests itself in the yield curve. Thus the observation in the regime of non-sequential double ionization was ensured. Already the ion spectra alone deliver crucial information about the ionization process: Due to momentum conservation and the fact, that the momentum of absorbed photons is negligible to a good degree, the recoil ion carries the information about the momentum sum of all emitted electrons. Whereas the momentum distribution of singly charged ions is strongly peaked around small momenta $p_\perp$ in the direction perpendicular as well as parallel ($p_\parallel$) to the laser polarization axis, the momentum distribution of the higher charge states Ne^{2+} and Ne^{3+} gives a completely different picture: The momentum distribution of multiply charged ions exhibits a pronounced minimum at small longitudinal momenta and is peaked to higher values of a few a.u., giving rise to a characteristic double-hump structure in the momentum spectrum.
This structure is again explained by the electronic motion of the ionized electrons in the laser field as presented in section 1.1.5: For all tunneling phases ωt_0, for which the electron can return to the origin and acquires enough energy to further ionize the ion via a electron-electron colission (tunneling phases close to 108°, where the maximum drift energy of $3.17U_p$ is acquired), the laser field has a small value at the return time, i.e. at the instant, when the second electron is promoted to the continuum. In analogy to the case of elastic rescattering, the second electron can now acquire a large drift momentum, which is mirrored in the recoil ion momentum distribution, which maps the net momentum of the emitted electrons. If the initial tunneling process takes place at a half cycle of the field with negative field strength, it will gain the same drift energy, but in the opposite direction, contributing to the other peak of the double-hump structure.
For the other mechanisms discussed, the momentum distribution is expected to have a maximum at zero momentum, since the emission of both electrons takes place with no notable time difference on the time scale of the laser field. Therefore both electrons will gain the same drift energies. As the probability for ionization for the first electron is highest at the peak field strength, the corresponding drift energies are close to zero.
The unique signature of the rescattering mechanism in the ion momentum spectrum enabled to determine it as the by far dominant channel in non-sequential double ionization. Investigations on different species of noble gases (He, Ne and Ar) revealed atom specific differences in the depth of the central minimum of the momentum distribution. In a more complete picture of recollision induced multiple ionization, reaction pathways like electron impact excitation (instead of ionization) followed by field ionization have to be taken into account [Feu01], [Rud04a]. This process is called RESI (Recollision-Excitation plus Subsequent field Ionization). The amplitude of the different recollision induced processes in multiple ionization was shown to depend strongly on the atomic level structure [Jes04].

Chapter 2

Laser Cooling and Trapping of Lithium

As pointed out in the introduction, it is possible to deflect, decelerate and confine atoms in specially tailored light fields. In the preparation of ultracold atomic gases the dissipative spontaneous force plays the central role, which can reduce atomic velocities down to the range of some cm/s. In a magneto-optical trap (MOT) an ensemble of of atoms and can be spatially confined and cooled to temperatures below 1 mK by means of the scattering force exerted by resonant laser beams.
This chapter first reviews the basic principles of laser cooling and trapping, and their experimental application. Further, the specific properties of ^{7}Li related to laser cooling are presented.

2.1 Principles of Laser Cooling and Trapping

2.1.1 The Spontaneous Force

The technique of laser cooling relies on the fact, that by the absorption of a photon by an atom not only energy, but also momentum is transferred from the light field to the atom. So with each photon absorbed, the atom receives a momentum of $\Delta\mathbf{p} = \hbar\mathbf{k}$ where $\mathbf{k}$ denotes the wave-vector of the photon field (in units of $2\pi m^{-1}$):

$$p = \frac{E}{c} = \frac{h\nu}{c} = \frac{h}{\lambda} = \hbar k. \tag{2.1}$$

In the subsequent spontaneous decay of the excited state another photon is emitted, whereas this emission on average occurs isotropically.
If an atom is placed inside a directed resonant laser beam it undergoes many cycles of directed absorption followed by isotropic spontaneous emission. Since the momenta transferred by spontaneous emission $\hbar\mathbf{k}'$ will average out to zero over many cycles, the atom experiences a net momentum-transfer in direction of the laser beam.
A theoretical treatment of the interaction of near-resonant, monochromatic and intense

light with atoms as present in laser cooling is mostly carried out by treating the atom as a two-level atom coupled to a classical electromagnetic field via the electric dipole moment between the two states involved.
The rather phenomenological expressions for the radiation forces on an atom displayed throughout the next sections can be developed in a rigorous way from the framework of the Rabi Two-level-system theory and optical Bloch equation formalism. Since their derivation requires rather lengthy algebraic manipulations and does not contribute much to an adequate understanding of laser cooling and MOT-operation as required within the scope of this thesis, it shall just be noted, that a thorough treatment is presented in [Met99], [Tan92] and references therein.
In the case of Lithium the photon momentum of 671 nm-light of the D2-transition amounts to $9.30 \cdot 10^{-28}$ kg m/s or $4.7 \cdot 10^{-4}$ a.u., corresponding to an atomic recoil velocity of 8.474 cm/s. Though these momenta may appear negligibly small, the high resonant scattering rates possible on dipole transitions can produce a substantial force on an atom, as illustrated in the following:
In the steady-state situation, which is given, when the atom is irradiated by a monochromatic field of constant intensity, the rates of absorption and spontaneous emission are in equilibrium and the photon scattering rate can be expressed as the product of the spontaneous decay rate γ and the excited state population ρ_{ee}:

$$\Gamma_{\mathrm{sc}} = \gamma \rho_{ee}. \tag{2.2}$$

An expression for the excited state population in dependence of the intensity I and the near-resonant detuning δ of the incident radiation is derived from the stationary solution of the optical Bloch equations. Originally developed in the context of magnetic resonance spectroscopy, where spontaneous decay rates are negligible, because they scale with the transition frequency ω_0 as ω_0^3, the effect of spontaneous emission has to be included by the phenomenological damping factor $\gamma = 1/\tau$, where τ is the natural lifetime of the excited state. The solution for the population of the excited state is [Met99]:

$$\rho_{ee} = \frac{s}{2(s+1)} = \frac{s_0/2}{1 + s_0 + (2\delta/\gamma)^2} \tag{2.3}$$

with

$$s = \frac{|\Omega|^2/2}{\delta^2 + \gamma^2/4} = \frac{s_0}{1 + (2\delta/\gamma)^2} \tag{2.4}$$

and

$$s_0 = 2|\Omega|^2/\gamma^2 = I/I_s. \tag{2.5}$$

The *on-resonance saturation parameter* s_0 normalizes the intensity I to the saturation intensity. The *saturation parameter* s takes into account a detuning $\delta = \omega_0 - \omega$ of the light field's frequency ω with respect to the atomic transition frequency ω_0. The *saturation intensity* I_s is defined as the intensity, at which the excited state fraction amounts to 1/4 (see (2.3)).

Ω is the *Rabi frequency*, which describes the coupling energy between the atomic dipole moment and the light field and is given by

$$\Omega = -\frac{e}{\hbar} E_0 \langle e| e\hat{r} |g\rangle , \tag{2.6}$$

with e is the electron charge and E_0 the amplitude of the electric field. The bra-ket expression is the dipole matrix element between the ground state $|g\rangle$ and the excited state $|e\rangle$.
By the above relations, the saturation intensity can be defined in terms of experimentally accessible quantities:

$$I_s = \pi hc/(3\lambda^3\tau). \tag{2.7}$$

For the D2-line of ^{7}Li, the on-resonance saturation intensity is 2.55 mW/cm^2. Thus the transition can be strongly driven already with modest laser intensities.
The excited states of optical transitions commonly used in laser cooling experiments exhibit radiative lifetimes τ on the order of 20–30 ns. If the transition is strongly driven and an excited state population of almost 50% can be assumed, the scattering rate approaches $\gamma/2$, corresponding to $18.45{\cdot}10^6$ scattered photons per second in the case of the ($2^2S_{1/2}$–$2^2P_{3/2}$) transition of lithium (or other alkaline metals). The maximum spontaneous force F exerted by resonant light on the atom is

$$F = \hbar k \Gamma_{\mathrm{sc}} = \hbar k \frac{\gamma}{2}. \tag{2.8}$$

For the light lithium atom, resonant scattering can produce an acceleration as large as $1.577{\cdot}10^6$ m/s^2 or 160000 times earth's gravity.
Figure 2.1 depicts the dependence of the achievable scattering rate on the detuning δ and the laser intensity (expressed in terms of the saturation parameter s_0). The general expression for the spontaneous force F_{sp} in terms of these parameters reads

$$F_{\mathrm{sp}} = \hbar k \frac{\gamma}{2} \frac{s_0}{1 + s_0 + (2\delta_0/\gamma)^2}. \tag{2.9}$$

To make efficient use of this force, the spectral power density distribution of a laser has to be concentrated in an interval narrower than the transition's natural linewidth (FWHM) $\Gamma = \frac{1}{2\pi\tau}$, which is 5.87 MHz in the case of lithium. This condition is well fulfiled by modern tunable single mode cw-lasers such as dye-lasers or external cavity diode lasers (ECDL), which typically feature linewidths of 1 - 2 MHz.
Furthermore, even very small velocities (Doppler-shift) or external fields (e.g. Zeeman-shift due to magnetic fields) can shift the transition completely out of resonance. A velocity of 3.97 m/s is sufficient to shift the resonance of a Li-atom by an entire natural linewidth compared to an atom at rest. On the other hand it is just this sensitivity of the resonance condition that is exploited in laser cooling techniques, as will be laid out in the following sections.

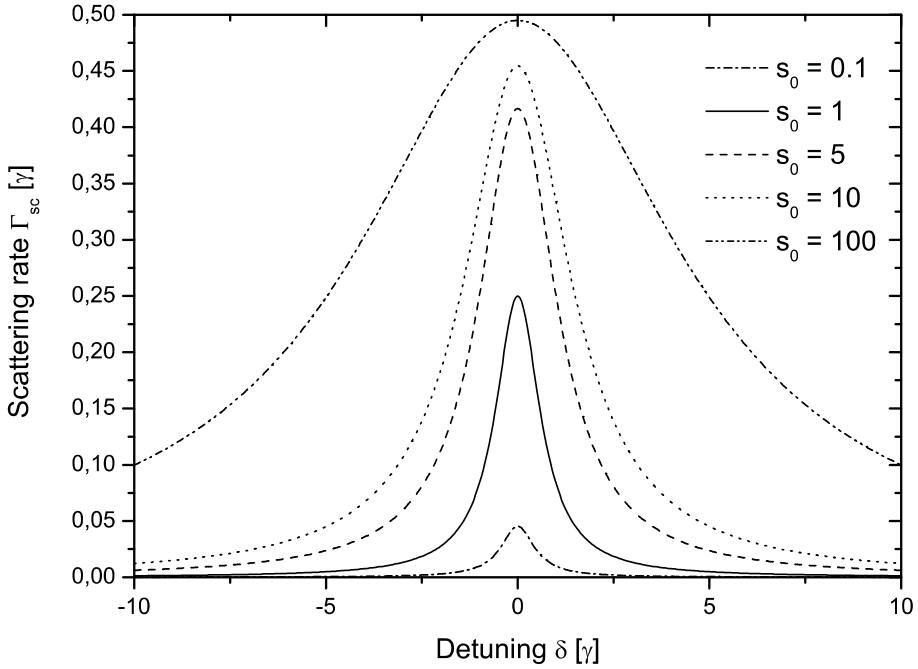

Figure 2.1: Spontaneous scattering rate $\Gamma_{\rm sc}$ as a function of the detuning δ for different saturation parameters s_0. Due to saturation around the center frequency and still growing absorption in the wings, the line profile broadens with increasing intensity. This effect is known as 'power broadening'. The power-broadened linewidth (FWHM) amounts to by $\gamma' = \sqrt{1+s_0}$.

2.1.2 Doppler Cooling

So far we have only considered the effect of light on atoms at rest. For atoms moving with a velocity $\mathbf{v}$ the laser frequency ω seen in the rest frame of the atom gets shifted by the Doppler effect. The detuning δ_0 is now replaced by a velocity dependent effective detuning δ containing the Doppler term $-\mathbf{kv}$:

$$\delta = \omega - \omega_0 - \mathbf{kv}. \tag{2.10}$$

Depending on its velocity, the atom is shifted into or out of resonance. The velocity dependent scattering force reads:

$$\mathbf{F}_{\rm sp}(\mathbf{v}) = \hbar\mathbf{k}\frac{\gamma}{2}\frac{s_0}{1+s_0+\left(2(\delta_0-\mathbf{kv})/\gamma\right)^2}. \tag{2.11}$$

Consider an atom moving in the light field created by two counter-propagating laser beams with wave vectors $\mathbf{k}$,$-\mathbf{k}$: The atom sees the beam it is moving towards *blue detuned* (meaning at higher frequency). If the beams are red detuned with respect to the atomic transition frequency ($\delta_0 \equiv \omega - \omega_0 < 0$), the atom will always see the counter-propagating beam closer to resonance, and its spontaneous scattering rate increases. The beam in-line with the velocity component is always shifted away from resonance. Thus more momentum is transferred from the beam directed against the direction of motion of the atom. This

way an imbalance in the radiation pressure arises, effectively slowing down the atom and bringing about a confinement in velocity space. The net force of the two beams is given by:

$$\mathbf{F} = \mathbf{F}^+ + \mathbf{F}^- = \sum \pm\hbar\mathbf{k}\frac{\gamma}{2}\frac{s_0}{1 + s_0 + (2\delta_\pm/\gamma)^2} \tag{2.12}$$

with

$$\delta_\pm = \delta_0 \mp \mathbf{kv}.$$

This expression can be linearized in v under the condition $|k \cdot v| \ll \gamma$:

$$F = \hbar k^2 \frac{8s_0(\delta/\gamma)}{(1 + s_0 + 4(\delta/\gamma)^2)^2} \cdot v = -|\alpha|\, v. \tag{2.13}$$

The force represents a viscous damping term in the equation of motion of the atom, asymptotically reducing its velocity to zero (see 2.2). This setup can be generalized to three dimensions with 3 orthogonal pairs of laser beams. The atoms move through the light field, as if it was a viscous liquid, this is, why this configuration was called 'optical molasses'. The natural velocity scale of an optical molasses is set by the quantity $v = \gamma/k$,

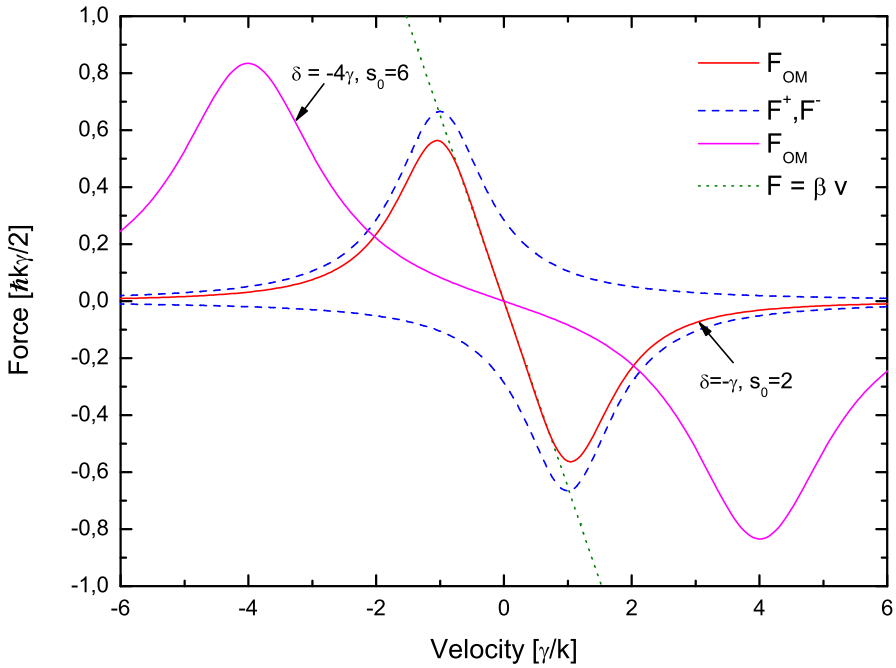

Figure 2.2: Velocity dependent force F in an one-dimensional optical molasses in units of the maximum spontaneous Force $\hbar k\gamma/2$. The red curve shows the total force F_{OM} as the sum of the single beam forces F^+, F^- (dashed blue lines), calculated for a detuning of one linewidth γ and a saturation of $s_0 = 2$. The dotted green line is the linear approximation for small velocities. The magenta curve depicts the situation for a large detuning of 4γ and higher saturation of $s_0 = 6$.

sometimes referred to as the capture velocity, defined by the velocity, where the Doppler-shift corresponds to an entire natural linewidth.

2.1.3 The Magneto-Optical Trap

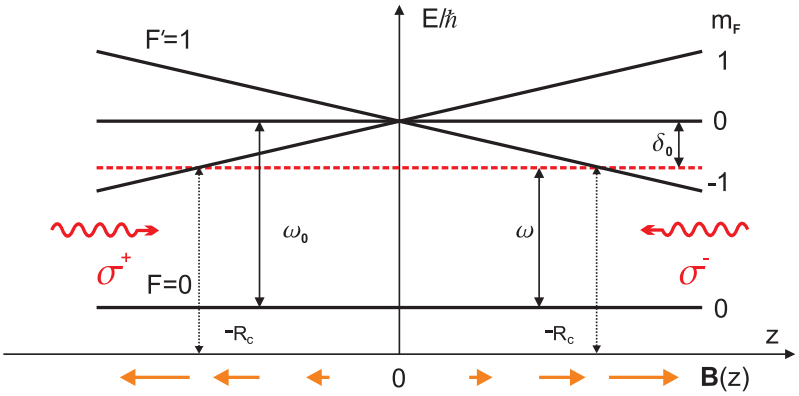

Figure 2.3: A simple 1-dimensional model of a magneto-optical trap.

The principle of a velocity-dependent scattering rate leads to capture and compression only in momentum space. With the magneto-optical trap, shortly MOT, the concept of the optical molasses is extended by a position dependence of the scattering force, providing also spatial confinement. The operating principle of the MOT is best explained in a simple 1-dimensional model: A model atom is considered with a ground state $|g\rangle$ of total angular momentum $F = 0$ and an excited state $|e\rangle$ of total angular momentum $F' = 1$ with the respective magnetic sublevels $|m_{F'} = +1\rangle$, $|m_{F'} = 0\rangle$ and $|m_{F'} = -1\rangle$ (the considerations carried out here apply equally well to any $(F = N \rightarrow F' = N + 1)$-system). This atom is placed in a magnetic gradient field along the z-axis $B(z) = B'_z z$ and irradiated by a pair of counterpropagating circularly polarized laser beams of opposite helicity, which are again red-detuned with respect to the zero-field atomic transition frequency. The magnetic field induces a position-dependent Zeeman shift of the magnetic substates of the $F' = 1$ manifold $\Delta E = (\mu_e - \mu_g)B(z) = \Delta\mu B(z)$, where μ_e, μ_g are the magnetic momenta of the ground and excited states involved. For an atom at a position on the positive z-axis the transition $(F = 0, m_F = 0 \rightarrow F' = 1, m_{F'} = -1)$ is shifted closer to resonance, while the $(F = 0, m_F = 0 \rightarrow F' = 1, m_{F'} = +1)$ transition becomes increasingly off-resonant. If σ^--light is shone in from the right-hand side, predominantly photons from this beam are scattered, creating a force that drives the atom back towards the center of the trap. By convention, $\sigma^\pm$-light has the polarization, that drives transitions with $\Delta m = \pm 1$ [1].
The effective detuning of (2.10) is supplemented by the position-dependent Zeeman detuning:

$$\delta^\pm = \delta_0 \mp kv \pm \Delta\mu B(z)/\hbar. \tag{2.14}$$

Substituting into equation (2.12), and again performing a linearization for small v,z for

[1] It is common practice in quantum optics, to choose a fixed-in-space quantization axis, e.g. the direction of propagation of the laser light. At the zero crossing of the magnetic field, the sign of the magnetic field is reversed instead of the quantization axis.

$|(\Delta\mu B'_z/\hbar)z| \ll \gamma$ analogous to (2.13), one obtains:

$$\begin{aligned} F &= \hbar k^2 \frac{8s_0(\delta/\gamma)}{(1+s_0+4(\delta/\gamma)^2)^2} \cdot v + \hbar k \frac{\Delta\mu B'_z}{\hbar} \frac{8s_0(\delta/\gamma)}{(1+s_0+4(\delta/\gamma)^2)^2} \cdot z \\ &\equiv -\alpha v - \kappa z. \end{aligned} \tag{2.15}$$

Equation (2.15) describes a damped harmonic oscillator and indicates that the atoms, once inside the MOT region perform damped harmonic oscillations around the center of the MOT, with a spring constant κ and a damping coefficient α. The oscillation frequency is given by $\omega = \sqrt{\kappa/m}$ and the damping rate is $\beta = \alpha/(2m)$. κ and α are related by:

$$\kappa = \frac{\Delta\mu B'_z}{\hbar k}\alpha. \tag{2.16}$$

Inserting typical values for a standard lithium MOT, δ=2γ, s_0=4, B'_z=10 G/cm, $\delta\mu$=μ_B yields the values ω_0=1.04 $\cdot 10^4$ s^{-1} for the oscillation frequency and β=5.8 $\cdot 10^4$ s^{-1} for the damping rate, indicating a strongly overdamped motion inside the trap.

Generalization to Three Dimensions

The scheme discussed above led to the idea, to extend it to three dimensions as shown in Figure 2.4 in order to provide a truly three-dimensional confinement for a sample of atoms. The 'standard-MOT' configuration consists of three orthogonal pairs of σ^+/σ^--polarized laser beams. A linear magnetic gradient field (near to the zero of the field) along each dimension is generated by a set of two coaxial coils in *anti-Helmholtz configuration* (opposite currents of equal magnitude in each coil). This kind of field configuration is called a spherical quadrupole field, as it corresponds to a 2-dimensional quadrupole field rotated around the coils' symmetry axis (z-axis).
For a given B'_z along the symmetry axis it follows from Maxwell's law

$$\nabla \cdot \mathbf{B}(\mathbf{r}) = \frac{\partial B_x}{\partial x} + \frac{\partial B_y}{\partial y} + \frac{\partial B_z}{\partial z} = 0 \tag{2.17}$$

and the cylindrical symmetry of the field:

$$\left.\frac{\partial B_x}{\partial x}\right|_{y=z=0} = \left.\frac{\partial B_y}{\partial y}\right|_{x=z=0} = -\frac{1}{2}\left.\frac{\partial B_z}{\partial z}\right|_{x=y=0}. \tag{2.18}$$

The radial gradient is just half of the axial gradient and the field vector components have opposite directions, i.e. if the axial component is pointing towards the center of the trap, the radial components are pointing outwards.
Consequently, the radial spring constant of the trap is equally reduced to half its axial value, leading to a slightly elliptic shape of the atom cloud. Quoted values for the field gradient always refer to the stronger axial gradient, and are typically on the order of 10-20 Gauss.
A detailed modeling of the dynamics of a 3D-MOT is a difficult task [Tow95], due to the interplay between the atoms position and velocity, the local polarization of the light

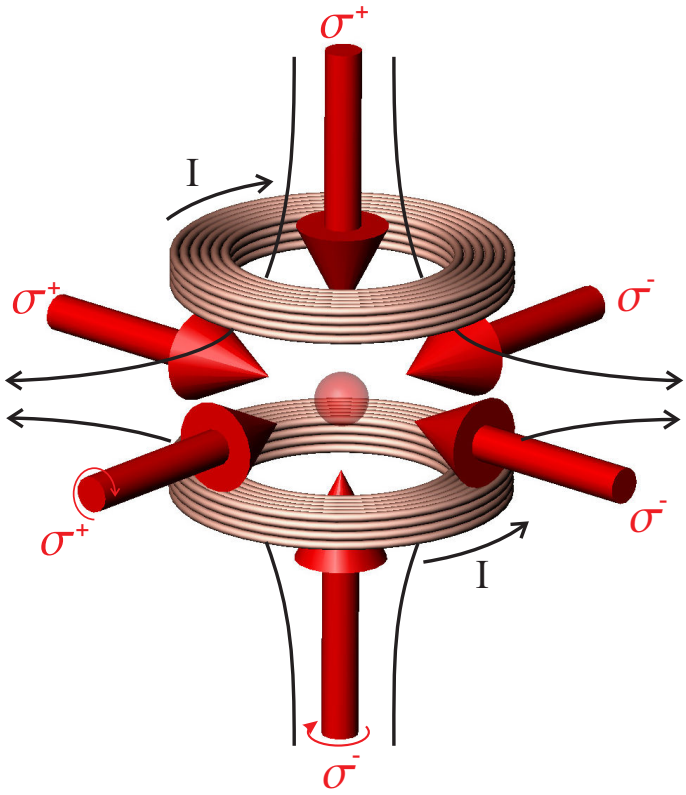

Figure 2.4: Principle of the magneto-optical trap: A pair of anti-Helmholtz coils generates a spherical quadrupole magnetic field. 3 pairs of red detuned counterpropagating beams of circularly polarized laser light provide the trapping force.

field created by the 3 pairs of beams and the spatially varying magnetic field vector. However, the main properties of 3D-MOTs are surprisingly well described in terms of the simple Doppler-theory presented above. Furthermore, the concept of the 3D-MOT proves to be quite robust and to work even under far from ideal conditions, provided the laser frequencies are stable and set right.

Capture Range

The points $\pm R_c$, where atoms at rest are in resonance with one of the laser beams and the spontaneous force attains its maximum, define the *capture radius* of the trap (see Fig. 2.3):

$$R_c = \frac{\hbar\delta}{\Delta\mu\frac{\partial B}{\partial z}}. \tag{2.19}$$

In this way, a boundary for the volume, into which slow atoms enter and subsequently get trapped, is established. If R_c is larger than the radii of the laser beams applied, the capture radius is determined by the beam diameters.

Likewise, the *capture velocity* v_c defines the maximum velocity, for which atoms entering the trap region are slowed down completely. An atom having the velocity v_c at $-R_c$ should come to a standstill at R_c and perform a damped motion towards the trap center. It is reasonable to assume that only the velocity dependent force plays a substantial role in the capture process. By estimating that the atom experiences the maximum spontaneous force $F_{sp,max} = \hbar k\gamma/2$ along the distance $2R_c$ an upper limit for the capture velocity can be established:

$$v_c = \sqrt{2R_c\hbar k\gamma/m}. \tag{2.20}$$

Figure 2.5 gives a more conservative estimate of the capture velocity v_c, assuming the stopping distance to be only R_c. Still, for the light lithium atom, relatively high capture

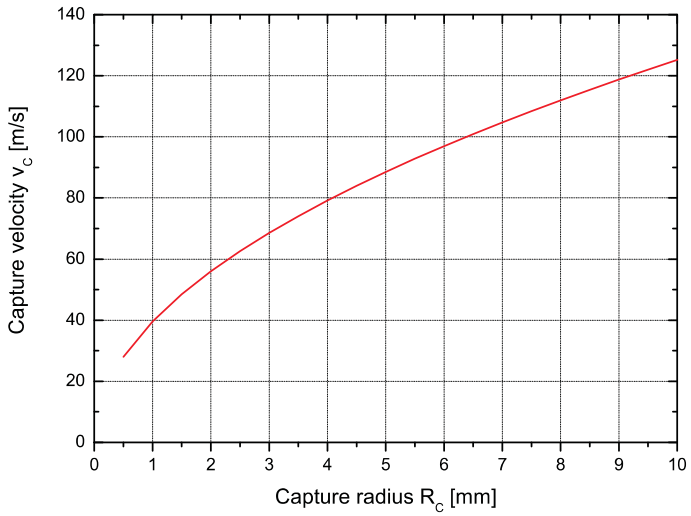

Figure 2.5: An estimate for the capture velocity v_c dependent on the capture radius of the trap.

velocities are achieved: Measurements of the capture velocity of ^{133}Cs [Lin92] and ^{23}Na [Mun01] yielded values between 11 m/s and 40 m/s for Cs (depending on the detuning and beam diameter) and 25 m/s for Na. The cooling transition of cesium exhibits a similar linewidth ($\gamma/2\pi$=5.18 MHz), but a longer wavelength of 852 nm, leading to a lower photon recoil ($\hbar k_{Li} > \hbar k_{Cs}$), therefore it is reasonable to assume, that for lithium capture velocities of

$$v_{c,Li} = \sqrt{m_{Cs}/m_{Li}} \approx 4v_{c,Cs} \tag{2.21}$$

are realistic.

2.1.4 Dynamics of the Magneto-Optical Trap

There is a variety of schemes to load atoms into a magneto-optical trap, comprising pulsed and continuous modes of operation. Most common techniques are loading from the low velocity fraction of a thermal background gas of the desired species (if no stringent vacuum conditions are required) [Mon90], or from a collimated, slow atomic beam, for example generated by a so called Zeeman slower [Phi82] or a 2D-MOT [Sch02].

The steady state of a continuously operated MOT is a dynamic equilibrium: The number of trapped atoms is given by the balance between various loss channels and the rate at which new atoms can be captured by the MOT. The behaviour of the atomic cloud in terms of the atom number N can be described in terms of a rate equation [Wal94b]:

$$\frac{\mathrm{d}N}{\mathrm{d}t} = L - RN - \beta \int \mathrm{d}V n(\mathbf{r})^2. \tag{2.22}$$

L is the loading rate in atoms/s, R the one-body loss rate rate per atom, which is the inverse of the lifetime τ_{MOT} of the trap population. The loss rate is essentially dominated by collisions of trapped atoms with thermal background atoms and molecules (and eventually hot atoms from a thermal atom source or from the high velocity tail of the loading beam). The atom density $n(\mathbf{r})$ dependent term $\beta \int \mathrm{d}V n(\mathbf{r})^2$ describes the loss due to collisions between trapped atoms, by which internal energy is converted to kinetic energy and at least one collision partner acquires enough energy to be ejected from the trap. At atom densities encountered in MOTs (10^9–10^{11} atoms/cm^3) the two-body loss rate is usually small compared to the one-body loss rate and will be neglected for now.
Describing the loading process by the initial condition $N(t_0{=}\,0) = 0$, equation (2.22) delivers

$$N(t) = \frac{L}{R}(1 - e^{-Rt}) = N_{\max}(1 - e^{-Rt}). \tag{2.23}$$

The atom number asymptotically saturates to its steady-state (maximum) value $N_{\max} = L/R$ with time constant $\tau = 1/R$. If the loading beam is shut off, an exponential decay of the trap results:

$$N(t) = N_0 e^{-Rt}. \tag{2.24}$$

The loss rate due to collisions of trapped Li atoms with background gas particles of species X is

$$R_X = n_X \sigma_{X-\mathrm{Li}} \sqrt{\overline{v^2}}, \tag{2.25}$$

where n_X is the number density, $\sigma_{X-\mathrm{Li}}$ the respective collisional cross section and $\sqrt{\overline{v^2}} = \sqrt{3k_{\mathrm{B}}T/m_X}$ the root mean square velocity. From the above it is obvious that capturing large atom numbers demands not only high loading rates, but, as the loss rate scales linearly with the background gas density, excellent vacuum conditions in the UHV-range ($p{<}10^9$ mbar) are required.

Two-Body Losses

Two basic mechanisms of inelastic collisions, that lead to quadratic trap loss, can be distinguished, the *state changing collisions* (SC) and the *radiative escape* (RE) [Jul91], [Wal94b]:

- In state changing collisions, the electronic state of one or both atoms is changed during the collision process, and the energy difference between final state and initial state is converted to kinetic energy. In the interaction between ground state atoms

one or both collision partners could be transferred from an upper to a lower hyperfine level of the ground state. For lithium, e.g. the following process is possible:

$$|2^2S_{1/2}, F = 2\rangle + |2^2S_{1/2}, F = 2\rangle \longrightarrow |2^2S_{1/2}, F = 1\rangle + |2^2S_{1/2}, F = 1\rangle + 2\Delta E_{\mathrm{HFS}}. \tag{2.26}$$

Each atom gains a kinetic energy corresponding to the full ground state hyperfine splitting. With $\Delta E_{\mathrm{HFS}}/h$ being 803.5 MHz, the gain in velocity is 9.7 m/s, which is still below typical capture velocities of the MOT. Thus, collisions between atoms in the ground state do not contribute significantly to the two-body loss rate.
Due to the inherent presence of excited state atoms in the trap, collisions between ground- and excited-state as well as two excited atoms have to be considered. For lithium, fine structure changing collisions (FSC), where one or two excited atoms switch from the $|2^2P_{3/2}\rangle$ to the $|2^2P_{1/2}\rangle$ fine structure state, constitute the main loss channel amongst the SC processes:

$$|2^2P_{3/2}\rangle + |2^2P_{3/2}\rangle \longrightarrow |2^2P_{1/2}\rangle + |2^2P_{1/2}\rangle + 2\Delta E_{\mathrm{FS}}. \tag{2.27}$$

The excited state fine structure splitting with an energy of $\Delta E_{\mathrm{FS}}/h$=10.052 GHz (or 0.48 K) is considerably larger than ΔE_{HFS}, leading to a velocity of 23.9 m/s for the process, where only one collision partner changes its HF-state and 33.9 m/s where both atoms involved undergo a fine structure transition, respectively. This velocity is on the same order as the capture velocity or depth of the trap potential. By variation of the trap depth, e.g. by an increase of laser intensity, this loss channel can be effectively suppressed, reducing the loss coefficient β by two orders of magnitude [Kaw93]. At the same time, this effect allowed for a separate observation of the loss rate induced by radiative escape [Rit95].

- A radiative escape event occurs, when one of two nearby ground-state atoms ($R_{\mathrm{abs}} \approx$ 100 nm) absorbs a resonant photon from the trap laser. The $S_{1/2}$+$P_{3/2}$ molecular potential has an attractive long ranged component falling off as R^{-3}, where R is the interatomic distance, due to the resonant electric dipole interaction. Within the lifetime of the excited state, the atoms are accelerated towards each other. Upon the emission of a red-shifted photon at closer internuclear distance R_{em}, the collision pair will find itself on the flat $S_{1/2}$+$S_{1/2}$ potential curve, sharing the kinetic energy $V_{S_{1/2}+P_{3/2}}(R_{\mathrm{abs}}) - V_{S_{1/2}+P_{3/2}}(R_{\mathrm{em}})$ gained in the acceleration process. The interaction between two excited atoms does not play a prominent role in radiative escape, since the $P_{3/2}$+$P_{3/2}$ potential falls off as R^{-5} and thus requires much closer interatomic distances to have a significant effect.

Inclusion of the two body effects into the model for the loading rate modifies the exponential loading and decay behaviour. The experimentally simplest indication that two-body processes contribute significantly to the overall trap loss, is a non-exponential decay component at the beginning of the decay curve, when the atom density is still high.
Under the mostly well fulfilled assumption, that the atom cloud has a Gaussian density

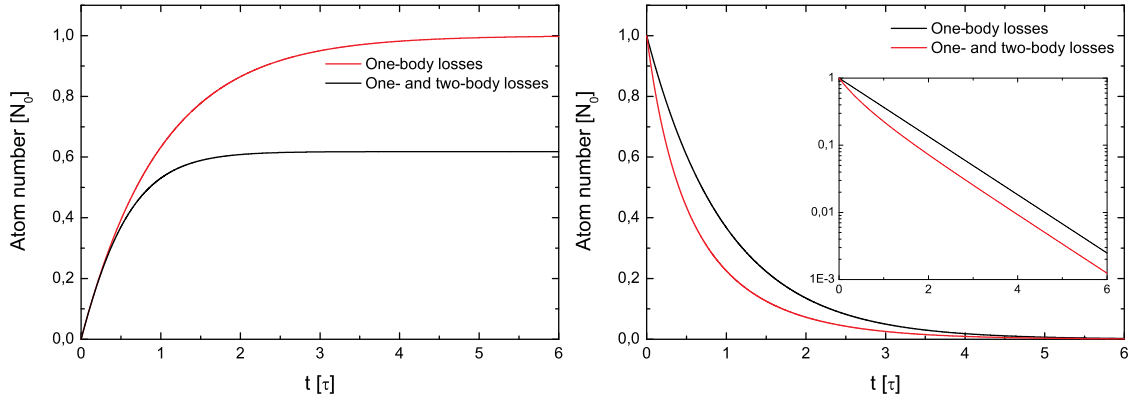

Figure 2.6: Loading curves (*left*) and decay curves (*right*), normalized to the steady state atom number $N_0 = R/L$. Time is given in units of the lifetime $\tau = 1/R$ of the atomic ensemble. The black curves represent the dynamics of the loading- and decay process with only one-body losses present, the red curves reflect the trap behaviour under the influence of one- and two-body losses. The inset in the right graph shows the decay curves in semi-logarithmic scale to illustrate the super-exponential decay at the beginning of the decay process, which is the characteristic signature of two-body effects. The two-body constant was chosen as $\beta'/R = 1$.

distribution with half $1/\sqrt{e}$-widths σ_z in the axial direction and σ_r in the radial direction (see also section 2.1.6), the integral in (2.22) reduces to

$$\beta \frac{N^2}{(\pi/2)^{\frac{3}{2}}\sigma_z\sigma_r^2} = \beta' N^2, \tag{2.28}$$

with β' being the effective two-body loss constant. The differential equation (2.22) can still be solved analytically upon inclusion of the 2-body loss term, leading to the following expression for the loading curve:

$$N(t) = \frac{\sqrt{L^2 + 4R\beta'}}{2\beta'} \tanh\left(\frac{\sqrt{L^2 + 4R\beta'}t}{2\beta'} + \operatorname{arctanh}\left(\frac{L}{\sqrt{L^2 + 4R\beta'}}\right)\right) - \frac{L}{2\beta'}. \tag{2.29}$$

The decay curve now reads

$$N(t) = N_0 \frac{Re^{-Rt}}{R + N_0\beta'(1 - e^{-Rt})}. \tag{2.30}$$

Figure 2.6 compares loading and decay curves with and without the contribution of 2-body losses.

2.1.5 Temperature of the Magneto-Optical Trap

Though a sample of laser-cooled atoms is not a system in thermal equilibrium, it can be assigned a temperature T by relating it to the average kinetic energy $\langle E_{\text{kin}} \rangle$:

$$\langle E_{\text{kin}} \rangle = \frac{3}{2} k_{\text{B}} T. \tag{2.31}$$

The model for describing the dissipative force (2.13) suggests that atoms could be cooled to arbitrarily low velocities and temperatures, but neglects the fact, that momentum exchange with the radiation field occurs in discrete quanta of $\hbar k$. Any atom recieves a stochastic momentum kick with every emission process. This corresponds to the atom performing a random walk in momentum space with steps of $\hbar k$, whose average value is zero, but its second moment, corresponding to kinetic energy, is not. So the random spontaneous emission constitutes a source of heating to the system [2]. This problem can be addressed in the framework of the Fokker-Planck equation and it can be shown, that under the conditions of laser cooling, a Maxwell-Boltzmann distribution is reproduced [Met99]. Equating the cooling (drift) and heating (diffusion) rate finally leads to an expression for the equilibrium temperature of the system. For low saturation, the model yields [Let88]:

$$k_{\mathrm{B}}T = \frac{\hbar\gamma}{4}\frac{1+(2\delta/\gamma)^2}{(2|\delta|/\gamma)}. \tag{2.32}$$

This function has a minimum for a detuning of $\delta = -\gamma/2$, corresponding to a temperature

$$k_{\mathrm{B}}T_{\mathrm{D}} = \frac{\hbar\gamma}{2}. \tag{2.33}$$

This temperature is named the *Doppler temperature* or *Doppler limit*. Within the model of Doppler cooling, it puts a fundamental limit on the temperatures achievable in MOTs and molasses. This quantitiy solely depends on the linewidth of the atomic cooling transition and is therefore on the same order of magnitude for most laser-coolable species.
The Doppler limit of lihium is 143 μK. The corresponding Doppler velocity is $v_{\mathrm{D}} = \sqrt{k_{\mathrm{B}}T/m} = 41.3$ cm/s, or expressed as momentum in atomic units, $p_{\mathrm{D}} = 0.0023$ a.u.
An even more fundamental limit is the *recoil temperature*, which is set by the recoil momentum of one scattered photon. For the light lithium atom a momentum of $\hbar k$ translates to a temperature of $T_{\mathrm{rec}} = 6$ μK or a velocity of $v_{\mathrm{rec}} = 8.5$ cm/s.
In contrast to the heavier alkali metals, temperatures below the Doppler limit [Let88], have not been observed in lithium MOTs or molasses, which can be attributed to their comparably high thermal velocity at usual molasses and MOT temperatures. This prevents the subtle optical pumping effects [Dal89], [Met99] induced by the spatially varying polarization vector of the light field, which is created by the superposition of the cooling beams, from taking effect.

2.1.6 Density of the Magneto-Optical Trap

For low atom numbers (typically $N{\approx}10^5$) any interaction between the trapped atoms can be neglected. The density distribution $n(\mathbf{r})$ for an ensemble of non-interacting particles of temperature T in a potential $U(\mathbf{r})$ then obeys a Boltzmann distribution

$$n(\mathbf{r}) = n_0 e^{-\frac{U(\mathbf{r})}{k_{\mathrm{B}}T}}. \tag{2.34}$$

[2] In a multi-beam configuration at high intensities, stimulated emission from one beam into another can take place, adding another source of stochastic heating.

According to equation (2.15), the atoms are stored in a harmonic potential

$$U = \frac{1}{2}\sum_{i=1}^{3}\kappa_i x_i^2. \tag{2.35}$$

The resulting density distribution is

$$n(\mathbf{r}) = n_0 e^{-\sum_{i=1}^{3}\frac{\kappa_i x_i^2}{2k_\mathrm{B}T}} = n_0 e^{-\sum_{i=1}^{3}\frac{x_i^2}{2\sigma_i}}. \tag{2.36}$$

The MOT cloud exhibits a Gaussian density distribution with half $1/\sqrt{e}$-widths

$$\sigma_i = \sqrt{k_\mathrm{B}T/\kappa} \tag{2.37}$$

and full widths at half maximum (FWHM) of $2\sqrt{2\ln 2}\sigma_i$.
The peak density n_0 is calculated as

$$n_0 = \frac{1}{(2\pi)^{\frac{3}{2}}}\frac{N}{2\sigma_r\sigma_z}, \tag{2.38}$$

Here the cylindrical symmetry of the MOT's gradient field as encountered in the usual experimental situation has been employed, leading to $\sigma_x = \sigma_y = \sigma_r$; see equations (2.15), (2.18).
With increasing density, there is a significant probability for a resonant photon that has been scattered by a MOT-atom, to be absorbed and reemitted by another atom. One emission–reabsorption process leads to an average relative momentum of $2\hbar k$ between two atoms, so this process gives rise to an effective repulsive force between the atoms. Adding atoms to the trap does not result in an increase in density any more, instead the cloud of atoms will expand, while the central density remains constant. The MOT is then said to operate in the *multiple scattering regime*. In typical MOT-configurations with low laser detunings it is reached at atom numbers exceeding some 10^5 atoms [Tow95].
For very large atom numbers, a considerable fraction of the laser power is absorbed within the outer shells of the cloud (optically thick MOT), partly shadowing the central region from the cooling light. Together with the above effect, this leads to a further reduction of density and an increase in temperature.

2.2 Cooling and Trapping of Lithium

2.2.1 General Properties of Lithium

Lithium is the third element in the periodic system with its three electrons (or nuclear charge of Z=3) and belongs to the group of the alkali metals. With a density of only half of that of water, it is the lightest of all metals. Due to its reactivity, it does not occur under atmospheric conditions in its pure form.
Commercially available elemental lithium comes e.g. in the form of 20 cm long dull grey

Property	Symbol	Value [Ref.]
Atomic Number	Z	3
Nucleons	$Z+N$	7
Natural Abundance	η	92.4 % [Wea83]
Atomic Mass	m	7.016 004 amu [Ems95]
		$1.165035 \cdot 10^{-26}$ kg
Nuclear Spin	I	3/2
1st Ionization Potential	$\mathrm{IP_{Li}}$	5.3917 eV [NIS07]
2nd Ionization Potential	$\mathrm{IP_{Li^+}}$	75.640 eV [NIS07]
3rd Ionization Potential	$\mathrm{IP_{Li^{2+}}}$	122.454 eV [NIS07]

Table 2.1: Basic atomic properties of ^{7}Li.

rods of 12 mm diameter with natural isotope abundances. Freshly cut surfaces appear in a shiny silver color. As all alkali metals, it is rather soft and can be cut with an ordinary knife. Due to its relatively low reactivity compared to sodium, potassium etc., it is relatively easy to handle. When exposed to ambient air, a crust of lithium oxide Li_2O, lithium hydroxide LiOH and lithium nitride Li_3N forms. Experimental preparation and storage are best performed under argon atmosphere.
Lithium has two stable isotopes, the bosonic ^{7}Li with a nuclear spin of $I = 3/2$ and the ^{6}Li with $I = 1$, which is a composite fermion. The natural abundances are 7.6 % for ^{6}Li and 92.4 % for ^{7}Li. Since at the present stage, the carried out and planned experiments are not sensitive to the quantum-statistical nature of the target, it is most efficient to trap ^{7}Li. However, since there is an D2-line isotope shift of 10 GHz [Wal03] and even smaller hyperfine splittings of the levels relevant to laser cooling when comparing ^{7}Li and ^{6}Li , the same laser system could be used to trap ^{6}Li as well, provided a set of optical modulators with matching center frequencies for fine tuning.
Table 2.1 lists some relevant fundamental properties of atomic ^{7}Li, amongst them the ionization potentials for all charge states.
As an essential prerequisite for spectroscopy, trapping and collision experiments, the involved substances have to be prepared in gaseous form. For most elements, simple heating of the solid or liquid phase inside a vacuum oven generates enough vapour pressure to form a thin atomic gas or beam. Some thermodynamic properties of lithium are presented in Table 2.2. The important vapour pressure curve and the generation of an atomic lithium beam are discussed in section 3.7.

2.2.2 Spectroscopic Properties of Lithium

In section 2.1.2 the principles of laser cooling have been eludicated by means of a model two-level system. Efficient laser cooling can only take place by means of driving a closed or *cycling transition*, i.e. the excited state must not spontaneously decay to any state other

Quantity	Symbol	Value [Ref.]
Density (300 K)	ρ	0.534 g/cm^3 [Wea83]
Melting Point	T_M	180.54 °C [Wea83]
Boiling Point	T_B	1342 °C [Wea83]
Heat of Fusion	Q_F	2.99 kJ/mol [Wea83]
Heat of Vaporization	Q_V	134.7 kJ/mol [Wea83]

Table 2.2: Basic thermodynamic properties of bulk ^{7}Li.

than the ground-state of the cooling transition[3]. For the alkali metals, this condition is only approximately fulfilled. Otherwise, optical pumping takes place, emptying the original ground state by transferring the atoms to the so called dark state. Fig. 2.7 displays the energy levels relevant to laser cooling of lithium. As for all alkalis, the D2-component ($2^2S_{1/2}$ – $2^2P_{3/2}$) of the prominent D-line is utilized as cooling transition. In principle the D1-line ($2^2S_{1/2}$ – $2^2P_{1/2}$) could be used as well, but carries only half the line strength of the D2-transition. The wavelength of this transition is in the visible at 671 nm and responsible for the characteristic, beautiful bright red colour of fluorescing lithium and our laser.

The radiative lifetime of the D-line transition is τ=27.10 ns [McA96], [Vol96], corresponding to a natural linewidth of $1/(2\pi\tau) = 5.87$ MHz. The ground $|2S_{1/2}\rangle$ state shows a characteristic hyperfine structure splitting, induced by the interaction of the nuclear magnetic moment with the electronic magnetic moment. On the D2-line, a cycling transition could be realized via the strong ($2^2S_{1/2}, F = 2$ – $2^2P_{3/2}, F' = 3$) transition (the prime labels the quantum numbers of the respective excited state), since the excited state can only decay back to the $|F = 2\rangle$ level (see Fig. 2.7). The quantum number F denotes the total angular momentum $\mathbf{F} = \mathbf{J} + \mathbf{I}$, where $\mathbf{J} = \mathbf{L} + \mathbf{S}$ is the total electronic angular momentum and $\mathbf{I}$ the nuclear spin. Due to the exceptionally small hyperfine splitting (hyperfine constant a_{HFS} = -3.055 MHz) of the $|2^2P_{3/2}\rangle$ state, all 4 hyperfine sublevels lie closely spaced in an frequency interval of only 18.33 MHz which is just three natural linewidths. Thus an off-resonant excitation of all allowed transitions is inevitable. The $|2^2P_{3/2},\ F' = 1, 2\rangle$ states can then decay to the $|2^2S_{1/2},\ F = 1\rangle$ ground state. This unresolved hyperfine structure induces a strong coupling between the two ground states, turning the D2-line of ^{7}Li into an effective λ-3-level system.

The Repumper Laser

To prevent all atoms being transferred from the $|F = 2\rangle$ to the $|F = 1\rangle$ ground state within a few scattering cycles, and thus being lost from the trap, the *repumper laser* is employed.

[3] A large number of successful experiments has been performed on metastable noble gases. The lifetimes of the metastable ground states of the cooling transitions have lifetimes between 20 s (Ne) and 150 s (Xe), well exceeding the storage- or cycle times of most cold atom experiments.

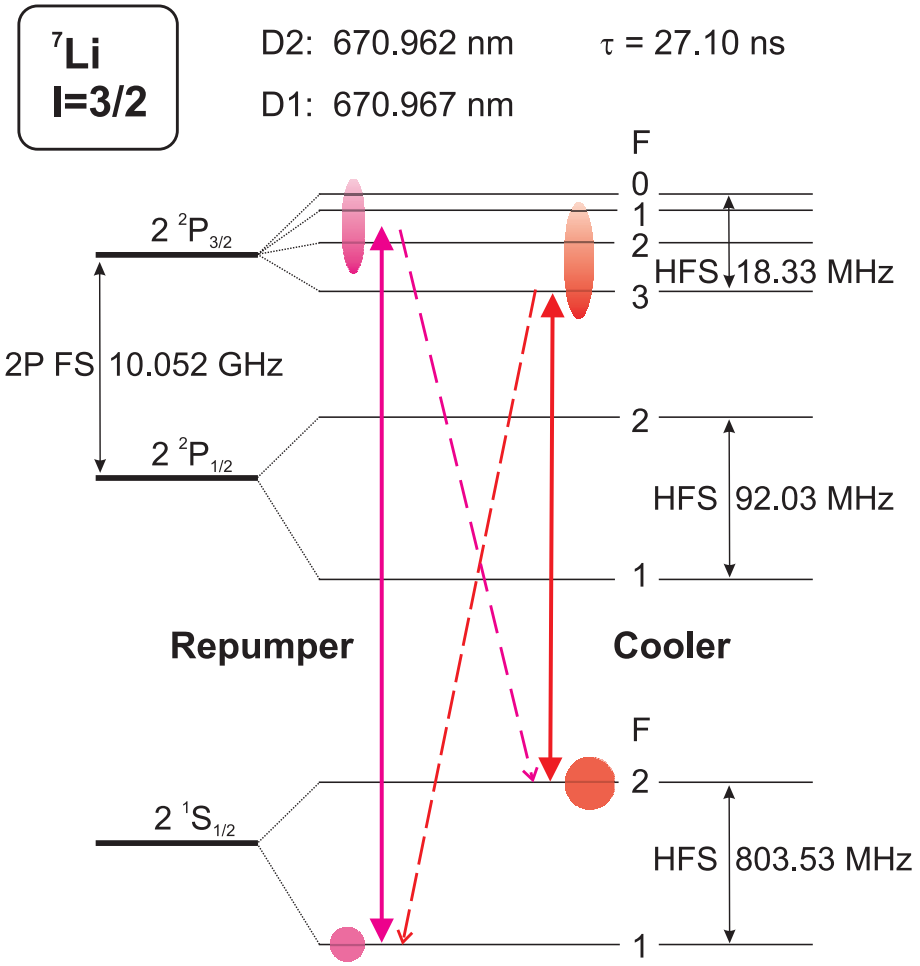

Figure 2.7: Schematic of the atomic levels of ^{7}Li relevant to laser cooling: The full lines indicate the 'closed transitions' of the cooler and repumper laser, dashed lines the decay channels to the other ground state. HFS: Hyperfine Splitting; FS: Fine structure Splitting.

It drives the transistions from the $|F = 1\rangle$ ground state to the $|F' = 0\rangle$, $|F' = 1\rangle$ and $|F' = 2\rangle$ excited states. From the they can decay back to the $|F = 1\rangle$ state. For the other alkali metals, apart from potassium, the hyperfine splitting of the excited state is much larger (e.g. a total of 496 MHz for ^{87}Rb), so the branching ratio to the unwanted ground state is rather low, though clearly apparent in the experiment. There, it is sufficient to guide one weak (a few mW) beam of matching frequency through the trap region to ensure an efficient repumping process.
For lithium, the situation is completely different: Due to the strong coupling of both ground states, the repumper contributes a considerable fraction to the scattering force. For effective trap operation, beams of about the same intensity have to be used, which should be carefully overlapped with the cooling beams to avoid imbalances in radiation pressure.

Quantitiy	Symbol	Value [Ref.]
Wavelength Vacuum D2($2^2S_{1/2}$–$2^2P_{1/2}$)	λ_{vac}	670.9767 nm [San95]
Wavelength Vacuum D1($2^2S_{1/2}$–$2^2P_{3/2}$)	λ_{vac}	670.9616 nm [San95]
Wavelength Air D2($2^2S_{1/2}$–$2^2P_{1/2}$)	λ_{air}	670.7764 nm [San95]
Wavelength Air D1($2^2S_{1/2}$–$2^2P_{3/2}$)	λ_{air}	670.7915 nm [San95]
Frequency D2	ν	446.8102 THz
Photon Energy D2	$\hbar\omega$	1.84786 eV
Lifetime 2^2P	τ	27.10 ns [McA96]
Natural Linewidth 2^2P	γ	36.90 $\cdot 10^6$ s^{-1}
		5.873 MHz
Saturation Intensity D2	I_s	2.54 $\mathrm{mW/cm^2}$
Hyperfine Structure Constant $2^2S_{1/2}$	a_{HFS}	401.76 MHz [Wal03]
Hyperfine Structure Constant $2^2P_{3/2}$	a_{HFS}	-3.05 MHz [Ort75]

Table 2.3: Specroscopic properties of ^{7}Li relevant to laser cooling.

2.2.3 Resonance Fluorescence and Atom Number

One key parameter in the determination of the properties of a MOT is the total number of trapped atoms. This could be done by measuring the attenuation of a weak large diameter probe beam guided through the trap. The simplest way to estimate the atom number, is to record the fluorescence emitted by the MOT, since the scattered light power should be proportional to the number of atoms in the trap. Equation (2.9) suggests that by knowledge of the saturation intensity, laser detuning and laser intensity at the position of the trap, the atom number can be determined.
The calculated value of the saturation intensity I_s always refers to the strongest transition between magnetic sublevels within a (J–J')-transition. For the D2-line of ^{7}Li these are the stretched transitions ($F = 2, m_F = \pm 2$ – $F' = 3, m_F = \pm 3$), which have a Clebsch-Gordan coefficient of 1. To do justice to the situation in a real MOT, one must calculate an average of all the transitions between the Zeeman sublevels of the ground and excited state, since due to the interference of the six MOT beams the field polarization, the local field intensity and the internal atomic state are a complicated function of the position of the atom [Tow95].
In a first approximation the light field in the MOT is considered to be unpolarized, i.e. any atom is on average exposed to three polarization components σ^+, σ^- and π of equal strength. Furthermore an equal distribution of the population over the ground state sublevels is assumed. Thus one can calculate an effective saturation intensity $\langle I_s \rangle$ by calculating the average square of the Clebsch-Gordan coeficients [Var88] of all allowed transitions within the respective hyperfine multiplet (here for the ($F = 2$ – $F' = 3$)

transitions) [Din92], [Mar98]:

$$\begin{aligned}\langle CG^2\rangle(F=2-F=3) &= \frac{1}{3}\frac{1}{5}\sum_{m_F=-2}^{m_F=+2}\sum_{q=-1,0,1} CG^2(F=2,m_F-F'=3,m_F+q)\\ &= \frac{7}{15}.\end{aligned} \tag{2.39}$$

The index q labels the polarization state of the light ($q=\pm1$ for $\sigma^{\pm}$ and $q=0$ for π), the prefactor of $\frac{1}{3}$ account for the average over the polarizations and $\frac{1}{5}$ for the average over the five magnetic sublevels of the ground state.
The averaged saturation intensity is

$$\langle I_s\rangle = \frac{15}{7}I_{\mathrm{sat}} = 5.46\mathrm{mW/cm}^2, \tag{2.40}$$

i.e. compared to a perfect two-level system, twice the intensity are needed to saturate the cooling transition. For most alkali atoms, this would be a good approximation to estimate the atom number from the emitted fluorescence, since the trap population mainly cycles on these transitions and there is no significant excitation of the other hyperfine structure levels.
However, for an estimate of the atom number within a factor of two, the above approximations are sufficient. For a more accurate description of the situation in the lithium atom, a rate equation model based on averaged transition rates should be considered, modeling the D2-line as a 3-level system, with the $|F=1\rangle$ and $|F=2\rangle$ states as ground states and combining the $|F'=0,1,2,3\rangle$ states to a single excited state.

Chapter 3

Experimental Setup

This chapter describes in detail the experimental apparatus developed in the course of this thesis. First of all, section 3.1 gives a general introduction to the principles and applications of the reaction microscope and momentum spectroscopy. Section 3.2 briefly discusses the experimental implications arising from the combination between a magneto-optical trap and a reaction microscope. The succeeding sections account for a description of the different components of the experimental setup.

3.1 Reaction Microscopes

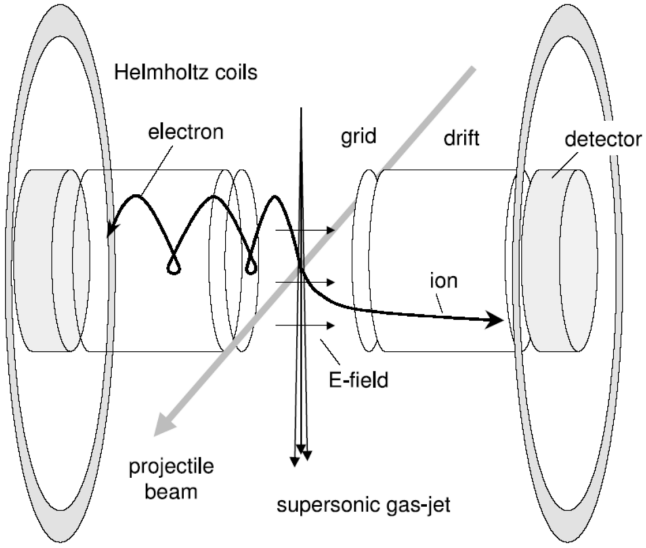

Figure 3.1: Schematic of a 'classic' reaction microscope, as used in ion-atom or ion-electron collisions. Ions and electrons produced by the projectile beam are guided towards position sensitive detectors by homogeneous electric and magnetic fields. The supersonic jet provides an internally cold target.

The reaction microscope allows kinematically complete experiments on the fragmentation

of atoms and molecules by particle impact, i.e. the final state momenta of all the charged fragments emerging from a collision process are determined simultaneously on an event-by-event basis.
Given a sufficient number of events, this corresponds to a direct mapping of the squared final state wave function of the collision system or Fully Differential Cross Section (FDCS). In an ionizing collision, an ion and one or several low-energetic electrons are produced. By recording the full momentum vector of each of the collision products, the full kinematics of this process can be reconstructed. For a total number of particles in the final state N (including the projectile), and provided precise knowledge of the initial momenta of the collision partners, a set of N-1 measured final momenta allows the determination of all kinematic parameters of the reaction by means of momentum conservation:

$$\mathbf{p}_{\mathrm{P}}^{\mathrm{i}} + \mathbf{p}_{\mathrm{R}}^{\mathrm{i}} = \mathbf{p}_{\mathrm{P}}^{\mathrm{f}} + \mathbf{p}_{\mathrm{R}}^{\mathrm{f}} + \sum_{j=1}^{n} \mathbf{p}_{\mathrm{e}j}^{\mathrm{f}} + \sum_{l=1}^{m} \mathbf{p}_{\gamma l}^{\mathrm{f}}. \tag{3.1}$$

Here, $\mathbf{p}_{\mathrm{P}}^{\mathrm{i}}$ denotes the initial (before the collision) and $\mathbf{p}_{\mathrm{P}}^{\mathrm{f}}$ the final (after the collision)

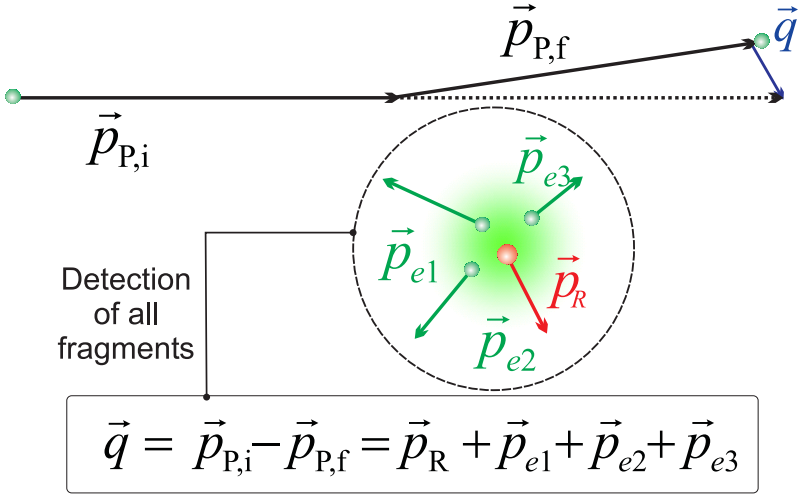

Figure 3.2: Detection of all target fragments (here triple ionization of lithium by electron impact) enables a kinematically complete mapping of the ionization process, if the initial momenta of target and projectile are well prepared. All kinematic quantities such as the net momentum transfer **q** from the projectile to the target atom can be reconstructed.

projectile momentum, $\mathbf{p}_{\mathrm{R}}^{\mathrm{i}}$, $\mathbf{p}_{\mathrm{R}}^{\mathrm{f}}$ are the initial and final momenta of the target atom and recoil-ion, respectively. $\mathbf{p}_{\mathrm{e}j}^{\mathrm{f}}$ are the momenta of the liberated electrons and $\mathbf{p}_{\gamma l}^{\mathrm{f}}$ the ones of eventually produced photons. The momenta carried and transferred by photons (even in multiphoton ionization) are usually negligibly small compared to the ionic and electronic momenta, so they can be omitted from the momentum balance to considerably simplify analysis and interpretation of data, and only have to be taken into account in the energy balance.
Assuming the target atom was prepared to a well defined initial momentum state, the

reference frame to describe the collision is chosen such that $\mathbf{p}_{\mathrm{R}}^{\mathrm{i}}$ can be set to zero. Compared to the momenta of the fragments, which are typically on the order of a few a.u. at maximum, the projectiles in an ion-atom- or electron-atom collision are usually high energetic and remain undetected.
The reaction microscope is essentially a combination of a recoil-ion spectrometer and an electron spectrometer, each with the capability to measure the momentum vector of the registered particles. This is accomplished by projecting the recoil ion and the ionized electrons onto time- and position sensitive detectors by weak electric- and magnetic fields. By knowledge of the external fields, the final state momentum vector (p_x,p_y,p_z) of a particle emerging from the collision can be recalculated from the impact position on the detector and the time of flight (x,y,t). The working principle of the reaction microscope is illustrated in Fig. 3.1
For the slow and low energetic recoil ion a homogeneous electric field of a few V/cm is sufficient, while the fast and high energetic electrons are additionally radially confined by a homogeneous magnetic field of a few Gauss.
The concept of imaging spectrometers has several advantages:
First of all, by properly adjusting the extraction fields, an acceptance for all target fragments of 4π can be achieved, i.e. there is no selectivity in energy or direction, and the whole final state phase space of the reaction is covered at once. This is the decisive advantage, when processes with low cross section or a larger number of fragments involved are examined. Already a kinematically complete measurement on single ionization by electron impact demands the coincident detection of 2 particles, not to mention double or triple ionization, where more particles have to be detected. Conventional electron spectrometers have typical detection solid angles of $\frac{\Omega}{4\pi} \approx 10^{-3}$. In a coincidence experiment, two detectors would be employed, where one of them is scanned over the angle with respect to the other detector to cover the different collision geometries. In this case, a reaction microscope brings about an increase in the detected phase space by a factor of 10^6.
Furthermore, the recoil-ion spectrometer identifies the species and charge state of the ion by its time-of-flight, thus allowing purification of the data from events stemming from ionization of residual gas atoms or when an electron was not detected. However, the experimentalist has to take care, that on average no more than one atom is ionized within one projectile shot. Multiple events can aggravate the identification of correlated electrons from the same source atom or even render it impossible.

3.1.1 Target Preparation

The high momentum resolution of the recoil ion spectrometer and the requirement that the initial momenta of projectile and target have to be well defined, demands that the momentum spread of the target due to thermal motion must be drastically reduced, i.e. the target gas has to be cooled. Therefore, this technique is known as COLd Target Recoil Ion Momentum Spectroscopy (COLTRIMS).
To understand the crucial importance of a cold target, it is instructive to consider some

representative values of kinetic energy and momentum: At room-temperature (≈300 K), the mean translational energy of a particle along one dimension is 130 meV. Expressed in terms of a momentum spread, which largely determines the achievable resolution in momentum spectroscopy, the momentum of an electron is smeared out by roughly 0.09 a.u., but the impact on the momenta of the much heavier ions is truly dramatic: The momentum spread of an ion at room temperature amounts to 4.17 a.u.$\sqrt{m[\text{amu}]}$, resulting in 8.3 a.u. for helium and 11.0 a.u. for lithium, which is, even for the lightest of target atoms, well above the momenta imparted on the electrons and ions in atomic fragmentation reactions, which are on the order of 1 a.u..

Supersonic Jets

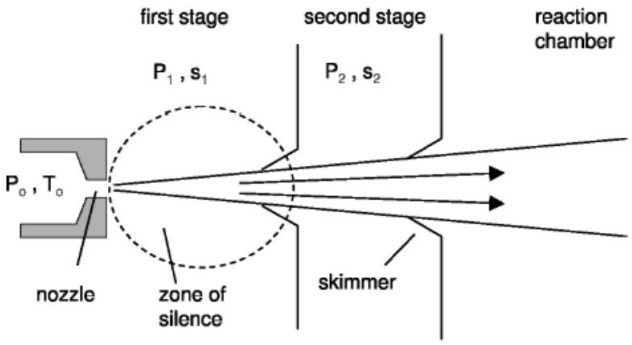

Figure 3.3: Schematic of a supersonic jet (from [Ull03b]). To reduce the gas load in the experimental chamber, two or more collimation- and differential pumping stages are needed.

The state-of-the-art method of preparing a cold target with temperatures in the sub-K range is adiabatic expansion of a pressurized gas (several bar) through a small nozzle with a typical diameter of 30 μm into a vacuum vessel, such that an internally cold atomic beam, the 'supersonic jet', is formed. In the process, the free enthalpy of the gas, $H = (5/2)k_{\text{B}}T$ (its internal energy plus the work $p\,\text{d}V$ required to press the gas through the nozzle), is almost entirely converted into directed translational energy. Depending on the parameters of the expansion process, such as nozzle diameter, pressure, temperature and the species of the used gas, internal jet temperatures of less than 1 K are easily reached, which can be further lowered if the gas is cooled down from room temperature prior to expansion, for example by a cryogenic nozzle or a cooled gas reservoir. Moshammer *et al.* [Mos96] report on internal temperatures of 2 mK for a jet of helium, that had been pre-cooled to 30 K. Through geometric collimation of the beam by conical apertures, called skimmers, almost arbitrarily low transversal (perpendicular to the propagation direction of the jet) temperatures and momentum spread can be realized, of course at the expense of target density. This method is readily applied to all kinds of atomic and molecular species

present in the gas phase at room temperature. For more details on the preparation of supersonic jets and their application to recoil-ion momentum spectroscopy, the reader is referred to [Mil88], [Ull03b], [Mos96].

Magneto-Optical Traps

The only other known method of preparing a dilute atomic gas with comparable and even lower temperatures is laser cooling, as applied in this experiment (described in detail in section 2.1). By laser cooling of atoms in magneto-optical traps target temperatures below 500 μK are routinely achieved.
In addition to its ultralow temperature a magneto-optical trap constitutes a well localized target with zero drift momentum and offers additional possibilities of initial target state preparation. Once trapped, the atoms have no superimposed drift velocity as in a supersonic jet and remain in the interaction zone for at least 1 ms even when the trapping potential is switched off, leaving enough time for further manipulation. Inherently the MOT-principle holds the possibility of examining excited states by simply irradiating the target with the MOT-lasers during the collision. In a more refined scheme, the electronic angular momenta of the ground and the excited state of the MOT-transition could be aligned with respect to a fixed-in-space axis by optical pumping to a particular magnetic sublevel. In combination with the recently completed polarized photo-electron source, a completely new field for fully differential studies opens up.
Furthermore, by the use of additional laser frequencies excitation to higher lying states is also possible, as well as photoionizing the atoms prior to the actual scattering process.

3.1.2 Reconstruction of Momenta

In a recoil-ion spectrometer, the residual ions are projected onto a position sensitive detector by weak homogeneous electric fields in a typical range of 0.5 V/cm to 2 V/cm over distances of a few 10 cm. The acceleration enforced on the ions is high enough to image them onto a detector with diameters of typically 40 to 80 mm irrespective of their initial momenta. In the reaction microscope, the ion spectrometer is extended by an electron spectrometer, employing the same field configuration. Due to their negative charge they are guided towards a second position-sensitive detector on the side opposite to the ion detector. With the electrons having about the same momenta as the ions and thus a much higher energy and velocity, the weak ion extraction field could only image a small fraction of them directly onto the detector. This problem is resolved by adding a homogeneous magnetic field parallel to the electric field, which is generated by a pair of coils in Helmholtz configuration: The field-induced cyclotron motion of the electrons now confines their trajectories within the spectrometer volume. This slightly complicates recalculation of the initial momenta, but enables a 4π-acceptance for electron detection as well.

Time and Position Focusing

The detected electrons and ions originate from an extended source volume given by the overlap of the projectile beam with the target, introducing an additional uncertainty into the calculation of their initial momenta. This effect is partly compensated, when the acceleration region (length a) of the spectrometer is followed by a field free (maintaining the maximum acceleration potential) *drift region* or *drift tube* of double the acceleration length $d = 2a$. Then the time-of-flight of particles with equal energies does not depend on their source point any more, provided the deviations from the origin are only small. This condition is called *time focusing*, also known as Wiley-McLaren configuration [Wil55]. By this configuration, larger interaction volumes can be tolerated without degrading the momentum resolution along the spectrometer axis (longitudinal momentum).
It is even possible, to realize field configurations, in which ions of same transversal momentum, but different starting positions transversal to the extraction direction, are imaged to the same spot on the detector, while at the same time the information on longitudinal momentum is preserved. This mode of operation is called *position focusing* [Dör97]. Its implementation requires the use of at least one electrostatic lens and substantially longer drift tubes ($\approx 5a$–$10a$). The optimum field profile has to be found from numerical simulation of the trajectories, as well as the momentum calibration. Nevertheless, this field configuration has the decisive advantage of maintaining a high resolution, if the source region extends over several mm in the direction perpendicular to the extraction field.

Ion Momentum Reconstruction

Due to the axial symmetry of the spectrometer fields, the imaging properties of a reaction microscope are best described in cylindrical coordinates. This axis of symmetry is given by the direction of the parallel magnetic and electrostatic fields, defining the direction of extraction. Whenever possible, the symmetry axis of the collision process under consideration (momentum of projectile beam, polarization of a laser field) is made coincident with the spectrometer axis. The momentum component along the spectrometer axis will be labeled longitudinal momentum or $p_\parallel$, the perpendicular component transversal momentum or $p_\perp$ in the following. From Newtonian dynamics it follows, that the time-of-flight of a particle of mass m, charge q and an initial longitudinal kinetic energy $E_\parallel$ is expressed by

$$t_\pm(E_\parallel) = f \cdot \sqrt{m} \left(\frac{2a}{\sqrt{E_\parallel + qU} \pm \sqrt{E_\parallel}} + \frac{d}{\sqrt{E_\parallel + qU}} \right), \tag{3.2}$$

where the '+'-sign in the denominator applies if the particle is emitted towards the detector, and the '−'-sign for the opposite direction. U is the acceleration potential, a the acceleration distance and d the drift length of the spectrometer. The prefactor f depends on the choice of units, if, for practical purposes, t is specified in ns, a and d in cm, $E_\parallel$ and qU in eV and m in atomic mass units amu, it has the value

$$f = 719.9 \cdot \frac{\text{ns}}{\text{cm}} \sqrt{\frac{\text{eV}}{\text{amu}}}. \tag{3.3}$$

From the measured time-of-flight $t(E_\parallel)$ of the ion, longitudinal energy and momentum are reconstructed. Solving (3.2) for the longitudinal momentum $p_\parallel(t) = \sqrt{2mE_\parallel(t)}$ can only be done numerically or by an approximating function, since there is no analytical expression for the inverse function of $t(E_\parallel)$. For the case of ions however, the energy gained from the extraction field qU (eV) is much larger than the initial kinetic energy $E_\parallel$ (meV), so that a first-order Taylor expansion for small energies around zero is justified:

$$\Delta t = t(E_\parallel) - t(E_\parallel = 0) \approx \left.\frac{\mathrm{d}t(E_\parallel)}{\mathrm{d}E_\parallel}\right|_{E_\parallel=0} \cdot E_\parallel. \tag{3.4}$$

For the longitudinal momentum $p_\parallel$ in atomic units one finds (using the same units as in (3.3)):

$$p_\parallel = 8.042 \cdot 10^{-3} \frac{\text{cm a.u.}}{\text{eV ns}} \frac{qU\ \Delta t}{a}. \tag{3.5}$$

This demands an independent determination of $t(E_\parallel = 0)$, which can be inferred from momentum conservation within the collision system or from the symmetry properties of the collisional process.
The transverse momentum $p_\perp$ of the recoil ion is derived from the arrival position (x,y) on the detector. To calculate $p_\perp$, the hit position of ions with vanishing transversal momentum (x_0,y_0) has to be assigned. This is done by finding the center of rotational symmetry in the position spectrum, if an axially symmetric reaction is studied. The recoil-ion's arrival radius $r = \sqrt{(x-x_0)^2 + (y-y_0)^2}$ obviously depends on its transversal momentum $p_\perp$ and its time-of-flight $t(E_\parallel)$. Time-of-flights for characteristic extraction voltages are on the order of some μs, whereas the width of the time-of-flight distribution is only a fraction of a few thousandths of the total time-of-flight. When calculating $p_\perp$ from the arrival position, the initial longitudinal momentum of the ion can be neglected. Employing (3.2), the transversal momentum is given by

$$p_\perp = 11.6 \frac{\text{a.u.}}{\sqrt{\text{amu eV}}} \frac{r}{2a+d} \sqrt{qU\ m}. \tag{3.6}$$

Electron Momentum Reconstruction

For the reconstruction of longitudinal electron momenta, which are unaffected by the magnetic extraction field, (3.2) equally applies. However, the initial energy $E_\parallel$ is on the same order of magnitude as the acceleration potential qU, so that the approximation (3.4) is no longer valid. In this case, the non-linear equation (3.2) has to be solved for $E_{e,\parallel}$ for each individual event, e.g. by the iterative Newton's method [Bro01].
The transversal motion is strongly affected by the guiding field: The electrons are forced onto a spiral trajectory, orbiting with a cyclotron frequency of

$$\omega = \frac{qB}{m}, \tag{3.7}$$

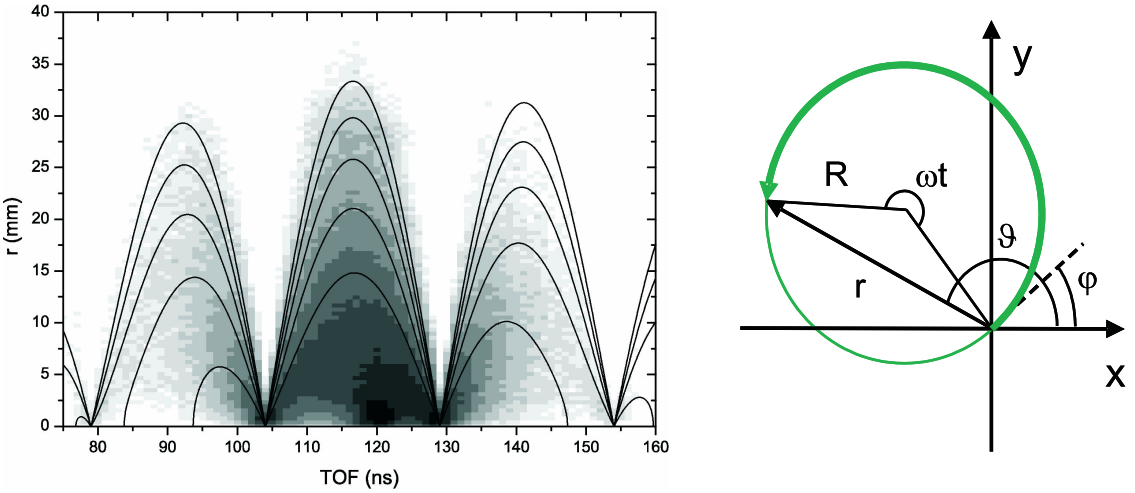

Figure 3.4: *Left*:Typical raw electron spectrum from single ionization of H_2 by 6 MeV proton impact, measured in our group: Radial displacement r of electrons on the detector is displayed vs. the electron time-of-flight. The solid lines are calculated impact coordinates for isotropically emitted electrons with kinetic energies between 10 eV and 50 eV (steps of 10 eV). *Right*: Defintion of the geometrical quantities involved in electron momentum reconstruction. The projection of the electron trajectory onto the detector plane is indicated in green.

which depends only on the strength of the extraction field B. The radius R of the cyclotron motion is proportional to the transversal momentum:

$$R = \frac{p_\perp}{qB}. \tag{3.8}$$

Figure 3.4 shows a projection of the trajectory onto the detector (x, y) plane. The origin of the coordinate system is again fixed by the impact position (x_0, y_0) of electrons with zero transversal momentum. By geometrical considerations the radius r of the hit position on the detector can be related to the cyclotron radius R and the time-of-flight t by

$$R = \frac{r}{2|\sin(\omega t/2)|}, \tag{3.9}$$

so with (3.8), one obtains

$$p_\perp = \frac{qBr}{2|\sin(\omega t/2)|}. \tag{3.10}$$

The initial emission angle in the detector plane ϕ is determined by

$$\phi = \theta - \mathrm{mod}(\omega t/2, 2\pi), \tag{3.11}$$

as in the experimental situation the electrons perform several full turns on their trajectories.
(3.9) demonstrates, that independent of their transversal momentum, all electrons with a time-of-flight that is an integer multiple of $T = \frac{2\pi}{\omega}$ will be mapped to the center point of the detector ($r = 0$). This implies that near these time-of-flights, all position information

is lost. Spectra with the time-of-flight t as abscissa and the hit radius r as the ordinate, show a characteristic nodal structure, with the nodes appearing at $t = T$. What may seem disadvantageous at first glance, actually allows an exact calibration of the absolute time-of-flight. In the experimental situation, the absolute time-of-flight of the electrons (some 10 ns) is hardly determined by direct measurement. The timing signals are likely shifted by signal delays and electronic processing times, which are on the same order of magnitude as the electrons' time-of-flight. Since the time difference between two nodes corresponds to one cyclotron period T, the actual zero point of the time axis can be extrapolated to be at an integer multiple of T ('the time-of-flight of an electron with infinite initial energy'). The left hand side of Fig. 3.4 is a typical electron spectrum, plotting the radial displacement r versus the time-of-flight t.
Reconstruction of the transversal momentum requires accurate knowledge of the axial B-field (see (3.10)), which is hardly measured inside the vacuum chamber or assesed from calculations with the needed precision. The time difference between the nodes in the time-of-flight spectrum yields an accurate measure for the cyclotron period T and together with (3.7) for the magnetic field B.
Nevertheless, this method of electron detection introduces some complications: Firstly, the transversal momentum resolution is dependent on the time-of-flight and on the hit radius r (a larger radius enables a more accurate determination of the angles θ, ϕ) and vanishes altogether at the nodal points. Still, this deficiency can be overcome by combining data sets from different runs with changed magnetic fields to shift the 'wiggle'-structure in time. Secondly, the ion trajectories remain not unaffected by the magnetic field. But as the cyclotron frequency of the ions is larger by a factor $m_\mathrm{R}/m_\mathrm{e}$ compared to the electron one, while the time-of-flight scales by $\sqrt{m_\mathrm{R}/m_\mathrm{e}}$ at most, the arc angle ωt covered by the ion trajectory is only a fraction of a full revolution. In most cases this effect is sufficiently compensated by rotating the ion position distribution by the corresponding angle.

3.1.3 Particle Detection

The time- and position sensitive detectors consist of a microchannel plate (MCP) for particle detection by secondary electron multiplication and an anode encoding the impact position of the charge cloud into electronic signals.
A multichannel plate consists of an array of glass tubes of a few micron diameter fused together to form a thin disc. Both faces of the disc are metallised to provide parallel electrical connections to all channels. With a potential difference of 1000 V between the faces, each channel becomes an independent electron multiplier with a gain of about 10^4. By stacking of 2 or 3 MCPs, the net gain is further enhanced. Due to the channel structure, the information about the impact position of the particle is preserved by the produced charge cloud. The charge cloud is accelerated towards and picked up by a position encoding anode, where it produces a voltage signal that can be processed electronically, to retrieve the impact position of the primary ion or electron.
Common techniques for position sensitive anodes are wedge-and-strip anodes [Mar81] and

delay-line anodes (see Section 3.4).

3.2 Combination of a Reaction Microscope with a MOT

Combining a MOT with a reaction microscope demands some major modifications on the conventional reaction microscope scheme. The otherwise relatively standard designs of the magneto-optical trap as well as the reaction microscope have to be adapted to be compatible with each other without sacrificing operability or performance. In the following sections, the mode of operation and the demands on the design of the setup are explained.

3.2.1 Mode of Operation

The most critical point in bringing both techniques together, is the fundamental incompatibility between the magnetic gradient field of the MOT and the requirements of electron momentum spectroscopy: The MOT magnetic field is typically operated at gradients of 5–30 G/cm, whereas the homogeneous electron extraction field of the reaction microscope is run at field strengths of 3 up to 10 Gauss. Because of the weak response of the recoil ions to magnetic fields, the presence of the MOT field is tolerable under certain circumstances [Wol97], when only the time-of-flight of ions is detected: Since the extraction proceeds parallel to the field lines of the MOT's quadrupole field, there is no noteworthy impact on the momentum distribution along the time-of-flight axis, indicating that no energy transfer between the longitudinal and transversal degrees of freedom occurs. In transversal direction, the influence of the magnetic field already leads to a distortion of the hit position image on the detector. A displacement and deformation of an ion spot into an ellipse, which would appear circular in the absence of the magnetic field, is observed [Ngu04]. To eliminate this effect, the magnetic field can be switched off during the data acquisition period, in order to create field-free conditions during ion extraction, as realized for example in the MOTRIMS-experiments on capture reactions with Na of Knoop *et al.* [Kno05], [Kno03], [Tur01]. In electron impact experiments, the technique of rapidly switching the magnetic fields has been applied to avoid the deflection of low energy electron beams. Examples are the measurements on the ratio of single- to double- and triple ionization of lithium atoms from a MOT-target by time-of-flight spectroscopy [Hua02], [Hua03], and the determination of the total scattering cross section of metastable helium He(2^3S_1) by observation of the impact induced trap loss in a MOT [Uhl05]. However, no momentum spectroscopy was carried out in the latter cases.
For momentum resolved spectroscopy of low energy electrons (<100 eV), where already small inhomogeneities of the extraction field can significantly reduce the resolution, it is crucial that the electron trajectories are not distorted by residual components of the MOT-field or stray fields of eddy currents, induced in conducting parts of the setup by the fast switching of the magnetic fields. If, on the other hand, the trapping forces of the MOT are turned off, the cloud of cold atoms will expand ballistically with thermal velocities, which, albeit low at representative MOT temperatures of about 1 mK, are still

on the order of 1 m/s for lithium. This means, after release from the trap, the cloud will diminish quickly within some ms and the atoms will be lost, making a reloading of the trap necessary. This process in turn takes several seconds.
Gathering enough events for the reconstruction of high dimensional fully differential cross

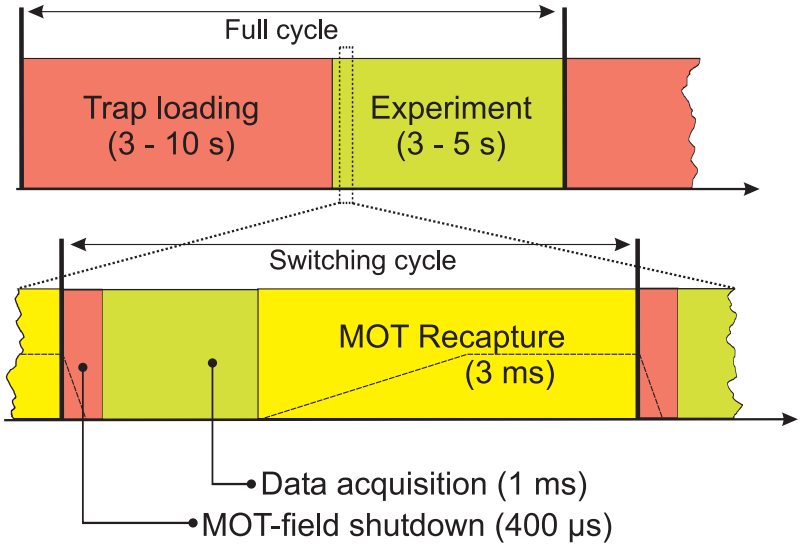

Figure 3.5: Schematic of the applied timing sequence. The dashed line gives the switching waveform of the MOT's magnetic field.

sections of rare events like triple-ionization requires highly efficient data acquisition, reducing 'dead times' due to loading of the trap as much as possible. Therefore a pulsed mode of operation is adopted, where the MOT-target is recycled by subsequent release and recapture several hundred times. Figure 3.5 presents a typical experimental timing sequence: Once the trap is loaded to the desired atom number or density, the loading beam is shut off, and the MOT-field is ramped down within 400 μs, leaving a field-free period of at least 1 ms for data acquisition, before the MOT-field is ramped up again and the expanded sample is recompressed and cooled again for approximately 3 ms. This cycle is repeated several hundred times, before the target density is considerably reduced and the trap has to be loaded again (see chapter 4). To accomplish a well defined, fast switching of the magnetic field, a current regulator, capable of switching currents of up to 100 A from an inductive load within 400 μs at repetition rates of 300 Hz, had been developed in cooperation with the electronics department of MPI-K (see section 3.5).
Compared to a reaction microscope using a supersonic jet, which is operated continuously, the MOT-setup demands precise and widely configurable timing of the experimental sequence on timescales ranging from seconds (trap loading) to 10 μs (field- and laser switching). Additionally, the system should be able to synchronize the sequence with any projectile trigger signal with microsecond accuracy. For this purpose an experimental control system based on an ADwin Gold (JÄGER MESSTECHNIK) real-time sequencer system was implemented (see section 3.8).

Process	σ^{3+}/σ^{2+}	σ^{2+}/σ^{+}
Electron impact 1000 eV	$1.08(0.15)\times10^{-3}$	$0.395(0.02)\times10^{-3}$
Photon impact 424 eV	$1.8(0.6)\times10^{-3}$	$3.7(0.1)\times10^{-3}$

Table 3.1: Ratios of triple- to double ionization and double- to single ionization by 1000 eV electron impact [Hua03], [Hua02]. Also shown are data by Wehlitz *et al.* on the ratios for photoionization by 424 eV photons from synchrotron radiation ([Weh98] for triple-to-double and [Hua99] for double-to-single ionization).

In view of the planned electron collision studies on the four- and five-body Coulomb continuum, realized by double- and triple ionization of lithium by low energy electron impact, we give some exemplary acquisition rates for kinematically complete events. These are based on the measured cross section ratios for triple-to-double and double-to-single ionization of Huang *et al.*, [Hua03] (see table 3.1). For electron energies closer to threshold, the corresponding cross section ratios will be even lower. Given an electron gun, that can be pulsed at a rate of 500 kHz, the cathode current is chosen such that about every tenth pulse an event is registered. This reduces the probability of two or more atoms being ionized by the same pulse to less than 10 %. As in electron collision experiments typically up to 5 times more electrons than ions are registered due to spurious background signals from secondary electrons and background gas ionization, an event rate of about 10 kHz for an electron-ion coincidence is expected. A detector efficiency for electron detection of roughly 50 % further reduces the coincidence rate for capturing a complete event of double- or triple-ionization.
Inserting the values of Table 3.1 yields a rate of 2 events per second for Li^{2+} and a Li^{3+} event every 1000 s or 15 minutes. Still the experimental dead time due to trap loading and the recapture process have to be taken into account. Using an exemplary experimental sequence with a loading time of 5 s, a data acquisition phase of 1 ms and a total of 3.5 ms for trap shutdown and recapture, repeated 1000 times, the duty cycle of the measurement will be 1 s in 8.5 or slightly above 10 %. This example demonstrates, that even with a maximized event rate by optimization of the MOT-parameters and the switching procedure, the acquisition of datasets on double- or triple ionization needs stable and reliable operation of the apparatus for periods from days to weeks.

3.2.2 Overview of the Setup

At the heart of the assembly is the combined ion- and electron spectrometer with an acceleration length of 10 cm and drift tubes of 20 cm length (displayed in Fig. 3.8 and Fig. 3.9). In order to achieve a good momentum resolution in the direction transversal to the extraction field, the spectrometer had to permit the use of large area MCP detectors with an active diameter of 80 mm. Since the radii of the cyclotron motion of the electrons have similar dimensions, when the possible transversal momentum resolution is fully exploited, a cylindrical volume of that diameter has to be enclosed by the spectrometer. Therefore

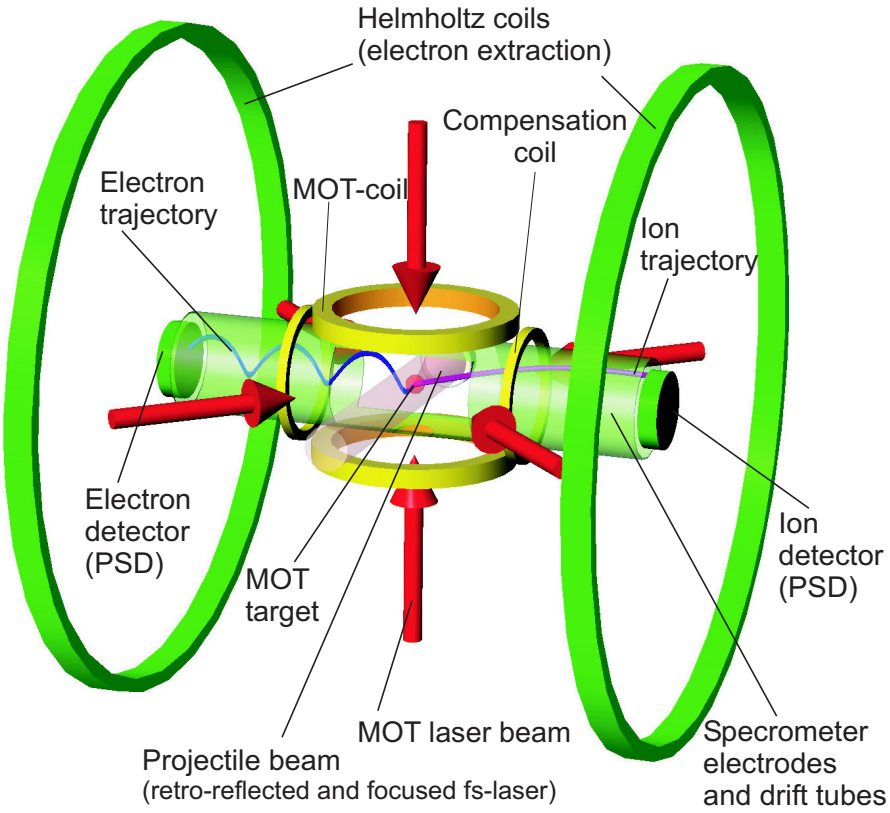

Figure 3.6: Schematic of the MOT reaction microscope, displaying the essential components of the spectrometer (green) and MOT (yellow). *PSD*: Position sensitive detector.

the pair of coils generating the gradient field for the MOT had to be built around the spectrometer, which in turn is a compact construction in order to allow a spacing between the anti-Helmholtz coils of no more than 10 cm (see section 3.5).
Since the six MOT laser beams need to access the center of the trap (four of them at angles of 45 degrees with respect to the spectrometer axis, and two from the top and bottom, respectively), the spectrometer has to be open at the sides. This also guarantees easy access to the trap region for any kind of projectile beam in an axis e.g. perpendicular to the spectrometer axis, as well as for diagnostic means and the atomic beam to load the trap.
The homogeneous electron extraction field is operated at field strengths of 3–10 Gauss. In contrast, the gradient of the MOT-field in the *radial* direction, i.e. also along the direction of extraction, has typical values between 5 and 10 G/cm. Thus the superimposed Helmholtz field of the spectrometer has a detrimental effect on the MOT, because it shifts the point, where the magnetic field is zero and which defines the position of the MOT, by several mm. This complicates alignment of the trapping and projectile beams and can degrade the resolution of the spectrometer, as the time focusing condition is not well fulfilled any more. For this reason, a pair of *compensation coils* in Helmholtz configuration along

the spectrometer axis is added, locally counterbalancing the extraction field to retain a well defined MOT position. This pair of coils is then switched simultaneously with the MOT-coils. The electron extraction field is generated by a set of Helmholtz coils of 1.8 m diameter, surrounding the whole apparatus, to ensure excellent homogeneity along the spectrometer's drift distance.
The problem of eddy currents induced by the switching of the magnetic field in nearby conducting objects, for instance the vacuum chamber, support structures and electrodes, is addressed by eliminating all closed conducting loops [Ded01]. This is achieved by cutting all ring-like structures like the spectrometer electrodes or the coil holder radially or inserting a piece of insulating material.
The materials for the in-vacuum components have to be carefully selected, since the following specifications must be met:
Firstly, vacua of 5×10^{-11} mbar or better should be achievable. The lifetime of the laser cooled sample and its loading rate are inversely proportional to the background pressure within the vacuum chamber, i.e. good vacuum conditions facilitate faster loading of the trap and enable higher target densities. At the same time, the rate of background events due to ionization of residual gas atoms and molecules is greatly reduced. This in turn demands, besides that only materials with low outgassing rates may be used, that the whole main chamber and its components must be bakeable at temperatures up to 200°C.
Secondly, to avoid distortions of the electron extraction field, all materials close to the spectrometer region should posses a relative permeability $\mu_\mathrm{r} = \mu/\mu_0$ of close to unity. This restricts the choice of materials to metals like low permeability stainless steel, aluminum and copper, polymers like kapton (polyimide) or PEEK (polyetheretherketone), ceramic materials like alumina and finally glass.
Efficient loading of the magneto-optical trap is accomplished by a directed beam of slowed down atoms from a Zeeman slower (see section 3.7). This method allows to maintain excellent vacuum conditions, while at the same time providing high loading rates.

3.3 Experimental Chamber and Vacuum System

The main vacuum chamber, also termed experimental chamber consists of a spherical body of 40.5 cm diameter and is manufactured of 1.4435 stainless steel. Figure 3.7 shows a top view and a side view of the chamber geometry. A total of 6 CF200, 4 CF100 and 12 CF63 ports are available, all of them pointing to the center of the chamber. The 6 CF200 ports are for access and the insertion of large parts like the spectrometer and the MOT-coils into the chamber. The ports along the (vertical) z-axis are occupied by the MOT-coil assemblies. Along the spectrometer (x-)axis, the detector chambers are attached. They consist of CF250 tubes of 24 cm length, enclosing the outer part of the drift tubes and the detectors. The detectors themselves are mounted on a CF250 flange and can be inserted or removed as a whole unit. Two CF150 ports and one CF100 port on the detector chamber provide additional mounting capabilities. Presently, a titanium sublimation chamber with water cooled deposition screens is attached on top of the electron detector housing. The

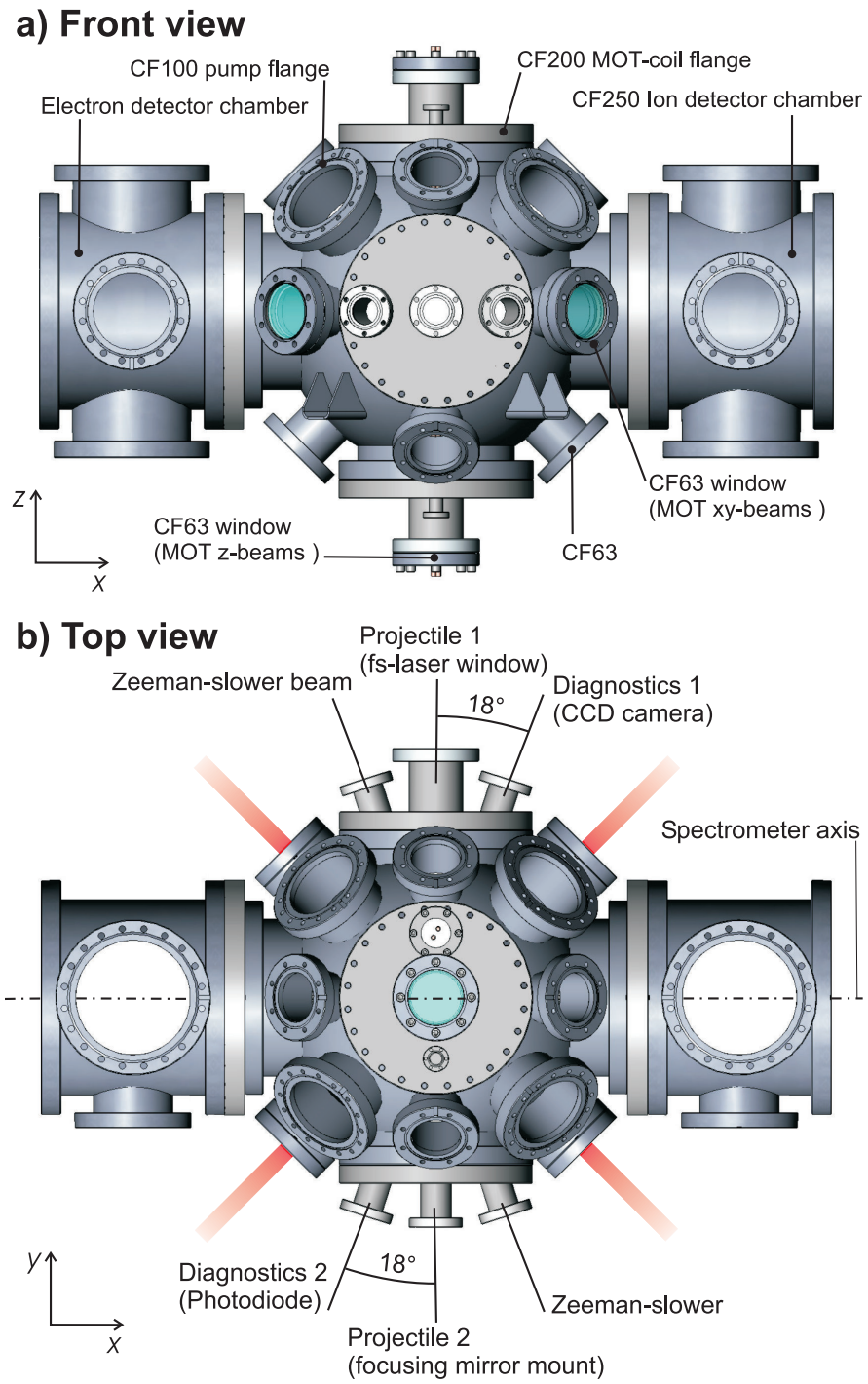

Figure 3.7: a) Top view of the experimental chamber. b) Front view of the experimental chamber.

remaining two CF200 ports are closed by one 2×CF40/CF63 and one 3×CF40 cluster flange. Line-of-sight access to the center of the chamber is only possible in the equatorial plane, since the other directions are obstructed by the MOT-coils and the spectrometer

electrodes.
As indicated in figure 3.7, these ports provide three axes through the center at mutual angles of 18 degrees. They are occupied by the Zeeman slower and its counter propagating laser beam, a photo diode and a CCD camera for monitoring the MOT fluorescence, and the projectile beam. In the measurements presented here, fs-laser pulses were used, which were focused onto the MOT-target by a spherical mirror inside the chamber, attached to an adjustable mirror mount. The six MOT-beams are introduced into the chamber through anti-reflection coated windows, the top and bottom beams passing through the MOT-coils. In the horizontal plane, the four CF63 flanges enclosing an angle of 45 degrees with the spectrometer axis (displayed with viewports in Fig. 3.7) are employed. The top CF100 ports are mainly used for the connection of pumps (two VARIAN 300 l/s turbo pumps and one SAES getter pump), whereas the remaining CF63 flanges can be utilised for ion gauges, electrical feedthroughs for the spectrometer voltages and other purposes.
All tubes and flanges are made of 1.4435 (316L) or 1.4429 (316LN) (DIN Werkstoff-Nr./AISI code) stainless steel, which have a low magnetic permeability (less than μ_{rel}=1.005 for 1.4429-steel), low outgassing rates and a high temperature stability (the knife edges of the flanges might get dull after repeated cycles of baking due to annealing of the material otherwise).

3.4 Spectrometer and Detectors

3.4.1 Time Focusing Spectrometer

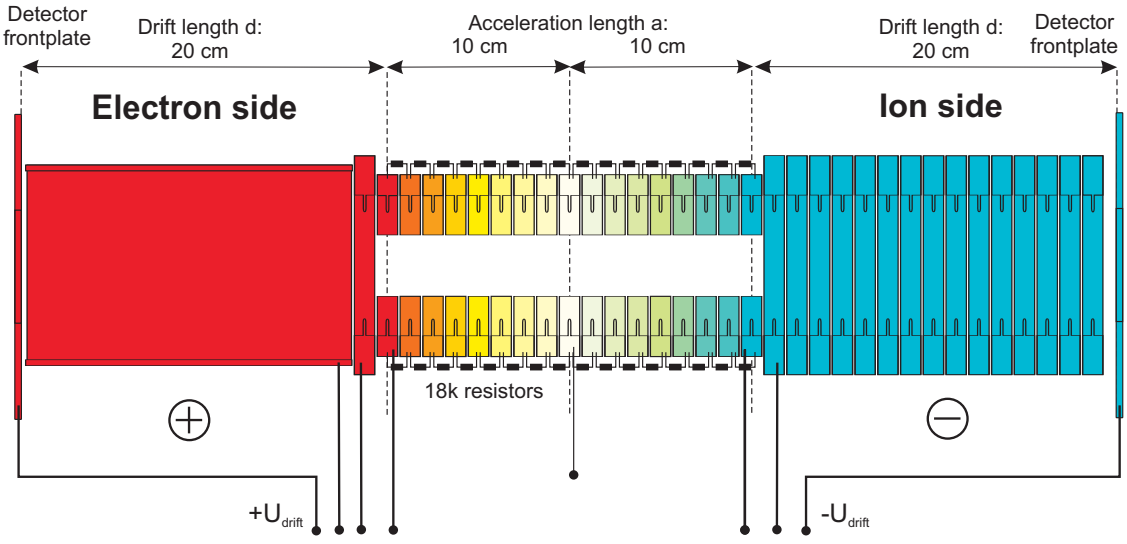

Figure 3.8: Schematic of the time focusing spectrometer and its electrical connections.

According to section 3.1.2, a time-focusing field geometry is achieved, if the acceleration length a is chosen half the length d of the field-free drift region. The spectrometer developed for the MOT-apparatus was designed with an acceleration length of a=10 cm and a

drift length of d=20 cm on the ion- as well as the electron side. The linear potential gradient of the acceleration region is emulated by a series of discrete ring electrodes: Adjacent electrodes are connected by resistors, thus forming a voltage divider, which ensures equal potential differences between the neighbouring electrodes. In this way, the homogeneous acceleration field is created.
For the ease of manufacture, all spectrometer electrodes were made from identical rings

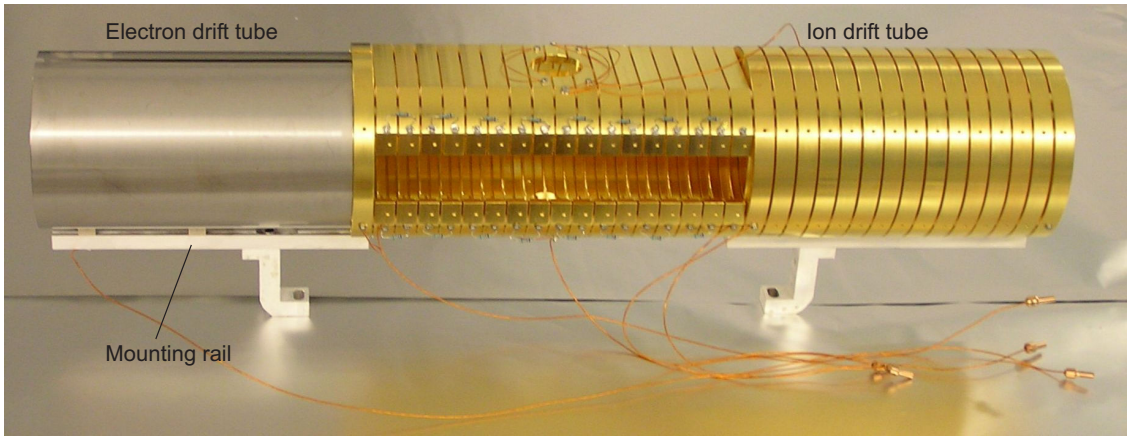

Figure 3.9: Photograph of the assembled spectrometer.

of AlMg3 aluminum alloy with an outer diameter of 11.2 cm. The rings forming the inner part of the spectrometer, were then cut accordingly to fit in between the MOT-coils. A nose along the inner circumference of the rings aims to fix the potential applied by the voltage divider at the middle of each electrode. This leaves a cylindrical volume of 83 mm for the particles trajectories, so that the full active area of the 80 mm diameter microchannel plates is covered by the charged particles. Due to the spatial constraints, the electrons' orbits can come very close to the electrodes' surfaces. In order to avoid a degradation in the resolution of the spectrometer due to inhomogeneous surfaces, e.g. layers of aluminum oxide, which may charge up, the spectrometer electrodes have been galvanically gold-plated. The induction of long lived ring currents within the electrodes by the rapidly varying trapping field, is avoided by cutting the rings radially.
The central acceleration part of the spectrometer does actually not consist of full rings, but of a top- and bottom array of electrodes, leaving a rectangular opening of 30 mm height at the sides of the spectrometer. This provides unhindered passage of large radius MOT-laser beams, which are introduced into the chamber at an angle of 45°with respect to the spectrometer axis, and full optical access to the target by any projectile beam and diagnostic means. The top- and bottom electrode arrays each have an independent voltage divider to apply the appropriate potentials. Each one is made of a chain of 16 ordinary 18 kΩ thin-film precision resistors, specified to 0.1% accuracy. Before the resistors were built in, they had been baked in a vacuum oven for outgassing and ageing. This procedure ensures, that the parts will not change their resistance after a bake-out in the vacuum chamber itself, and resistors, that experienced a change of value by the application of heat

can be singled out. The potential differences between opposing upper and lower electrodes arising from assymmetries between the two voltage dividers were measured and found to be on a level of 10^{-4} of the absolute value at most. Thus, they can be considered to be negligible.
For assembly, four M4 threaded rods are screwed into the end-electrode and 6×4 mm alumina ceramic tubes are slid onto them. The electrodes are then simply stacked up one upon another on these tubes. Ceramic spacers of 1.6 mm length, fitting into the 8 counterbores on each ring side, maintain the distance of 1 mm between the electrodes' faces and provide electrical insulation. The whole assembly is fixated by pressing the parts together by tightening a nut on a washer made of Vespel on the electron side.
The concept of using individual ring electrodes has the advantage that individual electrodes can be easily exchanged. In view of the planned upgrade of the ion spectrometer to a position-focusing geometry, a standard electrode can be replaced by an electrostatic lens element in a straightforward manner. For the electron branch of the spectrometer, no such modifications are expected, therefore the drift tube is simply made of a sheet of stainless steel, rolled to a diameter of 10 cm.
The spectrometer is screwed onto a mounting rail (see Figure 3.9), supported by ceramic rings for electrical insulation, while the electron drift tube rests on two seats made from PEEK. The whole spectrometer assembly is mounted onto a baseplate inside the main chamber. As indicated in figure 3.8, the end of the drift sections is defined by the frontplate of the detectors, which are set to the same potentials as the drift tubes.
Figure 3.10 is a drawing of one of the acceleration electrodes. It highlights some details of the construction of the electrodes. The overlap between the rings completely shields the inner of the spectrometer from the influence of external fields. Insulators in vacuum, such as the ceramic tubes used for insulation and as spacers, can charge up to very high potentials by attachment of stray electrons (electrons from an electron gun, secondary electrons produced by projectile or ionized electrons impinging on metallic surfaces) and severely disturb the spectrometer field, so this construction largely minimizes these problems.
Finally, a simulation with the of the spectrometer field was performed to test for any detrimental influence of the openings at the sides of the spectrometer. A CAD-model of a part of the spectrometer was imported to the TOSCA electrostatics solver and the potentials calculated. The influence of the opening turned out to be surprisingly uncritical, even though the boundary representing ground potential was placed only 1.5 cm away from the opening. Any potentially harmful influence is removed by attaching wires protruding into the horizontal plane to the lower and upper electrodes, to extend the volume of well-defined electrode potential.

3.4.2 Detector System and Data Acquisition

The time- and position resolved particle detection is accomplished by a combination of a MCP-stack in Chevron-configuration (2 plates) and delay-line anodes. Delay line anodes (Fig. 3.11) provide the best combination of high signal rate capability and good position

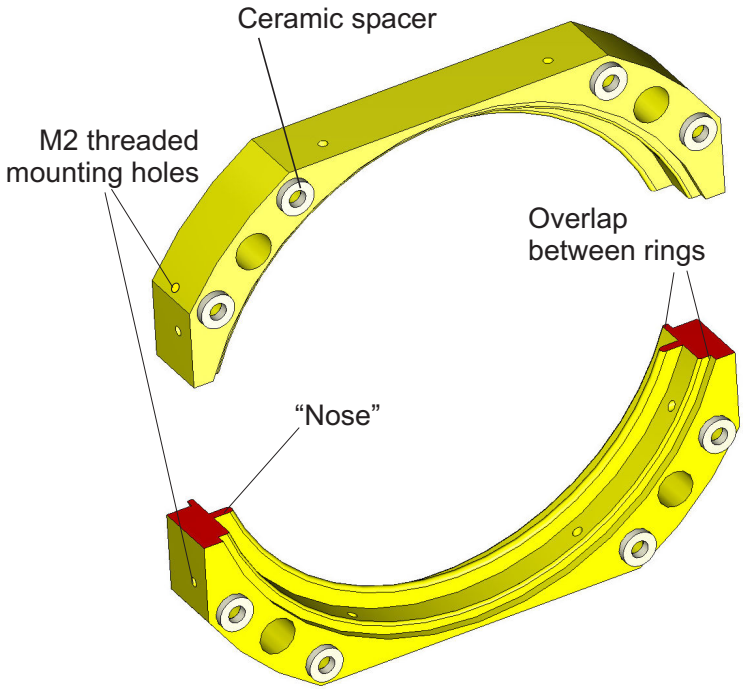

Figure 3.10: Detail view of an acceleration electrode.

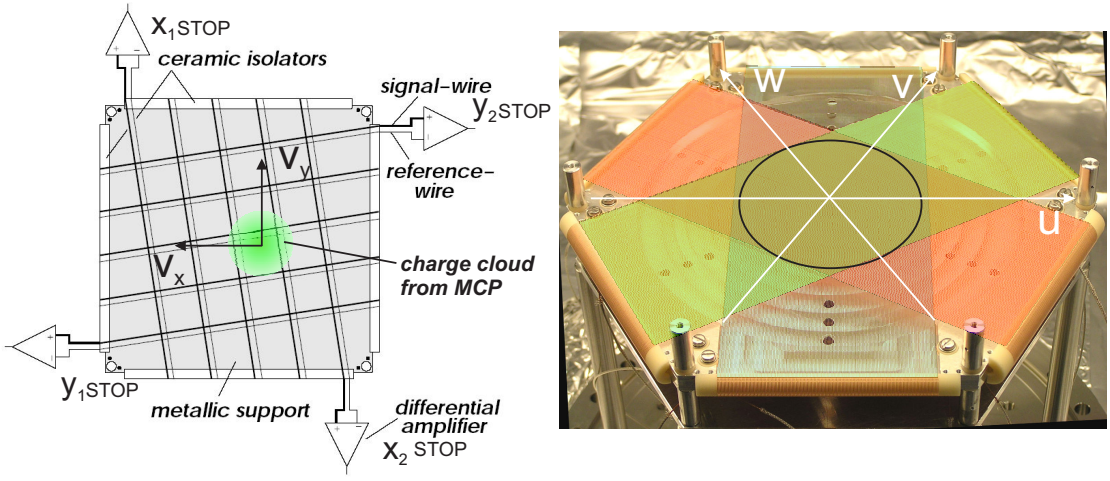

Figure 3.11: *Left*: Illustration of the principle of delay-line anodes. *Right*: Photograph of the home-built hexanode of the electron detector. The additional third layer of wire enhances the capability of reconstructing multiple events as in double- or single ionization.

resolution. Along each dimension, a wire is wound around a support frame with a pitch of 1 mm per revolution (see the schematic on the left hand side of Fig. 3.11). The electron cloud induced by an impacting particle is picked up by the positively biased wire and produces a charge pulse, that travels along the wire in both directions. The position

measurement is reduced to a time measurement: The start signal for the time-measurement is usually supplied in form of a trigger signal associated with the projectile beam or a particular reaction fragment like the first electron hit, whereas the stop-signals are derived from the pulses picked up at the each end of the delay-line's wire. The voltage pulses are capacitively outcoupled from the high-voltage supply lines, that keep the detector parts at the appropriate potentials. The signal from the impacting particle is then extracted by a differential amplifier, rejecting the common-mode noise on both wires. Further signal processing is done by constant-fraction discriminators (CFDs), converting the analog signal into a digital NIM-standard signal to provide a stop signal for the time-measurement by a time-to-digital converter (TDC).
To suppress ambient electro-magnetic noise picked up by the anode wire, in practice a pair of wires is used, the signal- and the reference wire. The signal wire is biased with a more positive potential in order to collect the main fraction of the charge. The difference between the arrival times of the signal generated by the charge cloud at both ends of the wire is proportional to the spatial coordinate. The position resolution is not fundamentally limited by the spacing of the wires, since the charge cloud extends over several turns of the wire. This effect and the pulse dispersion along the wire, lead to a cloud centroid averaging. Thus one can define an effective propagation velocity perpendicular to the wire's windings $v_\perp$ (typically on the order of 0.5 mm/ns), which relates the measured times to the position.
Assuming the propagation time to each end of the delay line is given by t_{left} and t_{right}, the measured times with respect to a common trigger signal at time t_0 relate to the position as follows:

$$x = v_\perp \left((t_{\text{left}} - t_0) - (t_{\text{right}} - t_0)\right) = v_\perp (t_{\text{left}} - t_{\text{right}}). \tag{3.12}$$

Adding instead of subtracting the measured times yields a constant value, which only depends on the total length of the signal path (anode wire and connecting cables). The so-called time-sum is used for a consistency check of the data to filter real events from noise.
The stop signal of the time-of-flight measurement is picked up from the high-voltage supply lines of the channel plate: The faces of the MCP-stack can be considered as plates of a capacitor. Upon particle impact, the generated cloud of secondary electrons effectively short-circuits cathode and anode side of the MCP-stack, leading to a voltage drop of a few ns width in the potential difference between front- and backside. This voltage spike is again coupled out and amplified for further processing.
A schematic of the data acquisition setup is found in section 5.1.2. For ion-detection a square shaped xy-anode with two layers of windings is employed. For electron detection a hexagonal delay-line anode [Jag02], briefly hexanode, was built (right hand side of figure 3.11). This delay-line anode allows registration of several electron hits arriving within a time interval of few nanoseconds as encountered in double or triple ionization. Since information about particle impact at times and positions very close to each other may get lost due to dead-times in electronic processing or merging of the pulses, a third layer

of wire collects redundant position information. This data can be used to reconstruct multiple events, where position signals along one of the three directions (u, v, w) were lost, in an off-line analysis [Dür06a].

3.4.3 Magnetic Electron Extraction Field

The magnetic electron extraction field is generated by a pair of large diameter coils approximately fulfilling the Helmholtz-condition $r = D$, where r the radius of the coil and D the mutual distance. They are encompassing the whole experimental setup to ensure a good homogeneity within the spectrometer region and in order not to interfere with protruding parts of the setup, such as the Zeeman slower or the support structure. The conductors are made of 24 turns of 8×1 mm WICU-tubing, plastics insulated copper tubes, that are mainly used for building installations. This enabled an easy manufacturing: After winding the coils on a wooden template, they were wrapped with several layers of duct tape for fixation and to make them self-supporting. The use of tubes also permits water cooling, as the coils have to carry currents up to 50 A.
The coils have an inner diameter of 156 cm and are mounted at a mutual distance of

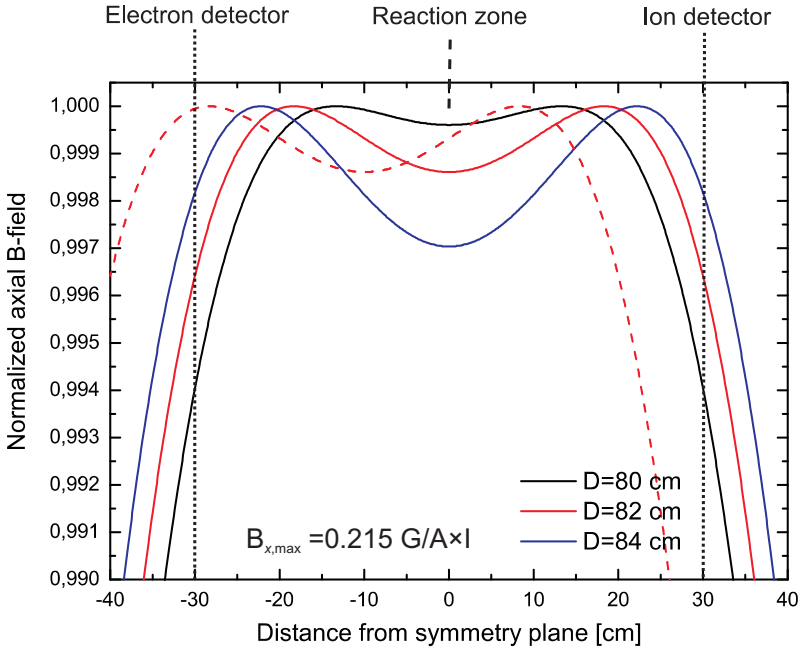

Figure 3.12: Calculated axial magnetic field B_x of the spectrometer coils for different coil spacings D. Each curve is normalized to its maximum value.

about 80 cm. With 4 winding layers in the axial and 6 layers in the radial direction, their cross section measures 50×70 mm^2. The axial magnetic field B_x of this configuration has been calculated for different coil spacings D (here D designates the distance between the inner faces of the coils). Figure 3.12 demonstrates that the homogeneity critically depends on the alignment of the coils, but a deviation of less than 0.5 % of the maximum value

throughout the whole spectrometer volume is easily maintained.
The present configuration, partly dictated by the spatial constraints of the support frame of the experiment, is symmetric with respect to the center region, and the coil spacing is 82 cm. If desired, the homogeneity in the electron branch of the spectrometer could be further enhanced to 0.1 % by shifting the coils 5–10 cm towards the electron detector as indicated by the red dashed curve. The field strengths that can be generated amount to 0.215 G/A$\times I$, requiring a current I of 23 A for a 5 G extraction field.
The optimum alignment and orientation of the coils, for example to compensate for the influence of the earth magnetic field, is best assessed from the quality of the electron time-of-flight spectrum (see section 3.1.2), which also enables an accurate determination of the absolute magnitude of the field.

3.5 MOT-Coils and Magnetic Field Switching

This section presents the design of the intra-vacuum MOT-coils and the unique switching circuitry developed for the high rate release-recapture process.

3.5.1 MOT-Coils

In order to accomplish the rapid switching of the magnetic fields, the following set of specifications was demanded from the MOT-coils:

- Field gradients along the coils' symmetry axis of up to 30 G/cm should be possible, e.g. in order to strongly compress the atomic cloud.

- The switching times have to be kept as short as possible, thus a low inductivity is required. Since the turn-on time constant $\tau_{\mathrm{on}} = L/R$ is ultimately limited by the inductivity L of the coils (R denotes the ohmic resistance of the circuit), a low inductivity allows faster rise-times of the current to the desired value. On the other hand, the decay time can be made arbitrarily small by introducing a load resistance R_{l} into the circuit such that the turn-off time τ_{off} reduces to $\tau_{\mathrm{off}} = L/(R+R_{\mathrm{l}})$. This in turn imprints a reverse voltage of $U_{\mathrm{ind}} = -L\frac{\mathrm{d}I}{\mathrm{d}t}$ proportional to the switching speed of the current $\frac{\mathrm{d}I}{\mathrm{d}t}$ and the inductivity L. Thus a low inductivity allows faster switching speeds and allows the use of materials and circuit elements less tolerant to high voltage levels.

- A rapidly varying magnetic flux as produced by switching of the MOT coils, through any large conducting connected surface or current loop induces eddy currents, which might decay much slower than the driving field and generate rather chaotic time-varying fields themselves. In an environment as sensitive to stray fields as an electron spectrometer, it is not advisable to mount switched conductors outside the vacuum vessel, as all the magnetic flux has to pass through its walls.

Approximating a circular coil by a single current loop of Radius r, carrying a current I, yields the following analytical expression [Dem95] for the magnetic field B_z along the symmetry axis of the coil (z-direction):

$$B_z(z) = \frac{\mu_0}{2(z^2+r^2)^{3/2}} I r^2. \tag{3.13}$$

When combining two of these coils with opposite currents of equal magnitude, placed at a distance $\pm D/2$ from $z = 0$, we obtain the following expression for the field gradient at the center:

$$\left.\frac{\partial B_z}{\partial z}\right|_{z=0} = (3/2)\mu_0 I r^2 D \left[\frac{D^2}{4} + r^2\right]^{-5/2} , \tag{3.14}$$

or, 3.14 expressed by an arbitrary ratio $\alpha = D/r$,

$$\left.\frac{\partial B_z}{\partial z}\right|_{z=0} = \frac{3}{2}\mu_0 I \frac{1}{r^2}\alpha \left[1 + \frac{\alpha}{4}\right]^{-5/2} . \tag{3.15}$$

For the true anti-Helmholtz configuration $r = D$ one gets the expression

$$\left.\frac{\partial B_z}{\partial z}\right|_{z=0} = \frac{3}{2}\left(\frac{4}{5}\right)^{(5/2)} \mu_0 I \frac{1}{r^2} . \tag{3.16}$$

This demonstrates two things: First, the smaller the coil dimensions r can be made, the higher the field gradient for a given current I, and second, any deviation from the Helmholtz condition $r = D$ for a given r will reduce the 'efficiency' of the coil in producing a gradient for a given current. This can be decisive when it comes to the choice of a suitable power supply or the problem of heat generation by the ohmic resistance of the coils.

For this and the above reasons, it was decided, to mount the coils within the vacuum chamber, bringing them as close as possible to the interaction zone. Provided the spatial constraints, first of all that the spectrometer electrodes have to fit in between the coils, and approximately conserving the Helmholtz geometry, one can estimate the total current necessary to produce a gradient of 30 G/cm.

For D=1.25r and with r=10 cm one finds from (3.15)

$$\left.\frac{\partial B_z}{\partial z}\right|_{z=0} [\mathrm{G/cm}] = 1.03 \cdot \frac{nI[\mathrm{A} \times \mathrm{turns}]}{r[\mathrm{cm}]^2} \tag{3.17}$$

a total current of 2918 A×turns.

Coils carrying a total current nI on this order of magnitude, even with a high number of windings n and when placed in air, require forced cooling in order to limit their operating temperature. Therefore it was necessary to devise a set of water-cooled coils which were UHV-compatible at the same time. If, as in this case, the dimensions of the coils (radius r) and the total current nI are largely determined by the experimental constraints, the only freedom of choice in the realization of the coil concerns the number of windings n: The necessary driving current I to produce the desired field is then proportional to $\frac{1}{n}$, whereas

the resistance R scales at least with the length of the conductor and thus with the number of windings: $R \propto n$. For the power dissipation $P = RI^2$ then $P \propto \frac{1}{n}$ holds, which seems to speak in favour of using as many turns as possible. To estimate the inductance of the magnet, the formula for a long air-core coil of length l is employed:

$$L = \mu_0 \frac{n^2 \pi r^2}{l}. \tag{3.18}$$

This suggests $L \propto n^2$. Hence for the time constant $\tau = \frac{L}{R}$, which cannot be modified during the turn-on process as discussed above, we find $\tau \propto n$. The assumption of ramping down any driving current I within the same time ($\frac{\mathrm{d}I}{\mathrm{d}t} \propto I \propto \frac{1}{n}$) yields $U_{\mathrm{ind}} \propto n$ according to

$$U_{\mathrm{ind}} = -L \frac{\mathrm{d}I}{\mathrm{d}t} \ . \tag{3.19}$$

Note that the considerations presented here, strictly apply only for one single coil. As our MOT-coils consist of a pair of anti-Helmholtz-coils connected in series, their mutual inductance has to be taken into account for deriving the total inductance of the circuit. However, for two identical coils of inductance L, the total inductance will always lie between $2L$ (no inductive coupling) and $4L$ (strongest inductive coupling). In conclusion, a magnet consisting of relatively few windings carrying a high current provides the best solution in terms of the switching behaviour.

Mechanical Assembly

Since the intra-vacuum placement of the magnets makes water cooling indispensable, 5×3 mm hollow copper wire (5 mm outer and 3 mm inner diameter) was used to construct the pair of coils, through which the current and cooling water flows simultaneously. Each coil has 24 windings, 4 layers in the axial dimension and 6 along the radial direction. Prior to making the coil, the copper tube had been wrapped with 2 layers of 0.125 mm-thick Kapton-HN foil for electrical insulation of the windings against each other and the coil holder. Thus a coil package with an inner diameter of 12 cm and an outer diameter of 19.5 cm is formed.
Figure 3.13 shows a CAD-model of a complete coil assembly. The coil assembly is mounted to a CF200-flange, so it can be conveniently removed or inserted into the vacuum chamber as a whole. Current and cooling water are guided into the vacuum chamber by a non-magnetic hollow copper wire feedthrough (CERAMASEAL RF power feedthrough). The joint between the coil tubing and the feedthrough is established by hard soldering. By blowing helium through the cooling water circuit and attaching a He-leak tester to the pumping systen, a leak rate of less than $2 \cdot 10^{-8}$ mbar l/s could be ascertained.
The two coils are spaced 10.4 cm apart, so that the spectrometer just fits in between. Special care has been taken to break any closed conductor loops to prevent eddy currents: The coil holder is slitted in order not to form a full circle, and three of the four suspensions of the coil holder are electrically interrupted by ceramic spacers made of Al_2O_3.

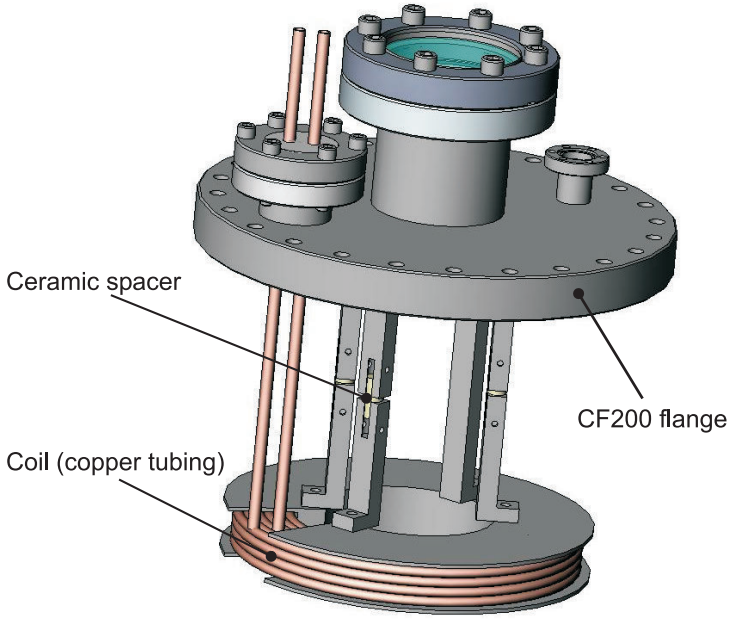

Figure 3.13: CAD-rendering of a MOT-coil assembly.

Electrical Characteristics

The MOT-coils are capable of producing an axial gradient of 0.282 G $cm^{-1}A^{-1}$. Figure 3.14 gives the calculated axial field gradient, where each turn of the coil has been approximated by a circular current loop.
With a series resistance of 44 mΩ a heat load between 54 W at 35 A (10 G/cm) and 440 W at 100 A (28 G/cm) is generated. So far the coils have been operated with currents up to 65 A in continuous duty, where the cooling proved sufficient. The inductance of one coil was measured to be 75 μH.

3.5.2 Magnetic Field Switching

The fast ramping of the magnetic field is one of the key features of the experiment. From the electronics side, the targeted specifications were not easy to achieve and the implementation of a reliable and stable circuit turned out to be a rather lengthy development.

Principle

Figure 3.15 shows the main components of the switching circuitry. The current regulating element is an Insulated Gate Bipolar Transistor (IGBT) of type EUPEC FZ 800 R 16 KF4 with a maximum current rating of 800 A and a maximum rated voltage between collector and emitter of 1600 V. The electrical power is supplied by a water-cooled switching power

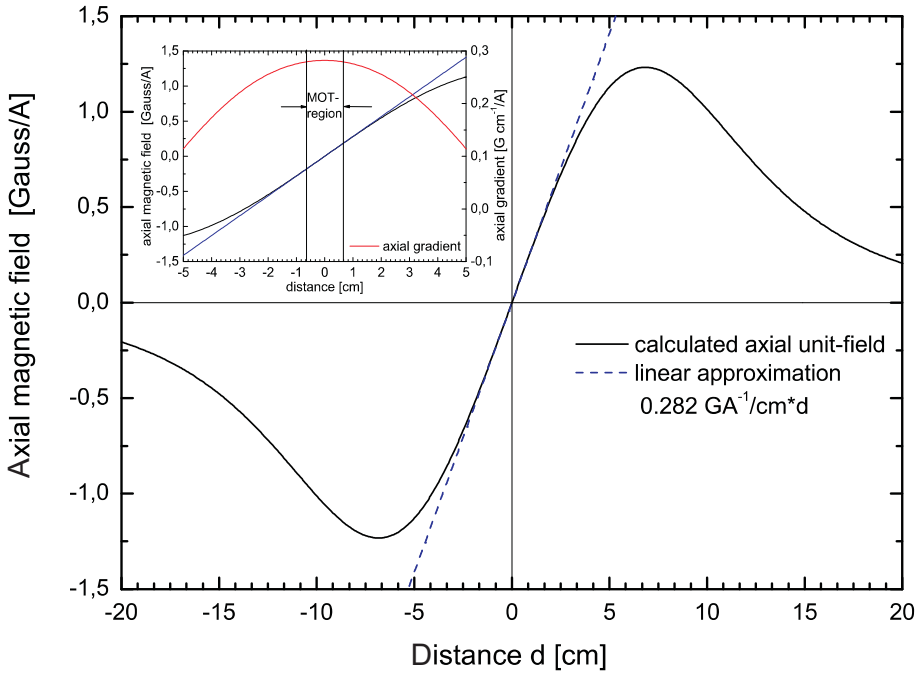

Figure 3.14: Calculated axial unit-field (for 1A) of the MOT anti-Helmholtz coils. The inset shows, that within the MOT region, the gradient can safely be assumed constant. According to 2.18, the radial gradient is exactly half of the axial one.

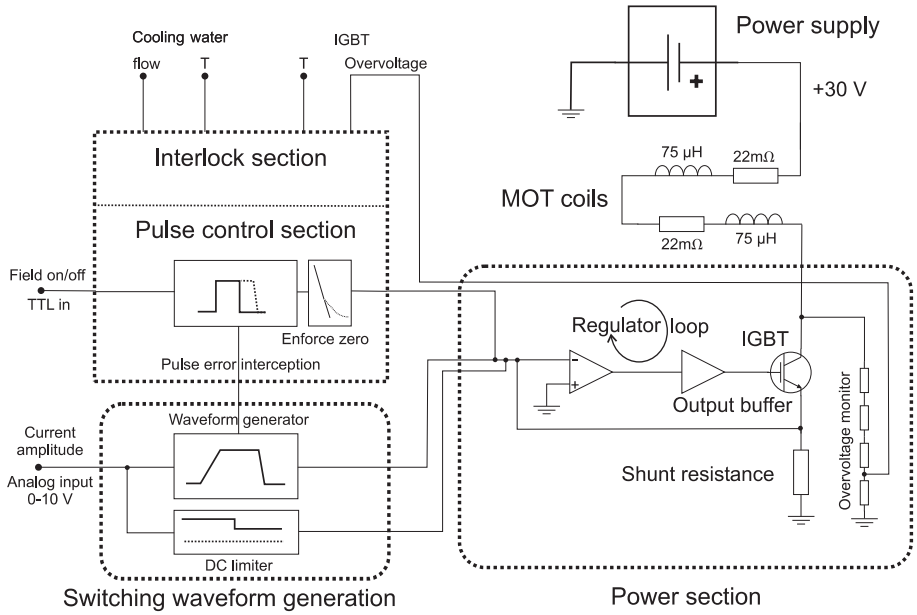

Figure 3.15: Block diagram of the field switching circuit.

supply (ELEKTRO-AUTOMATIK EA-PS 9072-170 S04), that can deliver a current of 170 A at a voltage of 70 V. It is operated in constant voltage mode, keeping the MOT-coils and the collector of the IGBT at a potential of 30 V. A shunt resistance at the emitter of the

IGBT senses the actual coil current and feeds the signal to the regulator loop.
To control the current through the MOT-coils, the MOT-switch is connected to the experimental control system. The ADwin-system supplies a voltage in the range of 0–10 V at the analog input of the regulator. This voltage defines the amplitude of the operating current and the amplitude of the switching waveform. In continous operation, the regulator follows the input voltage, so that, unless the voltage changes proceed too quick, the coil current can be arbitrarily modulated. For repeated fast switching, a TTL trigger signal is supplied. Upon the falling edge of the signal, the waveform generation section creates a falling voltage ramp which forces the regulator circuit to close the circuit. The ramp's waveform and the switching times are adjusted such that the induced voltage does not exceed 800 V, to rule out potential damage to the IGBT. If a rising edge is applied, a rising slope waveform is created by the waveform generator. With a supply voltage of 30 V risetimes for currents of 70A of 450 μs are possible.
To protect the IGBT from destruction by undefined operating conditions that could cause high voltage spikes, for example by applying of erroneous pulse sequences, a comprehensive interlock logic was developed. During the execution of a current ramp, the external input is locked, so that, e.g. during the 400 μs of rampdown time no trigger signal for turning on the current again is applied and vice versa. In such a case the regulator module will indicate a 'pulse error' and stop operation until it is manually reset by the push of a button. The minimum off time, the interlock logic permits, is 400 μs, the minimum on-time, after the start of the increasing current ramp is 2 ms.
At the same time, the operating conditions of the IGBT and the MOT-coils are monitored. Combined temperature and flow sensors measure flow velocity and temperature of the cooling water through the MOT-coil and the IGBT's heatsink. Thus operation without flow of cooling water is not possible.

Performance

The prototype of the magnetic field switch proved to be very reliable and failsafe in everyday-operation and provided sufficient performance for the recoil-ion measurements. Fig. 3.16 gives some waveforms of the current, captured with a high-current amperemeter clamp. A risetime of 400 μs for currents up to 70 A is sufficiently fast. The overshoot and ringing is not considered to be critical. It was found, that when ramping the set-point linearly to zero, the current curve turned from a linear decrease into a slow exponential decay for low currents, which seems to be due to the properties of the IGBT (which are generally not specifically designed for analog operation). To get rid of the exponential decay, a steeper set-point ramp is applied after an adjustable time relative to the trigger signal, to force the current to zero (visible as the slight kink at 160 μs in the current curve of Fig. 3.17). This does not completely eliminate the problem; at a current of about 2 A, an exponential decay with a time constant of 83 μs sets in. Extrapolating, the coil current reaches a level of 100 mA 500 μs after shutdown, and 10 mA after 700 μs. The time for

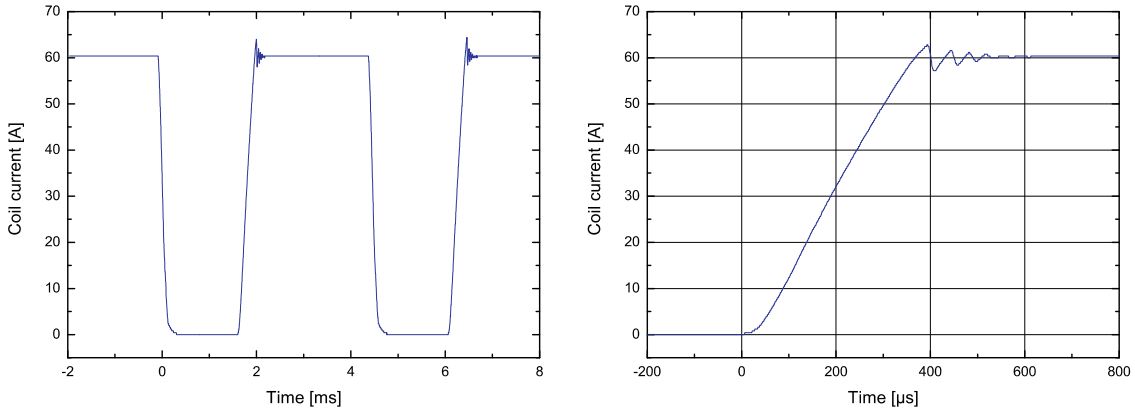

Figure 3.16: *Left*: Typical experimental current waveform recorded during field switching. *Right*: Zoom into the rising edge of the current pulse: A current of 60 A, corresponding to a field gradient of 17 G/cm is restored within 400 μs.

induced eddy currents to decay might be of the same order of magnitude.
The effect on the electron trajectories is difficult to estimate. Simulations showed, that the maximum absolute field strength very close (<1cm) to the MOT coils' windings is about 5 G/A. After 700 μs this field is reduced to 50 mG, which is less than 1% of the electron extraction field. The ultimate test and most sensitive probe for residual fields will be high resolution electron momentum spectroscopy itself.

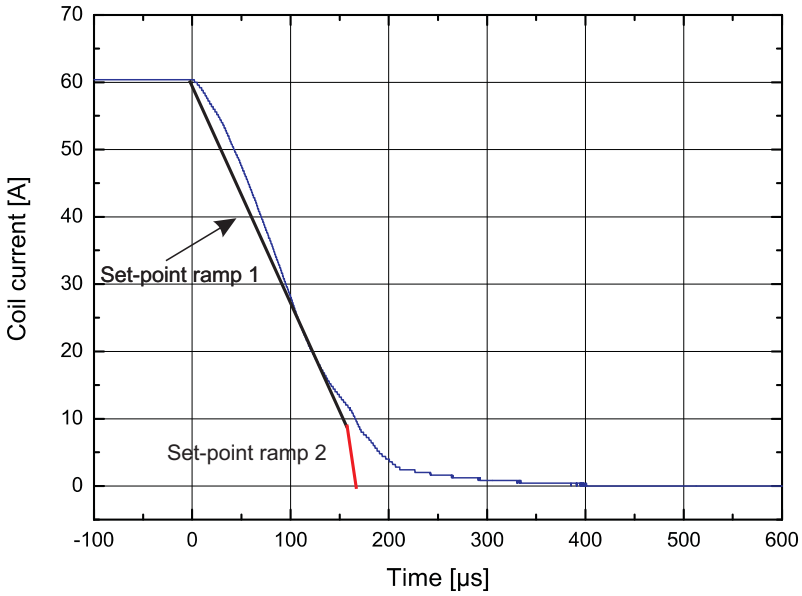

Figure 3.17: Falling edge of the current. To reduce the exponential tail in the ringdown of the current after a time delay of $\approx 160\mu$s a steeper set-point ramp is applied.

3.5.3 Compensation Coils

It has already been noted in section 3.2.2, that the superposition of the MOT gradient field and the homogeneous electron extraction field leads to an overall shift of the point, where the magnetic field is zero along the direction of the extraction field. A radial gradient of 5 G/cm, which is presently achievable in continuous operation, and an extraction field of 5 G magnitude leads to an overall shift of the MOT's loacation by 1 cm. Surprisingly the MOT can still be operated under these far from ideal conditions, provided the beam diameters of the MOT-lasers are large enough, and of course at the expense of atom number and recapture efficiency when the MOT field is switched. These effects could partly be compensated by adapting the alignment of the six laser beams to the new MOT location. Nevertheless, it is desirable, to maintain a well defined MOT-location at the center of the chamber and the spectrometer for two reasons: Firstly, in order not to violate the time-focusing condition of the spectrometer, and secondly, to avoid difficulties in overlapping the target beam with the cold target. E.g. a proper alignment of the fs-laser beam and its focusing mirror were hard to achieve with a shift of the MOT of several mm. Especially in view of the planned upgrade of the ion spectrometer to a position focusing geometry, a fixed target position would be favourable.
The idea to resolve this problem is, to place another pair of coils in Helmholtz configuration inside the vacuum chamber and close to the MOT region. The field of the compensation coils locally cancels out the extraction field to restore the original MOT quadrupole configuration.

Field Design

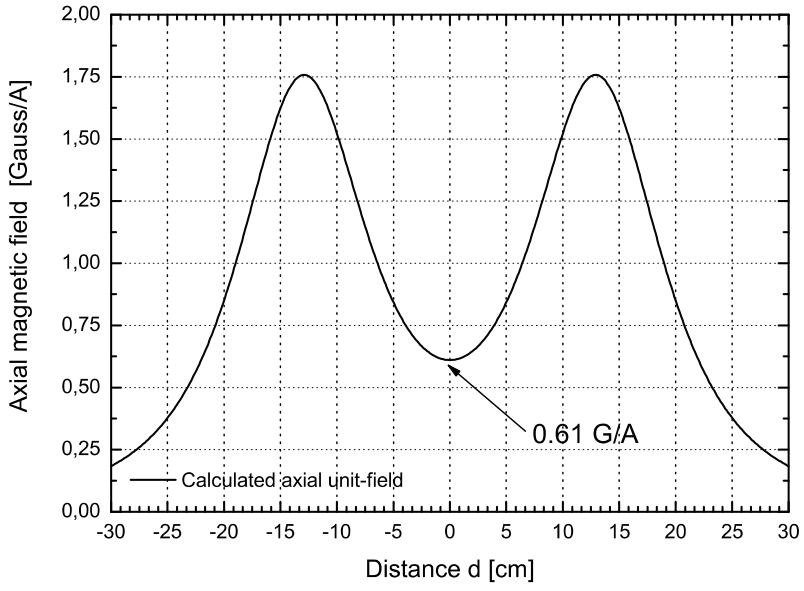

Figure 3.18: Calculated axial unit-field of the compensation coils.

Because of the spatial constraints imposed by the chamber geometry and in order not to obstruct optical access from the MOT-laser viewports, it is not possible to realize a true Helmholtz configuration, where the distance D between the coils equals their radius R. The configuration, that comes closest to this condition and is compatible with the rest of the setup, is realized by a pair of coils, whose inner faces are located at a distance of 12 cm from the symmetry plane. The inner radii are 7.4 cm (and 7.0 cm of the coil holder itself) to encompass the spectrometer electrodes.
The coils are wound from hollow copper wire to enable water cooling and electrically insu-

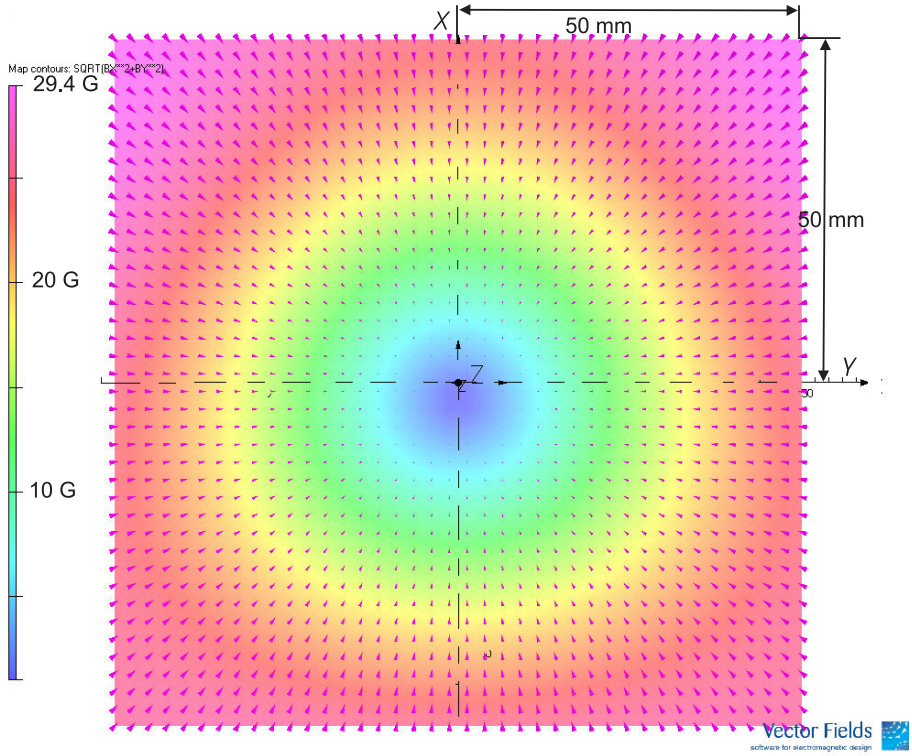

Figure 3.19: Superposition of the three magnetic fields in the horizontal xy-plane. The colour code represents the magnitude of the radial ($\sqrt{B_x^2 + B_y^2}$) field component, where the scale on the left hand side is given in Gauss. Additionally, the full field vectors are displayed.

lated by capton foil. With 4×1 mm copper wire 6 windings along the axial direction and 4 radial layers are realized, giving a total of 24 turns akin to the MOT coils. With 19.5 cm outer diameter they still can pass through the CF200 flanges. Figure 3.18 shows the axial field component parallel to the electron extraction field. Though not homogeneous overall, the homogeneity a few mm around the field minimum in the middle of the coils should be sufficient to make normal MOT-operation possible. The unit-field strength generated by the coils is 0.61 G/A, so for balancing a reasonably strong spectrometer field of 10 G, a coil current of 16.4 A is necessary, which is still comfortable to handle, in terms of heat dissipation as well as fast switching, when compared to the targeted MOT-currents of up to 100 A.

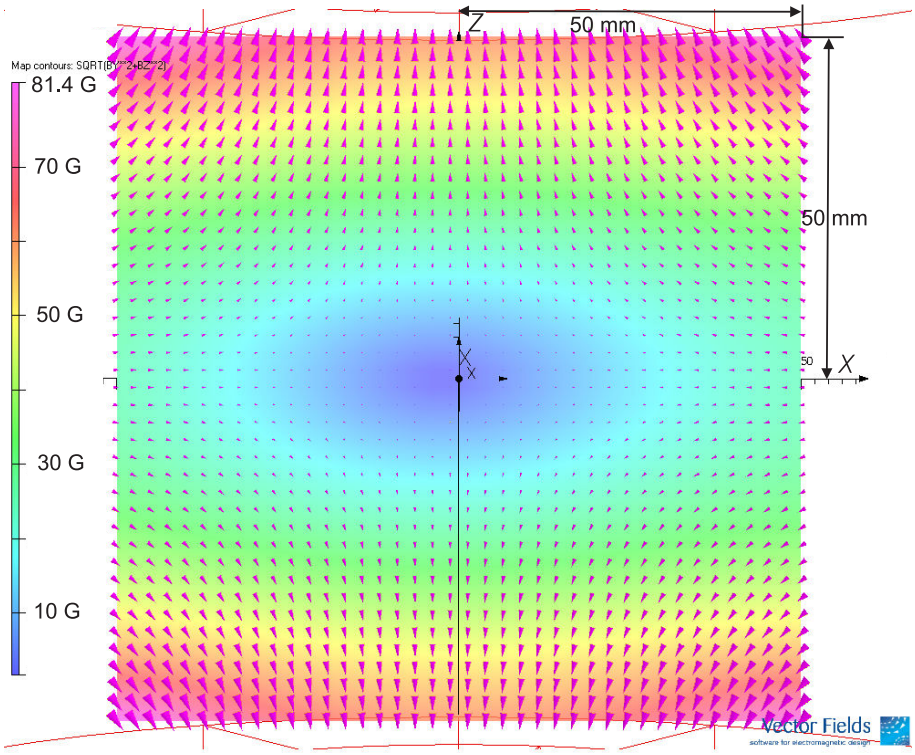

Figure 3.20: Superposition of the three magnetic fields in the vertical xz-plane. The colour code represents the magnitude of the radial ($\sqrt{B_x^2 + B_z^2}$) in-plane field component in, where the scale on the left hand side is given in Gauss.

To ensure that an acceptable field configuration is achieved by the combination of all three magnetic fields, a three-dimensional simulation of the magnetic field was performed, using the OPERA-3d software package and the corresponding electro-/magnetostatics solver TOSCA (VECTOR FIELDS). Figure 3.19 and Figure 3.20 depict the resulting magnetic field in the horizontal xy-plane and the vertical xz-plane, respectively. Each graph maps a patch of 10 $\times$10 cm^2 around the symmetry center of the coil configuration. The fields were calculated for a typical field configuration, that will be used in electron impact experiments. The spectrometer coils were driven by a current of 23.3 A, corresponding to an extraction field of 5 G, the MOT quadrupole field was assigned an axial gradient of 10.9 G/cm, corresponding to a current of 38.5 A. The compensation coils' current thus was set to 8.3 A to neutralize the extraction field. Figure 3.19 demonstrates that the MOT's radial gradient field is preserved, only slight deviations from the cylindrical symmetry indicate the presence of the other fields.
The same holds true for the cut in the vertical plane, where the anisotropy of the trapping gradient becomes apparent which is a factor of two higher along the z-direction. Both pictures indicate a minor shift of the field minimum to the negative x-direction (the coordinate system of the simulation has been replaced with the one given in figure 3.7). This is due to an improper balancing of the extraction and the compensation field, since the

currents put into the simulation were determined by a calculation of the field as sum over the discrete current loops, while TOSCA computes the field from the cross section of the coil and the current density, which leads to slightly different results. On the other hand, this emphasizes, that by variation of the current, the compensation coils provide also a convenient tool for fine tuning the MOT-position.
As the compensation coils are switched synchronously to the MOT-coils, no difficulties will arise. From a technical point of view, their fast switching is readily realized: With the coils having a series resistance of ≈0.1 Ω and a total inductivity similar to the MOT-coils (≈150 μH), a second copy of the MOT-switch, which is presently being built, fulfills all the specifications needed. As the maximum currents are only on the order of 15 A, neither the reverse voltages, nor the dissipated power are critical factors, as compared to the MOT-coils.

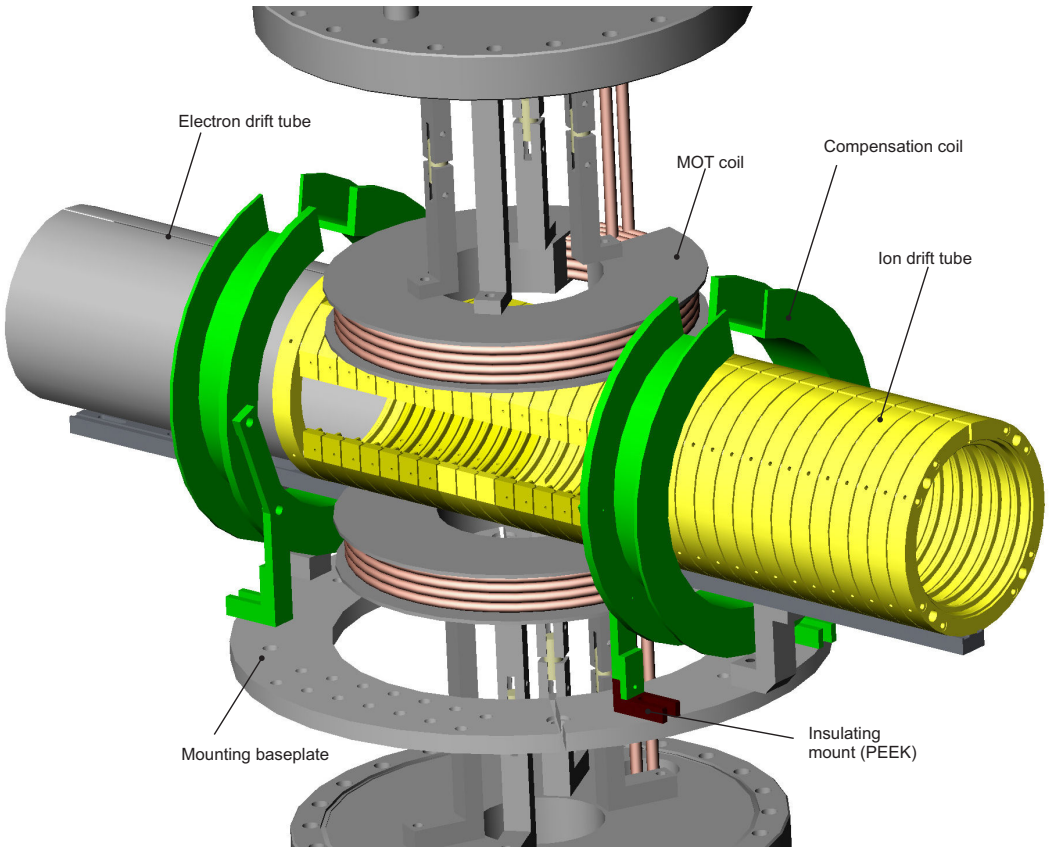

Figure 3.21: View of the interior of the vacuum chamber with the compensation coils (green).

3.6 Laser Systems

In chapter 2 the principles of laser cooling and trapping were explained. It was stated, that for a efficient and reliable operation of a magneto-optical trap, the linewidth of the laser source has to be a fraction of the natural linewidth of the cycling transition. The natural linewidth of the lithium cooling transition is 5.9 MHz; it is of the same magnitude as those of most species, that have been succesfully laser-cooled and trapped. Consequently, one demands from a suitable laser source not only a linewidth of about 1 MHz, but an absolute long term frequency stability of the same order of magnitude as well. This means, that the laser frequency has to be fixed with a relative accuracy of $2 \cdot 10^{-9}$!
For efficient laser cooling, a total laser power of some 100 mW should be available for the following reasons: The transition must be saturated strongly, even if the laser is detuned to the red by several linewidths. A high laser power then allows for larger beam diameters at the same saturation parameter, thus enhancing the geometrical capture cross section of the trap. Secondly, numerous optical elements introduce additional losses within the beam path, especially the acousto-optical modulators used for shifting and fine tuning of the laser frequencies, which have typical transmission efficiencies of 60–80%.
These requirements are fulfilled by tunable spectroscopic lasers, which are frequency stabilized ('locked') to an atomic frequency reference by active regulator circuits. The rapid development in the field of laser cooling and quantum optics in general is partly due to the growing availability of semiconductor lasers, namely laser diodes, since the late eighties. This technology made it possible to replace delicate and expensive tunable dye- or Ti:Sa lasers, together with their cumbersome pump lasers, such as Ar^+-lasers, by (often home built) frequency narrowed diode lasers, using cheap commercial laser diodes.
In the near-infrared, a broad selection of high-power single-mode laser diodes with output powers beyond 100 mW are available nowadays, which are particularly popular in laser cooling of rubidium (at 780 nm wavelength) and cesium (852 nm). At the wavelength of lithium (671 nm), i.e. in the red of the visible spectrum, the choice of semiconductor lasers is much reduced. Single-mode diodes operating at that wavelength are only available with powers up to 30 mW.
To circumvent this limitation in laser power, the goal was to build a simple, cost-effective semiconductor-based laser system by the use of a high-power multi-mode diode, also called broad emitter diode or broad area laser (BAL) (see Figure 3.24). This diode acts as an amplifier for frequency stabilized light by injection seeding it with the beam of a standard grating-stabilized spectroscopic diode laser as described by Praeger *et al.* [Pra98] for lithium. Though the performance of the system was much improved with time, this concept did finally not live up to the expectations, as it never reached the level of stability and beam quality required for our experiment. It was then decided to reactivate a dye-laser system, that had been modified for simultaneous operation on two modes with 800 MHz spacing, required for the excitation of the lithium D2-line for an earlier experiment. With the advent of tapered amplifiers operating at 671 nm and delivering output powers up to 500 mW, finally a laser source was available, that enabled reproducible and long-term

stable operation of the experiment. A tapered amplifier injected by a frequency stabilized diode laser is now used in routine MOT-operation.
In the following, these three laser systems used are briefly described and their benefits and drawbacks are discussed.

3.6.1 Broad Area Diodes

Laser cooling of lithium requires a bichromatic beam at a wavelength of 671 nm containing the frequencies of the cooling- and repumper transition (see section 2.2). When semiconductor lasers are used, one frequently applied solution is the use of pairs of master oscillators and slave lasers, where the master oscillator is a frequency stabilized external cavity diode laser (ECDL), whose output is coupled into the active layer of a single-mode diode [Sch98a]. At sufficiently high intensity of the seeding beam, its photons will account for most of the stimulated emission processes within the laser medium and the slave laser will take over the spectral characteristics of the master laser, wheras its eigenmodes are completely suppressed. The active layer of a laser diode forms a Fabry-Perot cavity, thus the field of the master laser is resonantly enhanced and the gain medium of the slave laser can be considered as a multipass-amplifier. Depending on the coupling efficiency of the seeding beam to the slave diodes cavity, i.e. how well the master beam's profile is matched to the spatial eigenmode of the slave laser, seeding powers between 100 μW and 2 mW are sufficient to achieve complete injection locking and to exploit the full specified output power of the slave diode.
The highest available free-running output power of single-mode diodes at the lithium wavelength is 30 mW. The output power of laser diodes is limited by the ratio of output power to the area of the output facet. Increasing the output power to beyond the maximum rated value, will result in faster ageing, i.e. characteristics of the diode like center wavelength, gain and threshold will gradually change and possibly degrade performance, and in the worst case in irreversible damage of the front facet.
In broad area lasers (BAL), also known as broad emitter diodes, the restriction in output power is overcome by extending the active layer at the p-n junction of the laser diode where the radiation is generated, to a multiple of that of a conventional diode. In a conventional diode, the active region has a cavity length of 1000 μm, and a width of typically 4 μm and height of 1 μm (size of the front facet). In a BAL, the width of the active layer is enlarged to up to 200 μm. Thus, the generated output power is enhanced, while the intensity at the front facet stays the same. Free running output powers as high as 2 W from a single emitter are obtained [Shv00]. Because of its large and highly asymmetric dimensions, the laser cavity (wave guide) supports several spatial and spectral modes, leading to a spectral bandwidth of the free running BAL of roughly 2 nm.
The quality of the far-field intensity profile is rather poor and far from Gaussian. It exhibits a characteristic structure with several maxima along the long axis of the junction. Moreover, the active layer of the BAL constitutes a non-linear medium, in which effects such as self-focusing and filamentation can arise from random fluctuations in current den-

sity and light intensity within the medium [Fey96], [Lan93], which further deteriorate the beam quality.
The spectral and spatial characteristics of the output can be much improved by injection-locking to a single-mode master laser. Unlike in the case of injection-locking of single mode diodes, the BAL is operated as a double-pass amplifier [Abb87]: The seeding beam is injected into the BAL at a small angle [Gol88], [Geh98]. After reflection at the back facet of the medium, the amplified beam leaves the BAL at the specular reflection angle. In this way, the amplification in multiple transverse eigenmodes of the BAL can be largely suppressed and a directed and approximately Gaussian beam of frequency locked light, that is spatially separated from the unlocked emission of the laser, such as a background of amplified spontaneous emission (ASE) can be picked off.
Several publications exist where this scheme of injection-locking has been investigated for its potential of application in spectroscopy or laser-cooling [Fey96], [Paw00], [Pra98], and successfully applied in a Bose-Einstein condensation experiment using rubidium [Shv00]. The master-slave system used in this experiment is thoroughly described in [Spi05], so it will be only briefly reviewed here. Some modifications on the setup and the performance are described.

Master Lasers

The master lasers of this setup are two external cavity diode lasers of type TOPTICA DL100L. These are grating stabilized lasers in Littrow configuration [Ric95] with an added correction mirror to correct for the beamwalk that occurs when the laser is tuned [Haw01]. A blazed reflection grating (2200 lines/mm) reflects the first order back into the diode, while the zeroth order reflection is used as output beam. The laser diode has an anti-reflection coated front facet to make it more suceptible to the feed-back light and to suppress the eigenmodes of the diode [Pat83]. The external cavity is formed by the back facet of the diode and the reflection grating, where the grating acts as a the frequency selective element, that determines the wavelength and bandwidth of the laser emission. The grating is mounted to a piezo-stack actuator that changes the grating angle (and cavity length) and allows for fast scanning of the frequency over a range of 20 GHz. Frequency stabilization is achieved in the same way: A regulator circuit controls the grating position such that small deviations from the set frequency are corrected. Thus long-term drifts of the laser frequency and perturbations in the acoustic regime up to several 100 Hz are balanced.
Alternatively the laser can be tuned by changing the cavity length. A change of the cavity length can occur by thermal expansion of the diodes active medium due to the dissipated power, or by a change in ambient temperature. A change in the forward current also alters the charge carrier concentration, which in turn modifies the refractive index of the gain medium and thus the effective resonator length. To suppress temperature fluctuations, the diode and the whole external cavity assembly are mounted onto a solid block of brass,

that is held at constant temperature to an accuracy of 10 mK by a Peltier element. Likewise, only low-noise power supplies (mostly dedicated laser diode drivers with low current ripple) should be used to operate frequency stable diode lasers. The tunability by current modulation is exploited in various schemes for laser stabilization and for sideband generation. Phase modulation by injecting a sinusoidal current with frequencies in the MHz to GHz range is used in the so called Pound-Drever-Hall stabilization scheme [Dre83] or for frequency modulation (FM-) spectrocopy [Bjo83].

Frequency Stabilization

For most stable locking of a laser to an atomic transmission line or the transmission fringe of a resonator, an error signal is required, that has a zero crossing at the center of the line. Dependent on the direction of deviation from the center frequency, the slope of the zero crossing generates a positive or negative error signal, which is sent to the feedback loop of the frequency stabilization.
In our setup, the technique of FM-spectroscopy is applied to derive an error signal for the frequency regulation of the master lasers from a Doppler-free absorption spectrum of atomic lithium vapor. This technique is a variation of the principle of saturation spectroscopy [Dem81].
In the simplest saturation spectroscopy setup, one beam is employed as pump- and probe beam at the same time by retro-reflecting it into itself. A weak laser beam of 1.5 mW and 1 mm diameter is split off from the master laser's output and sent through a lithium vapour cell as the pump beam. A retro-reflecting mirror at the other end of the vapour cell images the beam onto itself, so that it passes through the interaction region twice. By placing a quarter-wave plate in front of the mirror, the polarization of the backward travelling beam (effectively acting as the probe beam) is rotated by 90°with respect to the incoming beam. Upon leaving the cell, it is coupled out via a polarizing beam splitter and imaged onto a photodiode.
By measuring the photodetector signal in dependence of laser frequency, a saturated absorption spectrum is obtained, which features the characteristic Lamb dips superimposed on the Doppler broadened absorptive background.The lamb dips provide the relative frequency reference, since their position is independent of the operating conditions of the vapour cell. In principle, the absorption spectrum could be used for laser stabilization as well, but locking to the edge of an absorptive feature (side-of-fringe locking) still suffers from the drawback, that the lock point varies with the absolute signal level of the absorption signal and the laser cannot be locked to the center frequency of the line. A variation in laser power or optical density of the medium can shift the lock-point by several MHz.
In the present setup, the laser is stabilized on the cross-over resonance between the cooling and the repumper transition. The cross over is an experimental artefact, that occurs when two transitions with frequencies ω_1 and ω_2 spaced by less than the width of the Doppler profile, share a common level (in our case the unresolved $2^2P_{3/2}; F = 0, 1, 2, 3$ excited state

levels). There exists a certain velocity class v dv, for which the one beam is saturating the transition at ω_1, while the counter-propagating beam saturates the transition at ω_2. Optical pumping and rapid redistribution of the population between the two ground states occurs. Thus neither ground state population can be depleted, as in the case of the lamb dips. This is, why the cross-over resonance appeears as a maximum in absorption and not in transmission. From the resonance condition it is seen, that the cross-over resonance is located exactly in the middle in between the two transitions at $\omega_c = (\omega_1 + \omega_2)/2$ [Dem81]. Feature (b) in Fig. 3.22, which shows a scan over the D2-line, is identified as he cross-over resonance. The cooling- and repumper frequencies are generated by shifting the locked laser frequency by ±400 MHz with the aid of acousto-optical modulators. These frequency shifting devices also enable a fine tuning of the laser frequency to match the appropriate red detunings from resonance, that are required for MOT-operation, by varying the applied radio frequency signal. The desired dispersive lineshape of the error signal is generated

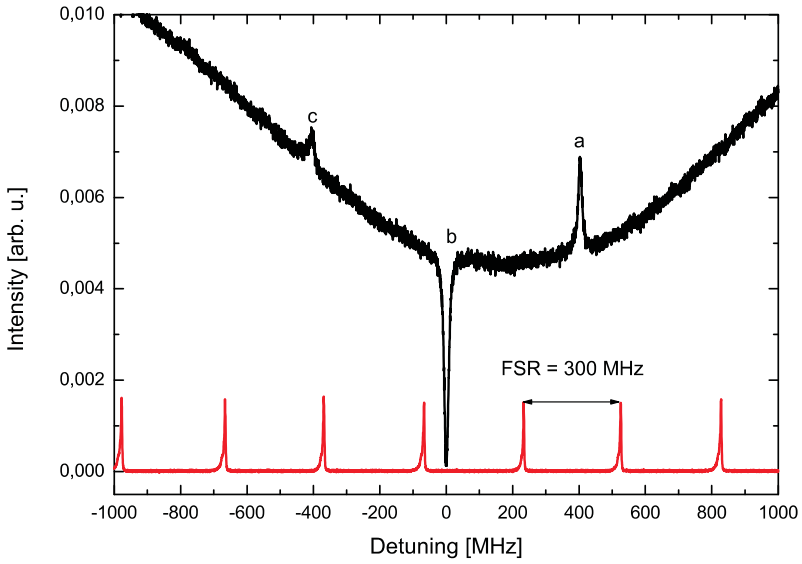

Figure 3.22: Saturated absorption spectrum of the ^{7}Li D2-line, featuring pronounced lamb dips. The feature (b) in the middle is the cross-over resonance, that provides the frequency reference. (a) $(2^2S_{1/2}, F' = 1\text{–}2^2P_{3/2}, F = 0, 1, 2)$ lamb dip; (b) Cross-over resonance (a)-(c); (c) $(2^2S_{1/2}, F' = 2\text{–}2^2P_{3/2}, F = 1, 2, 3)$ lamb dip.

by adding side bands to the laser frequency. By comparison of the relative phase of carrier frequency and the sidebands after transmission through the lithium vapour cell, the dispersion near the resonance is probed. According to the law of Kramers and Kronig, a minimum in dispersion corresponds to a maximum in absorption.
It is one of the advantages of diode lasers, that sideband generation is accomplished by modulation of the driving current. In practice, an RF-signal of a few mV peak-to-peak height is capacitively coupled to the current leads of the diode. The electric field magnitude of pase-modulated laser reads

$$E(t) = \frac{1}{2} E_0 (e^{i(\omega t - M \sin \Omega t)} + \text{c.c.}), \tag{3.20}$$

where $M = \delta\Omega/\Omega$ is the modulation index, Ω the modulation frequency and $\delta\Omega$ the modulation depth. The frequency spectrum of the modulated light consists of the carrier frequency ω and sidebands at frequencies $\omega \pm \Omega$, $\omega \pm 2\Omega$ etc. The relative intensity of the kth sideband compared to the carrier is obtained from the coefficients a_k of the Fourier expansion of (3.20):

$$\frac{|a_k|^2}{|a_0|^2} = J_k(M). \tag{3.21}$$

The J_k are Bessel-functions of the first kind. For low modulation indices $M \ll 1$, as applied for spectroscopic purposes, the first sideband dominates, whereas higher orders are of negligible magnitude. By passing through the sample, each of the three frequency components has acquired an attenuation δ_k and a phase shift ϕ_k described by the complex transmission coefficient T_k [Bjo83]:

$$T_k = e^{-(\delta_k + i\phi_k)}. \tag{3.22}$$

Retaining only the carrier and the first order sidebands in this considerations, the emerging wave has the field

$$E(t) = \frac{1}{2}E_0 \left(-T_{-1}\frac{M}{2}e^{i(\omega-\Omega)t} + T_0 e^{i\omega t} + T_1\frac{M}{2}e^{i(\omega+\Omega)t} + \text{c.c.} \right). \tag{3.23}$$

The intensity impinging on a photodetector is $I(t) = \frac{1}{2}\epsilon_0 c|E(t)|^2$. $I(t)$ contains beat signals between the carrier and the sidebands at difference frequency Ω, which can be detected by a photodiode, if Ω is within the bandwidth of the detector. Neglecting the rapidly oscillating terms at frequencies $\omega \pm \Omega$, that are averaged out, the signal picked up at the detector is

$$U(t) \propto e^{-2\delta_0}\left[1 + (\delta_{-1} - \delta_1)M\cos\Omega t + (\phi_1 + \phi_{-1} - 2\phi_0)M\sin\Omega t\right]. \tag{3.24}$$

The amplitudes of the dispersive in-phase component (sine-terms) and the quadrature component (cosine-terms) are easily extracted from $U(t)$ by means of phase sensitive detection. The detector signal is multiplied with the output of the local oscillator which provides the modulation frequency in a RF mixer. In general a mixer produces an ouput consisting of the sum-frequency and the difference-frequency of the applied input signals. If, for demodulation purposes, the carrier frequency is mixed with itself, the difference frequency will be a DC-signal. Depending on the relative phase between the local oscillator and the detector signal, a voltage is obtained, that is proportional to $(\delta_{-1} - \delta_1)$ or $(\phi_1 + \phi_{-1} - 2\phi_0)$ or a linear combination of both.
The lineshape of the error signal depends strongly on the ratio $R = \Omega/\gamma$ between the modulation frequency Ω and the natural linewidth of the transition γ [Bjo83]. For $\Omega \ll \gamma$, each sideband probes the resonance independently, directly mapping the absorption or phase shift of the resonance. If, on the other hand, Ω is of the same magnitude or smaller than γ, the cos-component is proportional to the derivative of the absorption curve and the sin-component is proportional to the second derivative of the dispersion. The standard

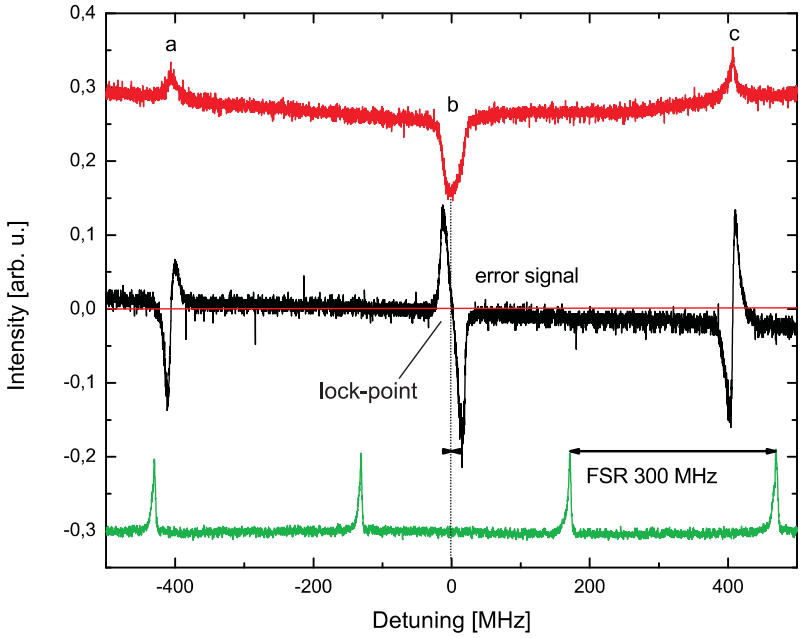

Figure 3.23: Red: Saturated absorption spectrum of the D2-line. Black: Error signal for laser stabilization generated by the Pound-Drever detector. Green: Marker etalon (300 MHz free spectral range)

modulation frequency of the Pound-Drever module of the DL100 is 20 MHz. Since the Doppler-free widths of the reference transitions are of the same order due to the unresolved hyperfine structure, the FM-spectroscopy produces a derivative of the lamb dips (see Fig. 3.23).

Spectroscopy Cell

The spectroscopy cells are a simple but effective design, consisting only of standard CF-components. The vapour cell consists of two connected 15 cm long CF16 tubes, with a welded in aperture of 2 mm at each end. They prevent the lithium from effusing out of the heated region, eventually rendering the entry windows opaque, and enforce a good overlap between pump- and probe beam within the whole interaction volume. The windows are placed on CF-tubes joined to the heated region. A gate valve allows for easy evacuation after refilling of the cell. A bifilar heating element (10 Ω) is wound around the whole interaction volume enclosed by the apertures. Typical operating temperatures around 350°C (2.7 A operating current) create a stable spectrum with pronounced lamb dips. The central CF-joint is sealed with a Ni-gasket, as these are less affected by exposure to high temperature than the standard copper sealings. After filling with Li and initial evacuation to 10^{-5} mbar, the cells have been constantly operated for more than two years without degradation of the spectroscopy signal.

Injection Locking

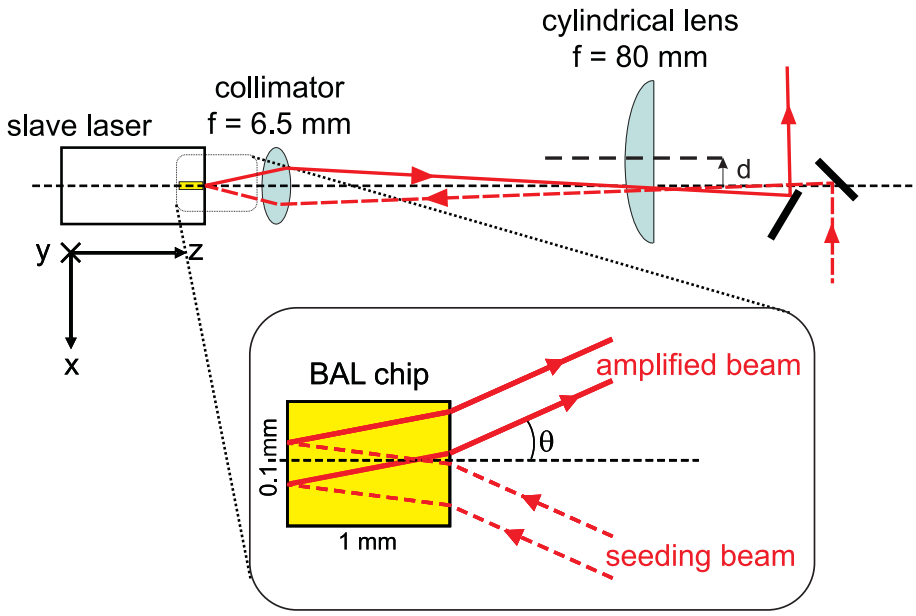

Figure 3.24: Coupling of the seed beam into the broad area laser. The enlargement shows the beam path inside the BAL's active layer.

The two slave lasers were COHERENT CR S-67-500C-100-H broad area high power diodes. One of them was later exchanged for a HIGH POWER DEVICES HPD1305-HHL-TEC, because it showed a particularly chaotic spatial mode structure and poor injection efficiency. Both devices, the discontinued COHERENT diodes and the HPD product, have very similar specifications. The emitter size is 100×1 μm (width×height), with a maximum free running output power of 500 mW at a center wavelength close to 670 nm, which is reached at a forward current of 800 mA. Both come in a high heat load package (HHL) with an integrated peltier cooler for temperature stabilization (an essential precondition for efficient injection locking). They are operated with an ILX LIGHTWAVE LDC-3700B laser diode current and temperature controller.

The optical setup for injection of the master beam is shown in Fig. 3.24. The slave lasers are mounted with the long dimension of the emmitter parallel to the laser table to keep the beam path in the horizontal plane. The polarization vector of the BALs is in the same plane, thus the polarization of the master beam is rotated by 90°prior to injection. Injection under a small angle is brought about by slight translation of a cylindrical lens perpendicular to its optical axis along the x-direction [Shv00]. Along this direction, this lens with a focal length f=80mm forms a telescope with the collimation objective of 6.5 mm focal length (MELLESGRIOT 06GLC001) in front of the emitter, to focus the incident beam to a spot size that matches approximately half the width of the emitter: Amplification of the master beam is most effcient, if its spot covers approximately one half of the front facet, so in- and outgoing beam cover as much of the active medium as

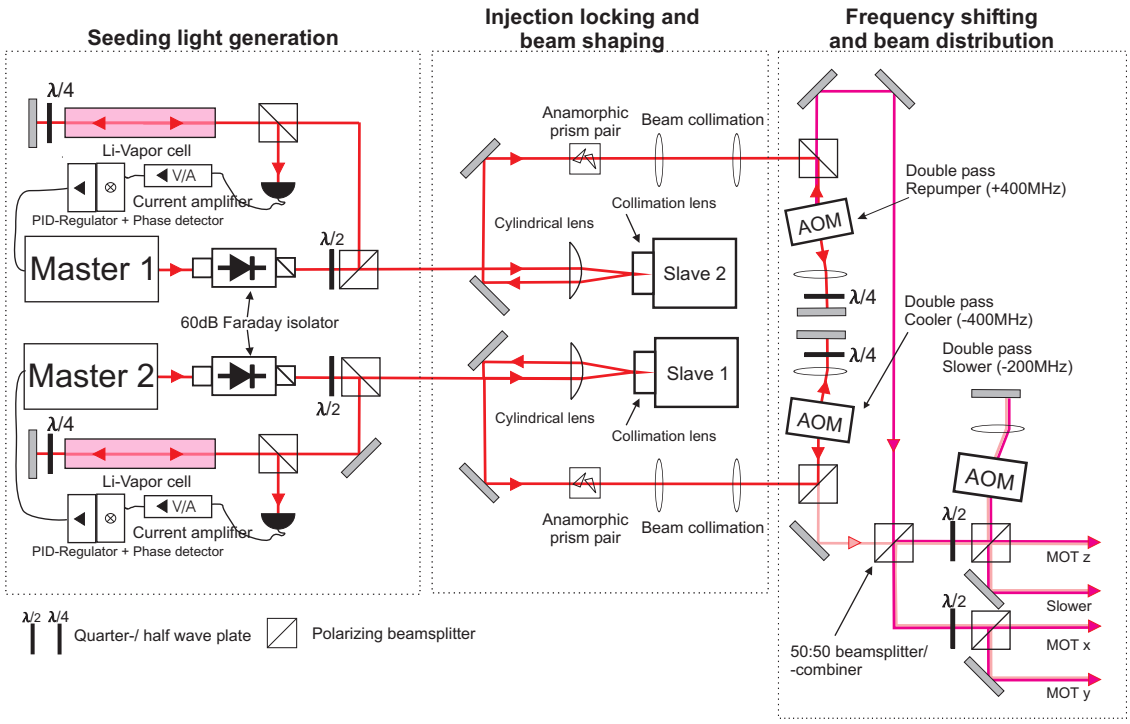

Figure 3.25: Schematic layout of the BAL-system. Not all optical components like steering mirrors and beam shaping elemnts are shown.

possible. The cylindrical lens does not act in the vertical y-direction, where the incoming beam must be tightly focused by the collimation lens in order to couple efficiently to the emitter with 1 μm height. Both lenses are translatable in the xy-plane via micrometer translation stages for optimum adjustment of injection angle and beam focusing.
In free running mode, the far-field of the BAL shows a characteristic pattern of distinct vertical stripes. To optimize the injection locking, one first has to make sure, that the seeding beam is reflected from the back facet of the BAL under an angle. Setting the current closely below the lasing threshold, the injection angle and eventually the focusing is changed, while monitoring the far-field profile, until one of the outer stripes begins to flash and turns into a bright spot. Further alignment is done by increasing the injected current and optimizing the output power of the amplified beam, which is separated from the eigenemission of the BAL by an iris aperture or a slit. For each injection geometry, there is a best combination of current and temperature: For efficient coupling of the master beam into the slave's cavity, it must be approximately resonant with the incoming light. The efficiency of the injection lock is quite sensitive to small variations of the optical cavity length [Spi05].
Figure 3.25 gives an overview of the layout of the BAL-laser system. Two independent master lasers are used, since the gain in the locked output of the slave lasers saturates at a seeding power of 10 mW. One master laser with an output of 15 mW after its optical isolator is therefore not sufficient, to extract the maximum output power from both slave

lasers.
Both master laser are locked to the cross-over signal of the ($2^2S_{1/2} - 2^2P_{3/2}$ transition (see Fig. 3.22) and independently shifted by approximately 400 MHz with the aid of acousto-optical modulators (AOM) to generate the appropriate cooling and repumper frequency. The AOMs have 200 MHz center frequency and are operated in double pass mode to avoid walking of the beam, when the applied radio frequency (RF) signal is varied to change the detuning. The detunings of both frequencies can be adjusted independently, which is helpful for finding advantagous settings for the MOT. Additionally the AOMs act as fast beam shutter. After frequency shifting, both beams are overlapped via a 50:50 non-polarizing beamsplitter. The emerging two mixed frequency beam are further split up into the three MOT-beams for each direction and the Zeeman slower beam, which is red-shifted by another 200 MHz in an AOM with 100 MHz center frequency operated in double pass configuration as well. The MOT itself is operated in the laser power saving retro-reflecting six beam configuration, which means that the incoming beams along each direction are backreflected by a mirror to form a pair of counter-propagating beams.
In order to enhance the mechanical stability of the delicate optical setup, the whole master-slave combination was mounted onto a massive aluminum breadboard that had been additionally temperature stabilized by cooling plates using a laser chiller. Likewise, the high power diodes were mounted to newly designed mounts. In this way, once established, the injection lock could be kept stable for several hours. Still the system suffered from some severe drawbacks, that made work with it very time-consuming and tedious: If the injection lock was lost once every few hours, for example due to long-term drifts of the temperature controller, the whole alignment procedure would have to be repeated. This in turn lacked a certain reproducibility: When the desired power level was restored, the beam profile and injection geometry had considerably changed, making an realignment of the whole subsequent beam path necessary. Due to the unfavorable beam characteristics (a structured, elliptic and astigmatic beam), it was difficult to shape the beam in a way, that allowed for a diffraction efficiency at the AOM of more than 50%. Since the repumper and the cooling light, which have to be well overlapped after frequency shifting, emerged from different sources with quite different beam characteristics, it was hard to imprint approximately the same beam parameters and to achieve the same diameter and degree of collimation for both frequencies and the three MOT-beams. Given the long beam paths necessary to reach the experimental chamber and its dimensions, this is a particularly intricate task. Still, under good conditions, a laser power of 80 mW on the cooler frequency and 60 mW on the repumper frequency could be extracted from the AOMs, leaving a total power of 45 mW for each MOT-beam.
On the rare occasion, when all the beams made their way up to the experimental chamber, no MOT was seen, though test measurements conducted with a dye laser had shown that trapping of atoms was straightforward to achieve, if enough laser power and a decent beam profile were available [Spi05].The spectrum of the locked part of the output was analyzed with a fiber coupled scanning grating spectrograph (Fig. 3.26). The locked spectrum shows an excellent suppression of the eigenmodes of the free runing BAL of more than

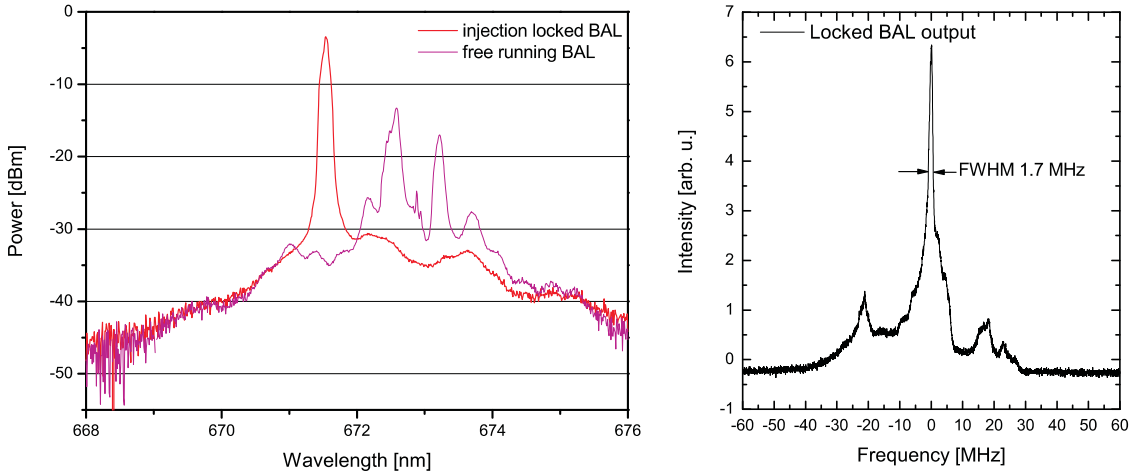

Figure 3.26: *Left*: Spectrum of the picked off beam portion of a BAL in free running mode (magenta) and frequency locked (red). The absolute frequency scale of the spectrograph was not calibrated. *Right*: Line profile of the locked BAL recorded with a scanning Fabry-Perot interfreometer of 300 MHZ free spectral range.

30 dB compared to the seeding frequency. The limited resolution of the spectrograph does not allow a statement on the narrow bandedness of the BAL's emission. This has been checked as well by means of a scanning Fabry-Perot interferometer with 300 MHz free spectral range. To have an additional frequency ruler, the seeding light was modulated with strong 20 MHz sidebands. The spectrum shown in Fig. 3.26 shows a very narrow spectrum that very closely matches the one of the master laser. The broad pedestal at the bottom of the line is partly due to the strong sideband modulation and also seen in the spectrum of the master laser. Thus the spectral properties can be considered to be sufficient for MOT operation. Though the exact reason for the failure of MOT operation remains unclear, it is very likely that the remnant transversal mode structure (which also prevented efficient mode cleaning by a spatial filter or a single-mode fiber) was one of the main factors.

3.6.2 Two-Mode Dye Laser

As the broad area lasers, despite all measures taken, did not perform as expected, and endangered the progress of the whole project, it was decided to reactivate a linear dye laser of type COHERENT CR-599-21, that had been operated by A. Dorn in investigations on the branching ratios between Auger- and radiative decay after combined laser and electron impact ionization of alkali metals. For efficient excitation of the lithium atoms on the $2^2S_{1/2}$–$2^2P_{3/2}$ transition, the laser had been modified for synchronous operation on two modes with a frequency spacing of ≈805 MHz, delivering the cooling and the repumper frequency in the same beam [Her75], [Lör95]. The dye laser was operated with a solution of DCM (4-dicyanomethylene-2-methyl-6-p-dimethylaminostyryl-4H-pyrane) in

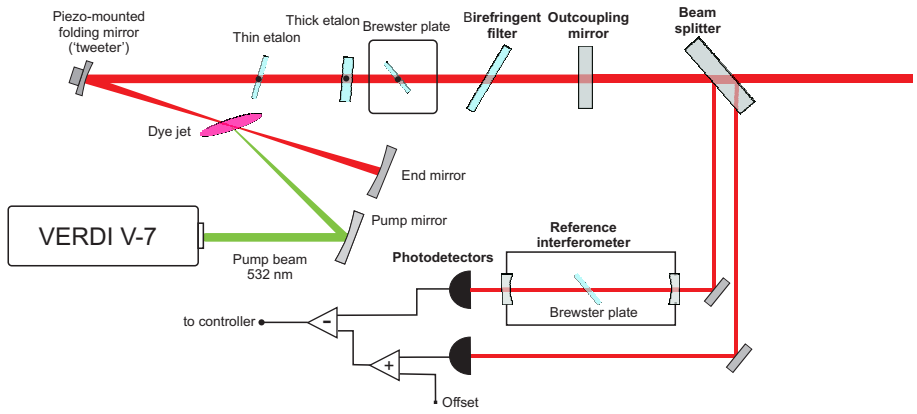

Figure 3.27: Cavity layout of the two-mode dye laser.

ethylene-glycol and pumped by a COHERENT VERDI V-7 pump laser. 200 mW of output power could be achieved, which did not need frequency shifting by AOMs, but could be directly passed to the experiment to assess the MOT was operable.

Stabilization of the Dye Laser

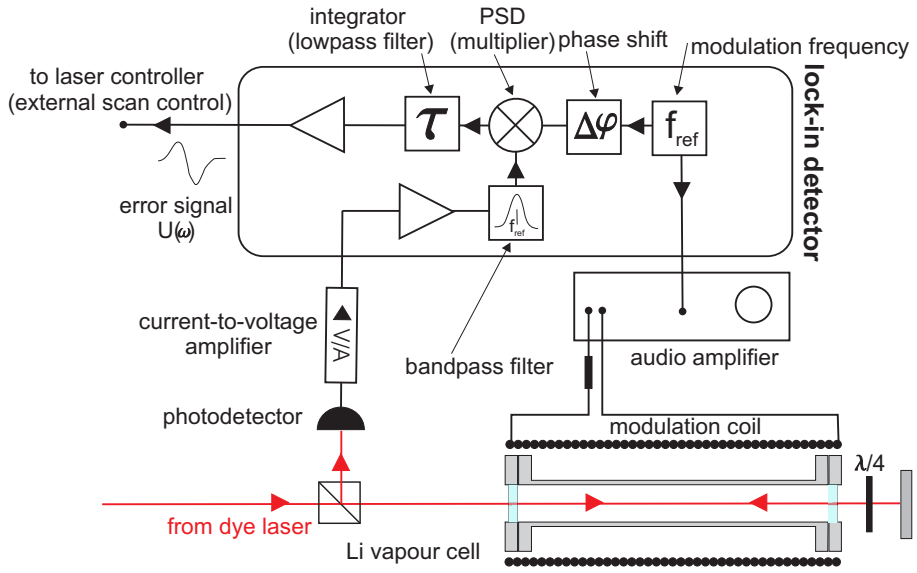

Figure 3.28: Stabilization scheme for the two-mode dye laser.

For long term frequency stabilization, a lock-in technique was applied [Mea82]. Using the same spectroscopy setup as for the semiconductor lasers, only minor modifications of the setup were necessary to obtain a working reference spectroscopy. Since it was not straightforward to modulate the laser frequency itself, the transition frequency of the atoms in the spectroscopy cell was modulated: A coil of magnet wire was wound around the spectroscopy cell. The frequency output f_{ref} of the lock-in detector was amplified by

a commercial audio amplifier and its output current applied to the coil. The alternating magnetic field slightly shifts the various magnetic sublevels of the ground and the excited state in and out of resonance, thereby periodically varying the absorption of the probe beam within the lithium cell. This has the same effect, as if the laser frequency ω was modulated $\omega(t) = \omega_0 + \omega_{\mathrm{mod}} \sin(2\pi f_{\mathrm{ref}} t)$. The amplified signal of the photodetector is fed back to the lock-in amplifier. The output of the lock-in detector corresponds to the derivative of the trasmission curve $T(\omega)$: Depending on the phase of detection, the same dispersive kind of error signal is obtained as from the Pound-Drever lock. Under laboratory conditions, relatively clear error signals with steep zero crossings could always be retrieved by proper choice of the phase of detection ϕ, integration time τ, preamplification of the signal and by adjusting the offset.
The error signal was applied to the external scan input of the dye laser, which accepts a signal between -5 V and 5 V. The voltage range of 10 V covers then a selectable frequency (10 MHz to 15 GHz) range around the adjusted center frequency, which is output at an scan input voltage of 0 V. If the laser was tuned to the MOT-transition, the lock-in signal could keep it stable for hours.
However, this kind of stabilization scheme is not suitable for canceling out short-term fluctuations in the acoustic frequency range. The reference frequency of the lock-in detector is in the kHz range, here it had been chosen as 2.2 kHz. This means that no frequency deviation on a timescale shorter than several cycles of this frequency can be detected. At the extremely low signal-to-noise levels from the spectroscopy signal the integration time should be set such that the averaging/integration extends over a considerable number of cycles of the modulation signals. In order to obtain a smooth signal, integration times between 0.07 s and 0.7 s were used, which ultimately determines the bandwidth of the regulator loop.
For use with the COHERENT CR-599-21 this poses no problem, as it has a short-term frequency stabilization on its own: It is internally locked to a transmission maximum of a stable reference Fabry-Perot interferometer. This is necessary, as irregularities or small bubbles of air within the dye jet change the effective cavity length. The resonator has two fast acting frequency selective elements that can change the resonator length to correct for frequency excursions: One is a brewster-plate of 1 mm thickness, which can be rotated by $\pm 2^\circ$ at a frequency of 400 Hz. The other is the folding mirror ('tweeter'), which is mounted on a piezo-translator, which can apply frequency corrections of up to 1 GHz with a bandwidth of 10 kHz [Coh77]. Therefore, it is only needed to compensate slow frequency drifts on a timescale of seconds to minutes. Concluding, a simple but effective means of stabilizing a dye laser to an external frequency reference was implemented.

3.6.3 Tapered Amplifier

The use of the dye laser remained a short intermezzo, since at that time, tapered amplifiers at a wavelength of 671 nm with a specified output power of 500 mW became available. Tapered amplifiers (TA) are semiconductor based amplifiers, that can amplify a seed beam

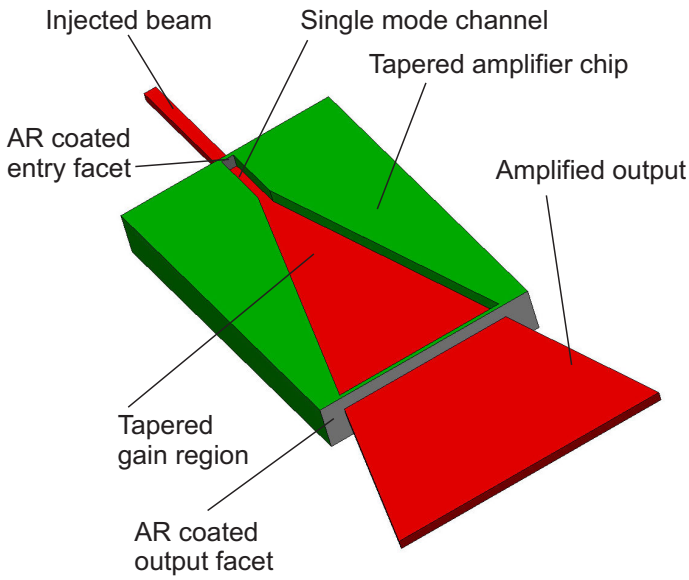

Figure 3.29: Principle of the tapered amplifier.

of a few mW to powers up to 1 W, while preserving an almost Gaussian beam shape. This is accomplished by using a special geometry of the active layer: The seed beam is coupled into a small single-mode channel at the anti-reflection coated rear facet of the tapered amplifier chip. The single-mode channel acts as a spatial mode filter akin to a single mode optical fiber, which lets only the transversal TEM_{00}-mode pass. The mode cleaned beam then enters the tapered gain region, where the lateral extension of the active layer is expanded in order to encompass more gain medium volume. The angle of the taper is matched to the diffraction limited angle of divergence of the Gaussian beam emerging from the single-mode channel. Thus, on passage through the gain medium, the spatial characteristics of the beam are preserved.
The TOPTICA TA 100 670 is capable of producing a frequency locked output of 550 mW from a seeding beam of 15 mW, which is provided by one of the frequency stabilized diode lasers. After passing through a 60 dB optical isolator to prevent light from being back reflected into the TA chip, still 400 mW are available to the experiment.
The overall layout of the system, displayed in Fig. 3.30, follows closely the concept of the broad-area-laser system presented in section 3.6.1. The tapered amplifier finally provided the long-term stability and reproducibility urgently needed for conducting measurements, that must be run under the same conditions for several days, as it provides stable and reliable MOT-operation virtually 'at the push of a button'. During the multiphoton ionization measurment campaign, no major realignment was necessary and the laser stayed in lock for several days, making unattended operation of the experiment possible.

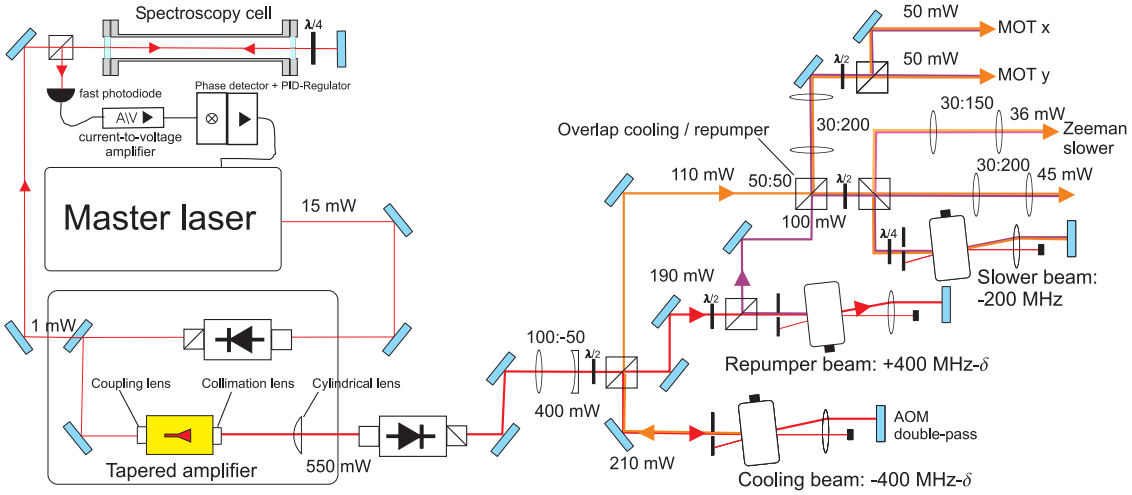

Figure 3.30: Setup of the tapered amplifier-based laser system.

3.7 Atomic Beam Source

Loading of a magneto-optical trap requires a source of slow atoms, which provides a sufficient flux of atoms with a velocity lower than the capture velocity of the trap, which is typically on the order of a few 10 m/s. The large possible accelerations in the interaction of atoms with resonant light, suggests the use of the spontaneous force to decelerate atoms from thermal velocities of several hundred m/s to almost zero over a distance of less than one meter.

The most common and widely applied technique to produce slow atomic beams is the Zeeman slower [Phi82], [Lis99], [Ded04], where a spatially varying magnetic field keeps the atomic transition in resonance with a counter-propagating laser beam via the Zeeman effect at any point along the atom's trajectory. This method has the advantage that it provides a continuous, directed flux of atoms at trappable velocities, which can be turned on or off within milliseconds, furthermore the vacuum is not impaired by any hot parts inside the main experimental chamber or a large number of atoms emitted into any other solid angle than the trap's. A well designed oven - Zeeman slower system is of crucial importance to atom trapping experiments, since the flux of slow atoms delivered to the trap region ultimately determines the loading rate and the steady state population of the MOT. Besides the gain in the maximum number of trapped atoms, a high loading rate enables shorter loading times and hence faster experimental cycles.

3.7.1 The Principle of Zeeman Slowing

The purpose of a Zeeman slower is to deccelerate a large fraction of atoms from a thermal beam with different, high initial velocities to the same low final velocity. Again, the dissipative nature of the spontaneous force becomes evident, since the atoms are not deccelerated by the same velocity, but effectively 'bunched' into a particular final velocity

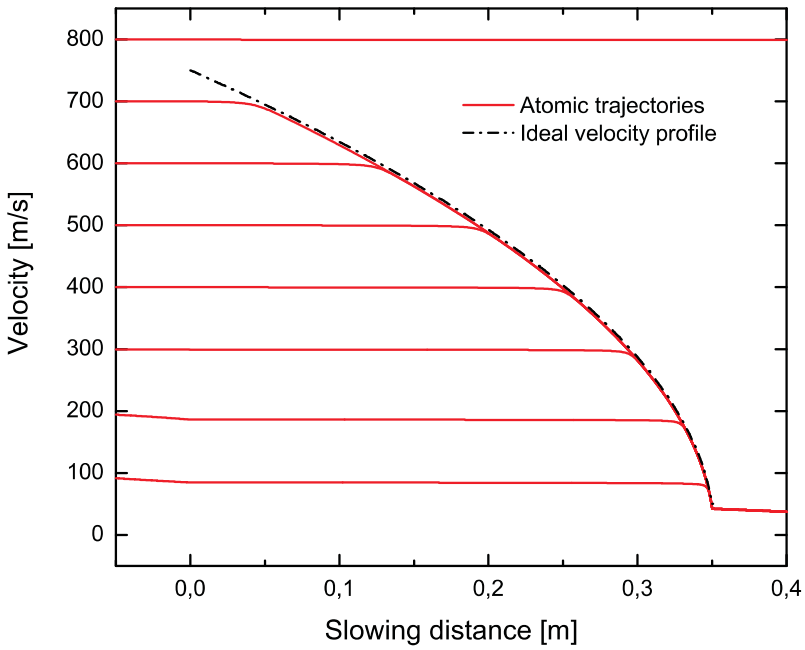

Figure 3.31: Illustration of the principle of Zeeman slowing: Calculated phase space trajectories $v(z)$ (red curves) for atoms with different initial velocities in a Zeeman slower with ideal field profile. Once in resonance with the slowing laser, they are uniformly deccelerated to the same end velocity $v_{\mathrm{end}} = 50$ m/s.

class irrespective of their initial velocity [Mol97], which would not be possible by applying a conservative potential. An atom moving with velocity v towards a counter-propagating laser beam, which is detuned to the red of the transition under consideration will come into resonance with the beam when the resonance condition for the effective detuning δ is fulfilled:

$$\delta = \delta_0 + kv = 0, \tag{3.25}$$

with the laser detuning $\delta_0 = \omega - \omega_0$, where ω is the laser frequency and ω_0 the rest frequency of the atomic transition. Hence a laser detuning to the red of the transition has negative sign. On resonance and under the condition of high saturation, the maximum acceleration conveyed to the atom is

$$a_{\mathrm{max}} = \frac{\hbar k}{m}\frac{\gamma}{2}. \tag{3.26}$$

As its velocity is quickly reduced and the Doppler detuning changes, the atom drops out of resonance. This occurs, when the Doppler shift is larger than about half the natural linewidth $\gamma/2$. In velocity space, this linewidth corresponds to only 4 m/s, so even in the limit of high saturation $s_0 \gg 1$ a change in velocity of some 10 m/s can be expected at maximum.

To keep the atom in, or at least close enough to, resonance all along its trajectory, the transition energy is tuned by the difference of the Zeeman energies of the ground state and the excited state in a magnetic field B. The frequency shift induced by the Zeeman

effect $\delta_Z = \Delta\mu B/\hbar$ is added to the resonance condition (3.25):

$$\delta = \delta_0 + kv - \Delta\mu B/\hbar = 0. \tag{3.27}$$

$\Delta\mu$ denotes the difference between the magnetic momenta of the respective ground and excited state μ_g and μ_e.
An atom with initial velocity v_0, that is slowed down with a constant deceleration $a < a_{\max}$, traces the following phase-space trajectory:

$$v(z) = v_0\sqrt{1 - \frac{z}{z_0}}, \tag{3.28}$$

with $z_0 = v_0^2/2a$ being the stopping distance. Inserting $v(z)$ into (3.27) yields the spatial dependence of the slower field:

$$B(z) = B_{\text{offset}} + B_0\sqrt{1 - \frac{z}{z_0}} \tag{3.29}$$

$$B_{\text{offset}} = \frac{\hbar}{\Delta\mu}\delta_0 \tag{3.30}$$

$$B_0 = \frac{\hbar}{\Delta\mu}kv_0. \tag{3.31}$$

Consequently, the length of the slower is determined by the maximum initial velocity v_0 that is to be slowed down as well as the achievable acceleration $a_{\max}$, given by the mass of the atom and the linewidth of the respective transition. In the design of a Zeeman slower a constant decceleration of $a = \eta a_{\max}$ is assumed, where η is a safety factor to account for an eventual low saturation of the transition and inevitable deviations of the magnetic field gradient from the ideal profile. Common values for η lie in the range from 0.8 to 0.4. If somewhere along the trajectory the field decreases too steeply, the resonance condition is not well fulfilled any more and the actual decceleration will be lower than the design value. As the atoms progress further into regions of lower field strength, the discrepancy between the ideal and actual phase space trajectory becomes larger and larger, further reducing the scattering rate. The atoms will finally come completely out of resonance with the slowing beam and drop out of the slowing process. The maximum field strength required is determined by the maximum initial velocity that is to be slowed down. Atoms faster than v_0 never become resonant with the slowing light and pass the slower unhindered. Typical slower designs exhibit lengths between 30 cm and 1 m and can slow initial velocities between 500 and 1000 m/s.
The design parameters depend strongly on the atomic species: The maximum achievable deceleration depends on the lifetime of the excited state and the mass of the atom. In general, effusive ovens are used to feed the slower with a reasonable flux of thermal atoms. The temperature of the oven is adjusted such that the thermal velocity distribution of the effusive beam contains enough flux of atoms in the low velocity tail, i.e. at velocities, that can be captured and slowed down.

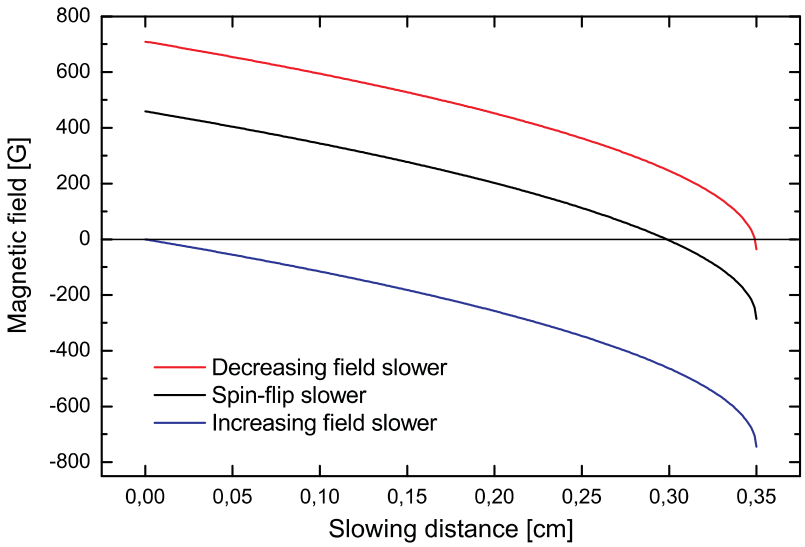

Figure 3.32: Ideal field profiles for a lithium slower with a capture velocity v_0 of 700 m/s and a final velocity of 50 m/s, calculated with a safety factor of 0.45. The increasing-field design (blue curve) requires a detuning of 1.04 GHz, the spin-flip type (black curve) operates with 400 MHz. The decreasing field slower has small red detuning of 50 MHz.

Types of Zeeman Slowers

The freedom of choice in the detuning δ_0 of the slowing laser allows three different field configurations for Zeeman slower operation, each having its own distinct benefits and disadvantages.
If the magnetic field strength $|B(z)|$ has its maximum value at the beginning of the deceleration distance to compensate for the Doppler shift of the fastest atoms, one speaks of an *decreasing field geometry* (see Fig. 3.32). The slowing laser has to be operated at a small red detuning to be in resonance with atoms of the final velocity v_{end} under zero field conditions. The main drawback is the required detuning of only a few linewidths to reach low final velocities: Since the slower laser beam has to pass through the MOT region to oppose the atomic beam, the MOT is easily perturbed by the additional light pressure of the slowing beam. This problem can be adressed by using a a lightly blue or red detuned slower laser and adding an additional positive or negative offset field. However, due to the slow decrease of the slower field towards the trap center, the end of the slowing length is not well defined and atoms that have already passed the slower are still exposed to near resonant light, so that they continue to slow down and eventually might come to a halt and are pushed back into the opposite direction. Decreasing field slowers are mainly used, when the slower exit is very close to the trap region, so that the radial gradient field of the MOT can be merged with the field of the Zeeman slower to effectively form the last part of the deceleration field.
The configuration, where the magnetic field is zero at the beginning of the slowing distance and reaches its maximum value at its end, is called *increasing field slower*. Obviously the

slower laser must be far red detuned to balance the Doppler shift of the fastest slowable atoms according to $kv_0 + \delta_0 = 0$. The extraction of the slow atoms from the slower is greatly facilitated by the well defined maximum and subsequent sharp decrease of the slower field, which lets the atoms drop out of resonance immediately. Disadvantages of this concept are strong residual fields at the location of the MOT, which eventually have to be balanced. The large laser detunings of about 1 GHz (e.g. for lithium and v_0=700 m/s) required are hardly generated by acousto-optical modulators (AOM).
The concept of the *spin-flip slower* tries to combine properties of both the above types (see figure 3.32): The atom's trajectories start in a decreasing field, which crosses the zero of the magnetic field along the slowing distance and reverses its direction to rise again to a maximum value. The terminus spin-flip slower is somewhat misleading, since the magnetic momenta of the atoms retain their orientation when crossing the zero field region, they are just reversed ('flipped') with respect to the magnetic field's direction. The position of the zero crossing is determined by the available laser detuning $\delta_0 = kv(z)$. For lithium and a detuning of 200 MHz it occurs at the position (as realized in this experiment), where the atoms' velocity is 140 m/s. The spin-flip slower avoids high field gradients close to the MOT, permits a defined termination of the slowing process and thus a handle for changing the end velocity, as well as the use of detunings, that are largely harmless to the MOT. In addition, the absolute field strength needed, to achieve the desired capture velocity v_0 is reduced due to the zero-crossing of the field. This is of great practical importance, since coils generating fields on the order of 1000 G tend to be bulky constructions that require high currents and water-cooling. Figure 3.32 compares calculated ideal field profiles of the three designs.

Zeeman Slowing of Lithium

The transition used for the deceleration of the ^{7}Li-atoms is the cycling or closed transition of the D2-line ($2^2S_{1/2}, F = 2, m_F = +2$ – $2^2P_{3/2}, F' = 3, m_{F'} = +3$) ($|g\rangle$ – $|e\rangle$). As noted before, the adequate form of the Zeeman slower field depends on the difference in the energy shift of the atomic states as a function of the magnetic field strength. The maximum fields encountered in Zeeman slowers are on the order of 500 to 1000 G. Concerning lithium, the small hyperfine splitting of the ground and excited state involved in laser cooling leads to decoupling of the electron and nuclear spin at these moderate fields. A description of the progression of the energy levels with increasing magnetic field by the Zeeman effect is therefore not appropriate, as will be discussed in the following:
For weak magnetic fields the progression of the ground state $|g\rangle$ can be described by the normal Zeeman effect of the hyperfine structure. In the weak field regime, the interaction energy of the coupled nuclear and electronic magnetic moment $\boldsymbol{\mu}_F^g$ with the external field $\mathbf{B}$ is given by (3.32). For reasons that will become clear later, the hyperfine interaction energy $V_{I,J}(F)$ is included as a constant offset:

$$\begin{aligned} E_{\mathrm{Z}} &= -\boldsymbol{\mu}_F^g \cdot \mathbf{B} + V_{I,J}(F) \\ &= m_F g_F \mu_{\mathrm{B}} B + V_{I,J}(F). \end{aligned} \tag{3.32}$$

The above relation holds, as long as the Zeeman energy is small compared to the magnetic coupling energy V_{IJ} between the total electronic and the nuclear angular momentum. Here g_F is the Landé g-factor for the F=2 ground state and has the value g_F=$\frac{1}{2}$. The g-factor calculates as follows:

$$g_F = g_J \frac{F(F+1)+J(J+1)-I(I+1)}{2F(F+1)} - g_\mathrm{N}\frac{\mu_\mathrm{N}}{\mu_\mathrm{B}}\frac{F(F+1)+I(I+1)-J(J+1)}{2F(F+1)}, \quad (3.33)$$

where g_N is the nuclear g-factor and μ_N the nuclear magneton. The ratio of the Bohr magneton to the nuclear magneton $\mu_\mathrm{N}/\mu_\mathrm{B}$ is as small as the ratio of the electron mass to the mass of the proton $m_e/m_p \approx 1/1836$, so the second term of (3.33) can be neglected. g_J in turn is the total electron angular momentum g-factor as given by (3.34) and has the value g_J=2.

$$g_J = 1 + \frac{J(J+1)+S(S+1)-L(L+1)}{2J(J+1)}. \quad (3.34)$$

The coupling energy (or hyperfine-splitting) for a particular state with quantum numbers F, I and J is

$$V_{IJ} = \frac{a_\mathrm{HFS}}{2}(F(F+1)-I(I+1)-J(J+1)). \quad (3.35)$$

a_HFS denotes the hyperfine constant of the particular fine structure state, the relevant ones for the $|2^2S_{1/2}\rangle$ and $|2^2P_{3/2}\rangle$-states are presented in Table 2.3, for $|g\rangle$ we have $a_\mathrm{HFS} = h\cdot$ 401 MHz and $V_{IJ}(F=2) = \frac{3}{4}a_\mathrm{HFS}$. As the interaction energy of the electronic magnetic momentum of the ground state $g_J m_J \mu_\mathrm{B} B$ with the external field is $h \cdot 1.4$ MHz/G$\cdot B$[G], both energies are of the same magnitude at field strengths of above 100 G. The external field cannot be considered as weak perturbation to the system and formula (3.32) no longer applies.

For much higher field strengths ($B >$ 800 G), the energy levels are accurately described by the *Paschen-Back effect* of the hyperfine structure (sometimes also termed *Back-Goudsmit effect*). In the Paschen-Back regime, the energy shift is composed of the Zeeman energies of the now uncoupled and independently aligned total electron angular momentum **J** and nuclear spin **I**:

$$\Delta E_\mathrm{PB} = m_J g_J \mu_\mathrm{B} B - m_\mathrm{N} g_\mathrm{N} \mu_\mathrm{B} B + m_I m_J a_\mathrm{HFS}. \quad (3.36)$$

Inserting the appropriate quantum number m_J=$\frac{1}{2}$ and g-factor g_J=2 yields the same linear dependence on the magnetic field as for the weak field case. The third term of the above equation represents the mutual interaction energy and reproduces the zero field hyperfine shift of (3.32) with $(\frac{3}{2}\cdot\frac{1}{2})a_\mathrm{HFS}$.

The field dependence in the intermediate regime, which just happens to cover the operating range of a Zeeman slower, is difficult to calculate and no general analytical description is available. Luckily for the case of interest here, if $F = I \pm \frac{1}{2}$, namely F=2 and I=3/2, a

closed form analytical expression exists, which is known as the *Breit-Rabi formula* [MK97]:

$$\begin{aligned} E_{\mathrm{BR}} &= -\frac{a_{\mathrm{HFS}}}{4} + m_F g_{\mathrm{N}} \mu_{\mathrm{N}} B \pm \frac{\Delta E_0}{2}\left(1 + \frac{4m_F}{2I+1}x + x^2\right)^{1/2} \\ \text{with } x &= \frac{g_J \mu_{\mathrm{B}} - g_{\mathrm{N}} \mu_{\mathrm{N}}}{\Delta E_0} B \quad \text{and} \quad \Delta E_0 = a_{\mathrm{HFS}}\left(I + \frac{1}{2}\right). \end{aligned} \tag{3.37}$$

For the $|F = 2\rangle$ ground state, ΔE_0 corresponds to the full hyperfine splitting $\Delta E_0 = 2a_{\mathrm{HFS}}$ of 803 MHz of the $|2^2S_{1/2}\rangle$ ground state. Its Landé g-factor is $g_{J=\frac{1}{2}} = 2$. The small contribution of the nuclear magnetic moment shall be neglected once again, this reduces x to

$$x \approx \frac{2\mu_{\mathrm{B}} B}{\Delta E_0} = \frac{\mu_{\mathrm{B}} B}{a_{\mathrm{HFS}}}$$

and, after inserting all quantum numbers, the Breit-Rabi expression to

$$E_{\mathrm{BR}} \approx -\frac{a_{\mathrm{HFS}}}{4} + a_{\mathrm{HFS}}(x^2 + 2x + 1)^{1/2} = -\frac{a_{\mathrm{HFS}}}{4} + a_{\mathrm{HFS}}(1 + x). \tag{3.38}$$

This equation holds the important result, that the progression of the ground state (or more precisely the state evolving from the ground state) of the cycling transition is always linear with the magnetic field:

$$\Delta E_{\mathrm{BR}}(F = 2, m_F = +2) = \frac{3}{4} a_{\mathrm{HFS}} + \mu_{\mathrm{B}} B. \tag{3.39}$$

Yet the upper state of the cycling transition $|2^2P_{3/2}, F' = 3, m_{F'} = +3\rangle$ has to be adressed. As a consequence of the weak hyperfine interaction of the $|2^2P_{3/2}\rangle$ state with a hyperfine constant of $a_{\mathrm{HFS}} = -3.05$ MHz, the interaction energy $V_{I',J'}(F' = 3) = \frac{9}{4} a_{HFS}$ amounts to only $h \cdot (-6.86)$ MHz. The g-factors are $g_{F'}{=}\frac{2}{3}$ and $g_{J'}{=}\frac{4}{3}$. This means, that the intermediate regime is approached at fields exceeding 2 G. For the fields present within the Zeeman slower, the excited state is always in the Paschen-Back regime and the field dependence of the upper level is described by

$$\Delta E_{PB}(J' = 3/2) = m_{J'} g_{J'} \mu_{\mathrm{B}} B, \tag{3.40}$$

where the contribution of the nuclear magnetic moment and the hyperfine energy $\frac{9}{4} a_{HFS}$ have been dropped. The appropriate quantum number is $m_{J'}{=}\frac{3}{2}$.
Now the field-induced energy shift of the slower transition $\Delta E(B)$ is obtained:

$$\begin{aligned} \Delta E(B) &= \Delta E_{PB}(J' = 3/2) - \Delta E_{\mathrm{BR}}(F = 2, m_F = +2) \\ &= \mu_{\mathrm{B}} B(m_{J'} g_{J'} - 1) \\ &= \mu_{\mathrm{B}} B. \end{aligned} \tag{3.41}$$

This confirms a convenient linear dependence of the slower transition's detuning on the magnetic field. The large separation of the adjacent hyperfine levels in high fields drastically reduces the probability of near-resonant excitation of levels other than the upper level of the cycling transition, rendering it an almost ideal two-level system.

Nevertheless, the repumping frequency is introduced into the slower beam as well. When the atoms approach the slower, they pass through a region where the field increases from zero to its maximum value, so in the region of weak magnetic fields, optical pumping occurs, which transfers the atoms to the $|F = 1\rangle$ ground state manifold. In a spin-flip slower, the zero-field region along the slowing distance makes the use of a repumper necessary.
For completeness and reference, the progression of the individual magnetic sublevels of the MOT-transition with the magnetic field is presented in Figures 3.33 and 3.34. The values were obtained by a numerical calculation, using a modified MATHEMATICA-script, published in M. E. Gehm's PhD-thesis [Geh03], where it was used to calculate the Zeeman splitting in ^{6}Li. In brief, the code generates a list of all sublevels for a fine structure state specified by the quantum numbers I and J. The combined (sum-)Hamiltonian of the hyperfine interaction and the interaction with the external magnetic field is set-up in the $|J, m_J\rangle \bigotimes |I, m_I\rangle$ product basis. The $|J, m_J\rangle\,|I, m_I\rangle$ are not eigenstates of the hyperfine interaction hamiltonian (which are the $|J, I, F, m_F\rangle$ states), so the hyperfine part of the total hamiltonian and consequently the total hamiltonian is non-diagonal in the $|J, m_J\rangle\,|I, m_I\rangle$-representation. The program then computes all the eigenvalues of the hamiltonian for each individual value of the magnetic field. The curves reflecting the adiabatic evolution of the energy levels are then obtained by plotting the eigenvalues versus the magnetic field strength. The experimentally determined values of the g-factors employed in the calculation are listed in Table 3.2.

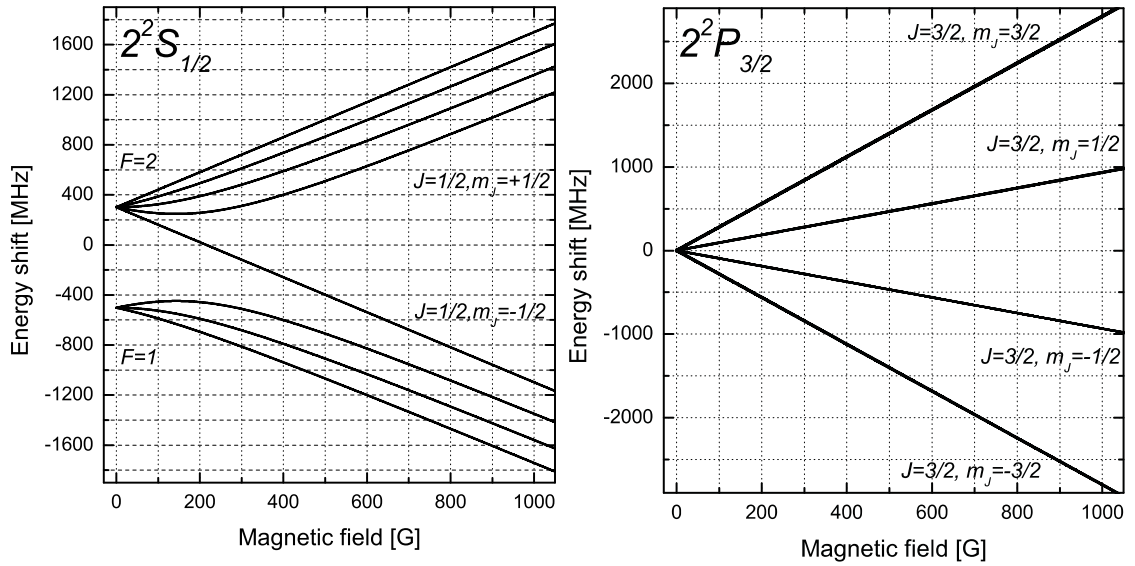

Figure 3.33: Magnetic field dependence of the $2^2S_{1/2}$ ground state and $2^2P_{3/2}$ excited state magnetic sublevels. For the $2^2P_{3/2}$ states, the small contribution of the nuclear Zeeman energy, which is $\approx g_N/g_J = 1130$ times smaller than the electronic one, together with the small hyperfine splitting makes the curves tracing the $|J, m_J\rangle$ states appear fourfold degenerate.

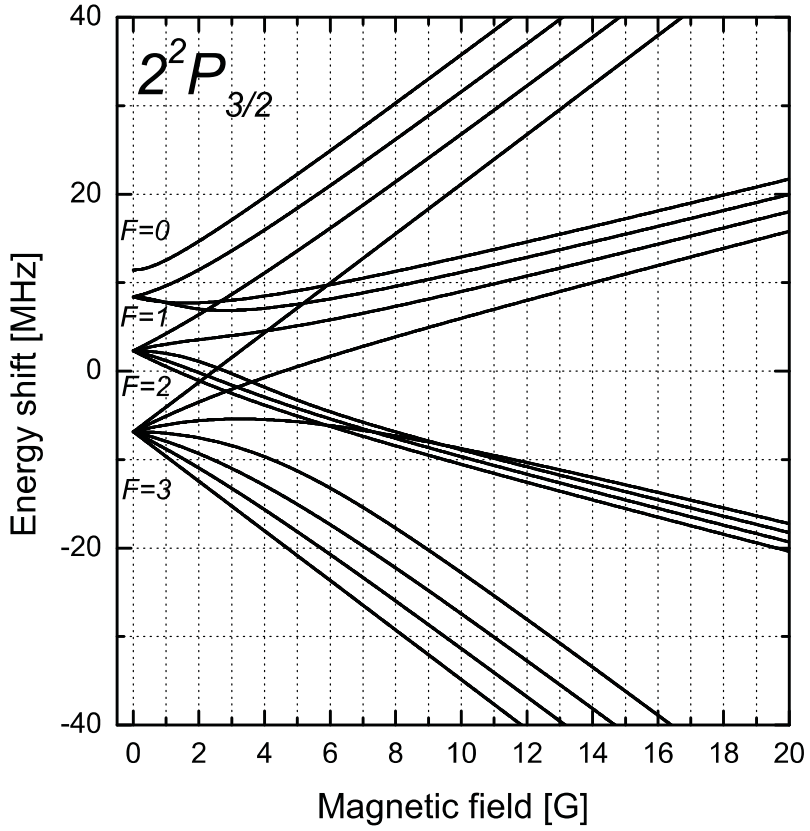

Figure 3.34: Magnetic field dependence of the $2^2P_{3/2}$ excited state sublevels in the low field regime. Already at minor fields of a few Gauss, as encountered in the MOT's gradient field, significant deviations from the linear Zeeman effect occur, leading to a complicated pattern of the energy splitting with several level crossings.

Quantitiy	**Symbol**	**Value [Ref.]**
Electronic g-factor $2^2S_{1/2}$	g_J	2.002301 [Ari77]
Electronic g-factor $2^2P_{3/2}$	$g_{J'}$	1.335 [Ari77]
Nuclear g-factor ^{7}Li	g_N	-0.001182 [Ari77]
Hyperfine structure constant $2^2S_{1/2}$	a_HFS	401.76 MHz [Wal03]
Hyperfine structure constant $2^2P_{3/2}$	a_HFS	-3.05 MHz [Ort75]

Table 3.2: Hyperfine constants and g-factors used in the calculation of the Zeeman splittings.

3.7.2 Zeeman Slower

The present Zeeman slower setup was constructed in the course of a diploma thesis [Spi05]. The design parameters were a maximum initial velocity v_max of 700 m/s and a safety factor

$$a = \eta a_\mathrm{max} \tag{3.42}$$

with $\eta = 0.5$. Thus the required length of the slowing section is just ≈ 35 cm, which allows a rather compact construction of the whole slower system. There are two basic methods

to technically realize the desired slower field profile: One common method employs one or two solenoidal coils with a varying number of winding layers along the beam tube according to the desired field profile. Though it has the advantage that it can be operated with a single power supply, it is very sensitive to geometrical deviations (e.g. due to inaccuracies in the winding pattern or variations in the diameter of the wire or tubing used) from the calculated ideal current distribution, therefore often the implementation of correction coils after construction is necessary.
Alternatively, the magnet can be split up into a number of different sections, which can be addressed with individual currents, so the sum of the individual fields will match the appropriate field profile. In this way, it is easier to compensate for imperfections in the manufacture of the coils and a greater flexibility in the choice of operational parameters is provided. For instance the maximum initial velocity could be increased to beyond the design value determined by the safety factor, and the detuning of the slowing laser or the end velocity are readily varied.

Mechanical Design

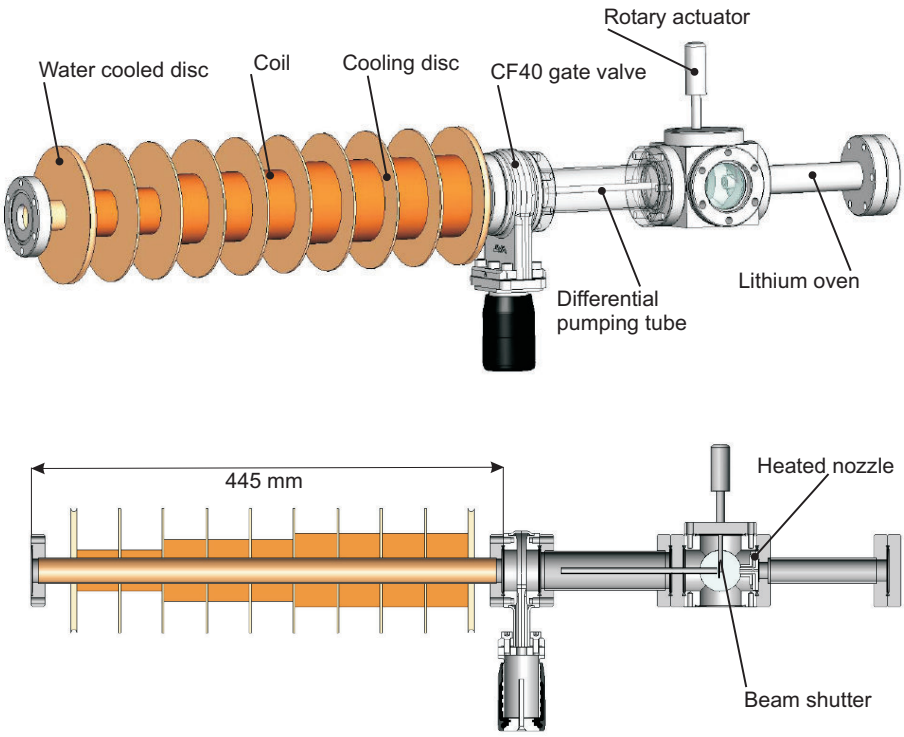

Figure 3.35: Zeeman slower and oven chamber.

Our design (see Fig. 3.35) features a set of nine coil sections of 40 mm length each along

the beam direction, which are wound around a 25×1 mm copper tube that is directly integrated into the vacuum system via welded-on CF40 flanges at the ends. The sections are separated by 2 mm thick copper discs of 120 mm diameter soldered onto the tube, which served as coil formers during manufacture of the slower and provide efficient air cooling to the coils and the tube. The last disc at each end of the slower has an integrated water cooling tube, which acts as an additional heat sink. The coils themselves are made of 1.8 mm diameter magnet wire and consist of 23 windings in the axial direction and 15 (where the field is highest) to 5 radial layers of wire (close to the chamber). In order to bring the slower exit as close as possible to the center of the chamber, the Zeeman slower tube is directly linked to the main chamber. At the entry side of the slower the oven chamber is attached. The vacua of the oven and the experimental chamber can be shut off from each other by a CF40 gate valve residing in between the oven chamber and the slower. Thus maintenance work on either the oven part or the main chamber can be performed without having to break the vacuum in the other part.
The oven chamber consists of a CF40 cube chamber with an edge length of 7 cm. Its ports are occupied by the lithium oven construction itself, a window for optical inspection, e.g. to check the alignment of the slower laser, a rotary feedthrough actuating the lithium beam shutter, and a CF40 four-way cross. The CF40 cross houses an ion gauge for monitoring the pressure within the oven section, additional feedthroughs, for example for the heating current of the oven nozzle are installed here. At the bottom part of the cross, a VARIAN V-70 turbo pump with a pumping speed of 68 l/s is installed, which is responsible for maintainig the vacuum of the oven chamber. Since pressures of up to 10^{-6} mbar are tolerable in the oven section, it is directly connected to the fore-vacuum with a base pressure of $1.3 \cdot 10^{-3}$ mbar.

Differential Pumping

The molecular flow resistance (and thus the differential pumping effect) of the slower tube with its relatively large diameter of 25 mm is not sufficient to shield the main chamber's vacuum from the influence of potentially harmful higher pressures in the oven section. To exclude any such influence, a differential pumping tube with a length of 146 mm and 4 mm inner diameter, fed through a CF40 flange, is inserted at the cube's port facing the slower. The pressure difference that can be maintained between the two vessels, is estimated in the following way:
In analogy to Ohm's law, a pressure difference between two vacuum vessels (pressures p_1, p_2), connected by a tube of conductance C, drives a particle flow (current) q of

$$q = p_1 \dot{V}_1 = C(p_1 - p_2). \tag{3.43}$$

The quantitiy q is given in units of $[q]$=mbar·l/s and is proportional to the particle flux. In steady state, the current through the tube into the high vacuum region with pressure p_2 is equal to the rate at which particles are removed by the pump. This rate $p_2 \cdot S$ is given

by the pumping speed S of the pump, which is specified in $[S]$=l/s. This flux conservation is expresed by

$$q = p_1\dot{V} = p_2 S. \tag{3.44}$$

Substituting (3.43) into (3.44) yields the ratio of the pressures dependent on the flow conductance C and the pumping speed S

$$\frac{p_1}{p_2} = 1 + \frac{S}{C}. \tag{3.45}$$

The conductance of a tube with inner radius r and length l in the regime of molecular flow is calculated as [Wut97]

$$C = \frac{\pi r^2 \bar{v}}{4}\left(1 + \frac{3}{8}\frac{l}{r}\right)^{-1}, \tag{3.46}$$

where $\bar{v}$ is the mean thermal velocity

$$\bar{v} = \sqrt{\frac{8}{\pi}\frac{k_\mathrm{B}T}{m}}. \tag{3.47}$$

The differential pumping tube exhibits a conductance of 0.065 l/s for H_2O (commonly the most abundant contaminant in otherwise leak free vacuum systems due to its desorption from the walls of the vessel) at room temperature. Conservatively estimating the pumping speed of the pumps of the main chamber with 500 l/s, a pressure ratio of p_1/p_2 of 10^4 can be maintained. In practice, no degradation of the main chamber UHV has been observed. After an initial period of operation, where the hot surfaces of the oven parts are 'baking out' and release large amounts of contaminants, the pressure in the oven chamber varies between $\approx 5 \cdot 10^{-7}$ mbar at highest temperature and $2 \cdot 10^{-8}$ mbar in cold state.

Magnetic Fields and Optimization of the Existing Setup

After completion of the Zeeman slower, the axial fields of the individual coils had been mapped with a Hall probe. The measurements showed that the field profiles were significantly deviating from the calculated curves, as they were narrower and had a higher maximum value altogether. The measured fields of each coil were then approximated by fitting them with Voigt-profiles (a Voigt profile is the convolution of a Lorentzian with a Gaussian, usually encountered in spectroscopy to model Doppler-broadened Lorentzian spectral lines, when both widths are of similar magnitude [Hum79]) which reproduced the measured curves well, so that a dataset with uniformly spaced points, covering the whole range of the slower and beyond was available. The superposition of the field profiles generated by the Voigt-fits was then fitted to the calculated ideal field gradient with the nine coil currents as fit-parameters [Spi05]. Due to their reduced width, the sum of the real coil fields is much harder to adapt to the desired field: The best current fit curve still emulates relatively well the overall progression of the field, but shows a superimposed sinusoidal modulation, with the minima of the bumps occurring at the positions of the separating

discs. This has the effect that some sections at the rising edge of the bumps have an almost vanishing or even positive field gradient, thus not contributing to the slowing length at all, whereas the falling edge produces stronger field gradients, which is hard for the atoms' trajectories to track. So it was unclear, whether the slower could be brought to work, despite the foreseen safety factor.
As the power supplies for the coils were not finished at that time and due to the lack of

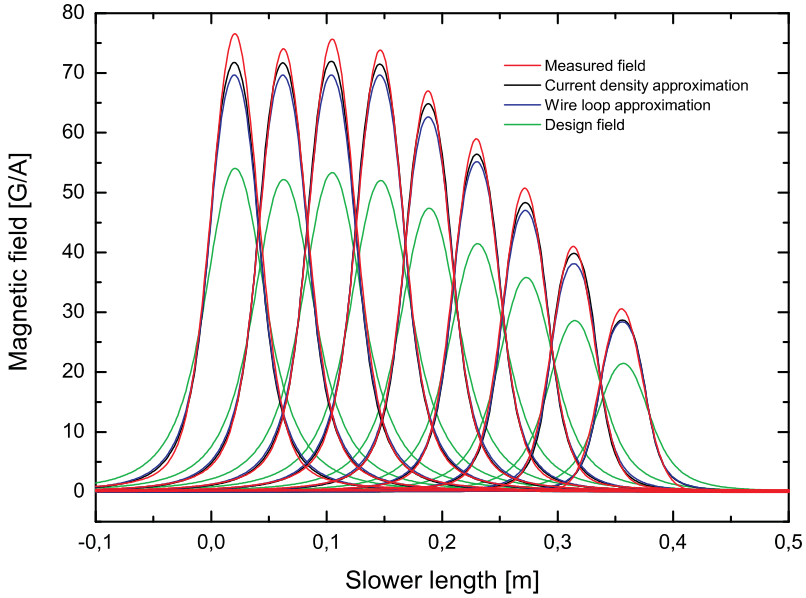

Figure 3.36: Comparison between the design field (green), the measured field (red) and the approximations based on the coil geometry (black: Biot-Savart integral over continuous current density, blue: Sum field of individual wire loops).

a reliable, powerful laser source, it was not possible to test the function of the Zeeman slower in practice. To check, whether the existing setup could be made work, e.g. by reducing the maximum captured velocity v_0 or by strongly saturating the transition to flatten out the bumps, and to have a versatile design tool at hand for the case that a new slower would have to be built, a virtual slower was modeled in MATLAB.
The program consists of two parts: One that determines the currents for a given set of coils, that best match an optimum field geometry. The second part calculates atom trajectories for a given magnetic field.
In the first script, the user has to specify the intended parameters of operation, being the maximum initial velocity, end velocity, laser detuning, the length of the slower and the characteristic data of the atomic species. With these parameters, the ideal field gradient is calculated. The user can also specify the geometry of the coil sections. The resulting axial fields of the individual coils are then calculated by the program. Alternatively, datasets describing the fields can be imported. Using the coil currents I_k as fit parameters, the program then performs a least squares fit of the individual unit fields over the slowing

distance to the ideal field profile. In other words, the quantity

$$\left(\int_{z=0}^{L} \mathrm{d}z \left(B_{\mathrm{ideal}}(z) - \sum_{k=1}^{n} I_k B_k(z) \right) \right)^2 \tag{3.48}$$

is being minimized, where $B_{\mathrm{ideal}}(z)$ is the ideal slowing field, $B_k(z)$ are the actual fields of the coil sections for a current of 1 A and I_k are the respective coil currents. As output, the currents necessary to achieve the best approximation of the ideal field, the resulting sum field and the residue of the fit are obtained. When no externally generated data for the $B_k(z)$ is available, for instance when modeling a new slower design, two different methods are applied to calculate the coil fields: One approximates the coil field by the sum of individual wire loops, where the inner radius, length of the section, the dimensions of the wire used and the number of winding layers define the coil's structure. For cross checking, the dimensions of the coils' cross sections and the total current ($I_k \times$turns) can be specified. In this case, the axial field is computed by integration of the current density over the cross section of the coil package, using the integral of formula (3.13). As displayed in Figure 3.36, there is reasonable agreement between the measured slower field and the fields calculated on the basis of the existing coil's dimensions. The simulation also revealed the cause for the mysterious discrepancy between real and designed slower field: If the inner radius (radius of slower tube) of the coil is doubled, the calculation reproduces the original design curves. A confusion of radius and diameter due to ambiguous labeling of a variable in the MATHEMATICA-script (described in [Har03]) used for the slower design is most likely the reason.

The second script, called the *flight simulator*, calculates the trajectories along the beam direction of the atoms inside the Zeeman-slower. Once again, the user can supply a magnetic field profile or, by choice a set of individual coil fields and the corresponding set of currents. For an arbitrary number of different initial velocities, the trajectories are plotted in a graph or written into a file. Usually the (most instructive) phase space trajectories $v(z)$ are used to judge the performance of the slower. As the full data produced by the simulation is held in memory, the time-dependence of position, velocity and acceleration ($z(t)$, $v(t)$, $a(t)$) are accessible as well. One can easily vary operational parameters, like currents, detuning and saturation parameter of the slowing beam, in order to find the optimum settings or to test for their sensitivity to deviations.

The integration of the equation of motion

$$m\ddot{z} = F(\dot{z}, z) \tag{3.49}$$

is accomplished by the simple Euler forward method. Though not as efficient and robust as more sophisticated methods of solving differential equations, such as Runge-Kutta methods, it produces accurate results, provided the step-size is chosen small enough. The optical force F depends on the detuning $\delta(B(z), \dot{z})$ according to (2.11), which in turn is a function of the local magnetic field $B(z)$ and the instantaneous velocity v as given in (3.27). Since $F(\dot{z}, z)$ contains only smoothly varying functions, the problem can be adequately solved by choosing a reasonably small time-step Δt. When dealing with initial

velocities of 1000 m/s at maximum and slowing lengths of a few 10 cm, a timestep of 1 μs can be considered sufficient. As the magnetic field $B(z)$ is only given at discrete data points z_i, it is interpolated by a cubic spline curve, enforcing a smooth curve to avoid possible problems due to the discontinuity of the magnetic field representation.
Figure 3.37 shows a trajectory simulation in a field configuration optimized for an initial

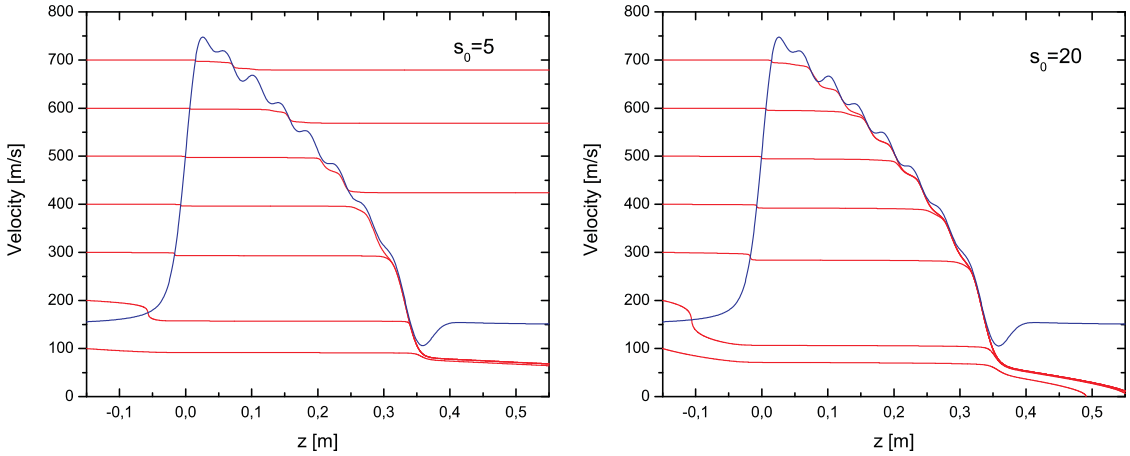

Figure 3.37: Simulated phase space trajectories of atoms in the Zeeman slower for a red detuning of the slowing laser of 224 MHz. The blue line maps the magnetic field, expressed in units of velocity ($v = \mu_B B/\hbar k + \delta_0/k$), indicating the velocity an atom should have to be exactly in resonance with the slowing laser. For medium saturation (s_0=5) of the slowing transition, the slowing process is interrupted (*left*), for high saturation of s_0=20 (*right*), the atoms stay in resonance due to power broadening of the absorption profile.

velocity v_0 of 750 m/s and a final velocity v_{end} of 50 m/s. For a low saturation parameter s_0, the atoms will drop out of resonance at the bumps in the field as expected. However, if enough laser power is available, which is the case when using the tapered amplifier as laser source, and the saturation parameter can be largely increased, the simulation shows, that the Zeeman slower should work quite well, as evident from Figure 3.37. When leaving the slower and entering the low field region, the atoms are still strongly influenced by the slowing beam. Due to their low velocity the atoms spend a considerable time in the laser field on their way to the trap region, and can scatter a large number of photons even from a far off-resonant beam. The capture velocity of the MOT is estimated to be in the range of 50–100 m/s, whereas the velocity of the atoms is much lower, when arriving at the trap. It is not desirable to reduce the velocity of the atoms too far below the critical value for the following reason: As the transversal velocity component of the atoms is not influenced by the slowing process, the long time-of-flight between the end of the slower and the MOT will lead to a significant broadening of the atomic beam, which has the consequence that most of the slow atoms will not pass through the capture region. In our setup, this effect is particularly pronounced, as the distance to the MOT is more than 30 cm.
In order to find a suitable field configuration, which does not reduce the end velocity of the atoms too much, the motion of atoms with different initial velocities in the light field

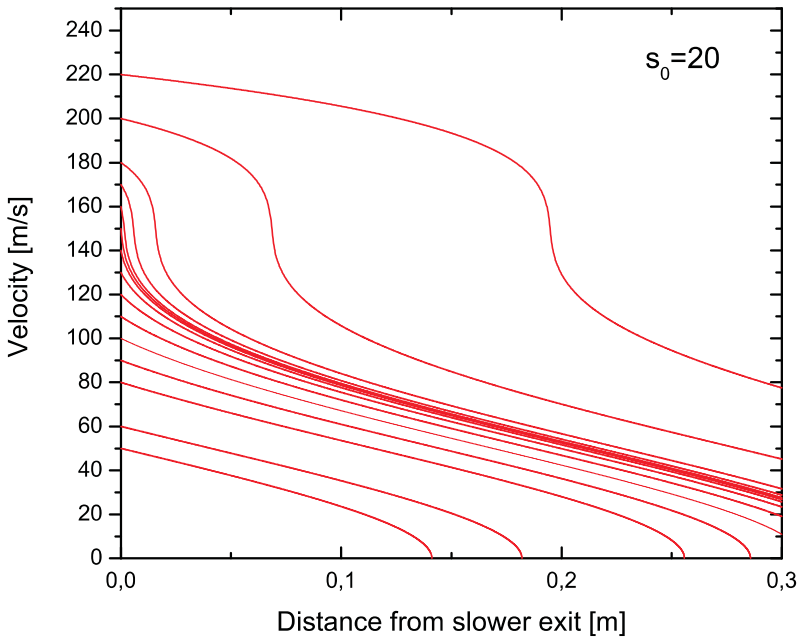

Figure 3.38: Simulated trajectories of atoms emerging from the Zeeman slower with different velocities. Because of their low velocity and the high saturation parameter, they experience a considerable friction force even under zero field conditions. At the standard slower detuning of δ=-224 MHz, resonance occurs at a velocity of 150 m/s.

of the slower beam (in absence of any magnetic field) was traced over a distance of 30 cm (Figure 3.38). The conclusion is, that for an optimum loading rate, the field configuration should be chosen such that the exit velocity v_{end} is quite above 100 m/s. In practice this is achieved by setting the current of the last (reversed) coil to zero, which indeed results in an increase in loading rate. The radial component of the MOT-field does not seem to have much impact on the slowing- and capture process. When reversing the coil-current, and thereby the direction of the magnetic field so that it would be in-line with the slower field, no change in loading rate was observed. Figure 3.39 shows trajectories for coil currents used in actual operation.

3.7.3 Lithium Oven

The thermal beam of lithium atoms required to feed the Zeeman slower is generated by an effusive oven. A resistively heated reservoir contains a few gramms of Li, which effuses through a small nozzle towards the experiment. The flux of atoms is conveniently controlled by the reservoir temperature, as it varies linearly with the equilibrium vapour pressure within the reservoir, as long as the condition for molecular flow through the nozzle is fulfilled. This is the case, as long as the mean free path of the atoms is larger than the nozzles dimensions. To avoid clogging of the nozzle by deposition of lithium atoms, it is heated to slightly larger temperatures than the oven resevoir itself.
A formula for the vapour pressure dependence on temperature of alkali metals is given

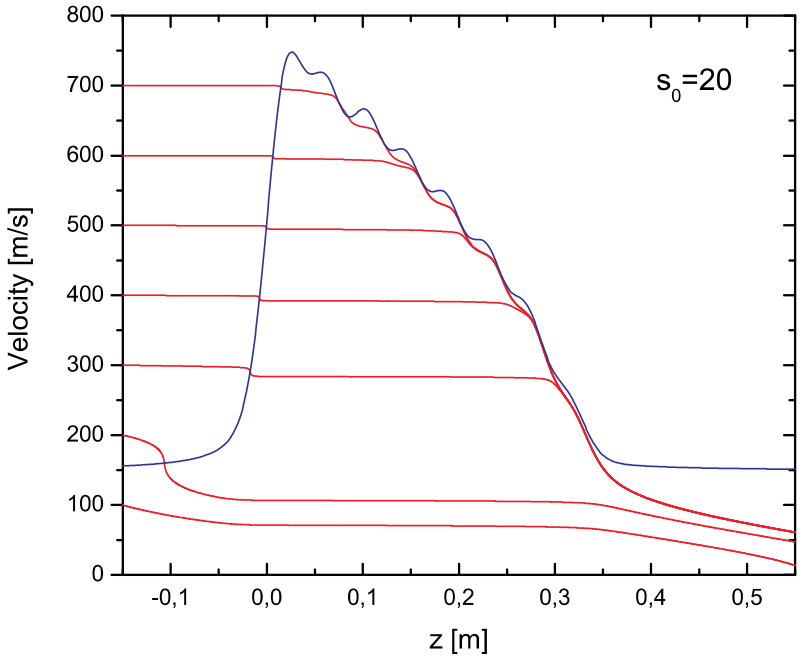

Figure 3.39: Simulated trajectories for currents as standardly applied in the experiment. The coil currents are (from entry to exit): 6.88 A, 5.82 A, 5.13 A, 4.64 A, 4.48 A, 4.32 A, 3.78 A, 2.73 A, 0 A.

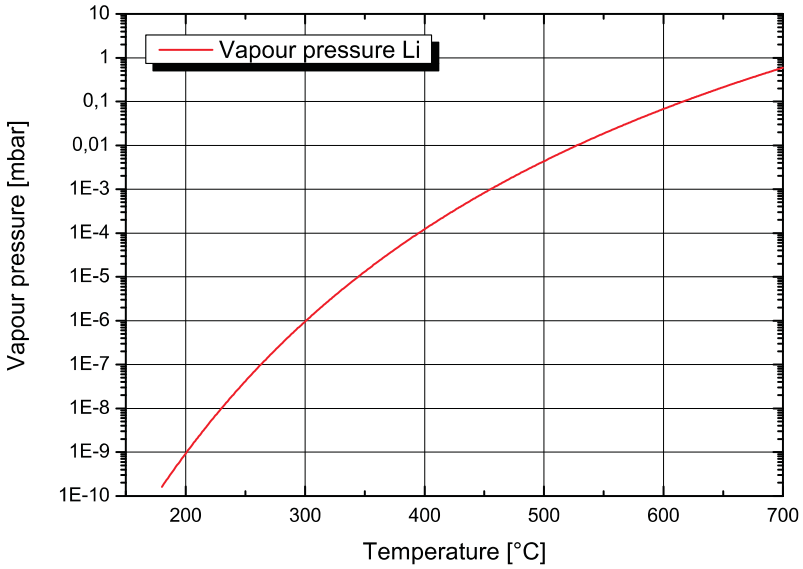

Figure 3.40: Vapour pressure curve of lithium.

by [Nes63]:

$$\lg p_{\mathrm{v}}[\mathrm{Torr}](T[\mathrm{K}]) = \lg A - B/T + CT + D \lg T. \tag{3.50}$$

For lithium, the coefficients are:

$$\begin{aligned} A &= 10.3454 \\ B &= 8345.574 \\ C &= -0.0000884 \\ D &= -0.68106. \end{aligned}$$

Fig. 3.40 gives the resulting vapour pressure curve, where the temperature is specified in °C and the pressure in mbar. Of the alkali metals, lithium has to be heated to the highest temperatures, to yield a sufficient flux of atoms from an effusive source. Nevertheless, the required temperatures in the range between 400°C and 550°C are quite moderate and no elaborate high-temperature oven constructions are needed.

CF-Oven

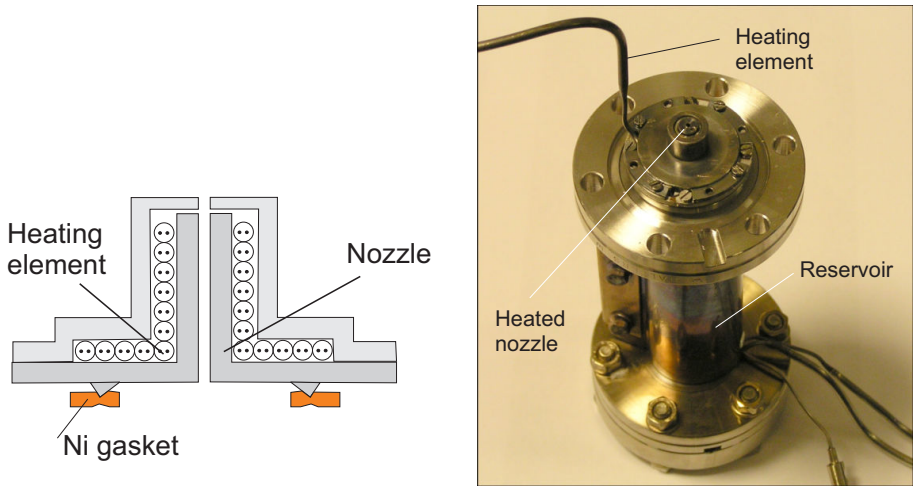

Figure 3.41: *Left:* Cut through the heated nozzle. *Right:* Photograph of the CF-oven.

For operating temperatures up to at least 500°C, an oven can be assembled of ordinary CF-parts, if gaskets made of nickel instead of copper gaskets are used for vacuum sealing [Sta05]. The oven developed for this experiment consists of a reservoir made of a steel tube of 10 cm length and a diameter of 3.5 cm. At each end a CF40 flange is welded on, one for attaching it to the cube chamber, the other one for refilling the oven without having to dismount it from the vacuum system (see Fig. 3.35). The CF40 flange, which connects to the oven chamber, has an additional CF16 knife edge and hole circle on its face to mount the heated nozzle (Fig. 3.41). Two THERMOCOAX bifilar heating elements were wound around the reservoir and tightly clamped to it by a stainless steel jacket. To avoid convective cooling and temperature gradients due to the large thermal mass of the refilling flange, the whole oven is packed in silica wool and wrapped with aluminum foil. The nozzle has a diameter of d=1 mm and a channel length of l=15 mm. According

to [Sco88], this geometry narrows the angular distribution of the effusing atoms to a cone with an angle of 5°in the regime of molecular flow, while at the same time the forward flux intensity is preserved. Thus the flux of atoms emitted into the solid angle of the capture region of the trap is not affected, but the number of atoms emitted into the vacuum chamber at large angles is much reduced. The nozzle temperature is adjusted independently by the current through the heating element coiled around it and can be monitored by a spot-welded type K thermocouple attached to the nozzle.
The oven provided reliable operation and the CF-components remained resealable even after heating to more than 500°C. The major drawback was the nozzle heating: After several days of operation at nozzle temperatures around 450°C, the heating elements showed a tendency to temporarily short-circuit, and finally burn. Without being heated separately, the nozzle quickly blocked within one day.

High Temperature Oven

To overcome this lack of reliability, the CF-oven was exchanged for an high-temperature oven, that had been originally used in producing a thermal beam of barium for electron spectrometry after combined laser and electron impact excitation [Nie98]. This oven was designed for continuous operation at temperatures higher than 800°C.
The oven itself is made of molybdenum because of its chemical resistivity, low thermal expansion coefficient and low magnetic permeability. The reservoir and the nozzle part are tightly toleranced and are sealed by pressing the parts together. Ruby balls provide thermal insulation against the front- and base plate pressing the oven parts together. The heating elements have been refurbished and consist of a 0.5 mm tantalum wire guided through insulator pearls (3 mm diameter, 4 mm length, 2 holes) of alumina. In analogy to the bifilar heating elements, the wire passes each insulator twice to avoid stray magnetic fields by the heating current. An oven temperature of 570°C is reached for currents of 3.2 A (6.6 V) applied to the nozzle heating and 3.3 A (10.2 V) to the oven body.
This oven enables risk-free operation at temperatures beyond 500°C, which has proven helpful in increasing the loading rate of the trap. Instead of a channel the nozzle is merely an aperture of 1 mm diameter. Thus a larger contamination of the oven chamber with lithium is observed and the lithium stored in the reservoir is depleted more quickly. A schematic of the oven construction is depicted in Fig. 3.42.

3.8 Experimental Control

In contrast to a standard reaction microscope, operating with a continuous jet of target atoms, conducting experiments with the MOT requires an elaborate timing of the different experimental phases with an accuracy of at least 10 μs. For a simple adaption of the trap's operating parameters, for example the off-time of the trap, the strength of the magnetic field gradient or the loading time of the trap, to best fit the needs of the measurement performed, these should be accessible 'on-line' from a user-friendly interface. It is also

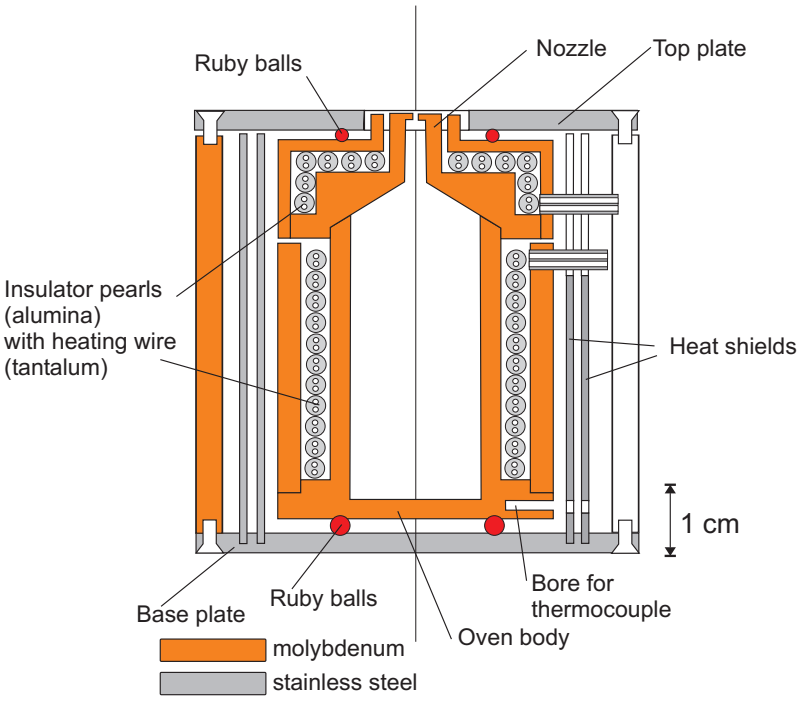

Figure 3.42: Schematic of the high-temperature oven (after [Nie98]).

desirable, to synchronize the switching of the trap field with an arbitrary projectile trigger with the same temporal resolution.
For this purpose, an ADwin Gold real-time sequencer system is employed to control all relevant experimental parameters. This system consists of an independent real-time controller that provides a number of analog and digital input and output channels. It is programmed via a standard personal computer and can also exhange data with the PC for reading out measured data or changing parameters of the systems output to the experiment. This section describes the integration of the ADwin system into the experiment and the user interface based on LabView.

3.8.1 The ADwin-System

The ADwin Gold DA system is an complete microcomputer with an 32bit-processor (Analog Devices SHARC ADSP 21062) and 16 MB of memory. In principle it operates independently from any PC-based system and generates output signals, acquires signals from the analog inputs and performs arithmetic operations on them (in conjuction with the analog output channels e.g. digital regulators can be implemented) and responds to external trigger signals. An Ethernet-interface connects the system to a Windows-PC, which is needed for booting, programming and reading out data or transferring the parameters of the experimental sequences to the ADwin.
It provides 8 analog output channels, that can generate voltages between -10 V and + 10 V (25 mA ouput current, enough to drive 50 Ω loads) with 16 bit resolution and 8 analog

inputs covering the same voltage range and either 12 bit (0.5 μs sampling time) or 16 bit DAC-resolution (5 μs sampling time). 32 bidirectional digital channels (DIO) working with TTL logic levels are available, of which 16 are configured as inputs and 16 as outputs. The ADwin is programmed via a programming language called ADbasic. The programs are written with a special editor on a PC and then compiled and transferred to the ADwin for execution. Processes, which demand exact timing, are best implemeted as a so called high priority process. For a program which updates the output channels in well defined time intervals, a cycle time is chosen, which could be as low as 1μs. This means that the programm (in the following called process) is called in a strict timing scheme, i.e. in our case every 10 μs. Compared to conventional programming, one has to take care, that the program is structured such that the complete instruction block to be executed, after the process is called, can always be processed in less than the cycle time. This is necessary, because within the cycle of 10 μs enough processor capacity and computing time must be available to complete other internal processes, which manage the communication between the ADwin and the PC. If this is not the case, timing conflicts between the different processes emerge and the behaviour of the system will become rather indeterministic and unstable.
One of the benefits of the ADwin system is, that parameters used in a program can be

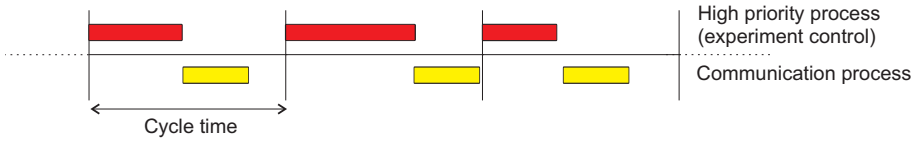

Figure 3.43: Illustration of real-time process timing on the ADwin system.

updated directly from the controlling PC, even during the program/sequence executes. For example, if one notices, that the off-time of the trapping field is possibly too long, the variable defining this time can be modified within the running program, without having to stop the measurement, edit and compile the program and to start the sequence anew. In this experiment, a LabView graphical user interface allows to conveniently set the parameters of the experimental sequence.
The following devices are presently controlled by the ADwin system:

1. MOT-field current control (Analog Out)
2. MOT-field on/off (DIO)
3. CAMAC INHIBIT (DIO)
4. Slower field on/off (DIO)
5. Oven shutter open/closed (DIO)
6. CCD camera trigger (DIO)
7. AOM cooling laser on/off (DIO)

8. AOM repumper laser on/off (DIO)
9. AOM slower laser on/off (DIO)
10. Oscilloscope trigger (DIO)

Further devices of the setup could be interfaced to the ADwin system, for example the voltage-controlled oscillators (VCO) defining the laser frequency shift at the AOMs, which would greatly facilitate systematic optimization of the MOT parameters. Additionally the RF power applied to the AOMs and thus the amount of diffracted laser power could be varied by variable attenuators (MINI CIRCUITS ZAS-1) remote controlled by the ADwin system.

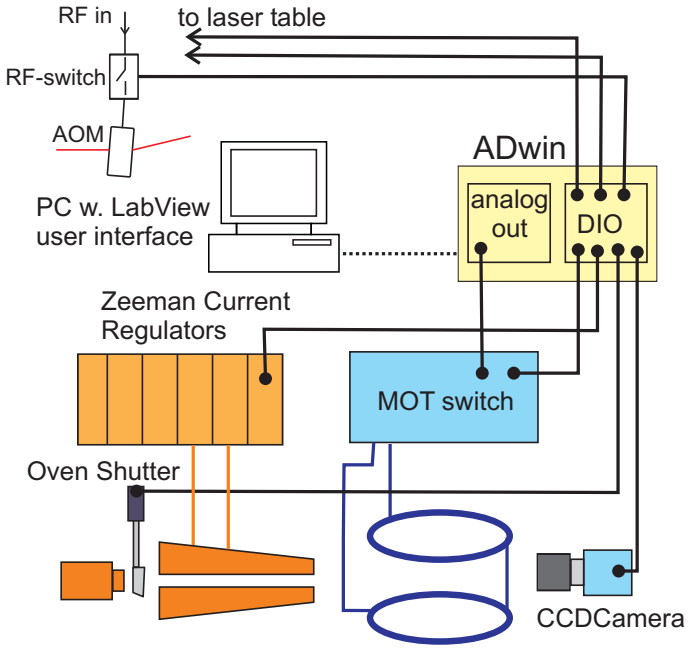

Figure 3.44: Devices connected to the experiment control system.

3.8.2 User Interface

At present, two main programs are at hand: One holds continuously the set values for the analog and digital outputs and changes the state of an output channel only 'at the push of a button' on the LabView front panel. It is mainly used for adjustment and optimization purposes.
The other program was specifically designed for the needs of the multiphoton ionization measurements: It consists of two nested loops: The outer loop controls the loading process of the trap, whereas the inner loop controls the measurement procedure, which is repeated several hundred times. The parameters of three subsequent switching steps, i.e. the switching times and the output states and voltages of the inner and outer loop are configurable from the front panel. If more steps are required, as in the case of the temperature

measurement, these have to be implemented directly in the ADBasic program.
Exploiting synergies with the ^{6}Li degenerate Fermi gas project of S. Jochim, which will also use a LabView/ADwin based system to control the experimental sequences, an extended version of the experimental control system is being developed in collaboration with the electronics departement of MPI-K. The new software will enable experimental sequences with an arbitrary number of steps and the generation of waveforms at the analog outputs.

Chapter 4

Characterization of the Lithium Target

After reliable and reproducible operation of the lithium-MOT had been established, a series of measurements was carried out to determine the basic parameters of the trap, such as atom number and temperature and to elicit the potential for their optimization. Of particular interest was the response of the trap to the periodic switching of the magnetic field under different conditions and the question, which timing schemes could be applied to guarantee most efficient use of the target atoms.

4.1 Diagnostic Methods

A lithium MOT consisting of only 10^5 atoms is already easily recognized by the bare human eye. As the trapped atoms are highly efficient light scatterers, information about fundamental MOT properties can be easily obtained by monitoring the emitted fluorescence light. The most basic method is the registration of the emitted fluorescence by a sensitive photodiode, which provides information about the total number of the emitting atoms and its variation with time, providing convenient access to loading and decay rates. By imaging the MOT with a CCD-camera, besides the total fluorescence, additional information about the spatial extent of the cloud is gained, which allows the extraction of the density profile. When short exposure times of a few hundred microseconds are sufficient to yield enough signal to noise ratio, the dynamics of the MOT on a timescale of milliseconds is accessible, such as its ballistic expansion when the confining potential is switched off. This possibility is exploited in the temperature measurement, where the rate of expansion of the cloud is determined from a sequence of pictures.
Though more advanced imaging technologies for the observation of trapped atoms exist, which are widely used to probe the properties of ultracold degenerate quantum gases, such as absorption imaging or phase-contrast imaging [Ket99], the plain fluorescence based methods deliver enough information for a relatively large sample of atoms like the MOT. A minor drawback is an inherent uncertainty on the relation between scattered, respectively

detected, fluorescence light and the number of atoms, as it is quite sensitive to the experimental conditions, such as the detuning and saturation parameter of the laser beams. Especially for lithium the atom number is not easily calculated, because the excitation and decay rates from and to both ground states and their population ratio have to be taken into account. Commonly, absolute atom numbers (and derived quantities such as density) are specified with an accuracy of an overall factor of 2, if much care has been taken in calibration and modeling of the detection system and the atoms' response to the laser field, the relative error can be reduced to 20-30% (see section 2.2.3).
The fluorescence detection systems used in this experiment are described in the following.

4.1.1 Photodiode

A photodiode provides a convenient tool for on-line monitoring of the trap population and loading rate, especially for aligment and optimization purposes by just connecting it to an oscilloscope. For this experiment, a high sensitivity large area photodiode of type HAMAMATSU S-1336-44BK with an active area of 3.6×3.6 mm^2 is used. Light levels at the diode of 1 nW have to be detected. The diode has a sensitivity of 0.37 A/W at a wavelength of 670 nm, so to read out the signal with an acceptable signal-to-noise ratio, the diode is directly interfaced to a home-built transimpedance amplifier with a transimpedance gain (current-to-voltage conversion factor) of 2.5×10^8 V/A, both built into a compact metal housing to shield the circuitry from enviromental electronic noise.
The circuit is made of an AD627 low noise operational amplifier, wired in the current-to-voltage converter configuration with a 250 MΩ resistor in the feedback loop.
A 25.4 mm diameter lens with a focal length f=80 mm images an area of nearly 10×10 mm^2 in the MOT plane onto the active surface of the diode and is mounted in an xy-translator to optimize the signal. A bandpass interference filter with a central wavelength of 671 nm and a FWHM of the transmission curve of 10 nm eliminates most of the room light and other sources of non-resonant stray light. It has a specified transmission of at least 60% at the center wavelength and is mounted directly in front of the diode.
The complete detector assembly including the filter has been calibrated independently: The diode was irradiated with well controlled light powers from 10 nW to 100 nW. This was achieved by coupling a beam from the master laser into a single mode optical fiber. By intentional misalignment, the output power at the fiber exit, which was placed directly in front of the diode, could be varied in a controlled manner between 10 nW and 150 nW. The incident light power was measured with a OPHIR Nova II powermeter with a silicon sensor. Though every care has been taken to reduce the influence of any straylight, we estimate the power measurement to be reliable to ±5%. A linear fit through the measured values gave a calibration factor of 60.53 mV/nW, which is in fair agreement with the theoretical value of 54.57 mV/nW when calculated with the specifications of the filter and the diode.
The fluorescence signals obtained by the photodiode exhibits noise proportional to the light/signal level, with a peak-to-peak noise envelope of about 10% of the signal level, thus

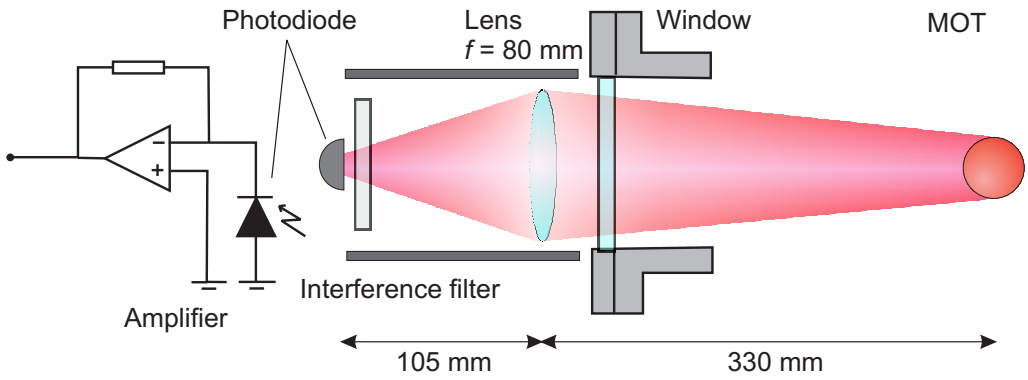

Figure 4.1: Setup of the fluorescence monitor diode. A 1"-diameter lens covers almost the whole solid angle available for light collection at the CF40 window port (30 cm away from the trap) and images it to the photodiode.

the obtained signal traces are usually smoothed before further processing. Alternatively, a lowpass-filter can be inserted downstream. The high susceptibility to noise is presumably due to the extremely high transimpedance gain and can hardly be avoided. Attaching a similar photodiode to a commercial amplifier with a maximum gain of 10^8 V/A produced even higher noise levels.

4.1.2 Fluorescence Imaging

The second diagnostic tool is a CCD camera of type Pixelfly QE (PCO IMAGING). This camera has a 2/3"-CCD sensor with a resolution of 1392×1024 pixels and a quantum efficiency of 45% at a wavelength of 670 nm. The image data is read out with 12 bit dynamic range, corresponding to 4096 intensity levels. A macro lens with focal length f=50 mm and optical aperture of 12.5 mm ($f/\#$=4), placed directly at the viewport images the MOT onto the chip. The camera can be triggered by the camera control software or externally via a rising edge TTL signal from the experimental control system.

Energy Calibration of the CCD Camera

The camera's sensitivity has been calibrated, to be able to determine the atom number directly from the MOT images. Therefore, the chip was irradiated with a low power laser beam of 671 nm wavelength of known intensity from a single-mode fiber. The gaussian beam was aligned in a way that it was completely imaged by the chip. Images were then recorded for different combinations of laser powers and exposure times. Assuming a linear and homogeneous response of the sensor all over the chip size, which is well fulfilled in the case of CCD-arrays, the pixelsum (sum of the bit-values over all pixels) is then proportional to the energy incident on the chip during the exposure interval. This procedure has been carried out for different laser powers between 90 nW and 3 μW with exposure times from 7 ms down to 300 μs. These are also representative values when capturing images of

the MOT. For calibration, first a background image (image taken with the laser turned off) is subtracted from the laser image to remove any offset due to residual stray light (which made up about 10% of the total pixelsum). Then the pixelsum of the image is calculated. To account for intensity fluctuations in the laser output, the average pixelsum of 20 pictures is calculated for each combination of laser power and exposure time, i.e. for each value of incident energy. A linear fit through the measured data points then provides the calibration factor η that relates the bit-value of one or several pixels to the collected light energy. For the low gain setting the value

$$\eta_{\text{low}} = 3.25 \cdot 10^8 \frac{\text{counts}}{\text{nJ}} \tag{4.1}$$

is obtained, in the high-gain mode, which is routinely used for MOT imaging, the conversion factor is

$$\eta_{\text{high}} = 7.62 \cdot 10^8 \frac{\text{counts}}{\text{nJ}}. \tag{4.2}$$

Spatial Calibration

By calibration of the imaging scale, the spatial extent of the MOT and its density distribution (or rather its projection along the camera's line of sight) can be determined quantitatively. To obtain a reliable value for the imaging scale of the camera system, the macro lens focus was adjusted to produce a sharp image of the MOT (the depth of field is less than 1 cm). Then a caliper was placed in the focal plane. From the image taken, the mm-gauge was cut out and projected onto the y-axis of the image (cyan line on the left hand side of figure 4.2). From the average distance in pixels between neighbouring minima of the resulting dataset, the imaging scale in mm/pixel was determined to be 38.0 μm/pixel. Though only a tiny fraction of the CCD-chip is used to capture images of the trap, enough information about the shape and the density distribution of the MOT is gathered: Since the atom cloud exhibits a smooth Gaussian-like shape with some random

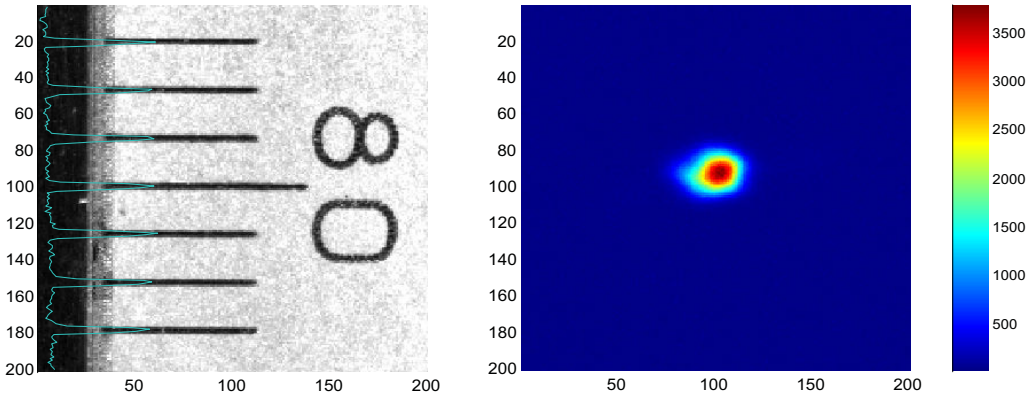

Figure 4.2: Both images show a section of 200×200 pixels of a full CCD-image. The left hand side image shows the mm-scale of a caliper, used to extract the imaging scale. The picture on the right shows a typical MOT with $7.0 \cdot 10^6$ atoms. The colourbar maps the light intensity in units of 12-bit grey-levels.

fluctuations in width under ordinary conditions, there are no features much smaller than the overall dimension of the MOT to be resolved. The concentration of the incident light on relatively few pixels enables very short exposure times of less than 1 ms, while still preserving an acceptable signal-to-noise ratio. This is of particular importance for the temperature measurements.

4.2 MOT Characteristics

Utilizing the MOT as a target for scattering experiments, the properties of interest in order to specify the 'performance' of the target are its density distribution and the area density (cross section), the temperature and its spatial extent.
Compared to a supersonic jet target, a MOT target can be varied in density over many orders of magnitude without much change in the other key properties, i.e. its temperature and size. Concerning density there is virtually no lower limit, the MOT can always be made arbitrarily thin by reducing the loading rate, loading time or reducing the field gradient. This capacity was of particular usefulness for adjusting appropriate event rates in the multiphoton ionization measurements.
For the study of other processes with low ionization cross sections or low projectile fluence, a dense target is desirable to maximize the event rate. Supersonic jets have typical densities of 10^{11} to 10^{13} atoms/cm^3, which are hardly achieved with a MOT. An optimization for the one or other parameter, e.g. temperature has not yet been done, since for the measurements performed this was not needed, but could be done in a straightforward (but time-consuming) manner with the implemented diagnostics. In the measurement presented in the following, it was tried to push the atom number and target density to its limits.

4.2.1 Loading Rate and Atom Number

The axial MOT field gradient was 9.5 G/cm. The red detuning of the laser frequencies from resonance that maximized the fluorescence signal was found to be $\delta = (-4 \pm 0.5)\Gamma$ for both the cooler and the repumper beam. To verify, that the maximum in the observed fluorescence signal on the photodiode corresponded indeed to a maximum in atom number, the trap was continously loaded for different detunings δ of both lasers. Then the detuning was suddenly switched to the reference value $\delta = -2\Gamma$ for the cooling laser and $\delta = 0$ for the repumper, which results in an instant increase of the fluorescence signal due to the increased scattering rate. The setting for the maximum atom number is found, when the fluorescence signal after the jump in detuning is highest.
This choice of parameters is in agreement with the measurements of Schünemann *et al.*, who presented an extensive characterization of their lithium MOT. They found, that atom number trap and loading rate were maximized for red detunings of both beams between -5Γ and -3Γ [Sch98a].

As discussed in section 2.2.3, a reliable determination of the atom number from the fluorescence emitted by the trapped atoms alone is not possible for a lithium-MOT. In the sense of providing a maximum conservative estimate for the atom number, the figures given here were calculated for a fully saturated transition, i.e. a scattering rate per atom of $\gamma/2$.
The measurement was performed with maximum powers of 50 mW in each of the radial beams and 45 mW in the axial beams. With a beam diameter $2w_0 = 12$ mm, this gives a peak intensity of about 88.4 mW/cm^2 in the center of a single beam. All six beams together lead to an on-resonance saturation parameter of s_0=200 at the location of the MOT, if the two-level saturation intensity is employed, and of $s_0 = 97$ for the transition-averaged saturation intensity $\langle I_s \rangle$ as given by equation (2.40). Taking into account the laser detuning of 4 linewidths from resonance, equation (2.2) yields a scattering rate of $0.75\frac{\gamma}{2}$ for the first case and $0.60\frac{\gamma}{2}$ for the latter case. Considering the multilevel structure of the lithium atom, the real atom number could be up to a factor of 1.6 higher and with it the other quantities derived from the absolute atom number. Under otherwise optimized

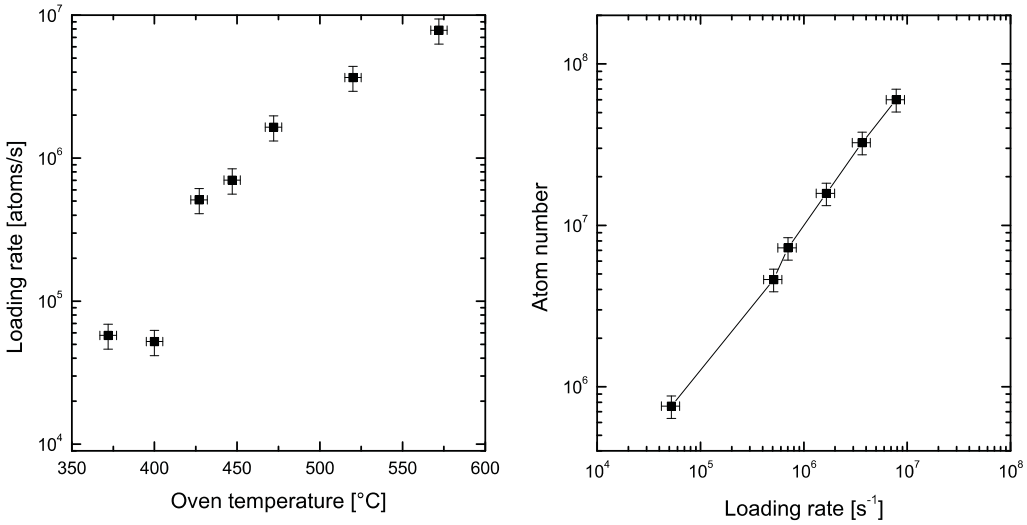

Figure 4.3: *Left*: Achievable loading rate in dependence on the temperature of the lithium effusive oven. *Right*: Equilibrium atom number vs. loading rate.

conditions, the main handle to bring about an increase in atom number and loading rate, is to increase the flux of atoms from the oven by increasing its temperature. The loading rate is directly extracted from the loading curves: For small times the initial slope of the loading curve directly yields the loading rate L, as can be seen from the derivative of (2.23). The left hand graph of Figure 4.3 shows the loading rate in dependence of the oven temperature and proves a steady increase in loading rate with the oven temperature. At a temperature of 572°C, a loading rate of $7.8 \cdot 10^6$ s^{-1} is achieved. According to (2.22), a linear increase with loading rate is expected, as evident from Fig. 4.3.
The maximum observed atom number was $6 \cdot 10^7$. The error bars for the atom number only contain the uncertainty in the solid angle covered by the fluorescence light collecting

elements (lens of photodiode, macro lens of CCD-camera), which is the greatest source of experimental error. Any model-dependent systematic error is not included and the given results should be viewed as a lower bound on the atom number.
There are two remarks to be made:
Firstly, the measurements had to be performed under unfavourable vacuum conditions with background pressures of $p = 1.8 \cdot 10^{-9}$ mbar and measured loss rates of $R \approx 0.15$ s^{-1} (trap lifetime $\tau \approx 6.6$ s). The maximum atom number can be much enhanced by a lower background pressure. Since a pressure of less than $5{\cdot}10^{-11}$ mbar has been achieved during the multiphoton ionization measurements, a significantly higher atom number should be possible (equation (2.25)) under these conditions. This will also help to reduce the experimental cycle time, as the linear increase of the loading curve before saturation sets in (see Fig. 4.4) extends towards higher atom numbers. One must, however, be aware of the fact that increasing the oven flux by a higher temperature produces predominatly fast, hot atoms that cannot be captured by the Zeeman slower and will induce additional collisional losses upon passing through the MOT-region. The time constant of the loading curve at an oven temperature of 572°C is $\tau_{\mathrm{load}} = 5.5$ s (Fig. 4.4), hinting at the additional losses through the thermal beam. The loss rate due to the lithium beam is then calculated as $R_{\mathrm{beam}} = 0.030$ s^{-1}, i.e. the limit of the trap lifetime imposed by the thermal beam is $\tau_{\mathrm{beam}} = 33.3$ s.
Secondly, the maximum loading rate of $7.8 \cdot 10^6$ s^{-1} is rather low. Schünemann *et al.* report a loading rate of $L = 6 \cdot 10^7$ s^{-1} at an oven temperature of 500°C, where in our experiment a rate of about $3 \cdot 10^6$ s^{-1} is expected. This is at least partly due to the large distance from the slower exit to the trap region, which is 34.5 cm in our setup. In the experiment of Schünemann *et al.*, this distance was only 17 cm. Additionally, the radial gradient field of the MOT coils employed (radius of 24 cm) was merged with the slower field [Eng97]. In our setup, this is not possible due to the much smaller intra-vacuum coils and the larger dimensions of the chamber. There is no possibility to bring the slower closer to the center of the chamber wihtout obstructing other axes of access.
The large distance between the end of the deceleration distance and the trap has dramatic impact on the loading rate: The slower reduces the atomic velocities only along the beam direction, while the transversal degrees of freedom remain unaffected. The slow atoms leaving the Zeeman slower will have a long time of flight to reach the MOT, leading to a drastic widening of the beam in the transversal plane, so that only a small fraction of the slowed down atoms will actually traverse the capture region of the MOT.
If higher loading rates are desired, implementation of a transversal laser cooling and beam collimation stage at the exit of the Zeeman slower should be considered, e.g. in form of a transversal Doppler cooling section [Tem02], 2D-MOT [Sch02], [Die98] or magneto-optical compressor (MOC) [Tem02]. This will drastically enhance the flux of slow atoms through the capture area of the trap.
No signs of an non-exponential decay due to two-body collisions were observed in the decay curves. These effects are on the one hand partly suppressed due to the deep trap (see section 2.1.4), on the other hand they are most likely masked by the high one-body loss

rate: According to data measured by Ritchie *et al.* [Rit95] and Kawanaka *et al.* [Kaw93] for high trap laser intensities, the two-body loss coefficient β lies below 10^{-12} cm^{-3}.

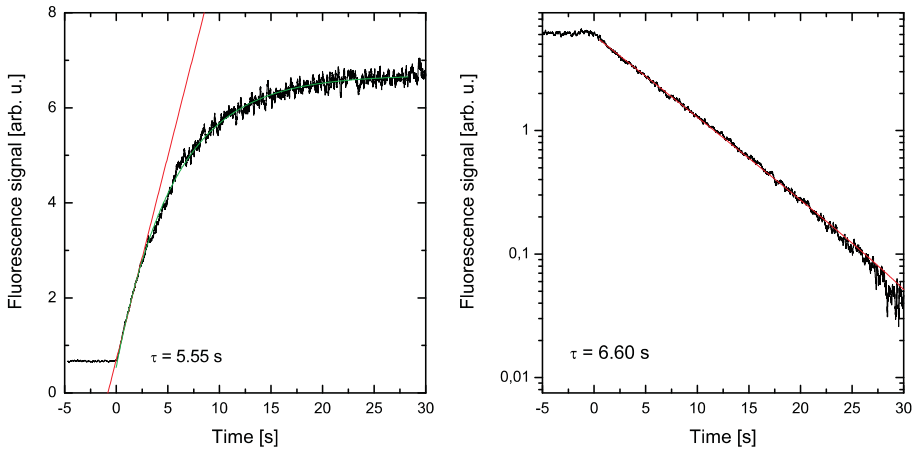

Figure 4.4: Typical loading curve (*right*) and decay curve (*left*) of the trap population (shown on a logarithmic scale), registered by monitoring the trap fluorescence with a photodiode. The red line in the decay curve is a fitted exponential decay function. There are no significant deviations, e.g. due to two-body losses, visible. Both curves were measured at a background pressure of $1.8 \cdot 10^{-9}$ mbar and an oven temperature of 570°C. The green line in the loading curve is a fit with equation (2.23). The slope of the red line gives the loading rate. The time constant of the loading curve is reduced compared to the decay constant due to collisions with thermal atoms from the loading beam.

4.2.2 Temperature

The most accurate method to measure the temperature of a magneto-optical trap, is the so-called time-of-flight method, where the size of the cloud is monitored during free expansion. After the MOT has been loaded to the desired atom number, the magnetic field and the laser are instantly switched off. After a time t, the cloud is illuminated for 100 μs by the MOT-lasers and an image is recorded by the CCD camera. This sequence is repeated a number of times, where t is increased in steps of 100 or 200μs. The recorded pictures are then analyzed by a MATLAB-script, which extracts the widths Σ_x and Σ_z of the clouds from the images. The density of the cloud quickly reduces upon expansion and with it the signal-to-noise ratio. To reconstruct the Gaussian width of the recorded column density distribution, the pixels are summed up along the dimension perpendicular to the one to be measured, which, assuming a Gaussian distribution of the cloud, does not change the width of the distribution, but much enhances the signal-to-noise ratio. The program then determines the Gaussian widths of the cloud at each timestep by a least-squares-fit. From the temporal variation of these widths the temperature is extracted.
The evolution of the expanding cloud is well described by a convolution of the initial density distribution

$$n(x_i, t = 0) \propto \exp\left(\frac{x_i^2}{2\sigma_i(t = 0)}\right) \tag{4.3}$$

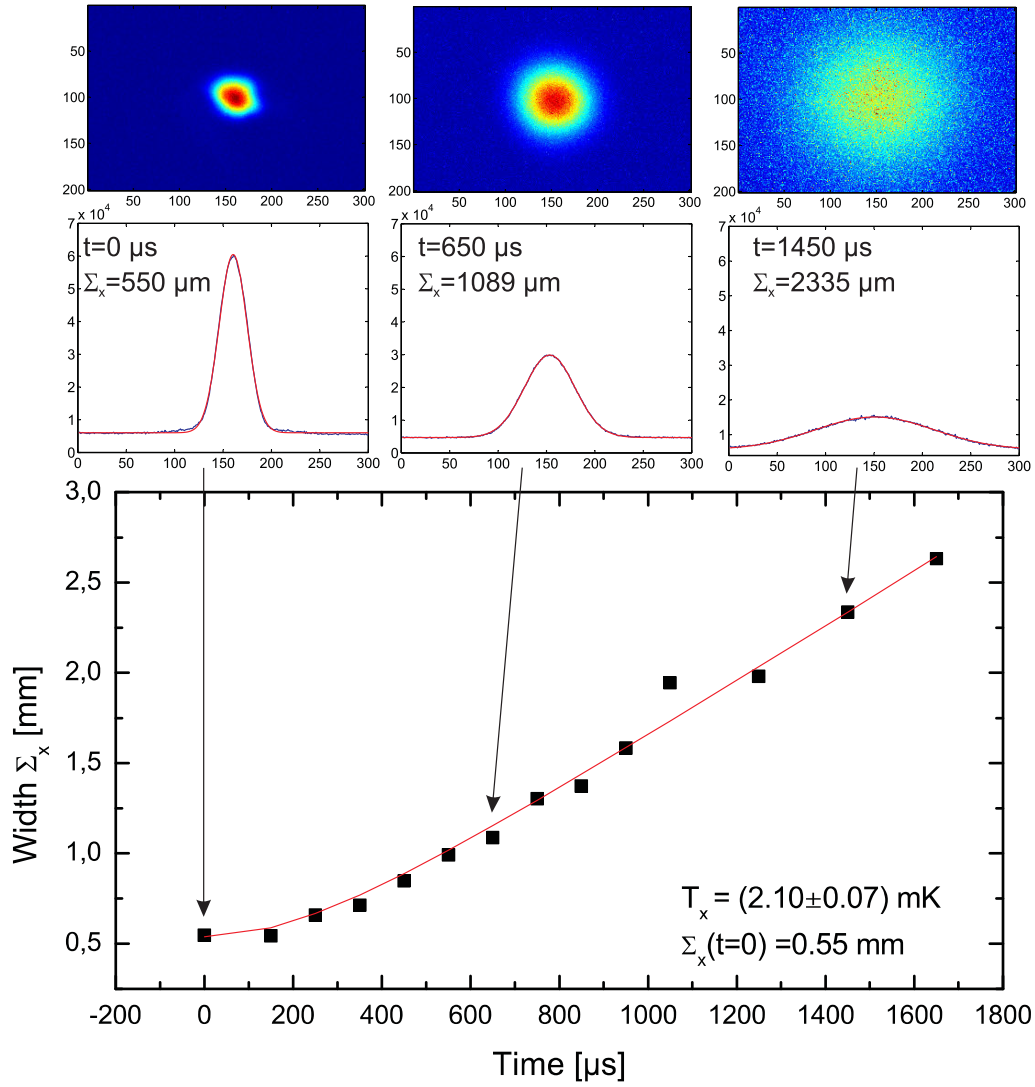

Figure 4.5: Illustration of the principle of the temperature measurement. *Top row*: Raw fluorescence image of the MOT (intensity is colour coded) in the trap (*left*) and after 650 μs (*middle*) and 1.45 ms (*right*) of ballistic expansion (scale is in pixels). *Middle row*: The above density distributions integrated along the vertical dimension (blue curves) and fitted gaussian distribution (red curves). The scale is again given in pixels. *Bottom panel*: Widths Σ_x of the density distribution as a function of expansion time. The red curve is a fit of (4.4) to the data points from which the temperature is determined.

with the time dependent density distribution of an expanding atomic 'point source' of atoms with a velocity distribution $n \propto \exp\left(-\frac{v_i^2}{2\sigma_{v_i}^2}\right)$ and $\sigma_{v_i} = \frac{1}{2}k_{\mathrm{B}}T$:

$$n(x_i, t) \propto \sqrt{\sigma_i(t=0) + \frac{k_{\mathrm{B}}T}{m}t^2}. \tag{4.4}$$

The temperature of the MOT along a particular axis is obtained by fitting function (4.4) to the experimentally determined widths $\Sigma_x(t)$ and $\Sigma_z(t)$. Figure 4.5 illustrates the principle of the temperature measurement by the time-of-flight method. The left hand graph of

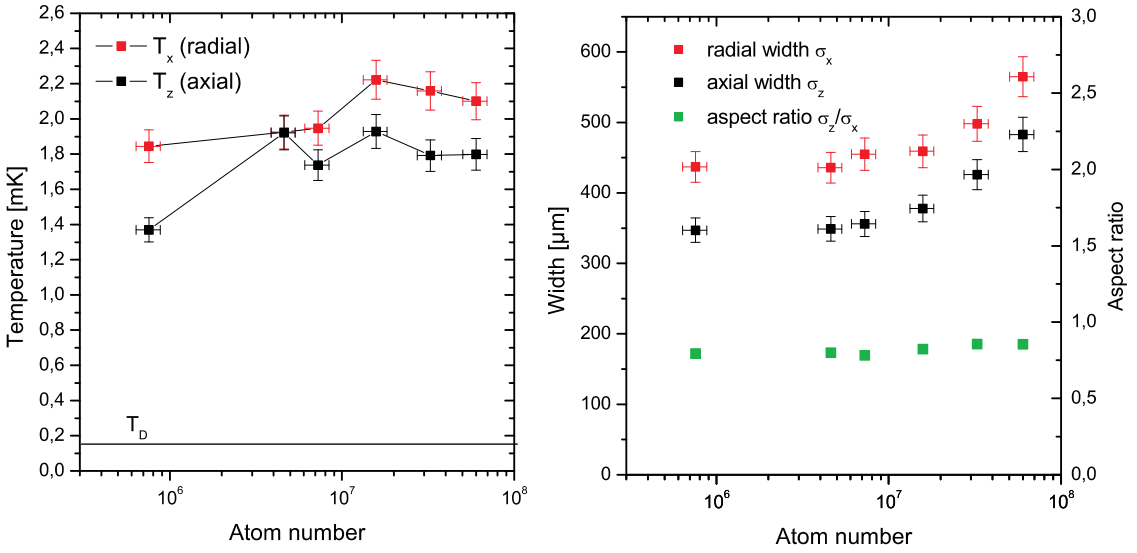

Figure 4.6: *Left:* Temperature of the MOT. The expansion rates in the radial and axial direction may differ from each other due to differences in the optical density of the cloud along the different axes and are assigned a temperature of its own. *Right:* Spatial extent of the Gaussian shaped cloud, σ_x, σ_z are the $1/\sqrt{e}$ half-widths.

Figure 4.6 gives the temperature along the radial direction T_x and the axial direction T_z (radial and axial with respect to the symmetry axis of the MOT's magnetic field). Under the chosen conditions, the temperature turned out to be rather high and did not notably depend on the atom number, i.e. it has its origin in the chosen set of laser and trap parameters. For a red detuning of 4-5 Γ, Schünemann *et al.* measured temperatures in the range of 1 mK and 1.5 mK, whereas temperatures in the 300 mK range are achieved for red detunings of 1-3 Γ. The extremely high laser intensities applied might be a source of additional heating in our measurement. The radii of the trap (right hand side of Fig. 4.6) are likewise not strongly affected by the atom number. In accord with the data given in [Sch98a], we find that at large laser detunings, the trap stays in the temperature-limited regime for populations up to at least 10^7 atoms. This means, that the density distribution is still determined by the Boltzmann-distribution of the atoms in the trap's potential and a blow-up of the trap due to multiple scattering of near-resonant photons plays no major role, since the cloud is still transparent to the detuned photons.
The relatively high MOT-temperature can still be viewed as uncritical in view of recoil-ion momentum resolution: A temperature of 2 mK leads to a momentum spread of $\Delta p = 0.008$ a.u., compared to 0.003 a.u. at $T = 300$ μK for temperature optimized lithium MOTs, which is both considered to be below the resolution of the spectrometer.

4.2.3 Target Density

As expected from the above considerations about the dependence of the trap volume on the atom number, the peak density n_0 increases almost linearly with atom number and

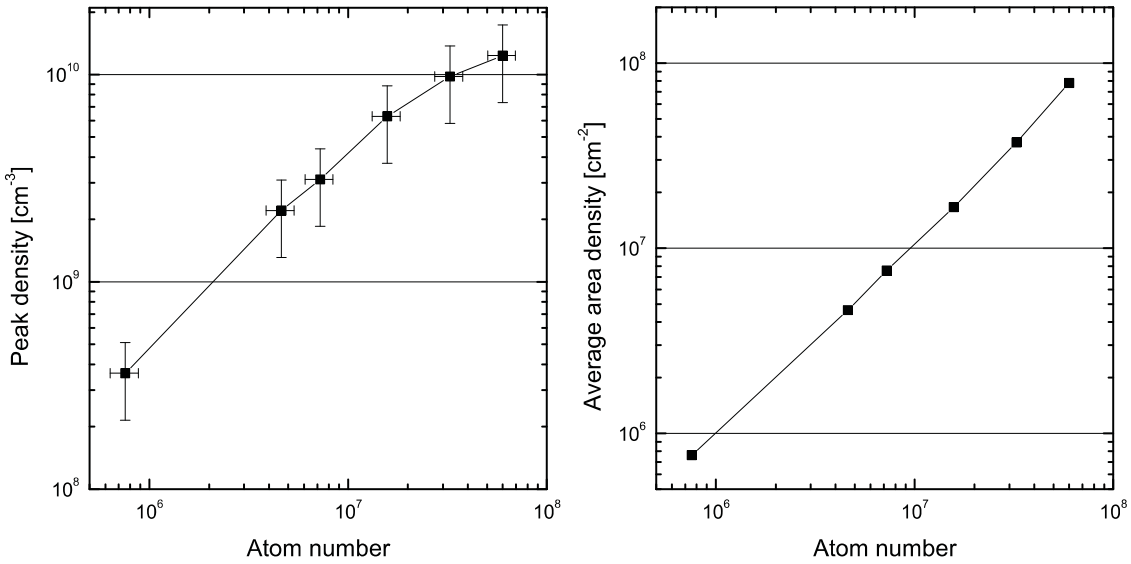

Figure 4.7: *Left:* Variation of peak density of the atom cloud with the number of trapped atoms. *Right:* Average number of atoms per cm^2 for the central region of the target ($\approx \sigma_y \sigma_z$) as seen by a projectile beam.

shows few signs of saturation (Figure 4.7). For an estimate of the target's area density, e.g. to calculate its interaction rate with a somewhat extended electron or ion beam (typical diameters 1 mm), an effective interaction volume with an cross section of $\pi\sigma_x\sigma_z$ is assumed. The average column density along the projectile direction (one of the radial directions) of this volume is also shown in Figure 4.7.

4.3 Recapture Efficiency

One of the main features of the experimental setup is the capability of rapid switching of the magnetic field. It is of particular interest, to quantitatively analyze the behaviour of the MOT, when the magnetic field is switched for data acquisition, especially in order to determine the experimental parameters that would enable most efficient use of the target. In the series of measurements presented here, the switching sequence was applied with increasing number of cycles, from 5 cycles to as many as 3000 cycles. At the beginning and end of each release-recapture run, an image of the MOT was recorded, to determine the ratio between initial and final atom number in order to extract the fraction of recaptured atoms.

The parameters that were varied to test for their influence on the recapture efficiency, are the release time, during which the magnetic field and the lasers are turned off, and the recooling time, when the atomic cloud is recaptured by ramping up the magnetic field and equilibrates again in the trapping potential. Measurements were conducted for two different diameters of the MOT-laser beams (6 mm and 12 mm). Additionally, the possibility

of shining in the trapping lasers during the release time to slow down the expansion of the cloud by creating an optical molasses was tested. However, this method is not applicable in the presence of the magnetic electron extraction field of the reaction microscope.

4.3.1 Release Time

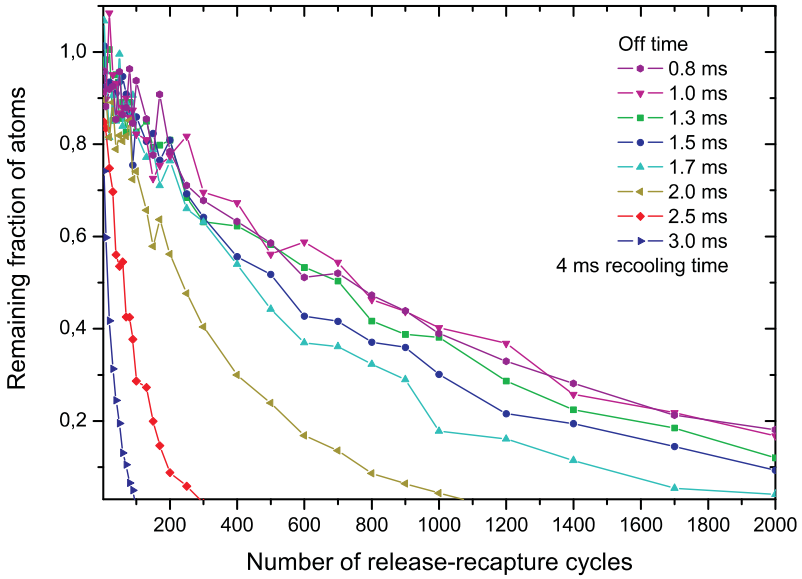

Figure 4.8: Fraction of recaptured atoms plotted vs. the number of switching cycles for a beam diameter of 12 mm.

Figure 4.8 plots the fraction of atoms remaining in the trap against the number of release-recapture cycles. The measurement has been performed with the trap loaded to about $7.5 \cdot 10^6$ atoms at a temperature of 2 mK and laser beam diameters (2 times the waist radius) of 12 mm. The off-time is defined by the time interval, in which the lasers and the trap field are shut down. At the end of the off-period, the lasers are turned on again and the MOT-field is ramped up with a risetime of 500 μs to recapture the atomic cloud. The time interval from the instant, where the ramp starts, to the point, where the field is ramped down again, is defined as the recooling time. In this measurement, a recooling time of 4 ms has been chosen. The result looks quite promising: When the off times are below 1.7 ms, over a thousand switching cycles can be performed, without reducing the atom number dramatically: the trap population is still higher than 30 % of its initial value. For off times larger then 2 ms seconds, a rapid decline of the recapture efficiency is observed, but if a particular measurement demanded a field free period that long, at least some hundred cycles are possible. Figure 4.9 shows the same data on a semilogarithmic scale. The fact, that the curves appear as relatively straight lines, suggests that they are well approximated by exponentials.
Another loss mechanism beside the loss induced by the trap recycling is to take into

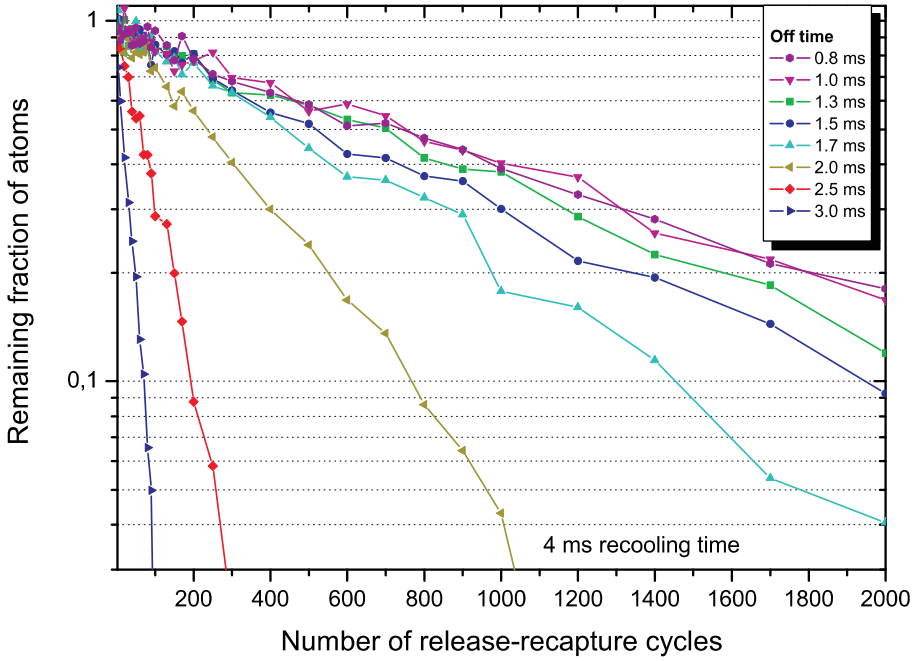

Figure 4.9: The data of Fig. 4.8 on a semilogarithmic scale.

account: The atoms are subjected to collisions with background gas molecules all the time. The data were taken under modest vacuum conditions, when the pressure in the chamber was as high as $1.6 \cdot 10^{-9}$ mbar and the associated one body loss rate was measured to be R=0.125 s^{-1}, corresponding to a time constant of τ=8.1 s. For 1000 switching cycles, the sample in the measurement presented here had spent the considerable time of 4.8 s to 7 s within the vacuum chamber, which alone is responsible for a decline in atom number to at least 55% of the intitial atom number.

Given the fact that the vacuum can be improved by almost two orders of magnitude in pressure, the loss rate should decrease proportionally, and allow for a much more economic use of the loaded trap. To separate the collisional loss of atoms from the loss due to the turned off trap potential, one can assume the following rate equation for the time-dependence of the atom number $N(t)$:

$$\frac{\mathrm{d}N(t)}{\mathrm{d}t} = -(R+S)N(t). \tag{4.5}$$

R is the one-body loss rate as defined in (2.22). S describes the additional atom loss brought about by switching in terms of an effective loss rate. It is reasonable, to assume, that S does not depend on the atom number (at least for atom numbers not too big), but depends only on the MOTs operational parameters. The solution of (4.5) for a loaded trap of N_0 atoms at t_0=0 is

$$N(t) = N_0 e^{-(R+S)t}. \tag{4.6}$$

Knowing R, which was determined independently, the switching loss rate S is obtained by simply dividing the measured data points by $\exp(-Rt)$. For a sequence with a switching

cycle period of T, a loss factor per cycle s is defined by

$$s = e^{-ST}. \tag{4.7}$$

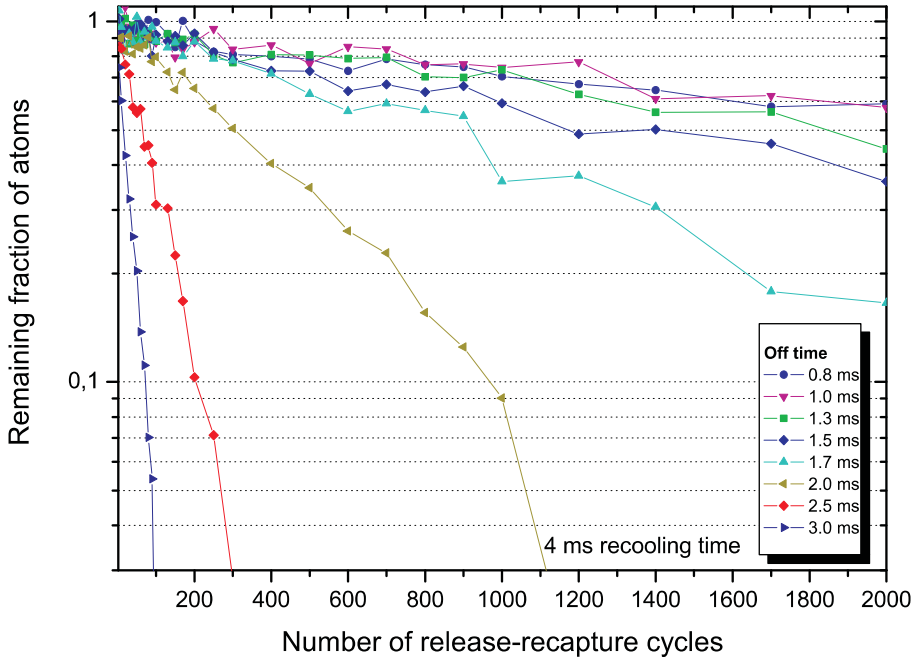

Figure 4.10: Recapture efficiencies for 12 mm trapping beam diameter after factoring out the loss rate due to background gas collisions.

4.3.2 Other Parameters

Besides the off time of the trap and the influence of the background pressure through the total experimental time, there are other trends recognizable from the data. This section lists some of the findings of the investigations.

Beam Diameter

It is intuitively clear, that a larger diameter of the MOT laser beams, and therefore a larger capture region will enhance the recapture efficiency and allow for longer data acquisition periods. In a larger trapping volume, only the fastest ('hottest') atoms will be able to leave the trapping volume during the period of free expansion. The graph on the left hand side of Figure 4.11 shows the recapture efficiency (corrected for collisional losses) for trapping beam diameters of 6 mm. The curves resemble closely the ones of Figure 4.10, apart from the fact, that the off times which result in the same net loss of atoms are about twice as long for a beam diameter of 12 mm. Directly comparing data for the two different trap configurations (right hand side of Figure 4.11), one finds, that off times of

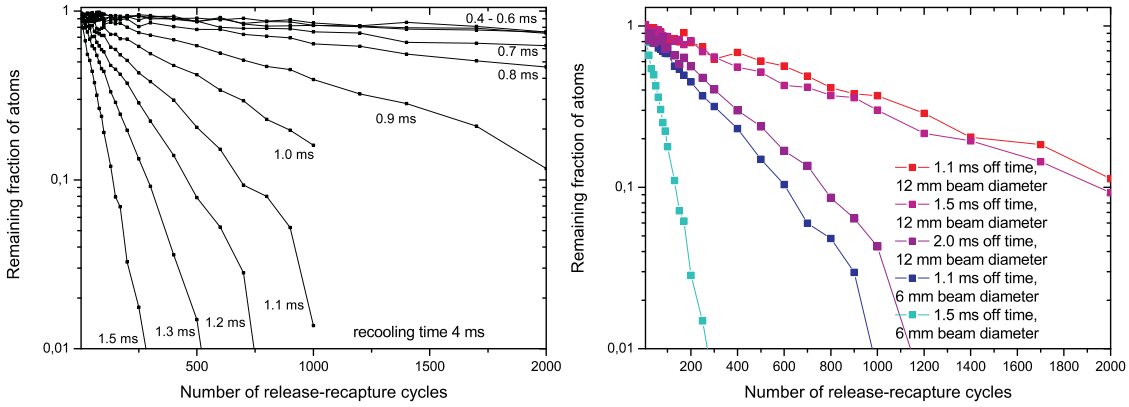

Figure 4.11: *Left*: Switching loss curves for MOT-beams with 6 mm diameter. The numbers next to the curves indicate the respective off times. The relative atom number is corrected for collisional loss. *Right*: Direct comparison of the recapture efficiency for beams with 6 mm and 12 mm diameter. By increasing the beam size, the recapture efficiency can be greatly enhanced.

1 – 1.5 ms, which have little impact on the trap population in the case of a large capture volume, introduce significant loss for the small beam configuration. In the course of the present implementation of fiber optics for beam transport from the laser to the reaction microscope, beam diameters of 22 mm will be realized. This will undoubtedly help to further improve the efficiency of the recapture process.

Recooling Time

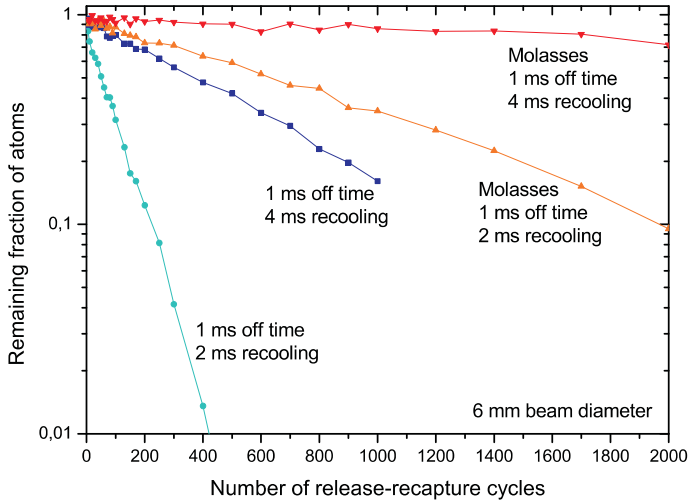

Figure 4.12: Influence of the recooling time on the recapture efficiency: For small diameter beams (6 mm), a longer recooling time drastically enhances the recapture efficiency. Shining the laser in while the magnetic field is off (molasses cooling) further reduces the loss rate. Relative atom number is corrected for collisional loss.

Another parameter, that was seen to influence the number of recaptured atoms, is the

recooling time, i.e. the time the atoms are held in the trap, before it is turned off again in the next cycle. For the small diameter beams, the recooling time is an important parameter, which has dramatic impact on the atom number (Figure 4.12).
The decrease in overall event rate by doubling the dead time for data acquisition in going from 2 ms to 4 ms recooling time, is more than balanced by the gain in atom number. This effect is still pronounced, when the additional collisional loss due to the longer time the atoms are held in the trap, is not singled out. When the expanded cloud is compressed with the rising edge of the magnetic field and the atoms are pushed back towards the trap center, some momentum is imparted to them, which has to be damped away. So there has to be enough time for the MOT to equilibrate and to transfer the excess energy to the radiation field. Since the rise time of the magnetic field is about 500 μs, the remaining 1.5 ms are not enough time for the MOT to reach the steady state.
For the 12 mm beam configuration a change in recooling time (varied between 2 ms and 8 ms) made no significant difference (not shown), indicating that the larger trapping region suppresses loss due to the enhanced mean kinetic energy. Given large beam diameters, the recooling time can be kept as short as possible, at least as long as an increase in target temperature can be tolerated. At present, the minimum up-time of the MOT-field is limited to 2 ms by the switching circuit.

Molasses Cooling

Another possibility to enhance the performance of the release-recapture sequence is molasses cooling by continuously shining in the MOT-lasers (Fig. 4.12), which seems to effectively slow down the ballistic expansion of the atomic cloud. Figure 4.13 demonstrates the dramatic enhancement in the remaining fraction of atoms, if an optical molasses is permanently applied. Even for off-times of 3 ms and longer, the lifetime of the sample is essentially determined by the collisional loss.
Unfortunately, an optical molasses is not applicable, when electrons are to be detected. When the MOT-field is switched off while the electron extraction field is present, there is no more zero-field position the atoms are trapped in. In the homogeneous electron extraction field, everywhere in space and for all atoms a situation is encountered, which (according to the simple MOT-model presented in Chapter 2) corresponds to the atoms sitting at a position several mm outside the MOT-center, where they experience a strong restoring force (Fig. 4.14). Thus the cloud will be pushed away by the beam components co- or counter-propagating with the field lines.
In fact this behaviour has been observed. By controlled exposure (100–1000 μs) of the atomic cloud to the MOT-light in the presence of the Helmholtz-field, the amount of momentum transferred to the atoms could be distinguished by monitoring the distance the atoms travelled within a millisecond, which was found to be up to 5 mm.
For recoil-ion measurements, this technique is readily applied, if the contribution of the excited state is examined. In a more refined switching scheme, for example in a laser

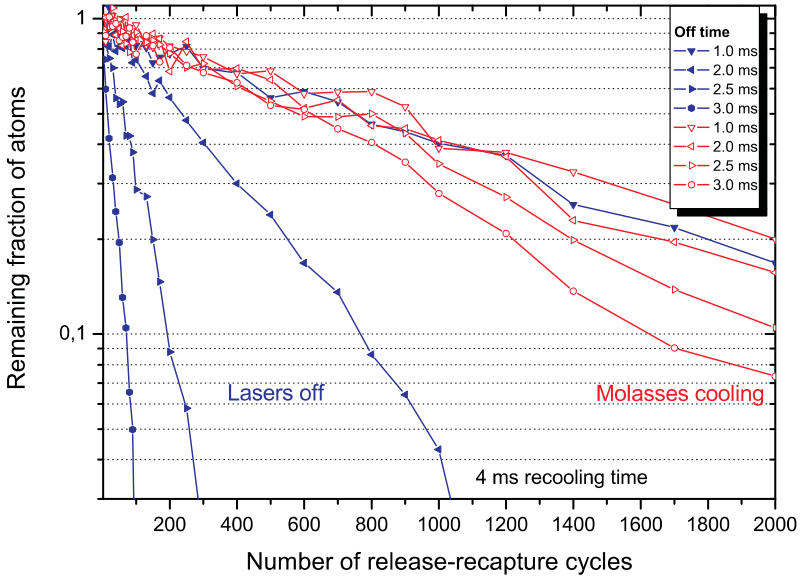

Figure 4.13: Red curves: Recaptured fraction, when the lasers are not shut down together with the magnetic field. Blue curves: Recaptured fraction, when both lasers and magnetic fields are switched. For better visibility of the individual curves, the data has not been corrected for collisional losses. The MOT-beam diameter was 12 mm.

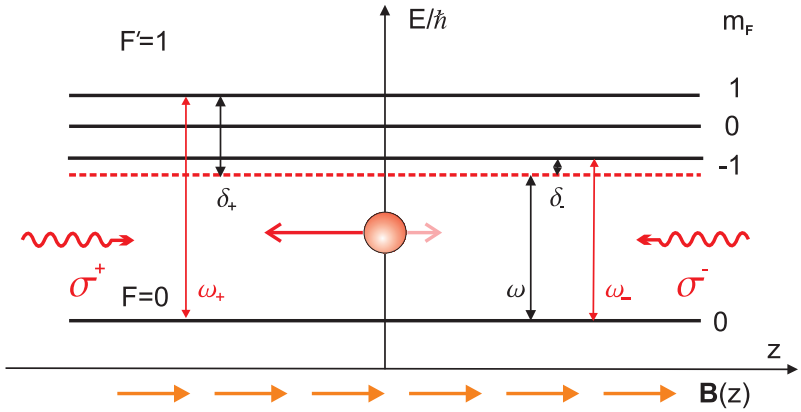

Figure 4.14: The pushing effect explained in a 1-dimensional model. The Helmholtz field shifts the σ^--transition ($\Delta m_F = -1$) into resonance with the laser frequency, while the σ^+-transition is shifted further away. The imbalance in the scattering rate produces a spatially constant net force on the atom.

ionization experiment, where the laser has a repetition rate of some kHz, the MOT-lasers could be synchronized such with the laser pulses that they are just switched off within a timing window of 20–40 μs around the laser pulse, to let the excited state fraction decay. The response time of the acousto-optical modulators employed as fast beam shutters is by far short enough to support such a scheme.

Chapter 5

First results

This chapter presents first measurements on multiphoton ionization of laser-cooled lithium performed with the new apparatus. First the experimental procedure and conditions are described. Then an overview of the specific properties and peculiarities of lithium in strong laser fields, compared to other species studied in strong field experiments, namely the noble gases, is given. The third part, finally presents the obtained data and describes our observations at least on a qualitative, phenomenological basis. Whenever possible, quantitative account for the experimental findings is given.

5.1 Experimental Procedure and Conditions

As a pilot experiment, measurements on multiphoton ionization in an intense Ti:Sa laser field were performed, using one of the group's fs-laser. Photoionization was an ideal candidate for first measurements: It is straightforward to implement, given a suitable laser source and constitutes an exceptionally clean collision system: With fixed energy and negligible momentum transfer from the photon field to the atom and only two particles in the final state, the photoelectron and the recoil-ion, the kinematics of the process is easily understood and evaluated. The small size of the interaction region of well below 1 mm, given by the size of the laser focus, makes it possible to obtain spectra with high momentum resolution.
Unfortunately a leakage at a feedthrough of the electron detector occured and no acceptable vacuum conditions could be brought about. In order to proceed quickly with the measurement, it was decided to skip electron detection, since only a limited amount of beam time at the fs-laser was to our disposal.
Concerning single ionization, this is not a severe drawback: For the case of single ionization, the recoil ion carries the same information as the photoelectron, so the measurement can be considered as kinematically complete. Even in experiments on double- or multiple photoionization, essential information about the collision process and the different reaction channels is extracted from the recoil ion spectrum. An at least qualitative understanding is already possible by analyzing the shape of the time-of-flight spectrum [Jes04], [Mos00].

The first spectra were taken at high peak intensities up to the PW-range in hope to collect doubly-charged ions and to possibly identify signatures of non-sequential double-ionization. It became soon clear, that there was no chance to gather sufficient statistics on that process, in fact, no doubly charged Li ions had been observed in these runs. This is not really surprising when considering the extraordinary high 2nd ionization potential of lithium of 75.6 eV.
The focus of the investigations was shifted to much lower peak intensities in the range between 10^{11} W/cm^2 and 10^{13} W/cm^2 and to the influence of the presence of Li($2p$) excited states in the trap. Some series of measurements were devoted to the estimation of the effects of the different modes of operation of the trap. A thorough and systematic approach to the measurements to tackle all the experimental as well as physical implications of the MOT-target was not possible in view of the given temporal constraints. But the data and experience gained in working with this new class of target certainly paves the way for upcoming investigations.

5.1.1 The fs-Laser System

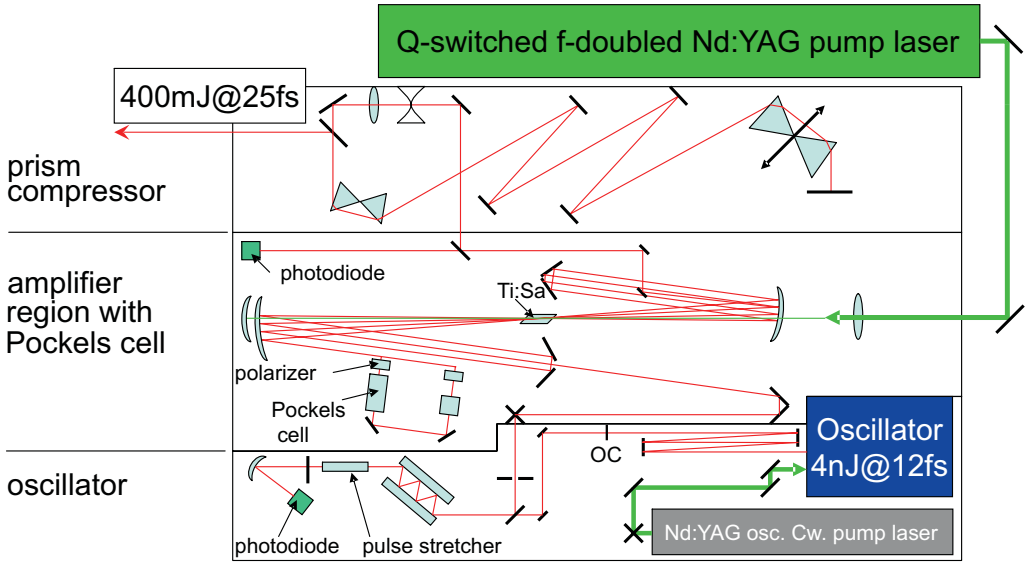

Figure 5.1: Schematic of the fs-laser used in the measurement.

The laser system used for the experiment is a titanium-sapphire oscillator-amplifier combination of type FEMTOLASERS Femtopower pro (see schematic in Fig. 5.1). It is capable of producing pulses of 25 fs length (FWHM) at 795 nm central wavelength with a pulse energy of up to 400 μJ at a maximum repetition rate of 3 kHz. During the measurements, the repetition rate was 2.2 kHz.
The pulses are created in a Kerr-lens mode-locked titanium-sapphire oscillator, delivering 13 fs pulses of 4 nJ energy at a rate of 75 MHz. To achieve peak intensities in the PW/cm^2 range, the pulses have to be amplified. This is done by means of Chirped Pulse Amplifica-

tion (CPA) [Str85]. The temporal envelope of the pulses is stretched to a thousand times the original length by imprinting a strong dispersion on the spectrum ('chirping'). Thus the peak intensity is reduced to values below the damage threshold of the amplifier crystal and other optical elements. A pulse picker, consisting of a Pockels cell and polarization optics, reduces the repetition rate to the kHz range, by only letting one pulse pass through the amplifier, when the amplifier crystal is pumped by the Q-switched pump laser. After multiple passes through the amplifier, the amplified pulse is recompressed by removing the chirp in a prism compressor. Here, also any dispersion picked up on the beampath to the experiment can be pre-compensated. The beam is then transferred to the experiment and enters the chamber through a anti-reflection coated window. Opposite to the laser window, a spherical silver-coated mirror of focal length f=75 mm is mounted in vacuum. It can be moved and tilted by means of a linear translator and an adjustable bellow to guide the focus into the MOT-target.

5.1.2 Data Acquisition

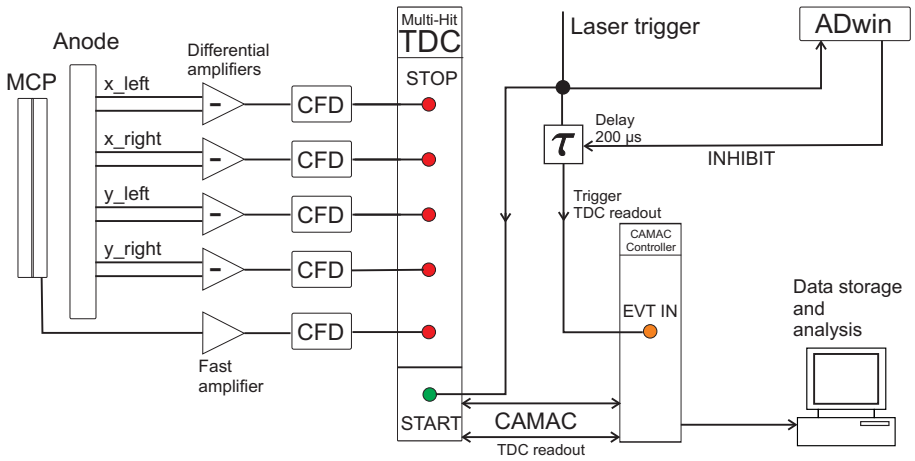

Figure 5.2: Simplified scheme of the data acquisition system.

By the use of a xy-delay-line detector for recoil-ion detection, all kinematic quantities are derived from signal arrival times with respect to an initial trigger signal. The fs-laser setup provides a NIM trigger signal for each emission of a light pulse from the amplifier, which is transferred to the experiment and starts the clock of a TDC (Time-to-Digital Converter). On ion impact, the MCP-stack of the detector creates a voltage spike that is capacitively picked up from the high voltage supply lines of the detector. This signal defines the time-of-flight of the ion. The subsequently arriving voltage pulses from the ends of the delay lines, and the channel plate are amplified and converted to logic level signals by constant fraction discriminators (CFD). Finally they are sent to the TDC as a stop signal. The TDC is a multi-hit TDC, which can register 3 stop signals per channel for one start signal. Since much less than one ion should be produced per shot, at least the detected multiple events can be excluded from data analysis. The raw data of the TDC's

registers is read out by a ROENTDEK CAMAC-controller, which transfers the data to a PC, where the events are written to the hard disk in a list mode file. The read-out of the TDC by the CAMAC-controller is initiated by a delayed copy of the laser trigger at the event-in port (EVT IN) of the controller. This signal can be blocked by the experimental control system. Thus ion signals produced during loading of the trap or while ramping the magnetic field are gated out. The period between two laser shots was 455 μs at a repetition rate of 2.2 kHz, which is approximately the same time, the magnetic field needs to completely ramp down. The switching sequence of the magnetic field and the trapping lasers was programmed such, that it synchronized itself with the lasers pulse train. After the end of the recooling time, the ADwin-system waits for a laser pulse trigger, before initiating the ramping down of the field (Fig. 5.3). After 400 μs, the data acquisition is unlocked, just in time for the next laser pulse to arrive. Usually, the trapping field was off for two laser shots before the atoms were recaptured.

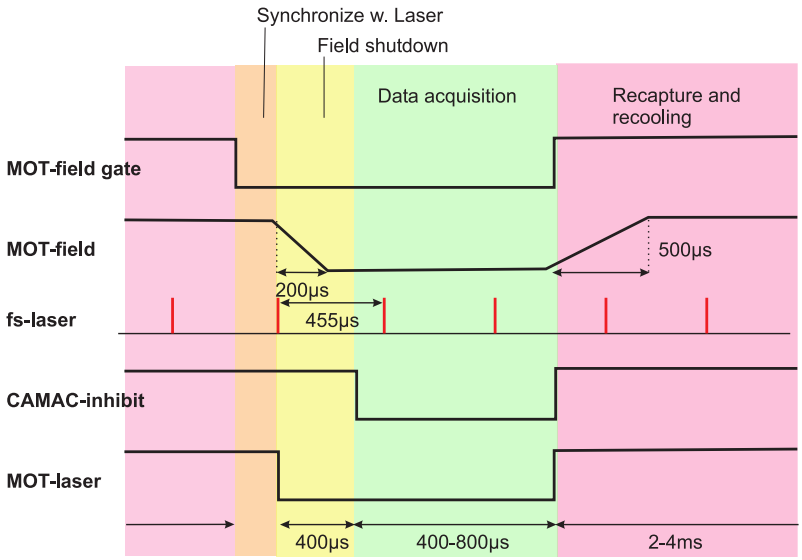

Figure 5.3: Timing sequence for field-free recoil-ion detection.

5.1.3 Intensity Calibration

Since the beam parameters and pulse duration of the fs-laser within the vacuum chamber were not exactly known, a simple method for determining the pulses' peak intensity in situ was applied [Aln04]. The main component of residual gas in the extreme UHV-range is molecular hydrogen H_2 which diffuses through the walls of the vacuum vessel. Time-of-flight spectra of the protons emerging from doubly-ionized H_2 for different intensities were taken. There are different fragmentation pathways for H_2 in an intense laser field [Rud05]: The fragmentation essentially proceeds in two steps. By single ionization of the neutral molecule, the vibrational wave packet of the ground state is transferred to the electronic ground state potential curve of H_2^+. As the wave packet is no longer an eigenstate of

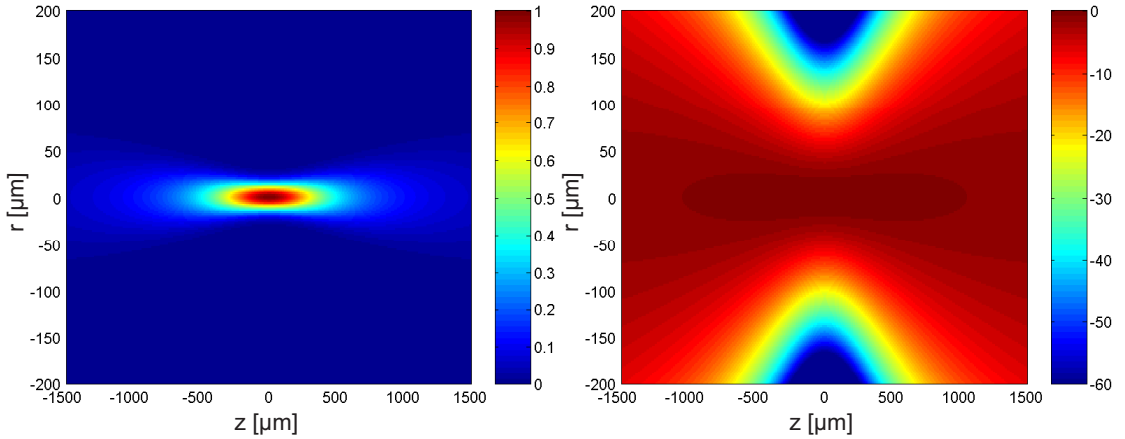

Figure 5.4: Intensity distribution within a Gaussian laser focus with waist w_0=19.8 μm (795 nm wavelength). Note the different axis scaling. *Left*: Relative intensity in linear scale. *Right*: Relative intensity in logarithmic scale. Figures in colourbar are in dB.

the molecular Hamiltonian, it starts to propagate on this potential curve. Via absorption of additional photons, it can switch to dressed potential curves, spaced by one photon energy, which leads to dissociation of molecule into a proton and a neutral H. The other fragmentation channel is sequential double ionization (SDI) much like in the atomic case. After removal of the second electron, the molecule then explodes due to the Coulomb repulsion of the residual protons. The kinetic energy of the protons is a sensitive probe for the internuclear distance R at the instant of ionization [Erg06]. The main difference to atomic ionization is an additional dependence of the ionization potential on R and an enhancement of the ionization rate at an internuclear distance between 3.5 and 7 a.u., which maps to a proton energy of 2–4 eV, due to an effect called charge resonance enhanced ionization (CREI) [Zuo95]. The different fragmentation channels produce distinct peaks, which are easily identified in the time-of-flight spectra. The relative height of the peaks varies in a characteristic manner in the range between 10^{14} W/cm^2 and 10^{15} W/cm^2, as the high energetic CREI-peaks emerge and begin to dominate over the dissociation peaks. Using our group's expertise in strong-field ionization of hydrogen, a series of spectra was recorded at known average laser power or pulse energy, respectively. By comparison with hydrogen spectra taken in experiments at the fs-laser reaction microscope with 25–30 fs pulses, which had been independently intensity calibrated, e.g. by the kink in the energy distribution at drift momentum $2U_p$, the measured output power of the laser could be related to the peak intensity of the pulse with a relative accuracy of approximately 30%. For an average output power measured at the laser of $\bar{P} = 50$ mW (22.5 μJ pulse energy), a peak intensity of $6 \cdot 10^{14}$ W/cm^2 was assumed. The standard calibration factor for categorization of the spectra was taken to be $I/\bar{P} = 1.2 \cdot 10^{16}$ cm^{-2}.
The intensity calibration also yields an estimate for the laser focus size inside the chamber: Assuming a pure Gaussian beam, that is focused to a waist radius w_0, with pulses of length

$\tau \approx 25$ fs, average power $\bar{P}$ and repetition rate ν_{rep}, the peak intensity is given by:

$$I_0 = \frac{2\bar{P}/\nu_{\mathrm{rep}}}{\pi\tau w_0^2}. \tag{5.1}$$

Solving for w_0 and inserting the known values, a waist radius of w_0=9.8 μm (corresponding to a spot size of 19.6 μm) is obtained. This is a rather large value compared to the 7 μm achieved in the fs-laser reaction microscope, but realistic, since not too much emphasis had been put on beam shaping and alignment prior to focusing. However the achieved intensities were by far sufficient.
The corresponding Rayleigh range z_0 amounts to z_0=380 μm, which is a rather large extension along the transversal spectrometer axis. Fig. 5.4 shows the intensity distribution within a focus of these dimensions.

5.1.4 Experimental Effects

This section briefly discusses the impact of the experimental settings on the obtained spectra. Many spectra had been taken during continuous operation of the MOT, since this allowed a higher overall event rate as compared to the switching mode with its inherent dead times due to the recapture and trap loading process. Therefore, it was important to clarify, what influence the presence of the gradient field of the MOT would have on the recoil-ion spectra. The question of momentum resolution is also addressed.

Influence of the Magnetic Field

To investigate the effect of the MOT's gradient field on the recoil-ions, series of spectra were taken under otherwise identical conditions. Figure 5.5 shows spectra recorded at zero magnetic field (pulsed mode) and for different field gradients. The lower spectrum in the time-of-flight spectrum (left hand side of Fig 5.5) was recorded with the MOT-field shut down during data acquisition and thus was not affected by the magnetic field. The spectra (containing contributions of ionization from the excited state of the MOT's cooling transition) do not show much difference in their overall shape or width. The effect of the magnetic field becomes only apparent in a slight shift of the peak positions towards larger time-of-flights with increasing field. This shift amounts to roughly 10 ns at most, which is negligible compared to the total time-of-flight of the ions of 24092 ns for an extraction field of 1 V/cm (the arrival time displayed in the spectrum was measured with respect to a delayed trigger signal). This indicates, that the magnetic field induces no significant energy transfer between the longitudinal and transversal momentum components. The longitudinal momentum calibration is not affected either.
The analysis of the position spectra gives a different picture: With increasing magnetic field, the center of the hit-position distribution will move away from the zero-field position. At the same time, the initially circular ion spot is deformed into an ellipse. This is in agreement with the observations of Nguyen *et al.* [Ngu04], who also report on trajectory simulations which confirmed this effect, and claim that the mean radius of the ellipse

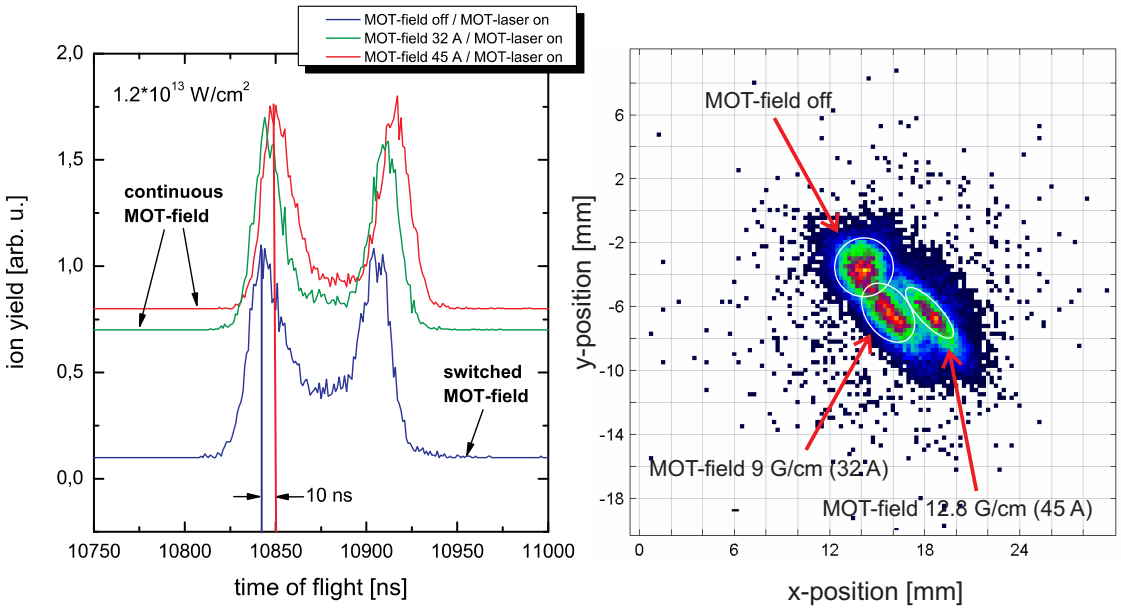

Figure 5.5: *Left*: Raw time-of-flight spectra taken for different MOT-gradients. The curves are arbitrarily shifted with respect to each other for visual convenience. The lower spectrum represents the field-free case. *Right*: Position spectra generated from the same datasets. There is a marked dependence of the hit-position and shape of the ion distribution on the magnetic field.

should be equal to the radius of the circular pattern, which would be obtained under field-free conditions. They also conclude, that the longitudinal resolution is not substantially affected.

When original, uncorrected position spectra are used to calculate transversal momenta or total energies, the ellipsoidal distortion of the position spectrum mimics much larger transversal momenta and energies than actually present in the momentum distribution.

Figure 5.6 reveals a correlation between the time-of-flight and the hit position on the detector. The y-coordinate describes the radial distance of the ion hit from the geometrical center of the detector (which coincides the symmetry axis of the spectrometer). In the presence of the MOT-field the time-of-flight is proportional to the distance from the symmetry center. However, the projection to the time-of-flight remains largely unaffected (compare Figure 5.5), but as mentioned above, the raw fully-differential datasets obtained during continous MOT-operation are not suitable for a quantitative analysis. The spectrum on the left hand side of Figure 5.6 was recorded under field-free conditions and is free of such correlation effects.

Resolution

In the case of coincident ion- and electron detection, the momentum resolution along the longitudinal direction (time-of-flight axis) and the transversal direction (position axis) of a measurement is inferred from the width of the momentum balance peak between the ion and the ejected electron(s). Since the electrons were not detected, this procedure is not

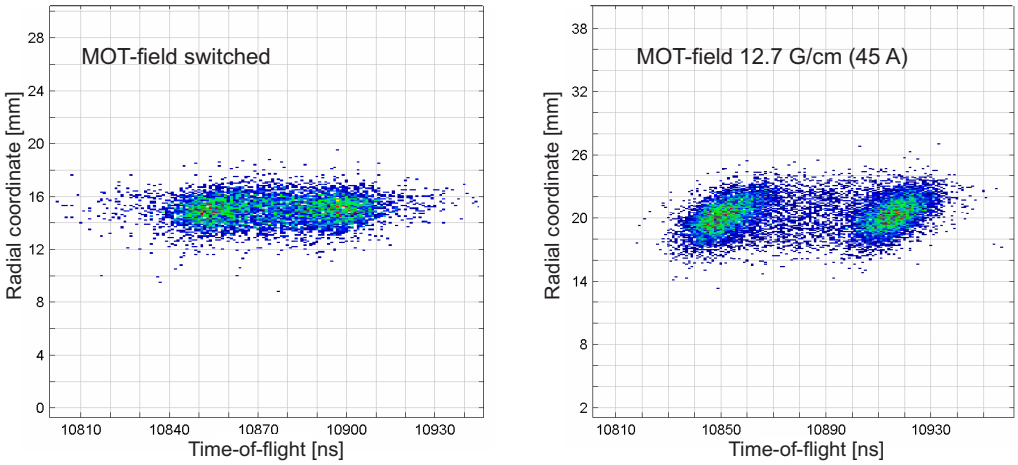

Figure 5.6: Correlation between time-of-flight and hit-position on the detector. The spectrum measured during continuous MOT-operation (*right*) exhibits a pronounced correlation, which is absent under field-free conditions (MOT operated in switching mode).

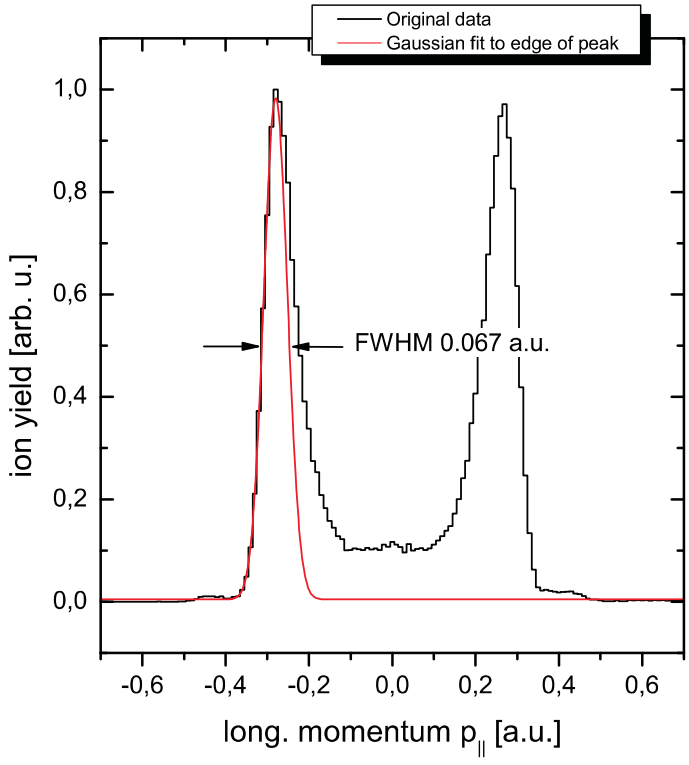

Figure 5.7: Determination of longitudinal momentum resolution.

applicable for the data presented here. To estimate an upper bound for the achievable resolution of the apparatus, a spectrum with remarkably narrow peaks and steep peak edges was picked out and a Gaussian fitted to the edge of the peak (Figure 5.7). The FWHM is found to be 0.067 a.u.. Target temperature is not the limiting factor to resolution, even

	1st IP [eV]	n	2nd IP [eV]
Li($2s$)	5.39	4	75.64
Li($2p$)	3.54	3	75.64
He	24.59	16	54.42
Ne	21.57	14	40.96
Ar	15.76	11	27.63
Xe	12.13	8	20.98

Table 5.1: n gives the threshold number of Ti:Sa photons to overcome IP. Data from [NIS07].

at a relatively 'high' MOT-temeprature of 2 mK, the width of the thermal momentum distribution corresponds to a FWHM of only 0.008 a.u.
The longitudinal resolution is mainly limited by the extraction field of 1 V/cm, which produced a relatively concentrated ion spot on the detector of 3 mm diameter. The lower limit for the transversal resolution is set by the time resolution of the TDC of 500 ps. With a propagation constant of the delay line of 1.98 ns/mm the position binning is limited to 0.25 mm, which at the set extraction voltage corresponds to a transversal momentum of 0.08 a.u..

5.2 Lithium in Intense Laser Fields

The extremely low first ionization potential of Li puts it in striking contrast to the noble gases almost exclusively used in strong field experiments with single atoms: The noble gases on the one side with their closed shell configuration exhibit the highest ionization potentials within the respective period of the periodic table, their first and second ionization potentials having a typical ratio of 1:2. Lithium as an alkaline metal with its loosely bound outer electron on the other hand features a modest ionization potential of only 5.39 eV. In contrast, its ionic core Li^+ in He-configuration has the highest second ionization potential of all singly charged ions. Table 5.1 lists the ionization potentials of Li and a selection of noble gases. It is basically the ionization potential IP, that governs the atom's response to the laser field: Deeply in the regime of multiphoton ionization, the threshold number of photons given by IP and the associated exponent of nonlinearity as defined in (1.15) determine the ionization rates at different intensities. For a Ti:Sa laser of 795 nm wavelength (1.56 eV photon energy), only 4 photons are required to ionize a lithium atom from its ground state. This means, that the order of nonlinearity of multiphoton ionization of lithium is by far lower as compared to helium or still xenon, and that the ionization rate should be magnitudes higher at low intensities.
Further differences in the response of the different species arise due to the dependence of the Keldysh parameter γ on the ionization potential. At a fixed laser frequency ω, it decreases as $\gamma \propto \sqrt{\frac{\mathrm{IP}}{I}}$, i.e. the lower IP, the lower the intensity at which the transition

	1st IP [eV]	I_{OBI} [W/cm^2]	γ	U_p [eV]
Li(2s)	5.39	$3.38{\cdot}10^{12}$	5.29	0.20
Li(2p)	3.54	$6.28{\cdot}10^{11}$	9.76	0.037
He	24.59	$1.46{\cdot}10^{15}$	0.53	86.1
Ne	21.57	$8.65{\cdot}10^{14}$	0.65	50.5
Ar	15.76	$2.47{\cdot}10^{14}$	1.0	14.6
Xe	12.13	$8.66{\cdot}10^{13}$	1.5	5.11

Table 5.2: Over-the-barrier intensities I_{OBI} of Li and some noble gases and the corresponding Keldysh parameter γ and the ponderomotive potential U_p at these intensities.

from multiphoton to the tunneling regime occurs.
Another quantity with a strong dependence on IP to keep in mind is the over-the-barrier intensity I_{OBI} as defined in Section 1.1.6. Scaling with IP^4, it shows remarkable differences between the atomic species. Concerning Ti:Sa radiation and pulses shorter than 100 fs, all of the noble gases can reach the regime of tunneling ionization $\gamma > 1$, before a saturation of the ion yield or barrier suppression occurs. For lithium, over-the barrier ionization should already occur at intensity levels, when multiphoton ionization is still the dominant ionization channel. According to Table 5.2, this is the case at a moderate intensity of about $3{\cdot}10^{12}$ W/cm^2, corresponding to a Keldysh parameter of 5.3. The MOT-target gives us the possibility, to mix in another species by excitation of the lithium atoms from the ground state to the $2^2P_{3/2}$-state by shining in the MOT-lasers. Having a zero-field ionization potential of only 3.54 eV, over-the-barrier ionization (OBI) sets in at field strengths corresponding to γ=19.3, which means that an abrupt transition from multiphoton to over-the-barrier ionization occurs.
It was pointed out by Delone *et al.* [Del98], that alkali atoms are ideal candidates for the observation of OBI. Since the electron spectra of tunneling ionization and above-barrier decay should be hard, if at all, to distinguish, the measurements should be performed at $\gamma \gg 1$, a condition that is easily fulfilled in our experiment. Thus, an superimposed background of tunneling ionization, e.g. from ionization at the edge of the laser pulse, can be excluded, and the contributions of OBI and multiphoton ionization to the ion yield can be separated. There is, however, no general theory of over-the-barrier ionization in this regime, which would predict an unique feature to identify over-the-barrier ionization as a dominating process.
From the above, it is obvious, that the nature of the photoionization process is characterised by three quantities: The properties of the light field are given by the photon energy $\hbar\omega$ and the intensity I. The properties of the atom are determined through its ionization potential IP. These are the quantities, that γ is composed of, which decides for a given laser frequency ω, whether the atom ionizes predominantly by a multiphoton or tunneling process. However, the over-the-barrier intensity introduces a discontinuity in this description, as it provides a third ionization channel, which is to a first approximation independent of the photon energy and solely depends on the field intensity. These rela-

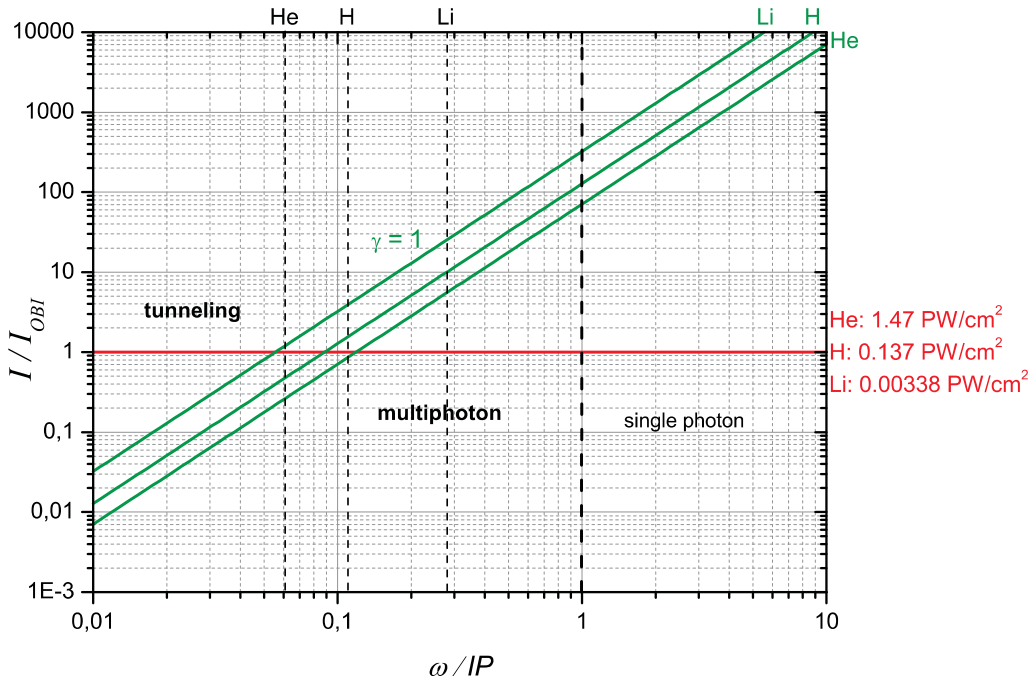

Figure 5.8: This plot demonstrates, that there is no universal scaling for the behaviour of atoms in intense laser fields. The vertical dashed lines correspond to the photon energy of a 800 nm wavelength Ti:Sa laser field.

tions can be combined in a diagram, devised by B. Feuerstein of MPI-K [Feu07], which immediately shows, which regimes of ionization are accesible for a particular atom at a particular photon energy.
In this diagram (Figure 5.8), the field intensity is scaled by the over-the-barrier intensity ($\tilde{I}$=I/I_{OBI}), and the photon energy is expressed in units of the ionization potential of the species under consideration ($\tilde{\omega}$=ω/IP). The consequence is, that there is no universal behaviour for photoionization of atoms. If, for different atoms, intensity and photon energy are provided such, that the experimental situation corresponds to the same point in 5.8, each atomic species still has to be assigned an individual Keldysh parameter (green lines). Equally, one could scale the intensity to that intensity, where γ=1 holds. Then an universal γ=1-line and atom-specific over-the-barrier lines would emerge.

Ionization Dynamics

In order to provide further insight into the ionization dynamics and to estimate the ionization probability for pulses with different peak intensities, Figure 5.9 shows the ionization probability $P(t_0 \to \infty)$ for atoms in the ground state and the excited state after a laser pulse of 25 fs duration. The ionization probaility at a time t_0 within the pulse is given by

$$P(t_0) = 1 - \exp\left(-\int_{-\infty}^{t_0} \kappa_N I(t)^N \mathrm{d}t\right), \tag{5.2}$$

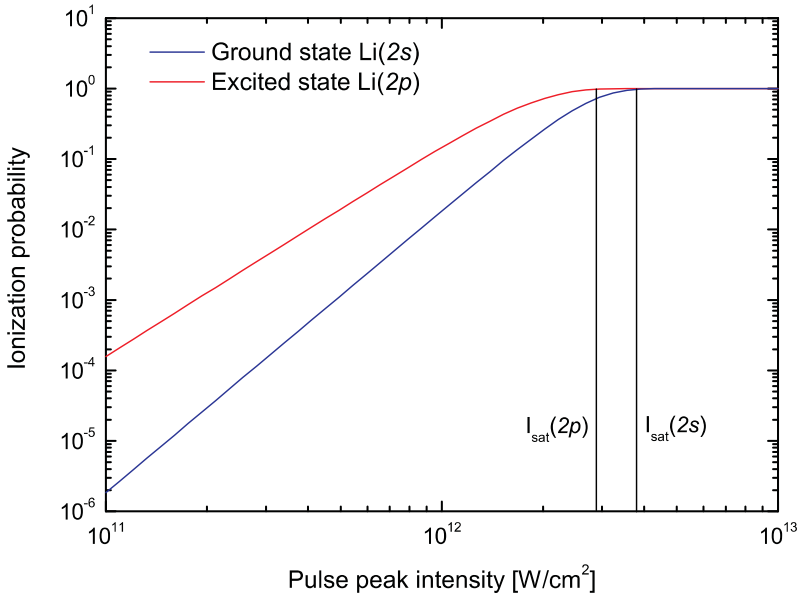

Figure 5.9: Calculated total ionization probability for Li($2s$) and Li($2p$) at the end of a 25 fs FWHM pulse, based on the multiphoton ionization cross sections from Table 5.3. At low intensities, ionization from the $2p$-state dominates. The ion yield saturates for both states around peak intensities 3–4·10^{12} W/cm^2.

	σ_n	κ_n
Li($2s$), N=4	$5.4 \cdot 10^{-111}$ cm^{8}s^3	$1.39 \cdot 10^{-36}$ W^{-4}cm^{8}s^{-1}
Li($2p$), N=3	$1.6 \cdot 10^{-79}$ cm^{6}s^2	$1.03 \cdot 10^{-23}$ W^{-3}cm^{6}s^{-1}

Table 5.3: Generalized cross sections for multiphoton ionization by Ti:Sa radiation (1.56 eV photon energy, 800 nm wavelength) for the incident photon flux given in photons s^{-1} (σ_n) and Wcm^{-2} (κ_n) [Mar07].

where N is the number of absorbed photons, κ_n the n-th order generalized cross section and $I(t)$ the temporal pulse profile. Some preliminary generalized ionization cross sections for Li($2s$) and Li($2p$) for 1.56 eV photon energy (800 nm wavelength) were supplied by S. Marmo from the group of N. L. Manakov from Voronezh State University, given in Table 5.3. These cross sections were calculated from lowest order perturbation theory and do not account for intermediate and intensity dependent resonances, but can give an estimate for the ionization yield from both states integrated over the whole pulse.

As displayed in Figure 5.9, three-photon ionization from the Li($2p$) excited state exhibits a higher ionization rate than the four-photon process from the Li($2s$) ground state up to the saturation intensity I_{sat}, which in this context denotes the pulse peak intensity, where ionization probability comes close to unity. It has to be noted, that this plot extrapolates the validity of the generalized cross sections derived from a perturbation theoretical treatment into intensity regimes, where this approach is not appropriate any more.

For pulses with peak intensities beyond the saturation intensity (in the experiment, peak intensities of up to 10^{16} W/cm^2 have been applied), most of the ions and photoelectrons

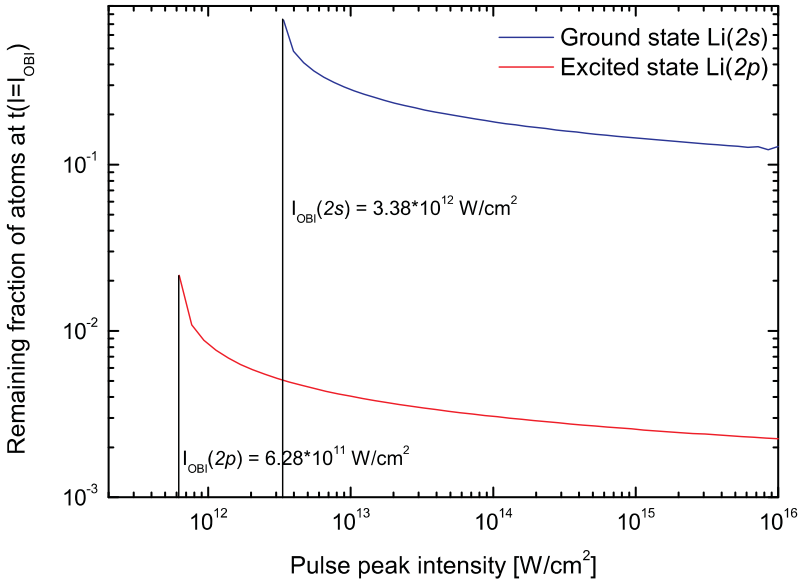

Figure 5.10: Fraction of atoms, that remain unionized, when the leading edge of the pulse reaches the over-the-barrier intensity I_{OBI}, calculated for a pulse length τ of 25 fs.

detected will be produced within the leading edge of the pulse and hardly any atom will ever experience the nominal peak intensity. Furthermore, for intensities approaching the respective over-the-barrier intensities, significant deviations from the predictions of perturbation theory are to be expected, since the laser field cannot be viewed as a weak modification of the atomic structure any more.
In Figure 5.10 the fraction of atoms that have withstood ionization within a pulse of 25 fs duration at the time t_{OBI}, where the over-the-barrier intensity I_{OBI} is reached, is plotted versus the peak intensity of the applied pulse. While the population of the excited state has been almost completely depleted when the over-the-barrier intensity is reached, there is a considerable fraction between 90 and 10% of ground state atoms, that will ionize at intensities higher than I_{OBI}. One can conclude, that the contribution of the excited state to the observed spectra, will always have predominantly multiphoton character and any high intensity features should arise from the ground state.

Focal Volume Averaging

Every experiment on ionization from a tightly focused Gaussian beam with a target of similar extension automatically performs a weighted averaging over a broad range of peak intensities, where the relative weights of the particular peak intensities are given by the volume of the iso-intensity shells within the focal volume. This fact has to be taken into account for correctly interpreting spectra taken at a particular laser intensity. Especially numerical calculations can only reproduce observed spectra to a good degree, if momentum distributions are calculated for many different peak intensities and the results are combined accordingly [Mor07].

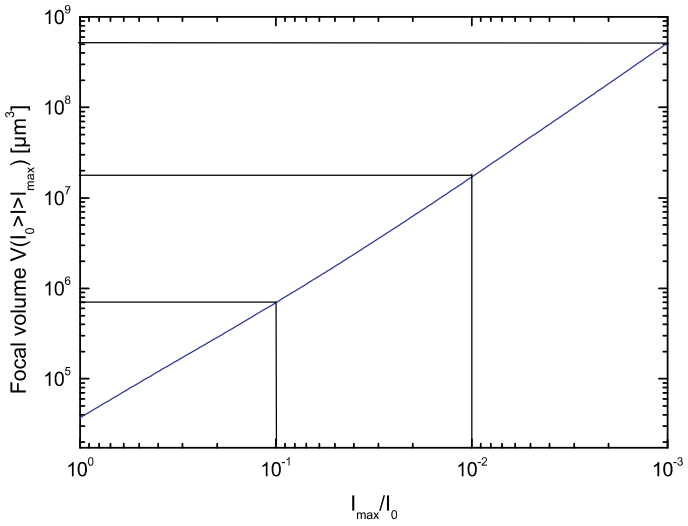

Figure 5.11: Volume enclosed in an iso-intensity shell of peak intensity $I_{\max}/I_0$, calculated for a Gaussian focus with dimensions as in the experiment, where I_0 is the nominal peak intensity.

Perry *et al.* [Per88], [Lar98] give an analytical formula for the total volume enclosed by an iso-intensity shell of intensity $I_{\max}$ (local peak intensity) for a Gaussian focus of waist radius w_0:

$$\begin{aligned} V(I > I_{\max}) &= V_0(\tfrac{2}{9}\xi^3 + \tfrac{4}{3}\xi - \tfrac{4}{3}\arctan(\xi)) \\ V_0 &= 2\pi w_0^4/\lambda \\ \xi &= \sqrt{I_0/I_{\max}}, \end{aligned} \tag{5.3}$$

where I_0 denotes the peak intensity of the laser pulse. Figure 5.11 demonstrates, that e.g. for a peak intensity I_0=10^{14} W/cm^2 the volume enclosing intensities between 10^{13} W/cm^2 and 10^{12} W/cm^2 range more than ten times larger than the one enclosing intensities larger than $I_{\max}$=10^{13} W/cm^2.

5.3 Results and Discussion

5.3.1 Ionization from the Ground State

This section presents results obtained on ionization of lithium from the $2^2S_{1/2}$ ground state, when the MOT was operated in the switching mode. There are not too many spectra available on pure ground state ionization, since the overall event rate in switching mode is rather low compared to continuous operation and in order to collect enough statistics, the measurements had to be run typically for several hours or over night.
These spectra provide a good starting point for the discussion, because they have a good resolution and their principal structure is easily explained. For the case of pure multiphoton ionization, 4-photon ionization from the ground state should produce electrons with an excess energy of 0.849 eV, corresponding to a recoil ion momentum of 0.25 a.u.. Since

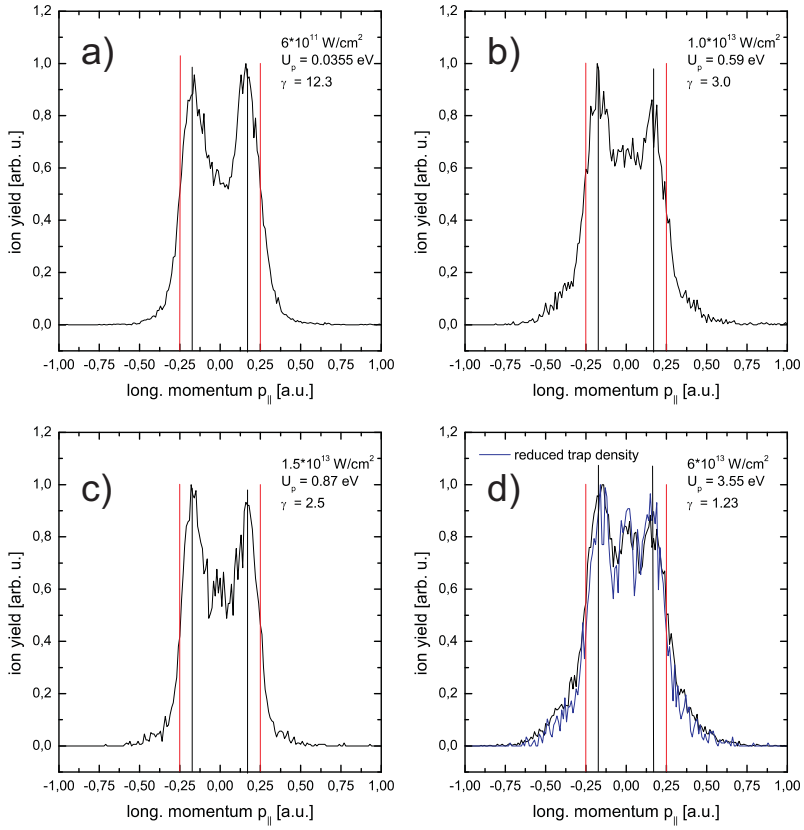

Figure 5.12: Longitudinal momentum spectra ($p_{\|}$, along the laser polarization axis) for different peak intensities for nominal peak intensities ranging from $1.6 \cdot 10^{11}$ W/cm^2 to $6 \cdot 10^{13}$ W/cm^2. The most notable feature is the intensity dependence of the central zero momentum peak.

the electron emission preferably occurs along the direction of polarization, a momentum distribution with two peaks (emission towards the detector and in the opposite direction) appear, which should have a maximum close to ± 0.25 a.u. (indicated by the red vertical lines in Fig. 5.12) and a minimum at zero momentum. The detailed structure of the spectrum is not trivial to describe, because the time-of-flight spectra are a projection of the cylindrically symmetric momentum distribution onto the symmetry axis. However, the peaks reproducibly appear at a longitudinal momentum of 0.17 a.u., as marked by the black vertical lines. The four spectra presented in Figure 5.12 were taken at peak intensities starting with $6{\cdot}10^{11}$ W/cm^2 in a) to $6{\cdot}10^{13}$ W/cm^2 in d), all except a) being greater than the over-the barrier intensity I_{OBI}. There is no noticeable shift of the peak position towards lower momentum with increasing intensity that could indicate any ponderomotive shift of the continuum. The most prominent feature is a peak emerging at zero momentum, which is not explained by a merging of the two 4-photon peaks, but has a peak characteristic on its own, as spectrum d) clearly shows.

5.3.2 Ionization from Ground- and Excited State

In the presence of excited states, i.e. when the trapping lasers are switched on during the measurement, the $2^2P_{3/2}$ state is populated by a significant fraction of 20–40% of the atoms. For the non-resonant case, multiphoton ionization occurs through absorption of three photons, leading to an excess energy of 1.137 eV and a corresponding recoil momentum of 0.29 a.u..
Therefore, the spectra consist of a superposition of ionization events from the ground state and from the excited state. In continuous MOT mode, spectra for peak intensities up to $14.4 \cdot 10^{15}$ W/cm^2 have been taken. Figure 5.13 depicts a sequence of longitudinal momentum spectra, which shows that the central zero momentum peak still grows with the peak intensity up to the 10 PW/cm^2 intensity range.
This central maximum becomes more prominent with increasing peak intensity. In direct comparison, the central maximum is more pronounced, when the target is exclusively populated by ground state atoms. This was verified by increasing the detuning of the trapping lasers, which leads to a drastic reduction of the excited state fraction in the target (Fig. 5.14). This confirms, that the central peak has its origin in ionization from the ground state. Furthermore, it seems to be a high intensity phenomenon, since its weight still increases with peak intensity in the PW/cm^2 range, though this is far above the saturation intensity. This observation can be understood, as according to the discussion on spatial averaging in section 5.2, at these intensities a larger volume is exposed to the high peak intensities needed to effectively ionize the ground state atoms. This model is further supported by the fact that the 4-photon peak increases its relative height as compared to the 3-photon peak as can be seen from the evolution of the spectra with peak intensity (Fig. 5.13 a)–e)). The superposition of the three-, four-photon and the zero momentum peak most likely causes the apparent shift in the peak positions.
There is no notable broadening of the momentum spectrum to values beyond $p_\parallel$=0.5 a.u., corresponding to an electron energy of 3.4 eV and at most 0.75 a.u. (7 eV). As the maximum drift momentum an ionized electron can acquire is $2U_p$ (see equation) (1.14)), one can infer, that few electrons are set free at instantaneous intensities greater than $5{\cdot}10^{13}$ W/cm^2.

5.3.3 Two-Dimensional Spectra

The left hand side of Figure 5.15 shows a two-dimensional momentum spectrum (transversal momentum component p_y vs. longitudinal momentum $p_\parallel$ (the spectrum is integrated over the third cartesian coordinate), taken under field-free conditions, for ionization from the ground state at an intensity of $6 \cdot 10^{11}$ W/cm^2, which exhibits a pronounced ring-like structure. The inward shift of the 4-photon peak towards lower momenta than expected is partly an effect of the projection of the data onto the longitudinal momentum axis. The left of Fig. 5.15 displays the same data, but the range of integration along the axis perpendicular to the paper plane is reduced to small momenta of $|p_x| < 0.05$ a.u.. If the projection is likewise restricted along the other transversal momentum component,

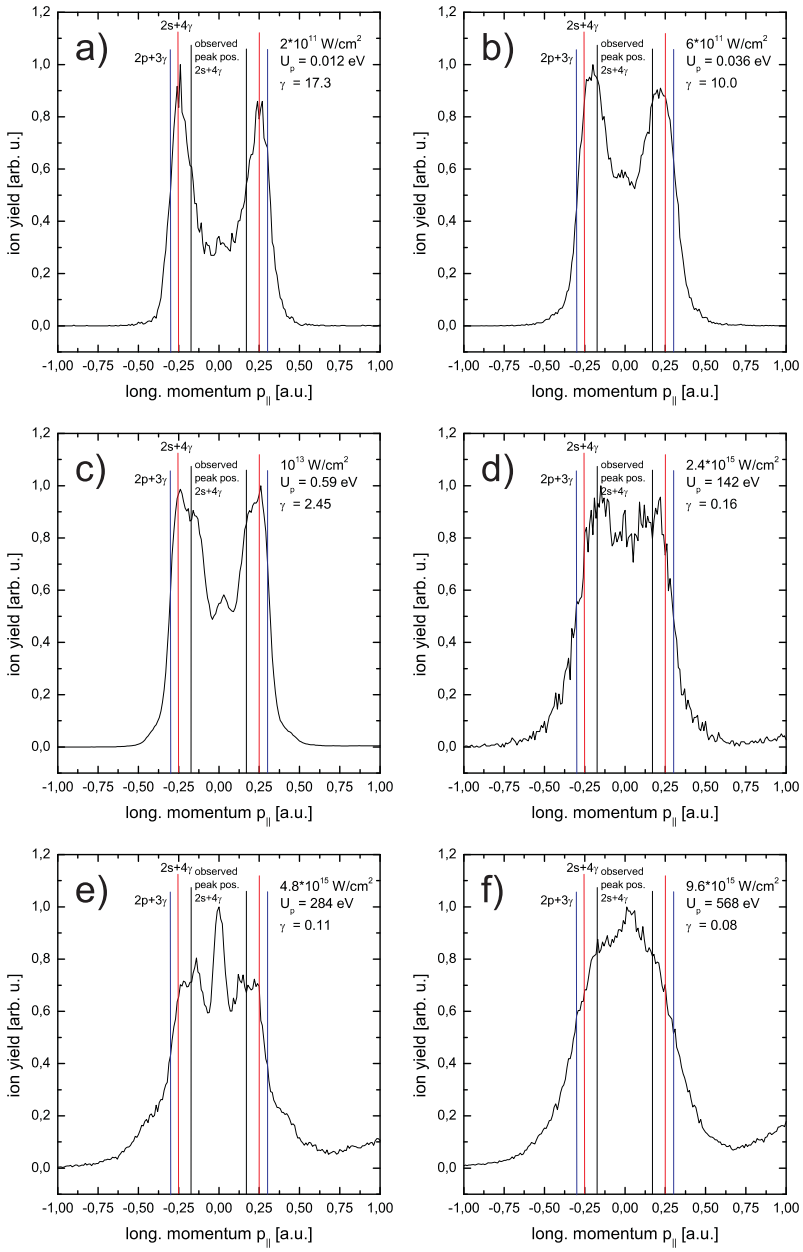

Figure 5.13: Longitudinal momentum spectra ($p_{\|}$, along the laser polarization axis) for different peak intensities for nominal peak intensities ranging from $1.6 \cdot 10^{11}$ W/cm^2 to $9.6 \cdot 10^{15}$ W/cm^2. The black vertical line marks the position, where the four-photon peak of the ground state ($2s + 4\gamma$) was found in Fig. 5.12, the red ones the momentum associated with the ($2s+4\gamma$)-process, and the blue ones the expected recoil momentum of direct ionization from the excited $2p$ state (0.29 a.u.). The value of γ refers to the ionization potential of the $2p$ state. The shoulder on the right hand side of the peaks in spectra d), e) and f) beyond momenta of 0.5 a.u. originates from the low velocity fraction of thermal atoms from the lithium beam used to load the trap passing through the focus. The atoms from the beam are well separated from the trapped atoms by their velocity component along the longitudinal direction.

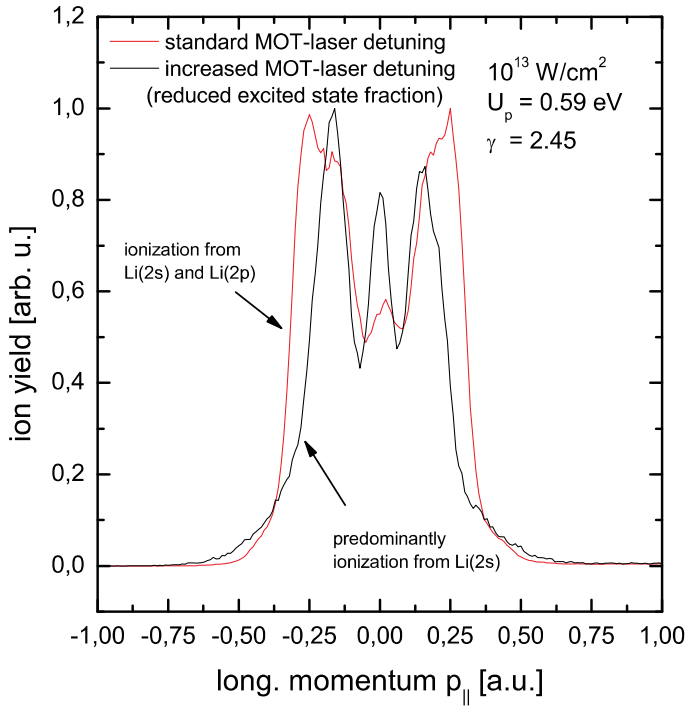

Figure 5.14: Identification of the central peak as a feature emerging from the ground state Li($2s$).

the four-photon peak is found at 0.20 a.u.. The residual shift of -0.05 a.u. from the expected 0.25 a.u. remains unexplained, if one assumes direct four-photon ionization from the ground state (see discussion in section 5.3.4). At this intensity it cannot be attributed to a ponderomotive shift of the continuum (0.3 eV), which is only reached at intensities ten

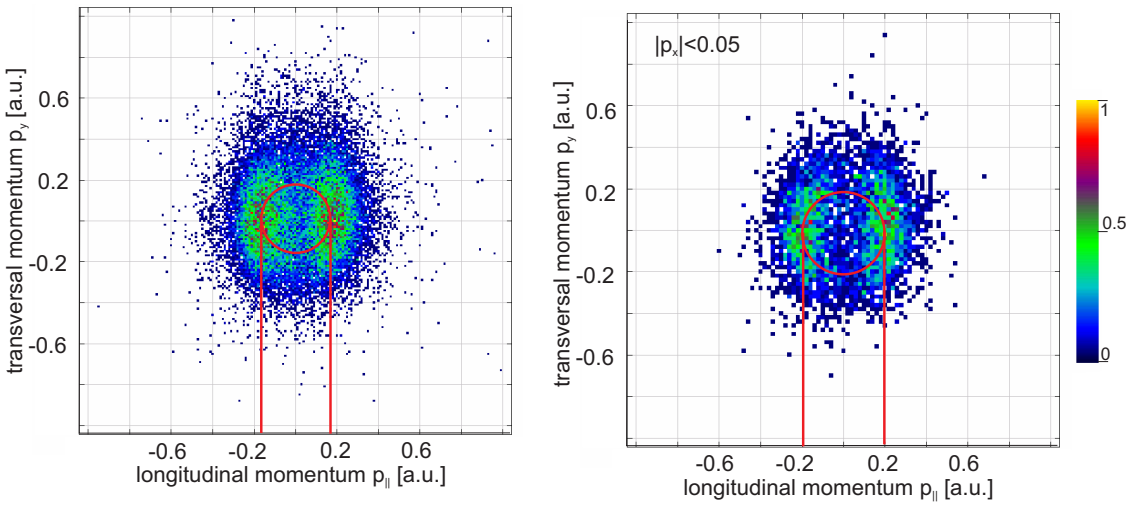

Figure 5.15: Two-dimensional momentum spectrum for 4-photon ionization of ground state Li($2s$) at an intensity of $6 \cdot 10^{11}$ W/cm^2. The left density plot is a projection, the right one a so called cut as described in the text. The colourbar maps the relative number of events per bin.

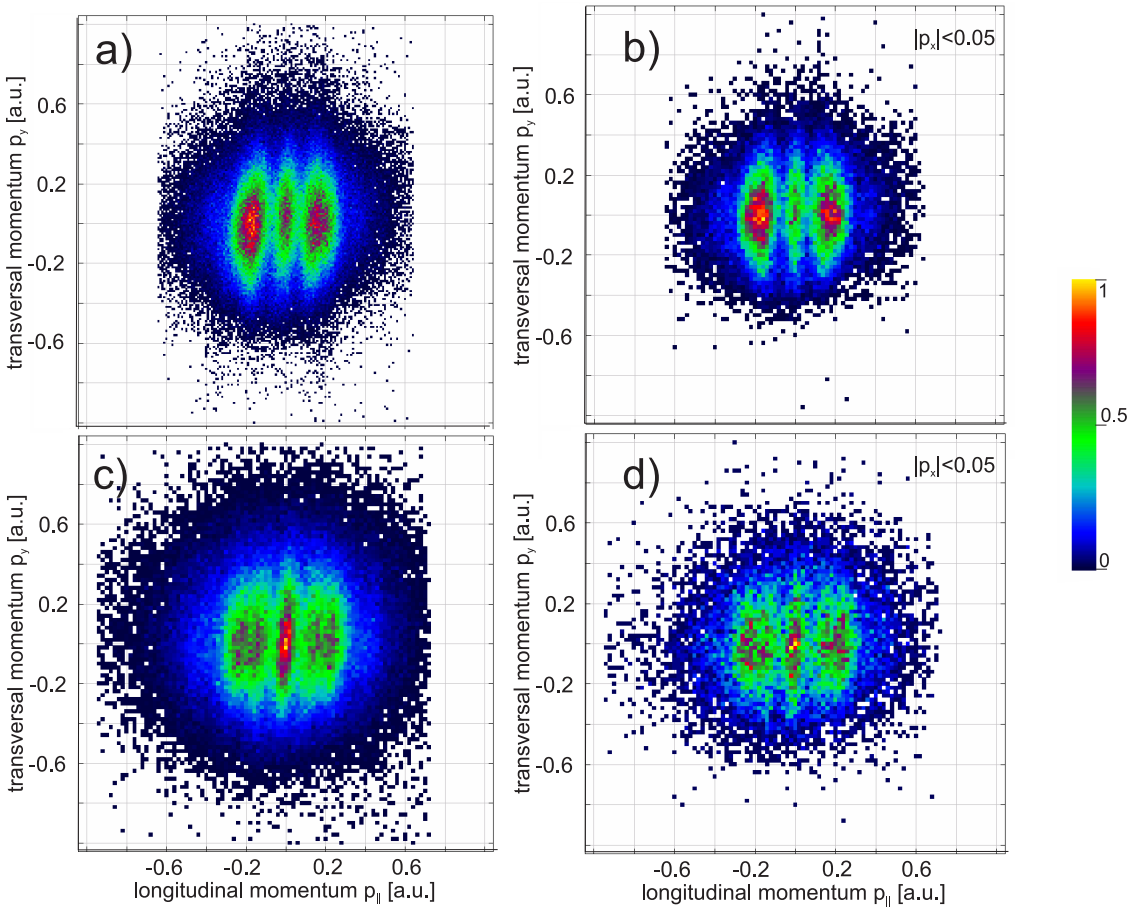

Figure 5.16: Two-dimensional momentum spectra of ionization from the ground and excited state for intensities of 10^{13} W/cm^2 (a) and b)) and $4.8 \cdot 10^{15}$ W/cm^2 (c) and d)). The colourbar maps the relative number of events per bin. a) and c) are projections, b) and d) are cuts as described in the text.

times higher. An error in the longitudinal momentum calibration can equally be excluded. Figure 5.16 shows two datasets, where the central maximum becomes clearly apparent. It is surprising to find, that the central maximum is rather extended along the perpendicular direction. This indicates that the electron emission for electrons with near zero longitudinal momentum should be preferably ejected perpendicular to the polarization axis. The large width of the peaks along the transversal momentum axis is partly due to the limited transversal resolution of $\Delta p_\perp \approx 0.08$ a.u. and the distortions induced by the magnetic field on the transversal momentum components. The transversal momentum data are not really suitable for a quantitative analysis, compared to the high resolution longitudinal momentum spectra but can still give a hint on the overall structure of the momentum distribution.

For future runs, measurements should be performed, where the polarization axis is aligned perpendicular to the direction of extraction, to have a direct comparison of the resolution along the spectrometer axis and perpendicular to it. Furthermore, the extraction voltage

should be further reduced in order to cover more of the detectors active area and thus gain in transversal resolution.
Nevertheless, all the spectra exhibit a peak for electrons emitted with near zero momentum, at least in the longitudinal direction, which is confirmed in any representation of the data.

5.3.4 Possible Mechanisms

From these findings, it is tempting, to attribute the zero momentum peak to an over-the-barrier ionization process of the $2s$ state. According to equation (1.31), this ionization channel should open at intensities higher than $3.38 \cdot 10^{12}$ W/cm^2. The evolution of the spectra with intensity presented in Fig. 5.12 speaks in favour of this assumption.
Over-the-barrier ionization is usually discussed in the context of ionization of noble gases, and the corresponding threshold intensities as given in Table 5.2 are in a range, where the Keldysh-parameter γ is close to unity. Under these circumstances the over-the-barrier process can be described as a natural extension to the picture of tunneling through the barrier created by the superposition of the effective nuclear potential and the classical electric laser field as presented in section 1.1.5. In the case of lithium, however, the over-the-barrier intensity is reached for an intensity and Keldysh-parameter $\gamma = 5.3$, where the multiphoton picture still applies. As stated before, it is not yet clear, what the characteristics of over-the-barrier ionization in this regime are, but a deviation in the spectra from the rather predictable pattern of the N-photon and ATI-peaks is likely.
Another ionization pathway to take into account, is so resonance-enhanced ionization (also called REMPI). The high bandwidth of the laser field (a measured 50 THz FWHM or 0.2 eV FWHM for 25 fs-pulses from the amplifier [Zro05]) and the broad range of intensities covered within the laser pulse enables a number of possible m-photon resonances during the pulse. These resonances lead to a population of various excited states, from which the atom then ionizes. The present data lacks the dynamic range to identify at most more than the first order ATI-peak or to resolve any side maxima enabling the identification of high lying intermediate states (compare Fig. 1.6), but for the explanation of the near-zero momentum peak one should take into consideration the possibility of a Freeman resonance (section 1.1.4) with near zero electron energy.
Figure 5.17 depicts a simplified level scheme of lithium. The blue arrows represent intermediate resonances originating from the ground state. Even when neglecting any intensity-dependent AC-Stark shifts (low intensity case), there is still a certain probability of excitation to the $4p$ and $4f$ level by a three-photon transition (and the $3s$ level via a two-photon transition) due to the bandwidth of the laser field. If one tentatively assumes, that the $4p$ and the $4f$ level exhibit an AC-Stark shift almost equal to the ponderomotive shift, Freeman resonances from these states at electron energies of $E_e(4p)$=0.69 eV and $E_e(4f)$=0.71 eV (momenta $p(4p)$=0.22 and $p(4f)$=0.23 a.u.) should be observed. This could partly explain, that the four-photon peak is generally found at lower momenta than

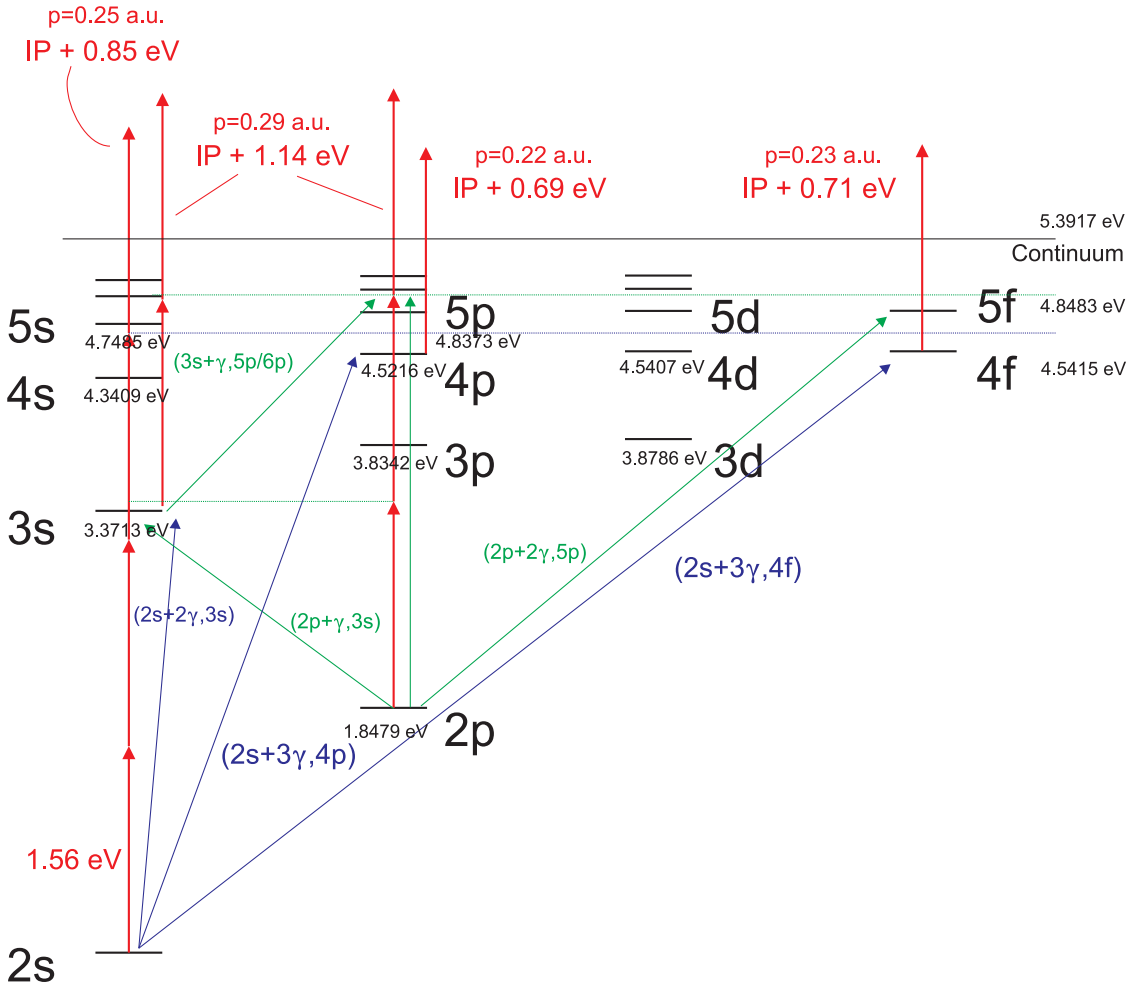

Figure 5.17: Simplified level scheme of lithium. The red arrows represent the photon energy. The blue and green arrows indicate possible resonances with intermediate states from the ground and the excited state, respectively. The red numbers give the excess energy for the respective ionization process and the associated ion/electron momentum.

the 0.25 a.u. from the direct 4-photon process from the ground state. The sensitive dependence of the ionization rate on intermediate resonances was studied theoretically by Tong *et al.* [Ton03] by the example of sodium in a 800 nm laser field for intensities between 10^{11} W/cm^2 and $5 \cdot 10^{11}$ W/cm^2 for different pulse lengths. They found, that the bandwidth of the laser field, which is inversely proportional to the pulse duration, can change otherwise off-resonant m-photon transitions into near-resonant ones and lead to an enhancement of the ionization rate.

Still the question has to be addressed, whether there exists a possibility for a zero energy Freeman resonance. Two states are found, that are almost one photon energy below the continuum threshold, namely the $3p$ and the $3d$ state with binding energies IP($3p$)=3.83 eV and IP($3d$)=3.88 eV. If it is again assumed that these states have an AC-Stark shift close to the ponderomotive value, and the (negative) intensity dependent shift of the ground

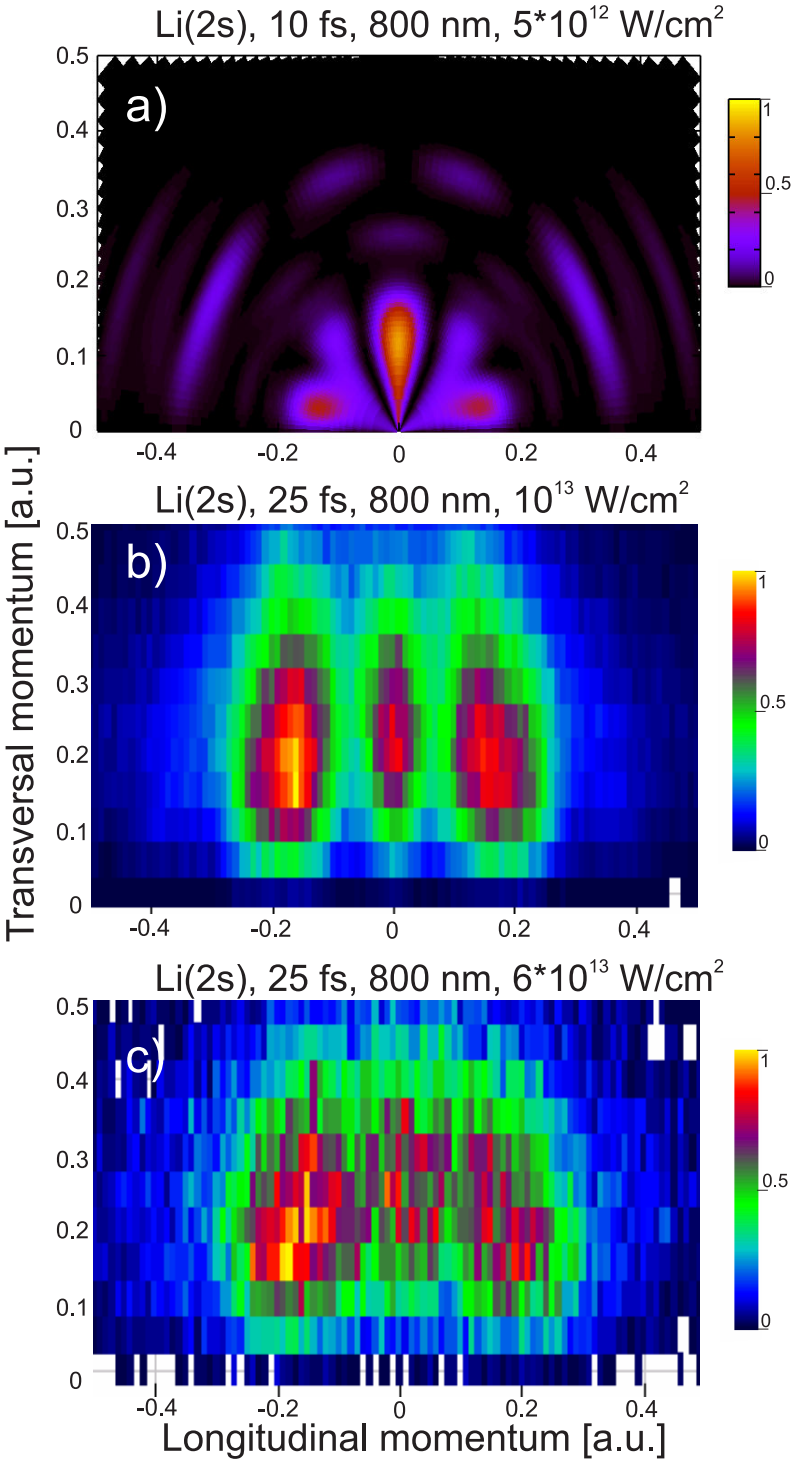

Figure 5.18: Comparison between a calculated momentum spectrum a), and two measured ones with parameters that come closest to the ones used in the calculation (b),c)). The colourbar gives the relative number of events per bin.

state is comparably small, then the $2s$ ground state could couple to the $3p$ state via three photons, provided the AC-Stark is high enough. This requires a ponderomotive shift of U_p=0.85 eV, which leads to an estimated resonance intensity of $1.43 \cdot 10^{13}$ W/cm^2. This estimated apperance intensity of the zero momentum peak for this mechanism is likely too high to significantly contribute in the spectra, since once again the focal volume effect has to be taken into account.

In order to identify the dominating ionization channels at the different intensities, a comparison of the experimental data with calculational results is often essential. For this purpose, several groups are presently performing momentum resolved calculations on lithium in intense laser fields, based on our experimental parameters. These include B. Najjari and A. Voitkiv from our own group at MPI-K, Heidelberg who employ the strong field approximation (SFA) [Rei94], D. Bauer, also from MPI-K, who is performing a numerical solution of the time-dependent-Schrödinger equation (TDSE) [Bau06] within the single active electron approximation (SAE). There, the atom is modeled as one electron in an effective nuclear potential, which is chosen such, that it generates matching binding energies for the bound states of the active electron. Results on lithium obtained by solving the TDSE will also be supplied by C. D. Lin from Kansas State University, Manhattan, Kansas.

Virtually on finishing this thesis, first calculated spectra became available. We were provided with a calculated momentum spectrum for a 10 fs pulse with a peak intensity $5 \cdot 10^{12}$W/cm^2 by C. D. Lin, as presented in Fig. 5.18 a). The electron ejection in the direction perpendicular to the polarization axis is reproduced and very pronounced. For comparison, Fig. 5.18 b) and c) depict two measured spectra taken under similar conditions in the same representation. Though our spectra appear stretched along the transversal momentum axis, what can be attributed to the low momentum resolution along that direction, the overall structure is reproduced by the calculation and supports the assumption that the electrons with near zero longitudinal momentum are ejected with a finite momentum component into the perpendicular direction.

A possible explanation lies in the angular distribution of the photoelectrons. In general, the angular distributions of multiphoton ionization are not easily predicted, even in the case of relatively few photons needed to ionize, as intermediate resonances occuring within the pulse can have a drastic influence [Pet84], [Gon75]. Exceptions are special cases like Freeman resonances, where a Rydberg state with a particular angular momentum l is resonantly populated and ionizes by absorption of just one additional photon. The selection rule for one-photon absorption from a linearly polarized light field $\Delta l = \pm 1$; $\Delta m = 0$ allows the identification of the Rydberg state by the angular distribution of the photoelectrons, e.g. electrons ionized from a nd-state with l=2 emerge as a superposition of a p- and a d-wave ($l' = l \pm 1$) [Rot90], [Sch98b], [Wie03]. In a first approximation, this selection rule is applied N times for N-photon absorption. For example in the case of lithium the ionized $2s$-electron can reach the s, d and g-continua. For high intensities, Chen *et al.* have derived an empirical rule from extensive TDSE calculations for different atomic systems, wavelengths and peak intensities which relates the number of peaks in the

two-dimensional spectra and thus the dominant angular momentum state of the outgoing electrons to the number of photons needed to ionize [Che06]: For ionization from both the $2s$ and the $2p$ state, the dominant angular momentum quantum number should be $l = 2$, leading to a d-wave with two nodes and three lobes in the angular distribution. This is in agreement with our observations from ionization from the $2s$ state at high intensities (Fig. 5.18). One must be aware, that this rule was derived from calculations modeling systems like Ar, He and H at laser intensities and wavelengths, that result in an Keldysh parameter γ close to unity, i.e. far beyond the regime of multiphoton ionization and a perturbative description of the system. Since in our measurements the third peak vanishes for low intensities one might speculate about the following: Firstly, the rule does not apply in the perturbative regime of pure multiphoton ionization, i.e. at low intensities. Secondly: For higher intensities, when a perturbative treatment no longer applies, the validity of the rule is restored. This might just be the case, when the over-the-barrier intensity is approached. Still, the observed pronounced maximum perpendicular to the polarization axis is somewhat peculiar. Most published photoelectron angular distributions (measured as well as calculated) show a marked forward characteristic, with only minor contributions by a sidelobe at 90° [Hum85], [Rot90], [Sch98b], this being still the case for a low number of absorbed photons [Wol88], [Nic92], [Dix81]. Petite *et al.* present a calculation for 4-photon ionization of cesium, which reveals sidelobes at 90°of almost the same strength as the forward lobe for intensities of 10^{10} W/cm^2 and of about 40% of the forward peak strength for intensities of $6 \cdot 10^{11}$ W/cm^2, which are not fully reproduced by the corresponding measurement [Pet84].
An upcoming focused measurement with improved resolution and further calculations will bring more insight into this issue. D. Bauer is presently completing a comprehensive dataset of calculations for different intensities, which can be analyzed for electron energy, emission angle and the contribution of the different partial waves.

Conclusion and Outlook

The aim of this work was to create a unique apparatus for the investigation of atomic ionization dynamics of lithium atoms and to perform first measurements, by combining two state-of-the-art experimental techniques of contemporary atomic physics for the first time: These are laser cooling and trapping of neutral atoms in the form of a magneto-optical trap (MOT) on the one side, and multi-particle imaging techniques, namely reaction microscopes on the other side. While the reaction microscope delivers the capability of measuring the full vector momenta of all charged fragments emerging from an ionization reaction in coincidence, the magneto-optical trap provides an ultracold, well localized target in order to fully exploit the possible momentum resolution of the reaction microscope. With this unique setup the three-electron 'model system' lithium becomes available as a target for kinematically complete measurements on atomic fragmentation by virtually all kinds of projectile species, which include electrons, ions, intense laser pulses or high energetic photons. This experimental versatility has so far been restricted to gaseous species that can be prepared in a supersonic gas jet to produce an internally cold target, first of all the noble gases.

In the course of this thesis, this complex and novel apparatus was planned, designed, assembled and taken into operation. This required the use of forefront technologies from a wide variety of fields: A newly designed vacuum chamber houses a compact combined electron and recoil-ion spectrometer in time-focusing geometry together with two time- and position sensitive detectors for coincident ion- and electron detection and a set of water-cooled intra-vacuum coils. The magneto-optical trap is now operated by a semiconductor-based master oscillator - tapered amplifier configuration, which can deliver over 400 mW of frequency-locked light to the experiment for operation of the magneto-optical trap. A Zeeman slower delivers a slow atomic beam for fast and efficient loading of the trap. To overcome the problem of the basic incompatibility between the electron spectrometer's homogeneous electron extraction field and the strong magnetic gradient needed for magneto-optical trapping the trapping field can be rapidly ramped up and down within 400 μs to create field free conditions for data acquisiton at rates as high as 300 Hz.

Despite (or because) many problems and setbacks had to be mastered, the whole setup finally demonstrates a superior reliability and ease of operation, which allows for trouble-free data acquisition during long-term measurement campaigns. A MOT-target of several 10^7 lithium atoms with a peak density of 10^{10} atoms/cm^3 and temperatures in the range

of 500 μK is loaded within few seconds, and can be released and recaptured for over a thousand experimental cycles before the trap population is reduced to 20% of its initial value and the trap has to be loaded again. The trapping parameters and sequence timings are widely configurable by the experimental control system, which enables an on-line optimization of the event rate and target properties. Background pressures of less than $5 \cdot 10^{-11}$ mbar meet the requirements even of the demanding high intensity laser experiments. Besides, in contrast to a supersonic gas jet, the target characteristics such as density and temperature can be varied over a wide range and determined independently any time by standard diagnostic means, to adapt the target to the requiremnets of the respective experiment. In addition, the magneto-optical trap provides the unique capability of further manipulation of the target atoms to prepare specific target states. Thus, an unparalleled experimental setup is ready for operation, providing a new class of target for the fully differential exploration of ionization reactions.

Upon completion of the setup, the first ever measurements on multiphoton ionization of lithium atoms in intense laser fields, using pulses of 25 fs duration at 800 nm wavelength from a Titanium:Sapphire ocillator-amplifier, were conducted. High resolution recoil-ion momentum spectra were obtained for a broad range of intensities, spanning from 10^{11} W/cm^2 to 10^{16} W/cm^2. While at lower intensities, structures as expected for pure multiphoton ionization were observed, spectra taken at high intensities showed surprising features, such as a pronounced electron ejection perpendicular to the laser's polarization axis at high intensities, which is not fully understood yet. Already in the first measurements, the marked differences in the atomic structure of lithium as compared to rare gas atoms became clearly apparent.
This in turn has also sparked the interest of theory groups in the issue of alkali metals in intense laser fields, and several theoretical calculations are presently under way, of which first results were presented in this thesis. As the data is still partly inconclusive due to a lack in statistics, a next round of multiphoton ionization measurements will be started soon with the aim to acquire comprehensive benchmark data for the calculations being done. As these measurements have hardly utilized the full capabilities of this experiment, this tellingly demonstrates the potential of our new setup and the possibilities for future research.

Concerning the experimental side, there is always the proverbial room for improvement: Presently, the ion spectrometer is being upgraded to a position focusing configuration, to preserve the ion spectrometer resolution in the directions transversal to the ion extraction field, when the reaction zone is somewhat extended. Thus one can still take full advantage of the ultralow momentum scatter of the lithium cloud, when working with electron (or ion) beams.
The laser system will also see a major upgrade in the near future: Optical fibers will be used for the transport of the trapping laser light to the experimental chamber. Thus the laser can be freed from its optical table and the whole apparatus is easily made trans-

portable, guaranteeing the ultimate flexibility in the choice of projectile beam sources, which extends to synchrotrons or the free electron laser (FEL) FLASH. Furthermore, the installation of a transversal Doppler-cooling section at the exit of the atomic beam source to enhance the flux of slow atoms through the MOT-region will boost the trap loading rate by a factor of hundred, reducing the dead-time due to loading of the trap and increasing the efficiency of data acquisition.

Among the experiments to be carried out in the near future are electron impact ionization of angular momentum oriented excited lithium atoms [Dor98], making use of the possibility of target preparation the MOT offers . In the field of multiphoton ionization, an idea is going to longer wavelengths up to 10 μm by means of an optical parametric amplifier (OPA), at which, by means of the higher ponderomotive potential, probabilities are higher to observe double ionization induced by the recollision mechanism.
With a fully transportable setup measurements at newest generation light sources like the free electron laser FLASH with its unmatched flux of soft X-ray photons in Hamburg will become possible. In a first campaign starting end of the year, the goal is to get a kinematically complete picture of single-photon induced double- and triple ionization, which is a sensitive probe for inter-electronic correlations. In conjunction with the simple atomic structure of lithium and the possibility of target state orientation the coherent soft X-ray pulses of FLASH will enable unprecedented insight into the correlated electron dynamics within the atom and in the three- and four-body Coulomb continuum.

The capabilities of our setup are not confined to the study of single atoms, as the sample of ultracold atoms in combination with the implemented diagnostic means organically enables to progress towards the exploration of collective phenomena.
One of the intriguing possibilities is the observation of ultracold neutral plasmas, formed by photoionization of laser cooled atoms at photon energies close to ionization threshold [Kil99]. This regime is of fundamental importance, as it allows for laboratory production of strongly coupled plasmas, where the Coulombic interaction energy between the particles E_C exceeds their thermal energy E_T, a condition that is otherwise only realized in extreme astrophysical environments such as the interior of white dwarves or gas giant planets, or as a transient state in solids and cluster targets upon irradiation with superintense laser pulses. Equilibrium in these systems is of particular interest, as it involves the establishment of spatial correlations between particles and possibly Coulomb crystallization if the coupling parameter $G = E_C/E_T$ is large enough [Poh04]. However, the strong coupling regime cannot be directly reached from the initial conditions provided by a MOT, as the plasma is created in a completely uncorrelated state. The subsequent conversion of potential into kinetic energy leads to a strong heating of both the electronic and ionic component of the system, which suppresses the formation of substantial correlations [Kuz02]. Further laser cooling of the ions during expansion of the plasma has been suggested to overcome this problem [Kil03], and molecular dynamics simulations seem to confirm the applicability of this method [Poh04]. With our MOT-target, a completely new regime of

ultracold strongly coupled plasmas becomes accessible: Owing to the extremely high photon fluence of the free-electron laser FLASH, already with the present specifications up to 10^6 trapped lithium atoms could be inner-shell ionized by 59 eV photons within a single FEL pulse train (either directly or by excitation to Rydberg states and subsequent photo- or field-ionization), thus creating an ultracold plasma of 'hollow' $Li^+(1s2s\ ^3S_1)$-ions. This highly excited, metastable state has a radiative lifetime of $\tau \approx 50$ s [Kni80]. In analogy to laser cooling of metastable helium, these ions are laser cooled via the $(1s2s\ ^3S_1$–$1s2p\ ^3P_2)$-transition. The corresponding wavelength of 548 nm is easily provided by dye lasers. In this way the first ion MOT and the first metastable, threefold inverted plasma – the internal excitation energy is larger than the Coulomb energy and, in the strong coupling-regime, much larger than the thermal energy – could be realized. Apart from optical diagnosis of the plasma, the intrinsic abiltiy of our setup to detect both electrons and ions can be used to great advantage, enabling unprecedented studies of ultracold strongly correlated plasmas and Coulomb crystallization.

Another path to explore starting from a magneto-optical trap is the wide field of atomic quantum gases. We are presently considering the implementation of a deep optical dipole trap [Gri00] for confinement of the laser cooled target atoms during the measurement process in order to forbear a permanent switching of the trap's magnetic field, thus further enhancing the efficiency of data collection. By evaporative cooling such a conservative atomic trap can provide lower target temperatures and higher densities than achievable by laser cooling alone and opens the door to experimentation on atomic samples in the quantum degenerate regime. The bosonic ^{7}Li itself is not the ideal candidate for the production of Bose-Einstein condensates, since the mean field interaction between the atoms becomes attractive at low temperatures, effectively rendering condensates with atom numbers larger than a few thousand unstable [Bra95], [Bra97]. However, due to the presence of the fermionic isotope ^{6}Li in natural lithium, simultaneous cooling and trapping of bosonic and fermionic lithium can be realized even by using the same laser source [Mew99]. Thus, the bosonic ^{7}Li could be employed as a sympathetic coolant for the fermionic population on the way to Fermi degeneracy. So far, the interaction of atoms in the compound of degenerate quantum gases with energetic projectiles and the response of the atomic collective has remained largely unexplored. In a pioneering experiment, Ciampini *et al.* have studied one- and two-photon ionization from a Bose gas of rubidium atoms in a magnetic trap, where the effect of the produced cold charged particles on the condensate in terms of heating and collective excitations was probed [Cia02]. In these systems, optical diagnostics in conjunction with the capabilities of momentum resolved particle detection of the reaction microscope could open up a completely new field of collisional physics.

Appendix A: Atomic Units

Quantity	Formula	SI units
Mass	m_e	$9.10938 \cdot 10^{-31}$ kg
Charge	e	$1.60218 \cdot 10^{-19}$ C
Length	a_0	$5.29177 \cdot 10^{-11}$ m
Velocity	v_0	$2.18769 \cdot 10^{6}$ m s^{-1}
Time	a_0/v_0	$2.41888 \cdot 10^{-17}$ s
Momentum	$m_e v_0$	$1.99285 \cdot 10^{-24}$ kg m s^{-1}
Angular momentum	$\hbar = a_0 m_e v_0$	$1.05457 \cdot 10^{-34}$ kg m^2 s^{-1}
Frequency	$v_0/(2\pi a_0)$	$6.57969 \cdot 10^{15}$ Hz
Angular frequency	v_0/a_0	$4.13414 \cdot 10^{16}$ s^{-1}
Energy	$e^2/(4\pi\epsilon_0 a_0^2)$	27.2116 eV
Electric field	$e/(4\pi\epsilon_0 a_0^2)$	$5.14221 \cdot 10^{11}$ V m^{-1}
Magnetic field	$\hbar/(e a_0^2)$	$2.35052 \cdot 10^{5}$ T
Intensity	$1/2\ c\epsilon_0 (e/(4\pi\epsilon_0 a_0^2))^2$	$3.50953 \cdot 10^{16}$ W cm^{-2}

Quantity	Formula	SI units	Atomic units
Electron mass	m_e	$9.10938 \cdot 10^{-31}$ kg	1
Elementary charge	e	$1.60218 \cdot 10^{-19}$ C	1
Planck constant	$\hbar$	$1.05457 \cdot 10^{-34}$ kg m^2 s^{-1}	1
Proton mass	m_p	$1.67262 \cdot 10^{-27}$ kg	1836.15
Atomic mass unit	amu $= \frac{1}{12} m(^{12}\mathrm{C})$	$1.66054 \cdot 10^{-27}$ kg	1822.89
Velocity of light	c	$2.99792 \cdot 10^{8}$ m s^{-1}	137.04
Influence constant	ϵ_0	$8.85419 \cdot 10^{-12}$ A s V^{-1} m^{-1}	$1/(4\pi)$
Induction constant	$\mu_0 = 1/(c^2\epsilon_0)$	$e\pi \cdot 10^{-7}$ V s A^{-1} m^{-1}	$4\pi/137.04^2$

Appendix B:
Pictures from the Lab

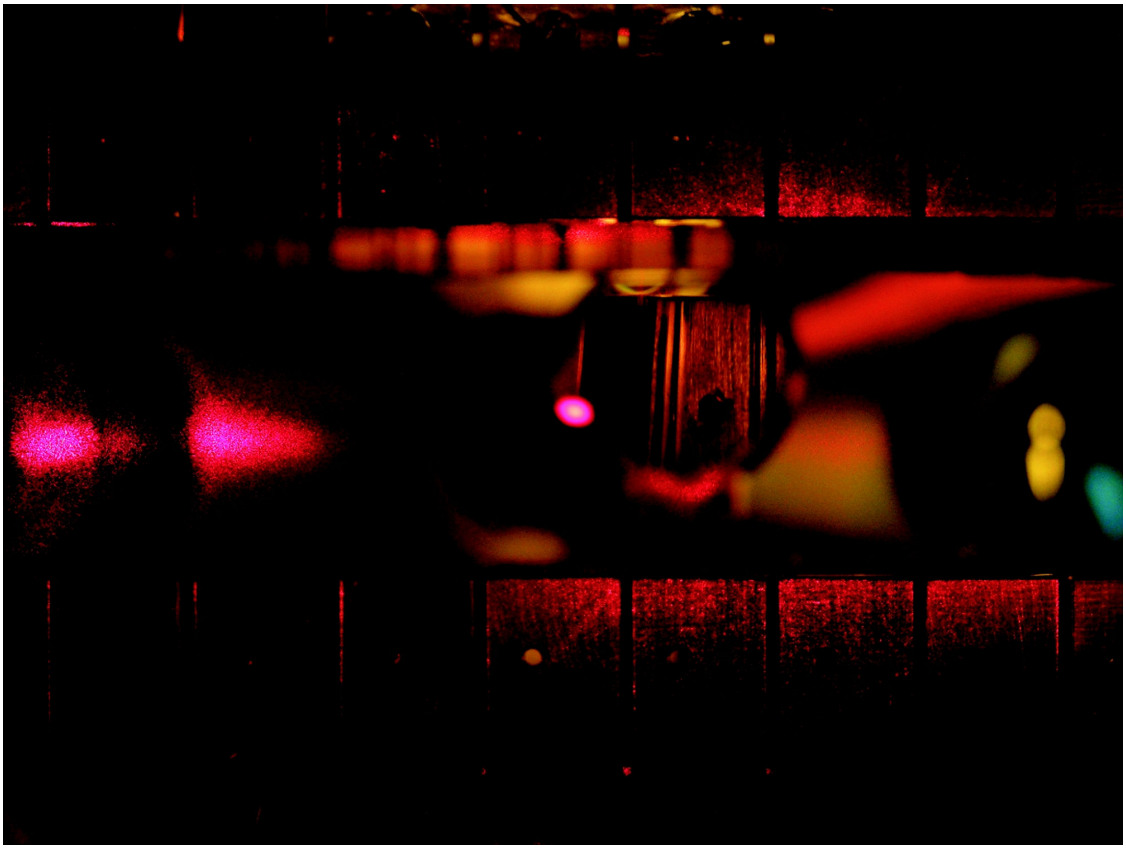

Lithium-MOT of about 10^7 atoms floating in between the spectrometer electrodes. The mirror in the background is for focusing the laser pulses.

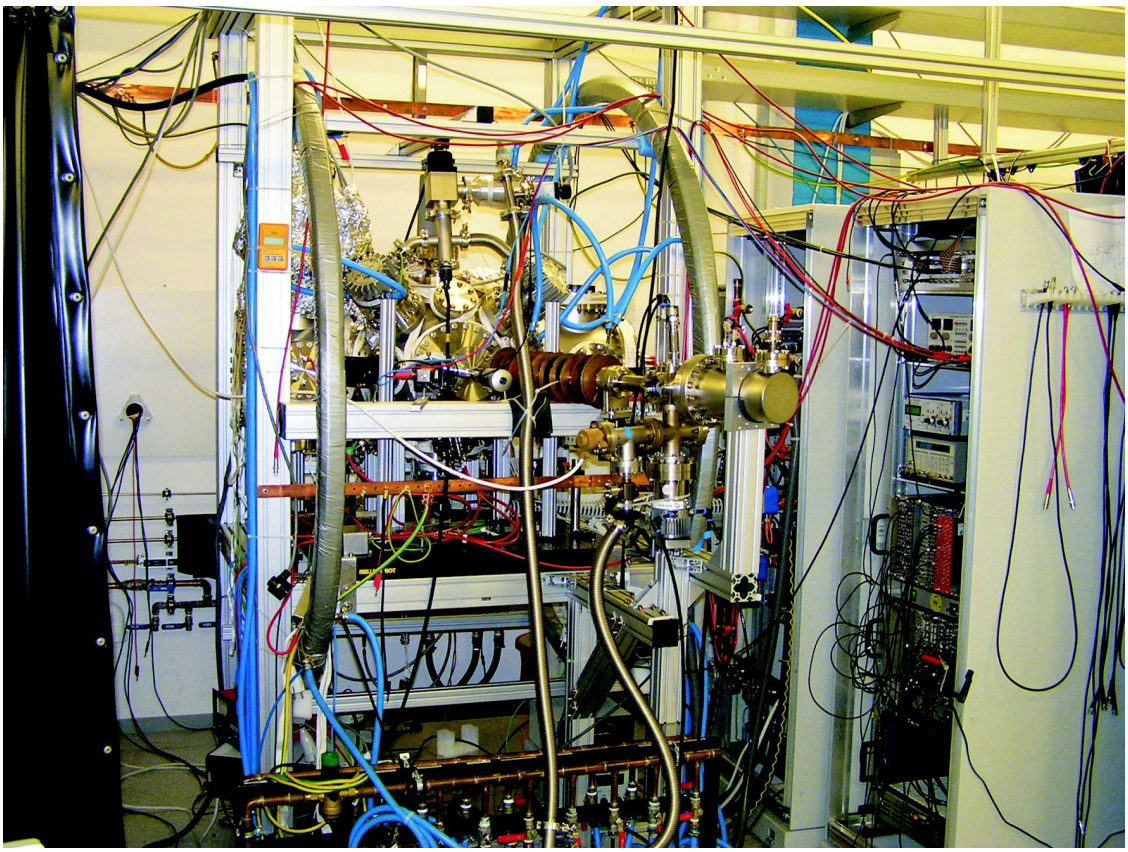

View of the experimental site. The lasers are hidden in the laser lab behind the wall.

Bibliography

[Abb87] G. L. Abbas, S. Yang, V. W. S. Chang, J. G. Fujimoto, *Injection behavior of high-power broad-area diode lasers*, Optics Letters **12**, 605 (1987).

[Ago79] P. Agostini, F. Fabre, G. Mainfray, G. Petite, N. K. Rahman, *Free-Free Transitions Following Six-Photon Ionization of Xenon Atoms*, Phys. Rev. Lett. **42**(17), 1127–1130 (Apr 1979).

[Ago89] P. Agostini, P. Breger, A. L'Huillier, H. G. Muller, G. Petite, A. Antonetti, A. Migus, *Giant Stark shifts in multiphoton ionization*, Phys. Rev. Lett. **63**(20), 2208–2211 (Nov 1989).

[Aln04] A. S. Alnaser, X. M. Tong, T. Osipov, S. Voss, C. M. Maharjan, B. Shan, Z. Chang, C. L. Cocke, *Laser-peak-intensity calibration using recoil-ion momentum imaging*, Phys. Rev. A **70**, 023413 (2004).

[Aln05] A. S. Alnaser, B. Ulrich, X. M. Tong, I. V. Litvinyuk, C. M. Maharjan, P. Ranitovic, T. Osipov, R. Ali, S. Ghimire, Z. Chang, C. D. Lin, C. L. Cocke, *Simultaneous real-time tracking of wave packets evolving on two different potential curves in H_2^+ and D_2^+*, Phys. Rev. A **72**, 030702 (2005).

[Amm86] M. V. Ammosov, N. B. Delone, V. P. Krainov, *Tunnel ionization of complex atoms and of atomic ions in an alternating electromagnetic field*, Sov. Phys. JETP **64**, 1191 (1986).

[And95] M. H. Anderson, J. R. Ensher, M. R. Matthews, C. E. Wieman, E. A. Cornell, *Observation of Bose-Einstein Condensation in a Dilute Atomic Vapor*, Science **269**, 198 (1995).

[Ari77] E. Arimondo, M. Inguscio, P. Violino, *Experimental determinations of the hyperfine structure in the alkali atoms*, Rev. Mod. Phys. **49**(1), 31–75 (Jan 1977).

[Aug89] S. Augst, D. Strickland, D. D. Meyerhofer, S. L. Chin, J. H. Eberly, *Tunneling Ionization of Noble Gases in a High-Intensity Laser Field*, Phys. Rev. Lett. **63**(20), 2212–2215 (1989).

[Bal79] V. I. Balykin, V. S. Lethokov, V. I. Mushin, *Observation of the cooling of free sodium atoms in a resonance laser field*, JETP Letters **29**(10), 560–564 (1979).

[Bal03] A. Baltuska, T. Udem, M. Uiberacker, M. Hentschel, E. Goulielmakis, C. Gohle, R. Holzwarth, V. S. Yakolev, A. Scrinzi, T. W. Hänsch, F. Krausz, *Attosecond control of electronic processes by intense light fields*, Nature **421**, 593 (2003).

[Bar04] M. Bartenstein, A. Altmeyer, S. Riedl, S. Jochim, C. Chin, J. H. Denschlag, R. Grimm, *Crossover from a Molecular Bose-Einstein Condensate to a Degenerate Fermi Gas*, Physical Review Letters **92**(12), 120401 (2004).

[Bau99] D. Bauer, P. Mulser, *Exact field ionization rates in the barrier-suppression regime from numerical time-dependent Schrödinger-equation calculations*, Phys. Rev. A **59**, 569–577 (1999).

[Bau06] D. Bauer, P. Koval, *QPROP: A Schrödinger-solver for intense laser-atom interaction*, Computer Physics Communications **174**, 396–421 (2006).

[Beb66] H. B. Bebb, A. Gold, *Multiphoton Ionization of Hydrogen and Rare-Gas Atoms*, Phys. Rev. **143**(1), 1–24 (Mar 1966).

[Bjo83] G. C. Bjorklund, M. D. Levenson, W. Lenth, C. Ortiz, *Frequency Modulation (FM) Spectroscopy*, Appl. Phys. B **32**, 145–152 (1983).

[Blo99] I. Bloch, T. W. Hänsch, T. Esslinger, *Atom laser with a cw Output Coupler*, Phys. Rev. Lett. **82**(15), 3008 (1999).

[Boe92] M. P. de Boer, H. G. Muller, *Observation of large populations in excited states after short-pulse multiphoton ionization*, Phys. Rev. Lett. **68**(18), 2747–2750 (May 1992).

[Bra95] C. C. Bradley, C. A. Sackett, J. J. Tollett, R. G. Hulet, *Evidence of Bose-Einstein Condensation in an Atomic Gas with Attractive Interactions*, Phys. Rev. Lett. **75**(9), 1687–1690 (Aug 1995).

[Bra97] C. C. Bradley, C. A. Sackett, R. G. Hulet, *Bose-Einstein Condensation of Lithium: Observation of Limited Condensate Number*, Phys. Rev. Lett. **78**(6), 985–989 (Feb 1997).

[Bre03] R. Bredy, H. Nguyen, H. Camp, X. . Fléchard, B. DePaola, *MOTRIMS as a generalized probe of AMO processes*, Nucl. Instr. and Meth. in Phys. Res. B **205**, 191–195 (2003).

[Bro01] I. N. Bronstein, K. A. Semendajew, G. Musiol, H. Mühlig, *Taschenbuch der Mathematik* (Verlag Harri Deutsch, Frankfurt am Main, 2001), 5th Edn.

[Cam89] P. Camus, M. Kompitsas, S. Cohen, C. Nicolaides, M. Aymar, M. Crance, P. Pillet, *Multiphoton single and double ionisation of strontium in the range 532-541 nm*, J. Phys. B: At. Mol. Opt. Phys. **22**, 445–458 (1989).

[Che99] S. Chelkowski, P. B. Corkum, A. D. Bandrauk, *Femtosecond Coulomb Explosion Imaging of Vibrational Wave Functions*, Phys. Rev. Lett. **82**(17), 3416–3419 (Apr 1999).

[Che06] Z. Chen, T. Morishita, A.-T. Le, M. Wickenhauser, X. M. Tong, C. D. Lin, *Analysis of two-dimensional photoelectron momentum spectra and the effect of the long-range Coulomb potential in single ionization of atoms by intense lasers*, Physical Review A (Atomic, Molecular, and Optical Physics) **74**(5), 053405 (2006).

[Chu86] S. Chu, J. E. Bjorkholm, A. Ashkin, A. Cable, *Experimental Observation of Optically Trapped Atoms*, Phys. Rev. Lett. **57**(3), 314–317 (Jul 1986).

[Cia02] D. Ciampini, M. Anderlini, J. H. Müller, F. Fuso, O. Morsch, J. W. Thomsen, E. Arimondo, *Photoionization of ultracold and Bose-Einstein-condensed Rb atoms*, Phys. Rev. A **66**(4), 043409 (Oct 2002).

[Coh77] Coherent, *Model CR-599-21 Scanning Single Frequency Dye Laser* (1977).

[Col01] J. Colgan, M. S. Pindzola, D. M. Mitnik, D. C. Griffin, I. Bray, *Benchmark Nonperturbative Calculations for the Electron-Impact Ionization of $Li(2s)$ and $Li(2p)$*, Phys. Rev. Lett. **87**(21), 213201 (Nov 2001).

[Col04] J. Colgan, M. S. Pindzola, F. Robicheaux, *Lattice Calculations of the Photoionization of LI*, Phys. Rev. Lett. **93**, 053201 (2004).

[Col06] J. Colgan, M. S. Pindzola, *Energy differential cross sections for the triple photoionization of lithium*, J. Phys. B: At. Mol. Opt. Phys. **39**, 1879–1887 (2006).

[Cor89] P. B. Corkum, N. H. Burnett, F. Brunel, *Above-threshold ionization in the long-wavelength limit*, Phys. Rev. Lett. **62**(11), 1259–1262 (Mar 1989).

[Cor93] P. B. Corkum, *Plasma perspective on strong field multiphoton ionization*, Phys. Rev. Lett. **71**(13), 1994–1997 (Sep 1993).

[Dah96] M. Dahan, E. Peik, J. Reichel, Y. Castin, C. Salomon, *Bloch Oscillations of Atoms in an Optical Potential*, Phys. Rev. Lett. **76**, 4508 (1996).

[Dal89] J. Dalibard, C. Cohen-Tannoudji, *Laser cooling below the Doppler limit by polarization gradients: simple theoretical models*, J. Opt. Soc. Am. B **6**, 2023–2045 (1989).

[Dav95] K. B. Davis, M. O. Mewes, M. R. Andrews, N. J. van Druten, D. S. Durfee, D. M. Kurn, W. Ketterle, *Bose-Einstein Condensation in a Gas of Sodium Atoms*, Phys. Rev. Lett. **75**(22), 3969–3973 (Nov 1995).

[Ded01] C. J. Dedman, K. G. H. Baldwin, M. Colla, *Fast switching of magnetic fields in a magneto-optic trap*, Rev. Sci. Instrum. **72**(11), 4055–4058 (November 2001).

[Ded04] C. J. Dedman, J. Nes, T. M. Hanna, R. G. Dall, K. G. H. Baldwin, A. G. Truscott, *Optimum design and construction of a Zeeman slower for use with a magneto-optic trap*, Review of Scientific Instruments **75**(12), 5136–5142 (2004).

[Del91] N. B. Delone, V. P. Krainov, *Energy and angular electron spectra for the tunnel ionization of atoms by strong low-frequency radiation*, J. Opt. Soc. Am. B **8**(6), 1207–1211 (1991).

[Del98] N. B. Delone, V. P. Krainov, *Tunneling and barrier-suppression ionization of atoms and ions in a laser radiation field*, Physics-Uspekhi **41**(5), 469–485 (1998).

[Del99] N. B. Delone, V. P. Krainov, *Multiphoton Processes in Atoms*, Springer series on atoms and plasmas (Springer, 1999), 2nd Edn.

[Dem81] W. Demtröder, *Laser Spectroscopy* (Springer-Verlag, 1981), 3rd Edn.

[Dem95] W. Demtröder, *Experimentalphysik 2* (Springer-Verlag, 1995), 1st Edn.

[Den99] L. Deng, E. W. Hagley, J. Wen, M. Trippenbach, Y. Band, P. S. Julienne, J. E. Simsarian, K. Helmerson, S. L. Rolston, W. D. Philips, *Four-wave mixing with matter waves*, Nature **398**, 218 (1999).

[Die94] P. Dietrich, N. H. Burnett, M. Ivanov, P. B. Corkum, *High-harmonic generation and correlated two-electron multiphoton ionization with elliptically polarized light*, Phys. Rev. A **50**(5), R3585–R3588 (Nov 1994).

[Die98] K. Dieckmann, R. J. C. Spreeuw, M. Weidemüller, J. T. M. Walraven, *Two-dimensional magneto-optical trap as a source of slow atoms*, Phys. Rev. A **58**(5), 3891–3895 (Nov 1998).

[Din92] T. P. Dinneen, C. D. Wallace, K.-Y. N. Tan, P. L. Gould, *Use of trapped atoms to measure absolute photoionization cross sections*, Optics Letters **17**(23), 1706 (1992).

[Dix81] S. N. Dixit, P. Lambropoulos, *Angular Distribution of Photoelectrons in Strongly Driven Multiphoton Transitions*, Phys. Rev. Lett. **46**(19), 1278–1281 (May 1981).

[Don02] E. A. Donley, N. R. Claussen, S. T. Thompson, C. Wieman, *Atom-molecule coherence in a Bose-Einstein condensate*, Nature **417**, 529 (2002).

[Dör97] R. Dörner, V. Mergel, L. Spielberger, M. Achler, K. Khayyat, T. Vogt, H. Bräuning, O. Jagutzki, T. Weber, J. Ullrich, R. Moshammer, M. Unverzagt, W. Schmitt, H. Khemliche, M. H. Prior, C. L. Cocke, J. Feagin, R. E. Olson, H. Schmidt-Böcking, *Kinematically complete experiments using cold target recoil ion momentum spectroscopy*, Nucl. Instr. and Meth. B **124**, 225–231 (1997).

[Dor98] A. Dorn, A. Elliott, J. Lower, E. Weigold, J. Berakdar, A. Engelns, H. Klar, *Orientational Dichroism in the Electron-Impact Ionization of Laser-Oriented Atomic Sodium*, Phys. Rev. Lett. **80**(2), 257–260 (Jan 1998).

[Dor01] A. Dorn, A. Kheifets, C. D. Schröter, B. Najjari, C. Höhr, R. Moshammer, J. Ullrich, *Double Ionization of Helium by Electron Impact: Complete Pictures of the Four Body Breakup Dynamics*, Phys. Rev. Lett. **86**(17), 3755–3758 (2001).

[Dor02a] A. Dorn, A. Kheifets, C. D. Schröter, B. Najjari, C. Höhr, R. Moshammer, J. Ullrich, *Double ionization of helium by electron impact in the impulsive regime*, Phys. Rev. A **65**(3), 032709 (Feb 2002).

[Dör02b] R. Dörner, T. Weber, M. Weckenbrock, A. Staudte, M. Hattass, H. Schmidt-Böcking, R. Moshammer, J. Ullrich, *Multiple Ionization in Strong Laser Fields*, Advances in Atomic, Molecular and Optical Physics **48**, 1–34 (2002).

[Dre83] R. Drever, J. Hall, F. Kowalski, J. Hough, G. Ford, A. Munley, H. Ward, *Laser Phase and Frequency Stabilization Using an Optical Resonator*, Appl. Phys. B **31**, 97–105 (1983).

[Dre01] M. Drescher, M. Hentschel, R. Kienberger, G. Tempea, C. Spielmann, G. A. Reider, P. B. Corkum, F. Krausz, *X-ray Pulses Approaching the Attosecond Frontier*, Science **291**, 1923–1927 (2001).

[Dru95] N. van Druten, R. Trainham, H. Muller, *Above-threshold ionization of cesium by 1.9-μm light*, Phys. Rev. A **51**(2), R898–R901 (Feb 1995).

[Dür06a] M. Dürr, *Electron Induced Break-up of Helium: Benchmark Experiments on a Dynamical Four-Body Coulomb System*, Phd thesis, Universität Heidelberg / Max-Planck-Institut für Kernphysik, Heidelberg (2006).

[Dür06b] M. Dürr, C. Dimopoulou, A. Dorn, B. Najjari, I. Bray, D. V. Fursa, Z. Chen, D. H. Madison, K. Bartschat, J. Ullrich, *Single ionization of helium by 102 eV electron impact: three-dimensional images for electron emission*, J. Phys. B: At. Mol. Opt. Phys. **39**, 4097–4111 (2006).

[Dür06c] M. Dürr, C. Dimopoulou, B. Najjari, A. Dorn, J. Ullrich, *Three-Dimensional Images for Electron-Impact Single Ionization of He: Complete and Comprehensive (e,2e) Benchmark Data*, Phys. Rev. Lett. **96**, 243202 (2006).

[Dür07] M. Dürr, A. Dorn, J. Ullrich, S. P. Chao, A. Czasch, A. S. Kheifets, J. R. Götz, J. S. Briggs, *(e,3e) on Helium at Low Impact Energy: The Strongly Correlated Three-Electron Continuum*, Phys. Rev. Lett. **98**, 193201 (2007).

[Ebe88] J. H. Eberly, J. Javanainen, *Above threshold-ionisation*, Eur. J. Phys. **9**, 265–275 (1988).

[Ehr69] H. Ehrhardt, M. Schulz, T. Tekaat, K. Willmann, *Ionization of Helium : Angular Correlation of the Scattered and Ejected Electrons*, Phys. Rev. Lett. **22**, 89 (1969).

[Eic00] U. Eichmann, M. Dörr, H. Maeda, W. Becker, W. Sandner, *Collective Multielectron Tunneling Ionization in Strong Fields*, Phys. Rev. Lett. **84**(16), 3550–3553 (Apr 2000).

[Emm06a] A. Emmanouilidou, J. M. Rost, *The Coulomb four-body problem in a classical framework: triple photoionization of lithium*, J. Phys. B: At. Mol. Opt. Phys. **39**, 4037–4048 (2006).

[Emm06b] A. Emmanouilidou, J. M. Rost, *Triple photoionization of lithium near threshold*, J. Phys. B: At. Mol. Opt. Phys. **39**(5), L99–L103 (2006).

[Ems95] J. Emsley, *The Elements*, Oxford Chemistry Guides (Oxford. Univ. Press, New York, NY, 1995).

[Eng97] H. Engler, *Aufbau eines Zeeman-Abbremsers und Inbetriebnahme einer magnetooptischen Falle für Lithium-Atome*, Diploma thesis, Universität Heidelberg / Max-Planck-Institut f. Kernphysik Heidelberg (1997).

[Erg05] T. Ergler, A. Rudenko, B. Feuerstein, K. Zrost, C. D. Schröter, R. Moshammer, J. Ullrich, *Time-Resolved Imaging and Manipulation of H_2 Fragmentation in Intense Laser Fields*, Phys. Rev. Lett. **95**, 093001 (2005).

[Erg06] T. Ergler, A. Rudenko, B. Feuerstein, K. Zrost, C. D. Schröter, R. Moshammer, J. Ullrich, *Spatiotemporal Imaging of Ultrafast Molecular Motion: Collapse and Revival of the D_2^+ Nuclear Wave Packet*, Phys. Rev. Lett. **97**, 193001 (2006).

[Ert85] W. Ertmer, R. Blatt, J. L. Hall, M. Zhu, *Laser Manipulation of Atomic Beam Velocities: Demonstration of Stopped Atoms and Velocity Reversal*, Phys. Rev. Lett. **54**(10), 996–999 (Mar 1985).

[Fab82] F. Fabre, G. Petite, P. Agostini, M. Clement, *Multiphoton above -threshold ionisation of xenon at 0.53 and 1.06 μm*, J. Phys B: At. Mol. Phys. **15**, 1353–1369 (1982).

[Fer88] M. Ferray, A. L'Huillier, X. F. Li, L. A. Lompré, G. Mainfray, C. Manus, *Multiple-harmonic conversion of 1064 nm radiation in rare gases*, J. Phys. B: At. Mol. Opt. Phys **21**, L31–L35 (1988).

[Feu01] B. Feuerstein, R. Moshammer, D. Fischer, A. Dorn, C. D. Schröter, J. Deipenwisch, J. R. Crespo López-Urrutia, C. Höhr, P. Neumayer, J. Ullrich, H. Rottke, C. Trump, M. Wittmann, G. Korn, W. Sandner, *Separation of Recollision Mechanisms in Nonsequential Strong Field Double Ionization of Ar: The Role of Excitation Tunneling*, Phys. Rev. Lett. **87**(4), 043003 (Jul 2001).

[Feu07] B. Feuerstein (2007), personal communication.

[Fey96] A. Fey-den Boer, K. A. H. van der Leeuwen, H. C. W. Beijerinck, C. Fort, F. S. Pavone, *Grating feedback in a 810 nm broad-area diode laser*, Appl. Phys. B **63**, 117–120 (1996).

[Fis04] M. Fischer, N. Kolachevsky, M. Zimmermann, R. Holzwarth, T. Udem, T. W. Hänsch, M. Abgrall, J. Grünert, I. Maksimovic, S. Bize, H. Marion, F. P. D. Santos, P. Lemonde, G. Santarelli, P. Laurent, A. Clairon, C. S. M. Haas, U. D. Jentschura, C. H. Keitel, *New Limits on the Drift of Fundamental Constants from Laboratory Measurements*, Phys. Rev. Lett. **92**, 230802 (2004).

[Fit92] D. N. Fittinghoff, P. R. Bolton, B. Chang, K. C. Kulander, *Observation of nonsequential double ionization of helium with optical tunneling*, Phys. Rev. Lett. **69**(18), 2642–2645 (Nov 1992).

[Fit94] D. N. Fittinghoff, P. R. Bolton, B. Chang, K. C. Kulander, *Polarization dependence of tunneling ionization of helium and neon by 120-fs pulses at 614 nm*, Phys. Rev. A **49**(3), 2174–2177 (Mar 1994).

[Fle01] X. Flechard, H. Nguyen, E. Wells, I. Ben-Itzhak, B. D. DePaola, *Kinematically Complete Charge Exchange Experiment in the $Cs^+ + Rb$ Collision System Using a MOT Target*, Phys. Rev. Lett. **87**(12), 123203 (September 2001).

[Fre86] R. R. Freeman, T. J. McIlrath, P. H. Bucksbaum, M. Bashkansky, *Pondermotive effects on angular distributions of photoelectrons*, Phys. Rev. Lett. **57**(25), 3156–3159 (Dec 1986).

[Fre87] R. R. Freeman, P. H. Bucksbaum, H. Milchberg, S. Darack, D. Schumacher, M. E. Geusic, *Above-threshold ionization with subpicosecond laser pulses*, Phys. Rev. Lett. **59**(10), 1092–1095 (Sep 1987).

[Fre91] R. R. Freeman, P. H. Bucksbaum, *Investigations of above-threshold ionization using subpicosecond laser pulses*, J. Phys. B: At. Mol. Opt. Phys. **24**, 325–347 (1991).

[Geh98] E. Gehrig, B. Beier, K.-J. Boller, R. Wallenstein, *Experimental characterization and numerical modelling of an AlGaAs oscillator broad area double pass amplifier system*, Appl. Phys. B **66**, 287–293 (1998).

[Geh03] M. E. Gehm, *Preparation of an optically-trapped degenerate Fermi gas of ^6Li: Finding the route to degeneracy*, Phd-thesis, Duke university (2003).

[Gol88] L. Goldberg, M. K. Chun, *Injection locking characteristics of a 1 W broad stripe laser diode*, Appl. Phys. Lett. **53**(20), 1900–1902 (November 1988).

[Gon75] Y. Gontier, N. K. Rahman, M. Trahin, *Effect of intensity on angular distribution of photoelectrons in multiphoton ionization*, Physics Letters **53A**(1), 83–84 (1975).

[Gon80] Y. Gontier, M. Poirier, M. Trahin, *Multiphoton absorptions above the ionisation threshold*, J. Phys. B: At. Mol. Phys **13**, 1381–1387 (1980).

[Gre02] M. Greiner, O. Mandel, T. Esslinger, T. W. Hänsch, I. Bloch, *Quantum phase transition from a superfluid to a Mott insulator in a gas of ultracold atoms*, Nature **415**, 39–44 (2002).

[Gri00] R. Grimm, M. Weidemüller, Y. B. Ovchinnikov, *Optical Dipole Traps for Neutral Atoms*, Adv. At. Mol. Opt. Phys. **42**(95) (2000).

[Hän75] T. W. Hänsch, A. L. Schawlow, *Cooling of gases by laser radiation*, Optics Communications **13**, 68–69 (1975).

[Har03] M. L. Harris, *Design and Construction of an Improved Zeeman Slower*, Masters Thesis, Trinity College, Duke University (2003).

[Haw01] C. J. Hawthorn, K. P. Weber, R. E. Scholten, *Littrow configuration tunable external cavity diode laser with fixed direction output beam*, Rev. Sci. Instrum. **72**(12), 4477–4479 (December 2001).

[Her75] I. V. Hertel, A. S. Stamatović, *Spatial hole burning and oligo-mode distance control in cw dye lasers*, IEEE J. of Quant. Electr. **11**, 210 (1975).

[Her03] J. Herbig, T. Kraemer, M. Mark, T. Weber, C. Chin, H.-C. Nägerl, R. Grimm, *Preparation of a Pure Molecular Quantum Gas*, Science **301**, 1510 (2003).

[Hua99] M.-T. Huang, R. Wehlitz, Y. Azuma, L. Pibida, I. A. Sellin, J. W. Cooper, M. Koide, H. Ishijima, T. Nagata, *Single and double photoionization of lithium*, Phys. Rev. A **59**(5), 3397–3401 (May 1999).

[Hua02] M.-T. Huang, L. Zhang, S. Hasegawa, S. H. Southworth, L. Young, *Measurements of the electron-impact double-to-single ionization ratio using trapped lithium*, Phys. Rev. A **66**, 012715 (2002).

[Hua03] M.-T. Huang, W. W. Wong, M. Inokuti, S. Southworth, L. Young, *Triple Ionization of Lithium by Electron Impact*, Phys. Rev. Lett. **90**(16), 163201 (April 2003).

[Hum79] J. Humlíček, *An efficient method for evaluation of the complex probability function: The Voigt function and its derivatives*, J. Quant. Spectrosc. Radiat. Transfer **21**, 309–313 (1979).

[Hum85] H. J. Humpert, H. Schwier, R. Hippler, H. O. Lutz, *Angular distribution of photoelectrons from above-threshold ionization of Xe*, Phys. Rev. A **32**(6), 3787–3789 (Dec 1985).

[Ino99] S. Inouye, T. Pfau, S. Gupta, A. P. Chikkatur, A. Görlitz, D. E. Pritchard, W. Ketterle, *Phase-coherent amplification of atomic matter waves*, Nature **402**, 641–644 (1999).

[Jag02] O. Jagutzki, A. Cerezo, A. Czasch, R. Dörner, M. Hattaß, M. Huang, V. Mergel, U. Spillmann, K. Ullmann-Pfleger, T. Weber, H. Schmidt-Böcking, G. D. W. Smith, *Multiple Hit Readout of a Microchannel Plate Detector With a Three-Layer Delay-Line Anode*, IEEE Transactions On Nuclear Science **49**(5), 2477–2483 (2002).

[Jen05] U. D. Jentschura, S. Kotochigova, E.-O. L. Bigot, P. J. Mohr, B. N. Taylor, *Precise Calculation of Transition Frequencies of Hydrogen and Deuterium Based on a Least-Squares Analysis*, Physical Review Letters **95**(16), 163003 (2005).

[Jes04] V. Jesus, B. Feuerstein, D. Fischer, A. Rudenko, F. Afaneh, C. D. Schröter, R. Moshammer, J. Ullrich, *Atomic structure dependence of nonsequential double ionization of He, Ne and Ar in strong laser pulses*, J. Phys. B: At. Mol. Opt. Phys **37**, L161–L167 (2004).

[Jul91] P. S. Julienne, J. Vigue, *Cold collisions of Ground-State and Excited-State Alkali-Metal Atoms*, Phys. Rev. A **44**, 4464–4485 (1991).

[Kas89] M. A. Kasevich, E. Riis, S. Chu, R. G. Devoe, *RF-spectroscopy in an Atomic Fountain*, Phys. Rev. Lett. **63**, 612–616 (1989).

[Kaw93] J. Kawanaka, K. Shimizu, H. Takuma, F. Shimizu, *Quadratic collisional loss rate of a ^{7}Li trap*, Phys. Rev. A **48**(2), R883–R885 (Aug 1993).

[Kee00] M. L. Keeler, L. W. Anderson, C. C. Lin, *Electron-Impact Ionization Cross Section Measurements Out of the 5^2P Excited State of Rubidium*, Phys. Rev. Lett. **85**(16), 3353–3356 (Oct 2000).

[Kel64] L. V. Keldysh, *Ionization in the field of a strong electromagnetic wave (Multi-phonon absorption processes and ionization probability for atoms and solids in strong electromagnetic field)*, Zhurnal Eksperimental'noi I Teoreticheskoi Fiziki **47**, 1945–1957 (1964).

[Ket99] W. Ketterle, D. S. Durfee, D. M. Stamper-Kurn, *Making, probing and understanding Bose-Einstein condensates*, arXiv:cond-mat/9904034v2 (1999).

[Kil99] T. C. Killian, S. Kulin, S. D. Bergeson, L. A. Orozco, C. Orzel, S. L. Rolston, *Creation of an Ultracold Neutral Plasma*, Phys. Rev. Lett. **83**(23), 4776–4779 (Dec 1999).

[Kil03] T. C. Killian, V. S. Ashoka, P. Gupta, S. Laha, S. B. Nagel, C. E. Simien, S. Kulin, S. L. Rolston, S. D. Bergeson, *Ultracold neutral plasmas: recent experiments and new prospects*, J. Phys. A: Math. Gen. **36**, 6077–6085 (2003).

[Kni80] R. D. Knight, M. H. Prior, *Radiative lifetime of metastable* 2^3S_1 Li^+, Phys. Rev. A **21**(1), 179–187 (Jan 1980).

[Kno03] S. Knoop, J. W. Turkstra, R. Morgenstern, R. E. Olson, R. Hoekstra, *Multi-electron processes in slow* He^{2+}*–Na collisions measured with MOTRIMS*, Nucl. Instr. and Meth. in Phys. Res. B **205**, 560–567 (2003).

[Kno05] S. Knoop, R. E. Olson, H. Ott, V. G. Hasan, R. Morgenstern, R. Hoekstra, *Single ionization and electron capture in* He^{2+}*+Na collisions*, J. Phys. B.: At. Mol. Opt. Phys. **38**, 1987–1998 (2005).

[Kon93] K. Kondo, A. Sagisaka, T. Tamida, Y. Nabekawa, S. Watanabe, *Wavelength dependence of nonsequential double ionization in He*, Phys. Rev. A **48**(4), R2531–R2533 (Oct 1993).

[Kra97] V. P. Krainov, *Ionization rates and energy and angular distributions at the barrier-suppression ionization of complex atoms and atomic ions*, J. Opt. Soc. Am. B **14**(2), 425–431 (1997).

[Kra06] T. Kraemer, M. Mark, P. Waldburger, J. G. Danzl, C. Chin, B. Engeser, A. D. Lange, K. Pilch, A. Jaakola, H.-C. Nägerl, R. Grimm, *Evidence for Efimov quantum states in an ultracold gas of caesium atoms*, Nature **440**, 315–318 (2006).

[Kru83] P. Kruit, J. Kimman, H. G. Muller, M. J. van der Wiel, *Electron spectra from multiphoton ionization of xenon at 1064, 532, and 355 nm*, Phys. Rev. A **28**(1), 248–255 (Jul 1983).

[Kuz02] S. G. Kuzmin, T. M. O'Neil, *Numerical Simulation of Ultracold Plasmas: How Rapid Intrinsic Heating Limits the Development of Correlation*, Phys. Rev. Lett. **88**(6), 065003 (Jan 2002).

[Lan93] R. J. Lang, D. Mehuys, A. Hardy, K. M. Dzurko, D. F. Welch, *Spatial evolution of filaments in broad area diode lasers*, Appl. Phys. Lett **62**(11), 1209–1211 (1993).

[Lar98] S. Larochelle, A. Talebpour, S. L. Chin, *Non-sequential multiple ionization of rare gas atoms in a Ti:Sapphire laser field*, J. Phys. B: At. Mol. Opt. Phys. **31**, 1201–1214 (1998).

[Let88] P. D. Lett, R. N. Watts, C. I. Westbrook, W. D. Phillips, P. L. Gould, H. J. Metcalf, *Observation of Atoms Laser Cooled below the Doppler Limit*, Phys. Rev. Lett. **61**(2), 169–172 (Jul 1988).

[Lew94] M. Lewenstein, P. Balcou, M. Y. Ivanov, A. L'Huillier, P. B. Corkum, *Theory of high-harmonic generation by low-frequency laser fields*, Phys. Rev. A **49**(3), 2117–2132 (Mar 1994).

[Li89] X. F. Li, A. L'Huillier, M. Ferray, L. A. Lompré, G. Mainfray, *Multiple-harmonic generation in rare gases at high laser intensity*, Phys. Rev. A **39**(11), 5751–5761 (Jun 1989).

[Lin92] K. Lindquist, M. Stephens, C. Wieman, *Experimental and theoretical study of the vapor-cell Zeeman optical trap*, Phys. Rev. A **46**(7), 4082–4090 (Oct 1992).

[Lis99] F. Lison, P. Schuh, D. Haubrich, D. Meschede, *High-brilliance Zeeman-slowed cesium atomic beam*, Phys. Rev. A **61**(1), 013405 (Dec 1999).

[Lör95] H. Lörch, *Elektronenspektrum von Lithium nach kombinierter Laser- und Elektronenstossanregung*, Diploma thesis, Universität Freiburg, Freiburg (1995).

[Mac02] J. A. MacAskill, W. Kedzierski, J. W. McConkey, J. Domyslawska, I. Bray, *Measuring cesium electron impact cross-sections using a magneto-optical trap*, Journal of Electron Spectroscopy and Related Phenomena **123**(2-3), 173–184 (May 2002).

[Mar81] C. Martin, P. Jelinski, M. Lampton, R. F. Malina, H. O. Anger, *Wedge-and strip anodes for centroid -finding position sensitive photon and particle detectors*, Rev. Sci. Instrum. **52**, 1067 (1981).

[Mar98] O. Maragò, D. Ciampini, F. Fuso, E. Arimondo, C. Gabbanini, S. T. Manson, *Photoionization cross sections for excited laser-cooled cesium atoms*, Phys. Rev. A **57**, R4110–R4113 (6 1998).

[Mar07] S. Marmo, N. L. Manakov (2007), personal communication.

[McA96] W. I. McAlexander, E. R. I. Abraham, R. G. Hulet, *Radiative lifetime of the* $2P$ *state of lithium*, Phys. Rev. A **54**(1), R5–R8 (Jul 1996).

[McG97] J. H. McGuire, *Electron Correlation Dynamics in Atomic Collisions* (Cambridge University Press, 1997).

[Mea82] M. L. Meade, *Advances in lock-in amplifiers*, J. Phys. E: Sci. Instrum. **15**, 395–403 (1982).

[Met99] H. J. Metcalf, P. van der Straten, *Laser Cooling and Trapping* (Springer-Verlag, 1999).

[Mev93] E. Mevel, P. Breger, R. Trainham, G. Petite, P. Agostini, A. Migus, J.-P. Chambaret, A. Antonetti, *Atoms in strong optical fields: Evolution from multiphoton to tunnel ionization*, Phys. Rev. Lett. **70**(4), 406–409 (Jan 1993).

[Mew99] M.-O. Mewes, G. Ferrari, F. Schreck, A. Sinatra, C. Salomon, *Simultaneous magneto-optical trapping of two lithium isotopes*, Phys. Rev. A **61**(1), 011403 (Dec 1999).

[Mil88] D. R. Miller, *Free Jet Sources*, in *Atomic and Molecular Beam Methods* (Oxford University Press, Oxford/new York, 1988).

[MK97] T. Mayer-Kuckuck, *Atomphysik: eine Einfuehrung*, Teubner Studienbücher : Physik (Teubner, Stuttgart, 1997), 5th Edn.

[Mol97] P. A. Molenaar, P. van der Straten, H. G. M. Heideman, H. J. Metcalf, *Diagnostic technique for Zeeman-compensated atomic beam slowing: Technique and result*, Phys. Rev. A **55**(1), 605–614 (January 1997).

[Mon90] C. Monroe, W. Swann, H. Robinson, C. Wieman, *Very Cold Trapped Atoms in a Vapor Cell*, Phys. Rev. Lett. **65**(13), 1571–1574 (September 1990).

[Mor76] J. Morellec, D. Normand, G. Petite, *Resonance shifts in the multiphoton ionization of cesium atoms*, Phys. Rev. A **14**(1), 300–312 (Jul 1976).

[Mor07] T. Morishita, Z. Chen, S. Watanabe, C. D. Lin, *Two-dimensional electron momentum spectra of argon ionized by short intense lasers: Comparison of theory with experiment*, Physical Review A (Atomic, Molecular, and Optical Physics) **75**(2), 023407 (2007).

[Mos94] R. Moshammer, J. Ullrich, M. Unverzagt, W. Schmidt, P. Jardin, R. E. Olson, R. Mann, R. Dörner, V. Mergel, U. Buck, H. Schmidt-Böcking, *Low-Energy Electrons and Their Dynamical Correlation with Recoil Ions for Single Ionization of Helium by Fast, Heavy-Ion Impact*, Phys. Rev. Lett. **73**(25), 3371–3374 (December 1994).

[Mos96] R. Moshammer, M. Unverzagt, W. Schmitt, J. Ullrich, H. Schmidt-Böcking, *A 4π recoil-ion electron momentum analyzer: a high-resolution "microscope"for the investigation of the dynamics of atomic , molecular and nuclear reactions*, Nucl. Inst. Meth. B **108**, 425–445 (1996).

[Mos00] R. Moshammer, B. Feuerstein, W. Schmitt, A. Dorn, C. D. Schröter, J. Ullrich, H. Rottke, C. Trump, M. Wittmann, G. Korn, K. Hoffmann, W. Sandner, *Momentum Distributions of Ne^{n+} Ions Created by an Intense Ultrashort Laser Pulse*, Phys. Rev. Lett. **84**(3), 447–450 (Jan 2000).

[Mos07] R. Moshammer, Y. H. Jiang, L. Foucar, A. Rudenko, T. Ergler, C. D. Schröter, S. Lüdemann, K. Zrost, D. Fischer, J. Titze, T. Jahnke, M. Schöffler, T. Weber, R. Dörner, T. J. M. Zouros, A. Dorn, T. Ferger, K. U. Kühnel, S. Düsterer, R. Treusch, P. Radcliffe, E. Plönjes, J. Ullrich, *Few-Photon Multiple Ionization of Ne and Ar by Strong Free-Electron-Laser Pulses*, Phys. Rev. Lett. **98**, 203001 (2007).

[Mul83] H. G. Muller, A. Tip, M. J. van der Wiel, *Ponderomotive force and AC Stark shift in multiphoton ionisation*, J. Phys. B: At. Mol. Phys **16**, L679–L685 (1983).

[Mul93] P. Mulser, S. Uryupin, R. Sauerbrey, B. Wellegehausen, *Pondermotive potential and dynamical Stark shift in multiphoton ionization*, Phys. Rev. A **48**(6), 4547–4550 (1993).

[Mun01] S. R. Muniz, K. M. F. Magalhães, P. W. Courteille, M. A. Perez, L. G. Marcassa, V. S. Bagnato, *Measurements of capture velocity in a magneto-optical trap for a broad range of light intensities*, Phys. Rev. A **65**(1), 015402 (Dec 2001).

[Nes63] A. N. Nesmeyanov, *Vapor Pressure of the Chemical Elements* (Elsevier Publishing Company, National Bureau of Standards, Washington D.C., 1963).

[Ngu04] H. Nguyen, X. Flechard, R. Bredy, H. A. Camp, B. D. DePaola, *Recoil ion momentum spectroscopy using magneto-optically trapped atoms*, Review of Scientific Instruments **75**(8), 2638–2647 (2004).

[Nic92] W. Nicklich, H. Kumpfmüller, H. Walther, X. Tang, H. Xu, P. Lambropoulos, *Above-threshold ionization of Cesium under femtosecond laser pulses: New substructure due to strongly coupled bound states*, Phys. Rev. Lett. **69**(24), 3455–3458 (Dec 1992).

[Nie98] J. Nienhaus, *Elektronenspektrometrie an freien Natrium- und Barium-Atomen nach kombinierter Laser- und Elektronenstoßanregung*, Doktorarbeit, Albert-Ludwigs-Universität, Freiburg i. Br. (1998).

[NIS07] *NIST Atomic Spectra Database* (2007), http://physics.nist.gov/PhysRefData/ASD/index.html.

[Ort75] H. Orth, H. Ackermann, E. Otten, *Fine and Hyperfine Structure of the 2^2P Term of ^7Li; Determination of the Nuclear Quadrupole Moment*, Z. Phys. A **273**, 221–232 (1975).

[Pan86] L. Pan, L. Armstrong, Jr., J. H. Eberly, *Comments on the effect of the ponderomotive potential in the above-threshold ionization processes*, J. Opt. Soc. Am. B **3**(10), 1319 (1986).

[Pat83] E. Patzak, A. Sugimura, S. Saito, T. Mukai, H. Olesen, *Semiconductor laser linewidth in optical feedback configurations*, Electronics Letters **19**, 1026 (1983).

[Pat01] T. Pattard, J. Burgdörfer, *Half-collision model for triple photoionization of lithium*, Phys. Rev. A **63**(2), 020701 (Jan 2001).

[Pau94a] G. G. Paulus, W. Becker, W. Nicklich, H. Walther, *Rescattering effects in above-threshold ionization: a classical model*, J. Phys. B: At. Mol. Opt. Phys. **27**, L703–L708 (1994).

[Pau94b] G. G. Paulus, W. Nicklich, H. Xu, P. Lambropoulos, H. Walther, *Plateau in above threshold ionization spectra*, Phys. Rev. Lett. **72**(18), 2851–2854 (May 1994).

[Paw00] T. Pawletko, M. Houssin, M. Knoop, M. Vedel, F. Vedel, *High power broad-area diode laser at 794 nm injected by an external cavity laser*, Optics Communications **174**, 223–229 (2000).

[Per88] M. D. Perry, O. L. Landen, A. Szöke, E. M. Campbell, *Multiphoton ionization of the noble gases by an intense 10^{14}-W/cm^2 dye laser*, Phys. Rev. A **37**(3), 747–760 (1988).

[Pet84] G. Petite, F. Fabre, P. Agostini, M. Crance, M. Aymar, *Nonresonant multiphoton ionization of cesium in strong fields: Angular distributions and above-threshold ionization*, Phys. Rev. A **29**(5), 2677–2689 (May 1984).

[Phi82] W. D. Phillips, H. Metcalf, *Laser Deceleration of an Atomic Beam*, Phys. Rev. Lett. **48**(9), 596–599 (Mar 1982).

[Poe01] M. van der Poel, C. V. Nielsen, M.-A. Gearba, N. Andersen, *Fraunhofer Diffraction of Atomic Matter Waves: Electron Transfer Studies with a Laser Cooled Target*, Phys. Rev. Lett. **87**(12), 123201 (2001).

[Poh04] T. Pohl, T. Pattard, J. M. Rost, *Coulomb Crystallization in Expanding Laser-Cooled Neutral Plasmas*, Physical Review Letters **92**(15), 155003 (2004).

[Pra98] M. Praeger, V. Vuletic, T. Fischer, T. W. Hänsch, C. Zimmermann, *A broad emitter diode laser system for lithium spectroscopy*, Appl. Phys.B **67**, 163–166 (1998).

[Pro96] M. Protopapas, C. H. Keitel, P. L. Knight, *Atomic physics with super-high intensity lasers*, Rep. Prog. Phys. **60**, 389–486 (1996).

[Raa87] E. L. Raab, M. Prentiss, A. Cable, S. Chu, D. E. Pritchard, *Trapping of Neutral Sodium Atoms with Radiation Pressure*, Phys. Rev. Lett. **59**(23), 2631–2634 (Dec 1987).

[Rei94] H. R. Reiss, V. P. Krainov, *Approximation for a Coulomb-Volkov solution in strong fields*, Phys. Rev. A **50**(2), R910–R912 (Aug 1994).

[Res99] T. N. Rescigno, M. Baertschy, W. A. Isaacs, C. W. McCurdy, *Collisional Breakup in a Quantum System of Three Charged Particles*, Science **286**, 2474 (1999).

[Ric95] L. Ricci, M. Weidemüller, T. Esslinger, A. Hemmerich, C. Zimmermann, V. Vuletic, W. König, T. W. Hänsch, *A compact grating-stabilized diode laser system for atomic physics*, Opt. Commun. **117**, 541–549 (June 1995).

[Rit95] N. W. M. Ritchie, E. R. I. Abraham, Y. Y. Xiao, C. C. Bradley, R. G. Hulet, P. S. Julienne, *Trap-loss collisions of ultracold lithium atoms*, Phys. Rev. A **51**(2), R890–R893 (Feb 1995).

[Rot90] H. Rottke, B. Wolff, M. Brickwedde, D. Feldmann, K. H. Welge, *Multiphoton ionization of atomic hydrogen in intense subpicosecond laser pulses*, Phys. Rev. Lett. **64**(4), 404–407 (Jan 1990).

[Rud04a] A. Rudenko, K. Zrost, B. Feuerstein, V. L. B. de Jesus, C. D. Schröter, R. Moshammer, J. Ullrich, *Correlated Multielectron Dynamics in Ultrafast Laser Pulse Interactions with Atoms*, Phys. Rev. Lett. **93**, 253001 (2004).

[Rud04b] A. Rudenko, K. Zrost, C. D. Schröter, V. L. B. de Jesus, B. Feuerstein, R. Moshammer, J. Ullrich, *Resonant structures in the low-energy electron continuum for single ionization of atoms in the tunneling regime*, J. Phys. B.: At. Mol. Opt. Phys **37**, L407–L413 (2004).

[Rud05] A. Rudenko, B. Feuerstein, K. Zrost, V. L. B. de Jesus, T. Ergler, C. Dimopoulou, C. D. Schröter, R. Moshammer, J. Ullrich, *Fragmentation dynamics of molecular hydrogen in strong ultrashort laser pulses*, J. Phys. B: At. Mol. Opt. Phys. **38**, 487–501 (2005).

[Sam90] J. A. R. Samson, *Proportionality of electron-impact ionization to double photoionization*, Phys. Rev. Lett. **65**(23), 2861–2864 (Dec 1990).

[San95] C. J. Sansonetti, B. Richou, R. Engleman, L. J. Radziemski, *Measurements of the resonance lines of ^6Li and ^7Li by Doppler-free frequency-modulation spectroscopy*, Phys. Rev. A **52**(4), 2682–2688 (October 1995).

[Sch96] R. S. Schappe, T. Walker, L. W. Anderson, C. C. Lin, *Absolute Electron-Impact Ionization Cross Section Measurements Using a Magneto-Optical Trap*, Phys. Rev. Lett. **76**(23), 4328–4331 (Jun 1996).

[Sch98a] U. Schünemann, H. Engler, M. Zielonkowski, M. Weidemüller, R. Grimm, *Magneto-optic trapping of lithium using semiconductor lasers*, Opt. Comm. **158**, 263–272 (December 1998).

[Sch98b] V. Schyja, T. Lang, H. Helm, *Channel switching in above-threshold ionization of xenon*, Phys. Rev. A **57**(3), 3692–3697 (1998).

[Sch02] J. Schoser, A. Batär, R. Löw, V. Schweikhard, A. Grabowski, Y. B. Ovchinnikov, T. Pfau, *Intense source of cold Rb atoms from a pure two-dimensional magneto-optical trap*, Phys. Rev. A **66**(2), 023410 (Aug 2002).

[Sch03] M. Schulz, R. Moshammer, D. Fischer, H. Kollmus, D. H. Madison, S. Jones, J. Ullrich, *Three-dimensional imaging of atomic four-body processes*, Nature **422**, 48–50 (2003).

[Sco88] G. Scoles (Ed.), *Atomic and Molecular Beam Methods*, Vol. I (Oxford University Press, New York, 1988).

[Shv00] I. Shvarchuck, K. Dieckmann, M. Zielonkowski, J. T. M. Walraven, *Broad-area diode-laser system for a rubidium Bose-Einstein condensation experiment*, Appl. Phys. B **71**, 475–480 (August 2000).

[Spi95] L. Spielberger, O. Jagutzki, R. Dörner, J. Ullrich, U. Meyer, V. Mergel, M. Unverzagt, M. Damrau, T. Vogt, I. Ali, K. Khayyat, D. Bahr, H. G. Schmidt, R. Frahm, H. Schmidt-Böcking, *Separation of Photoabsorption and Compton Scattering Contributions to He Single and Double Ionization*, Phys. Rev. Lett. **74**(23), 4615–4618 (Jun 1995).

[Spi05] F. Spiegelhalder, *Setting up a Lithium Magneto-Optical Trap as a Target for a Reaction Microscope*, Diploma thesis, Universität Heidelberg / Max-Planck-Institut für Kernphysik, Heidelberg (2005).

[Sta05] C. A. Stan, W. Ketterle, *Multiple species atom source for laser-cooling experiments*, Rev. Sci. Inst. **76**, 063113 (2005).

[Ste86] S. Stenholm, *The semiclassical theory of laser cooling*, Reviews of Modern Physics **58**(3), 699–739 (1986).

[Str85] D. Strickland, G. Mourou, *Compression of amplified chirped optical pulses*, Opt. Comm. **56**, 219 (1985).

[Tan92] C. C. Tannoudji, J. Dupont-Roc, G. Grynberg, *Atom-photon interactions* (John Wiley & Sons, 1992).

[Tem02] J. G. C. Tempelaars, R. J. W. Stas, P. G. M. Sebel, H. C. W. Beijerinck, E. J. D. Vredenbregt, *An intense slow and cold beam of metastable Ne(3s)* $^3P_2$ *atoms*, Eur. Phys. J. D **18**, 113–121 (2002).

[Ton03] X. M. Tong, Z. X. Zhao, C. D. Lin, *Abnormal pulse duration dependence of the ionization probability of Na atoms in intense laser fields*, J. Phys B: At. Mol. Opt. Phys **36**, 1121–1127 (2003).

[Ton05] X. M. Tong, C. D. Lin, *Empirical formula for static field ionization rates of atoms and molecules by lasers in the barrier suppression regime*, J. Phys. B: At. Mol. Opt. Phys. **38**, 2593–2600 (2005).

[Tow95] C. G. Townsend, N. H. Edwards, C. J. Cooper, K. P. Zetie, C. J. Foot, A. M. Steane, P. Szriftgiser, H. Perrin, J. Dalibard, *Phase-space density in the magneto-optical trap*, Phys. Rev. A **52**(2), 1423–1440 (Aug 1995).

[Tur01] J. W. Turkstra, R. Hoekstra, S. Knoop, D. Meyer, R. Morgenstern, R. E. Olson, *Recoil Momentum Spectroscopy of Highly Charged Ion Collisions on Magneto-Optically Trapped Na*, Phys. Rev. Lett. **87**, 123202 (2001).

[Uhl05] L. J. Uhlmann, R. G. Dall, A. G. Truscott, M. D. Hoogerland, K. G. H. Baldwin, S. J. Buckman, *Electron Collisions with Laser Cooled and Trapped Metastable Helium Atoms: Total Scattering Cross Sections*, Phys. Rev. Lett. **94**(17), 173201 (May 2005).

[Ull03a] J. Ullrich, R. Moshammer, A. Dorn, R. Dörner, L. P. H. Schmidt, H. Schmidt-Böcking, *Recoil-ion and electron momentum spectroscopy: reaction-microscopes*, Rep. Prog. Phys. **66**, 1463–1545 (2003).

[Ull03b] J. Ullrich, V. P. Shevelko, *Many-Particle Quantum Dynamics in Atomic and Molecular Fragmentation* (Springer, Heidelberg, 2003).

[Var88] D. A. Varshalovich, A. N. Moskalev, V. K. Kershonski, *Quantum Theory of Angular Momentum* (World Scientific, Singapore, 1988).

[Vol96] U. Volz, H. Schmoranzer, *Precision Lifetime Measurements on Alkali Atoms and on Helium by Beam-gas-laser spectroscopy*, Physica Scripta T **65**, 48 (1996).

[Wal93] B. Walker, E. Mevel, B. Yang, P. Breger, J. P. Chambaret, A. Antonetti, L. F. DiMauro, P. Agostini, *Double ionization in the perturbative and tunneling regimes*, Phys. Rev. A **48**(2), R894–R897 (Aug 1993).

[Wal94a] B. Walker, B. Sheehy, L. F. DiMauro, P. Agostini, K. J. Schafer, K. C. Kulander, *Precision Measurement of Strong Field Double Ionization of Helium*, Phys. Rev. Lett. **73**(9), 1227–1230 (Aug 1994).

[Wal94b] T. Walker, P. Feng, *Measurement of collisions between laser-cooled atoms*, Advances in Atomic, Molecular and Optical Physics **34**, 125 (1994).

[Wal03] J. Walls, R. Ashby, J. Clarke, B. Lu, W. van Wijngaarden, *Measurement of isotope shifts, fine and hyperfine structure splittings of the lithium D lines*, Eur. Phys. J. D **22**, 159–162 (2003).

[Wea83] R. Weat, M. Astle, W. Beyer (Ed.), *CRC Handbook of Chemistry and Physics* (CRC Press, Boca Raton, 1983), 64th Edn.

[Web00] T. Weber, M. Weckenbrock, A. Staudte, L. Spielberger, O. Jagutzki, V. Mergel, F. Afaneh, G. Urbasch, M. Vollmer, H. Giessen, R. Dörner, *Recoil-Ion Momentum Distributions for Single and Double Ionization of Helium in Strong Laser Fields*, Phys. Rev. Lett. **84**(3), 443–446 (Jan 2000).

[Web06] T. Weber, A. O. Czasch, O. Jagutzki, A. K. Müller, V. Mergel, A. Kheifets, E. Rotenberg, G. Meigs, M. H. Prior, S. Daveau, A. Landers, C. L. Cocke, T. Osipov, R. D. Muino, H. Schmidt-Böcking, R. Dörner, *Complete photofragmentation of the deuterium molecule*, Nature **443**, 1014 (2006).

[Weh98] R. Wehlitz, M.-T. Huang, B. D. DePaola, J. C. Levin, I. A. Sellin, T. Nagata, J. W. Cooper, Y. Azuma, *Triple Photoionization of Lithium*, Phys. Rev. Lett. **81**(9), 1813–1816 (Aug 1998).

[Wie03] R. Wiehle, B. Witzel, H. Helm, E. Cormier, *Dynamics of strong-field above-threshold ionization of argon: Comparison between experiment and theory*, Phys. Rev. A **67**(6), 063405 (Jun 2003).

[Wil55] W. C. Wiley, I. H. McLaren, *Time-of-Flight Mass Spectrometer with Improved Resolution*, Rev. Sci. Instrum. **26**(12), 1150–1157 (December 1955).

[Wol88] B. Wolff, H. Rottke, D. Feldmann, K. H. Welge, *Multiphoton-ionization of hydrogen atoms in intense laserfields*, Z. Phys. D - Atoms, Molecules and Clusters **10**, 35–43 (1988).

[Wol97] S. Wolf, H. Helm, *Ion-recoil energy measurement in photoionization of laser-cooled rubidium*, Phys. Rev. A **56**, R4385–R4388 (1997).

[Wol00] S. Wolf, H. Helm, *Ion-recoil momentum spectroscopy in a laser-cooled atomic sample*, Phys. Rev. A **62**(4), 043408 (October 2000).

[Wut97] M. Wutz, H. Adam, W. Walcher, *Handbuch Vakuumtechnik* (Vieweg, Braunschweig, 1997), 6th Edn.

[Zro05] K. Zrost, *Wechselwirkung von Atomen und kleinen Molekülen mit intensiven, ultra-kurzen Laserpulsen*, Phd-thesis, Universität Heidelberg / Max-Planck-Institut für Kernphysik, Heidelberg (2005).

[Zuo95] T. Zuo, A. Bandrauk, *Charge-resonance-enhanced ionization of diatomic molecular ions by intense lasers*, Phys. Rev. A **52**, R2511–R2514 (1995).

Erklärung

Ich versichere, daß ich diese Arbeit selbständig verfaßt und keine anderen als die angegebenen Quellen und Hilfsmittel benutzt habe.

Heidelberg, den 4. Juni 2007

Jochen Steinmann